EFFECTS OF NANOCARRIERS ON *SACCHAROMYCES CEREVISIAE*

by
Özlem Özbek
B.S., Chemical Engineering, Boğaziçi University, 2016

Submitted to the Institute for Graduate Studies in
Science and Engineering in partial fulfillment of
the requirements for the degree of
Master of Science

Graduate Program in Chemical Engineering
Boğaziçi University
2019

EFFECTS OF NANOCARRIERS ON *SACCHAROMYCES CEREVISIAE*

APPROVED BY:

Prof. Kutlu Ulgen (Thesis Supervisor)	.....
Assist. Prof. Nazar Ileri Ercan (Thesis Co-supervisor)	.....
Prof. Zeynep Petek Çakar	.....
Assoc. Prof. Bora Garipcan	.....
Assoc. Prof. Sezen Soyer Uzun	.....

DATE OF APPROVAL: 02.08.2019

ACKNOWLEDGEMENTS

First of all, I would like to express my sincere gratitude to my thesis supervisor Prof. Kutlu Ülgen and thesis co-supervisor Asst. Prof. Nazar İleri Ercan for their guidance, valuable support and motivation throughout this study. The advices they have given to me throughout this study were invaluable.

I would like to thank my thesis committee members, Prof. Zeynep Petek Çakar, Assoc. Prof. Bora Garipcan and Assoc. Prof. Sezen Soyer Uzun, for devoting their valuable time and effort to my thesis and providing guidance and recommendations.

I would particularly like to express my special thanks to Feyza Kevser Öner as she was always there through every step of this graduation journey. I am deeply grateful for her never ending support, friendship and encouragement in my life. I am also very thankful to my beloved friends Müge Kasım, Begüm Yağcı, Elif Esvap, Ayşegül Karakuş, Dilara Göreke, Selin Baç Bilgi, Özge Selçuk, Merve Yüce, Seymen İlke Kaykanat and Aysun Urhan for always being by my side and for their endless friendship, encouragement and support. I would also like to thank all of the members of KB440 for their support, motivation and encouragement.

Finally, my grateful thanks are extended to my family members. I would like to express my profound gratitude to my beloved grandmother Semiha Kın for her endless love, support, caring and patience throughout all my life. She was always by my side all the time and this accomplishment would not have been possible without her. I would like to express my thanks to my beloved brother Atay Kaan Özbek for his endless love, encouragement, motivation and sense of humor. I would like to thank my precious mother Belma Özbek and my precious father Sunullah Özbek for their endless love, encouragement and support. This journey would not have been possible without them. This thesis is devoted to my family for their love, trust and support throughout my life.

ABSTRACT

EFFECTS OF NANOCARRIERS ON *SACCHAROMYCES CEREVISIAE*

Nanocarriers have been studied widely owing to their promising features in the field of drug delivery and they improve pharmacokinetic properties, biodistribution, solubility and stability, provide controlled release and site-specific delivery of the therapeutic agents, and decrease the toxicology at the targeted site. Also, the nanocarriers exhibit unique physiochemical properties by the opportunity of changing their sizes, compositions, shapes and surface properties. The present study involves a combined approach of the characterization of the polystyrene latex nanoparticles (PSL NPs), DOPC liposomes and hybrid NPs (DOPC encapsulated PSL NPs) having different concentrations, sizes, surface charges and functional groups and the determination of their cytotoxicity effects towards the Sac6:RFP tagged *S. cerevisiae* cells as well as the investigation of the possible uptake mechanisms of the PSL NPs. DLS, ELS, STEM and TEM analyses were carried out to characterize the nanoparticles. CFU analysis and CLSM imaging were performed to determine the toxicity of the nanoparticles. Negatively charged PSL NPs do not show toxicity at 50 mg/L, while the concentration increase results in viability decrease, such that at 800 mg/L, the viability percentage of the cells is around 60%. 30nm-C-n PSL NPs are internalized by the cells and show toxic effect if they enter to the nucleus. 50nm-A-p and 100nm-A-p PSL NPs are non-toxic at 50 mg/L, but they are fully toxic after 100 mg/L concentration. They cover the cell surface and inhibit the cell viability. Hybrid nanoparticles exhibit opposite viability results compared to their PSL NP counterparts. The long-term toxicity effect study reveals that negatively charged and carboxyl functionalized PSL NPs at 100-200 mg/L concentrations do not show toxicity after 15 generations of NP exposure. Endocytosis inhibitor treatment experiments show that the PSL NPs are internalized by diffusion, partly microtubule dependent or a different factor mediated endocytosis.

ÖZET

NANOTAŞIYICILARIN *SACCHAROMYCES CEREVISIAE* ÜZERİNDEKİ ETKİLERİ

Nanotaşıyıcılar, ilaç dağıtımı alanındaki ümit verici özellikleri nedeniyle geniş bir şekilde çalışılmıştır ve farmakokinetik özelliklerin, biyolojik dağılımın, çözünürlük ve stabilitenin gelişmesini, terapötik ajanların kontrollü salınımını ve bölgeye özgü dağıtımını sağlarlar, ve hedeflenen bölgedeki toksik etkiyi azaltırlar. Ayrıca, nanotaşıyıcılar, boyutlarının, bileşimlerinin, şekillerinin ve yüzey özelliklerinin değiştirilebilmesi imkanı ile eşsiz fizyokimyasal özellikler sergiler. Bu çalışma, farklı konsantrasyonlara, boyutlara, yüzey yüklerine ve fonksiyonel gruplara sahip polistiren lateks nanopartiküllerin (PSL NP), DOPC lipozomların ve hibrit NP'lerin (DOPC kapsüllenmiş PSL NP'lerin) karakterizasyonunu, bunların Sac6:RFP işaretlenmiş *S. cerevisiae* hücrelerindeki sitotoksisite etkilerinin incelenmesini ve PSL NP'lerin olası hücre içine alım mekanizmalarının araştırılmasını içeren kombine bir yaklaşımdan oluşmaktadır. NP'leri karakterize etmek için DLS, ELS, STEM ve TEM analizleri yapılmıştır. NP'lerin toksisitesinin belirlenmesinde CFU analizi ve CLSM görüntülemeleri yapılmıştır. Negatif yüklü PSL NP'ler 50 mg/L'de toksisite göstermezken, konsantrasyon artışı canlılık azalmasına neden olmaktadır, örneğin 800 mg/L'de hücre canlılığı %60 civarındadır. 30nm-C-n PSL NP'lerin hücre içine alındığı ve çekirdeğe girdiği takdirde toksik olduğu görülmüştür. 50nm-A-p ve 100nm-A-p PSL NP'ler ise 50 mg/L'de toksik olmayıp, ancak 100 mg/L'den sonra tamamen toksik etkiye sahiptirler, hücre yüzeyini kaplar ve hücre canlılığına engel olurlar. Hibrit NP'ler, PSL NP karşılıklarına kıyasla zıt canlılık sonuçları sergilerler. Uzun süreli toksisite etkisi çalışması, negatif yüklü ve karboksil fonksiyonlu PSL NP'lerin 100-200 mg/L konsantrasyonlarda, 15 kuşak NP maruziyetinden sonra toksisite göstermediğini ortaya koymaktadır. Endositoz önleyici muamele deneyleri, PSL NP'lerin difüzyon, kısmen mikrotübüle bağlı veya farklı bir faktör aracılı endositozla hücre içerisine alındıklarını göstermektedir.

TABLE OF CONTENTS

LIST OF FIGURES

LIST OF TABLES

LIST OF SYMBOLS

a	Radius of the particle
D	Translational diffusion coefficient
d(H)	Hydrodynamic diameter
e	Electronic charge constant
f(κa)	Henry's function
I	Ionic strength of the dispersion medium
k	Boltzmann's constant
N_{Av}	Avogadro's number
T	Temperature of the sample
r_x	Net rate of cell mass growth
t_d	Doubling time of the yeast cells
x	Yeast cell mass per unit culture volume
ε	Dielectric constant
ε_0	Permittivity of the vacuum
ε_r	Relative permittivity of the medium
ζ	Zeta potential
η	Viscosity of the dispersion medium
κ	Debye parameter
μ	Specific growth rate of yeast cells
μ_{ep}	Electrophoretic mobility
μ_{max}	Maximum specific growth rate of yeast cells

LIST OF ACRONYMS/ABBREVIATIONS

3-D	Three dimensional
20nm-C-n	20 nm, carboxyl modified, negatively charged
30nm-C-n	30 nm, carboxyl modified, negatively charged
60nm-C-n	60 nm, carboxyl modified, negatively charged
50nm-A-p	50 nm, amine modified, positively charged
50nm-A-n	50 nm, amine modified, negatively charged
100nm-A-p	100 nm, amine modified, positively charged
100nm-A-n	100 nm, amine modified, negatively charged
200nm-A-n	200 nm, amine modified, negatively charged
CFU	Colony Forming Unit
CLSM	Confocal Laser Scanning Microscope
DLS	Dynamic Light Scattering
DMSO	Dimethyl Sulfoxide
DOPC	1,2-Dioleoyl-sn-glycero-3-phosphocholine
ELS	Electrophoretic Light Scattering
Em	Emission
Ex	Excitation
FITC	Fluorescein isothiocyanate
FL	Fluorescein
G(d)	Gaussian Distribution Function
IntDen	Integrated Density
Lat-A	Latrunculin-A
NP	Nanoparticle
OD	Optical Density
PBS	Phosphate Buffered Saline
PDI	Polydispersity Index
PSL	Polystyrene Latex
RFP	Red Fluorescent Protein
SEM	Scanning Electron Microscopy

STEM	Scanning Transmission Electron Microscopy
TEM	Transmission Electron Microscopy

1. INTRODUCTION

The delivery of the suitable treatment agents into a particular location in the body has become very important to provide efficient medical treatment. The usage of site-specific drugs ensures improved dosage control, decreases the side effect and toxicity of the drugs. Without drug targeting, the drugs may influence the other tissues, which are not diseased, and they may get out of the metabolism quickly before they can perform their functions [1]–[3].

There are mainly three aspects in the subject of drug targeting; (i) selection of the appropriate target at the specific stage of a disease, (ii) determination of a drug that provide the treatment of this specific disease efficiently and (iii) transportation of the drug to the specific target in the most stable form to eliminate the problems that may arise from immunogenic and nonspecific interactions. In this context, nanoparticles have been considered as beneficial carrier materials to target specific drugs to the diseased part of the body when they are bound to a particular ligand [4].

Recently, nanoparticles have been used in the studies of diagnosis, vaccination and treatment of certain diseases by the processes of drug targeting owing to their physical and chemical features [1]. Nanocarriers can be produced at various sizes, surface functionalization and morphologies. Some examples of nanocarriers include inorganic nanoparticles such as iron oxide and gold, and organic nanoparticles like polymeric nanoparticles, liposomes (closed vesicles which consist of phospholipid bilayers) and micelles [2].

Technologically developed drugs for drug targeting exhibit some advantages over the classical drugs owing to their improved pharmacokinetic features and lower toxicity [5]. However, possible unfavorable effects of nanoparticles in terms of the nanotoxicity have been a debate. Some studies have reported that nanoparticles cause low or no toxicity in eukaryotic cells compared to those in prokaryotic cells [6]. The toxicology of these materials should be further investigated to find out both the short-term and long-term effects on the living organisms and the environment [5].

The usage of hybrid of nanoparticles which consist of the combination of different types of nanoparticles has attracted great attention in the field of nanotechnology. The design and synthesis of hybrid nanoparticles provide several advantages in drug delivery systems as they improve the features of the nanoparticles by reducing or eliminating their negative effects [7]. This cooperative design of hybrid nanoparticles improves the physicochemical properties of the particles such as size, surface charge and morphology, provides mechanical stability and high drug loading capacity. By hybrid nanoparticle configuration, the therapeutic index of the drugs can be enhanced by enhancing their effectiveness, whereas the toxicity and the required drug dosage can be reduced [7], [8].

The cells take up the nanoparticles through the plasma membrane by an energy requiring mechanism like endocytosis or by passive penetration. The cell forms a closed endocytic vesicle to internalize the nanoparticles rather than taking them up directly. On the other hand, nanoparticles, which are internalized by the membrane penetration contact with the cell directly, that is favorable for drug targeting. However, the adhesion of the nanoparticles on the cell membrane causes cytotoxicity, because this event changes the permeability and structure of the cell membrane. The investigations related to the interaction of the nanoparticles with the cell membrane and the understanding of the uptake mechanism of the different types of nanoparticles by the different cells have become very important to increase the efficiency of the applications in drug targeting [1], [9].

Saccharomyces cerevisiae is a unicellular eukaryotic organism, which has been commonly used as a model for biological studies. *Saccharomyces cerevisiae* cells possess some similarities with the plant and animal cells in terms of the cellular structure and functional configuration. The major metabolic pathways present in the human are similar to those in *Saccharomyces cerevisiae* cells. The yeast cells have the orthologues of 30% of the genes related to certain diseases existing in humans. Hence, the investigations carried out in *Saccharomyces cerevisiae* cells in terms of the toxicology will provide an insight to figure out the toxicology in the human cells [10]. In this study *Saccharomyces cerevisiae* is used as the model organism to determine the endocytic pathway in the internalization of nanocarriers including polystyrene latex nanoparticles (PSL NPs), DOPC liposomes and hybrid nanoparticles were obtained by the encapsulation of DOPC phospholipids on to the PSL NPs.

In the second chapter of this thesis which is denoted as “Theoretical Background”, the types of nanoparticles, the toxicology of the nanoparticles on the living organisms and material characterization techniques are explained. In the “Materials and Methods” section, which is the third chapter, the experiments and the characterization methods carried out in this study are explained. In the fourth chapter, which is “Results and Discussion”, the results obtained by the experimental work and the characterization analyses are shown and discussed. In the fifth section, which is “Conclusions and Recommendations”, the acquirements in this study are given briefly and the recommendations are provided for the future studies.

2. THEORETICAL BACKGROUND

2.1. Types of Nanoparticles

Nanoparticles are colloidal materials which have sizes between 10 to 1000 nm. The types of the nanoparticles are divided into two parts: inorganic nanoparticles, such as iron oxide, quantum dots, silica, graphene and organic nanoparticles such as polymers, dendrimers, micelles and liposomes. Nanoparticles can be used in the diagnosis and the treatment of certain diseases such as cancer, congenital and autoimmune diseases. Specific molecules can be incorporated to them or nanoparticles are used without association of any molecule [11].

2.1.1. Inorganic Nanoparticles

Some of the widely used inorganic nanoparticles are explained below.

- Iron oxide nanoparticles

Iron oxide nanoparticles have iron oxide (Fe_3O_4) core coated by dextran to enhance the physical features of the material. Due to the magnetic characteristic, iron oxide nanoparticles are superior to be used as magnetic resonance imaging (MRI) contrast agent and they are used in therapeutic magnetic hypothermia. These properties make superparamagnetic iron oxide nanoparticles (SPIONS) to be used for both diagnostic and therapeutic purposes. But there are some drawbacks such as limited space in the core and the small loading volumes [12].

- Gold nanoparticles

Gold nanoparticles have been used in biomedical applications owing to their physicochemical and optical properties. But, because of the non-hollow organization, the internal loading is prevented, also they have limited biodegradation and biocompatibility properties [12].

- Mesoporous silica nanoparticles (MSNs)

Mesoporous silica nanoparticles (MSNs) have mesopores of 2 to 50 nm which are encircled by silica structure. Their loading capacity is high owing to the high surface area to volume ratio. Also, they have good biodegradability and biocompatibility properties. But there are some drawbacks such as low stability and rapid clearance [12].

- Carbon nanoparticles

Carbon nanoparticles like carbon nanotubes consist of one layer of graphite in a sheet or cylindrical configuration. They have superior loading capacity, excellent optical and electrical properties and low costs. They can be used in imaging and diagnostics due to the promising properties. However, they have low biodegradability and can cause pulmonary damage and accumulate in organs which make them unable to be used in *in vivo* systems [12].

- Quantum dots (QDs)

Quantum dots (QDs) generally comprise of cadmium selenide core and zinc selenide cap. They can be used in biosensing applications owing to their optical properties and bright color emission. However, the toxicology is a drawback to be used *in vivo* [12].

2.1.2. Organic Nanoparticles

Some of the widely used organic nanoparticles are explained below.

- Dendrimers

Dendrimers are branched polymer composites, generally synthetic, produced by controlled polymerization reactions. Dendrimers have a core surrounded by branched polymer chains. They can be produced in various size and shapes. Also, they are non-immunogenic and show superior solubility. However, further studies are needed to be carried out in terms of toxicity and biocompatibility [12].

- Polymeric micelles

Polymeric micelles have a structure of aggregated hydrophobic polymer core which is encircled by hydrophilic polymer chains. Their circulation time is long, because they are not taken up by the macrophage system due to the small size and hydrophilic property. Also, hydrophobic drugs can be incorporated to the hydrophobic exterior of the polymeric micelles. Although they have excellent biocompatibility, they are prone to the morphological changes and the release of the incorporated material [12].

- Liposomes

Liposomes are spherical closed vesicles with one ore bilayer membranes. They are made up of phospholipids or steroids. The formation of the liposomes is spontaneous when they are dispersed into an aqueous medium [13]. The size of the liposomes varies between 0.025 μm to 2.5 μm and it is a significant parameter to specify the circulation half-life of the liposome. Also, the number of bilayers affect the efficiency of drug encapsulation [14]. As a scope of the present study, detailed information about the liposome formation, types and preparation methods and their usage in drug delivery systems are explained in section 2.3.

- Polymeric nanoparticles

Polymeric nanoparticles are divided into two categories: nanospheres and nanocapsules. Nanospheres, which comprise of solid polymer matrix, have an ability to entrap hydrophobic drugs whereas nanocapsules, which include an aqueous hydrophobic core, can encapsulate hydrophilic substances. Polymeric nanoparticles are promising nanocarriers owing to their flexible conformations. They have also constant rate of release of encapsulated material. However, the purification and storage of these nanoparticles are difficult which prevent them to be produced for large scale applications [12].

2.2. Nanoparticles in Drug Delivery Systems

Nanoparticles can be produced with different sizes, shapes and surface properties to achieve the required pharmacological activity of the drug molecules. It was suggested that

the nanoparticles which have diameter between 5 to 10 nm are taken away from the circulation system and removed by the kidney. If the particle diameters are more than 15 μm, they accumulate in the organs of the body like liver, marrow, spleen. According to the type of the cell, the uptake and the biodistribution of the nanoparticles are determined. The nanoparticles which have sizes less than 20 nm are taken up by the cells via pinocytosis, and those less than 100 nm are internalized by the cells via phagocytosis. It was shown that the nanoparticles with sizes between 10 to 200 nm are more effective in most of the drug distribution systems [11].

Technologically developed nanoscale drug delivery systems have recently taken great attention in the field of nanomedicine [2]. The delivery of the suitable therapeutic agents into the specific location of the body is very significant to provide efficient treatment of the diseases. Without using drug targeting systems, some problems such as low effectiveness, deficiency in selectivity and weak biodistribution of the drugs can be encountered. The usage of drug delivery systems in the diagnosis and treatment of the diseases offers various advantages over the conventional drug applications [13]. The advantages of usage of nanoparticles in targeted drug delivery systems are as follows:

- They increase the efficiency of the drugs as they target diseased site of the body [11].
- Biodistribution of the drugs increases at the target cells, which minimizes nonspecific binding of drug molecules to non-diseased cells [2].
- They decrease the possible side effects and toxicity of the drugs [1], [11].
- They provide improved dosage control [3]. Lower dosages to reach therapeutic activity as the concentration of the drug is high target site of the body when nanoparticles are used [11]. Metabolism of the drug quickly or excretion without functioning are prevented [2].
- Rapid degradation of the drugs is prevented [11].
- Nanoparticles which have the desired biological and physicochemical characteristics are internalized by the cells easier than the larger substances [13].

In the design of novel nanoparticles, the incorporation and release of the drug, the drug formulation and the shelf life, biocompatibility, biodistribution and targeting, and the functionality of the molecule should be taken into consideration as fundamental

requirements [15]. Although the technologically developed drugs, which have improved pharmacokinetic features for drug targeting, are considered as advantageous over the classical drugs possible unfavorable effects of nanoparticles in terms of the nanotoxicity have been a debate [5]. Also, the potential adverse effects of the remainder materials after used as drug carriers should rigorously be considered [15]. In this aspect, the selection of the biodegradable nanoparticles with restricted lifetime is significant to be used in drug delivery systems [15].

2.3. Liposomes

Liposomes are spherical shaped closed vesicles which are made from natural non-toxic phospholipids and cholesterol. They have one or more bilayers and the polar heads are located at the interior (core) and the exterior aqueous phase of the liposome [14]. Liposomes are promising substances for drug delivery systems in terms of size flexibility, biodegradability, biocompatibility, low toxicity, hydrophilic and hydrophobic structure [11], [14], [16].

Due to the both hydrophilic and hydrophobic (called amphipathic) properties, liposomes are promising materials in drug delivery processes as both aqueous and lipid-based drugs can be incorporated. According to the preparation technique, size, surface charge and lipid composition, the properties of the liposomes can be changed. Also, the physicochemical properties such as fluidity and rigidity of the liposomes are affected by the type of the phospholipid used in the liposome preparation [14]. Liposomes have been widely used in the field of pharmaceutical and cosmetic industries owing to their superior characteristics to be used as carriers. Liposomes offer different type of drugs (hydrophilic or hydrophobic) to be entrapped without decomposition and to be released at specific targets which property makes them promising substances to be used in site-specific drug delivery. In spite of having several advantages of liposomes such as biocompatibility, biodegradability, non-toxic and non-immunogenic behavior, there are also some drawbacks in using liposomes. Some of the disadvantages are low solubility, short self-life, low stability and possibility of leakage of the encapsulated drug [14].

2.3.1. Liposome Formation

Amphiphilic molecules, such as phospholipids, surfactants, block copolymers are substances that have two discrete covalently bonded parts; one of the part attracts the polar solvents such as water and the other part attracts non-polar solvents such as hydrocarbons [17]. After the amphiphilic molecules are dispersed in a solvent, aggregates appear with different size and morphologies. Amphiphiles can form in different types; they dissolve in a solution, they form monolayer aggregates like micelles or accumulate as bilayers according to the type of the solvent, temperature and the concentration of the substance [16].

The phospholipid membrane shape becomes spherical after the driving force for vesicle formation becomes larger than the resistance of bending force. After the size of the phospholipid molecules reaches to a critical size, the shape of the structure becomes similar to disk during the process of vesicle formation. When the shape of the structure is round, the circumference of the phospholipid structure is minimum and this is favorable to keep its energy at minimum. To decrease the energy even more, the shape of the phospholipid structure becomes similar to a spherical can and finally it takes its spherical shape. The vesicle formation process is a spontaneous process because the energy of the system decreases uniformly [18].

2.3.2. Types and Preparation Methods of Liposomes

Liposomes are categorized according to their size and number of bilayers as follows [19], [20]:

- Small unilamellar vesicles (SUV), sizes between 20 to 100 nm,
- Large unilamellar vesicles (LUV), sizes between 100 to 1000 nm,
- Giant unilamellar vesicles (GULV), sizes larger than 1000 nm,
- Oligolamellar vesicles (OLV), size range 100–1000 nm,
- Multilamellar large vesicles (MLV), sizes larger than 500 nm,
- Multivesicular vesicles, sizes from 1000 nm to several thousand nanometers.

Liposomes have the ability of entrapping the hydrophilic agents into their aqueous cores and hydrophobic agents hydrophobic agents into their phospholipid bilayer membranes to protect from the external degradation. Since the membrane of the liposomes is similar to the biological molecules, they can easily be internalized by the cell membrane. Moreover, the ability of changing the size, structure, surface charge and functionalizations of the liposomes makes them promising for drug delivery applications [21].

For the commonly used liposome formulation methods, there are 5 main preparation stages [14], [20]:

- Lipids are dissolved in an organic solvent.
- Lipids are dried from organic solvent.
- Dried lipids (powder form) are hydrated in an aqueous media.
- Liposomes are purified or filtered to reach homogeneous size distribution.
- After preparation, liposomes are analyzed whether it is achieved the desired properties.

Liposomes can be synthesized by various methods which can be categorized as conventional methods that include the techniques suitable for laboratory-scale applications, and novel methods which are more favorable for large-scale applications because of the requirement of specialized equipments. The examples of the conventional liposome preparation techniques are thin film hydration method, which is the technique used in this present study, reverse phase evaporation method, solvent injection method, solvent injection method, detergent removal method and heating method, and the examples novel liposome preparation techniques are microfluidic channel method and supercritical fluidic method [20].

The conventional liposome preparation methods are explained below.

- Thin Film Hydration Method

The thin film hydration, also known as Bingham method, is the original technique that is applied for the preparation of liposomes which is easy to handle and used in widespread

[19]. The lipid is dissolved in an organic solvent and the solvent is evaporated and the lipids are dried on the surface of the flask forming a thin lipid film. Then the lipid film is hydrated with an aqueous medium. Sonication is commonly used to decrease the size of the vesicles to obtain small unilamellar vesicles (SUV) from Multilammellar Vesicles (MLV). There are two types of sonicators which are bath type and probe type sonicators. In probe type sonicator, the tip of the sonicator probe is placed inside the liposome solution and the ultrasonic energy is applied to break down the large vesicles and this method is highly effective. Some of the drawbacks of this method are the heat generation which can be eliminated by using ice bath and the possibility of contamination because of the contact with the sonicator probe. In bath type sonicator, the liposome solution in the vessel is placed in the water bath. In this method, the temperature control is easier and there is no possibility of contamination as solution does not contact directly with the component of the sonicator. Also, the extrusion method using the polycarbonate filters is used to decrease the size of the liposomes [20].

- Reverse Phase Evaporation Method

In this method water-in-oil emulsion is constituted between the aqueous phase which contains hydrophobic molecules and the organic phase which includes lipids and hydrophobic molecules. To homogenize the mixture sonication is carried out. The organic phase is eliminated with reduced pressure and the liposomal solution is formed. The liposomes without solution medium can be obtained by the methods such as dialysis, centrifugation or sepharose 24 column [20].

- Solvent Injection Method

In this method, the lipid dispersion in ethanol or diethyl ether is injected rapidly into an aqueous medium. As a result of this process, mostly polydispersed liposomes are obtained, but they are contaminated by the organic solvent because of the azeotrope formation with water. Also, these experiments are performed at room temperature or higher temperatures regarding the water miscibility of the organic solvent. These factors may decrease the stability and safety of the liposomes [20].

- Detergent Removal Method

In this method, the lipids are dissolved in aqueous medium including detergents at their at critical micelle concentrations (CMC). In the process of detergent removal, the phospholipid molecules are released individually to self-assemble into bilayered form. The process is carried out generally through dialysis bag, polystyrene-based absorber beads or gel permeation chromatography [20].

- Heating Method

This method attracts attention because of the exclusion of the organic solvents in the preparation of the liposomes. After one hour of hydration, the lipids are heated above their transition temperatures for one hour in the presence of glycerin or 3% propylene glycol which are hydrating agents. If cholesterol is included, the mixture is heated up to 100°C due to its melting point. The liposomes can be used without additional sterilization and the hydrating agents are not needed to be removed because the materials are suitable for the usage in pharmaceutical applications. Also, these materials prevent liposomes from coagulation and sedimentation and also the hydroxyl groups in them shows cryoprotective effect [20].

2.3.3. Liposomes in Drug Delivery Systems

Liposomes, which are spherical closed vesicles, have been the first drug carrier that is analyzed. The usage of liposomes as drug carriers present various advantages such as the increasing solubility of the of the drugs and the enhancing the pharmacokinetic properties such as quick metabolism, decreased side effects, improved therapeutic index and anticancer activity [13].

There are many factors which influence the drug release from the liposomes: composition of the liposome, osmotic gradient, pH and the environment. It was shown that the cells interact with the liposomes via fusion adsorption, lipid transfer and endocytosis. Various types of drugs have been incorporated to the liposomes such as anticancer drugs, antibiotics, neurotransmitters, anti-inflammatory, and antirheumatic drugs [13].

There are some debates regarding the usage of liposomes in drug delivery systems. For example, they tend to accumulate in the cells which are not targeted, hence it may cause cell death regarding to the drug molecule liposomes encapsulate. In this aspect, the development of novel liposomes, which contain specific biologic substances such as proteins, antigens, is very significant to increase the selectivity of the drug [13].

2.4. Liposome-Nanoparticle Hybrid Nanoparticles

Technologically developed nanoparticles take great attention in the field of nanotechnology especially for drug targeting processes. In this aspect the incorporation of different nanoparticles, called as hybrid nanoparticles, serves as promising systems in terms of decreasing or preventing the negative effects of one material in the presence of the other one while keeping its positive effects [7].

Liposomes, as mentioned earlier, are closed vesicles of phospholipid bilayers. Liposomes are non-toxic [11], biodegradable [11] and biocompatible [22] materials which have been recently used as drug carriers in the field of biotechnology. Both hydrophilic and hydrophobic substances can be incorporated into the liposomes [22] which property makes liposomes a good substitute for delivering specific substances into the cells of the organism. The properties of the liposomes can be changed according to the type of the lipid that arranges the fluidity or the rigidity of the vesicle, the size, the preparation technique, the lipid composition and the surface charge [14]. But, the mechanical instability of bare liposomes has been a debate [8]. Because there is a possibility of the leakage of the encapsulated substance outside of the liposomes [11]. Thus, to improve the physicochemical properties of the bare liposome, the nanoparticle encapsulation to form hybrid particle is a promising way for an effective drug delivery system. By means of the hybrid system, the mechanical stability, narrow size distribution, controlled morphology and the drug loading capacity of the liposomes are improved [8].

There are several techniques to encapsulate specific nanoparticles to the liposomes such as thin film hydration (TFH), interdigitation-fusion, reverse evaporation (REV), and lipid vesicle metallization. The multilamellar vesicles forms after most of these methods are applied, and then by carrying out extrusion, multilamellar vesicles turn into the unilammellar

vesicles. The nanoparticles which are not encapsulated by liposomes are removed from the solution by several methods such as ultra-filtration, ultra-centrifugation, gel filtration chromatography and dialysis. The different types of nanoparticle-hybrid systems can be formed according to the location of the nanoparticle in the liposome: nanoparticles within the lipid bilayer of the liposome, nanoparticles inside the aqueous core of the liposome, nanoparticles on the liposome surface, nanoparticle aggregates with the liposomes free nanoparticles with the liposome solution [22].

Liposome encapsulated nanoparticles were investigated by different studies. The assembly of the monodisperse sulfate-charged polystyrene submicrometer particles and zwitterionic/cationic lipid vesicles, consisting of 1,2-dipalmitoyl-*sn*-glycero-3-phosphocholine and 1,2-dipalmitoyl-3 trimethylammonium propane, was called LipoParticle [23]. The production of the assemblies of these materials in a stable form has been shown to be depended on the size homogeneity of the vesicle suspension, the charge of the lipid molecules, the vesicle-to-particle ratio and also the ionic strength. If cationic lipid molecules were used in the production of LipoParticles, the main driving force in the formation of assembly was found to be the electrostatic forces. These forces provided the connection of lipid polar heads and sulfate moieties of polystyrene particles and also had an effect on the stabilization of LipoParticles. Thus, when the continuous phase has low ionic strength, and the lipid substances have high cationic charge, then distinctive and reproducible LipoParticles can be obtained [23].

Liposomes prepared by Dioctadecyldimethylammonium chloride (DODAC), bromide (DODAB) or dihexadecyl phosphate (DHP) are favorable in terms of having rigid gel state at room temperature and possessing smoother interface than the other colloids. But the polydispersity is a problem. Polystyrene latex nanoparticles are quite homodisperse systems, which can be beneficial to remove the disadvantages. As a result, with the incorporation of liposomes and polystyrene latex nanoparticles, the particle-stabilized liposomes can be obtained successfully [24].

The phospholipid DLPC, 1,2-dilauroyl-*sn*-glycero-3-phosphocholine was used to produce liposomes, and negatively charged carboxyl surface functionalized polystyrene latex nanoparticles, which were 20 nm in diameter, were used to incorporate them within

the liposomes [25]. Liposomes were produced by extrusion method in 1% volume concentration and obtained as 200 nm in diameter. The nanoparticles were sonicated and incorporated with liposomes. Nanoparticles were adsorbed on the surface of the liposomes, this case was explained by the attractive forces between the polystyrene latex nanoparticles and liposomes and also by the entropy increase in the displacement of the water molecules on the surface of the liposomes by the nanoparticles [25].

2.5. Toxicology and the Uptake Mechanism of the Nanocarriers on *Saccharomyces cerevisiae* Cells

Latex beads are polymeric particles which are produced by the emulsion polymerization of a monomer such as styrene. In polymerization process of styrene, the monomer is stabilized with the surfactants and dispersed in an aqueous medium [26]. Polystyrene, whose linear formula is $[CH_2CH(C_6H_5)]_n$ consists of a linear hydrocarbon chain to which a benzene ring is attached to every second carbon atom [27]. Recently, polystyrene latex nanoparticles have attracted great attention because of the nanoscale size, uniform shape and narrow size distribution. They have been used in many areas such as biomedicine, food and textile industry, paint coating and optical sensor. However, their potential pollution effect in aquatic environment has been a debate and their usage requires great attention. Polystyrene latex nanoparticles can be classified in three major groups considering their surface charge: cationic, anionic or neutral. Their surface charge depends on the surface modifications that the commonly used functional groups are amine $(NH_2)^-$ and carboxyl $(COOH)^-$ groups. These surface modifications enable them to have similar molecular structure to the proteins and they can pass through the cell membrane for drug delivery systems [28].

The toxicity, internalization, dispersion and adhesion properties of Polystyrene Latex (PSL) Nanoparticles (NPs) with different functional groups (amine, carboxyl, sulfate) were investigated in *Saccharomyces cerevisiae* yeast cells [6], [29]. The diameters of the PS NPs were 50 nm. The viability of the yeast cells was determined by colony count methods as well as by confocal microscope. According to the experimental findings, PSL NPs with negatively charged surface groups caused very low or no toxicity in the yeast cells. As the charge on the yeast cells was negative, the PS NPs with negative charges and the cells

repelled each other and hence these PS NPs did not cover the cell surfaces and the cells maintained the viability. Positive amine (p-Amine) functionalization of PSL NPs resulted in high toxicity in 5 mM NaCl solution as a result of the strong attraction forces. Nevertheless, PS NPs with p-Amine surface charge did not affect viability in 154 mM NaCl solution as a result of the weaker attraction forces. From the confocal and atomic force microscopy analysis, the reason of the cell death in 5 mM NaCl solution was explained by the cells being coated by PSL NPs. Hence, the cells died because of the inhibition of NP transportation through the cell membrane. In 154 mM NaCl solution, the PS NPs were internalized through the process of endocytosis by the yeast cells and the cells continue to live [6], [29]. Also, when the results were compared with the findings of the previous study using 100 nm diameter PSL NPs, the size of the NPs was demonstrated to have little effect on the toxicity and uptake [29]. The effect of PSL NP size on the toxicity and the internalization was very low for NPs smaller than 100 nm [6].

The uptake mechanism of the nanocarriers, which contain the drug, is very important for their biological activity. These mechanisms are generally associated with the size of the particles. If the sizes of the particles are less than 500 nm, the non-phagocytic cells internalize the particles by an energy dependent process. If the particles are smaller than 200 nm, the cells internalize these particles by clathrin-coated pits. To provide effective internalization, the nanocarriers are targeted for the uptake of the receptors [4]. There are different uptake mechanisms, which are passive diffusion of the drug, nonspecific phagocytosis of a nanoparticle, drug uptake by pinocytosis and receptor-mediated endocytosis [4].

The toxicology and the uptake mechanism of oxidized multi-walled carbon nanotubes (MWCNTs) in the concentration range between 0–600 mg/L, have been investigated when MWCNTs were subjected to *Saccharomyces cerevisiae* yeast cells for 24 h [10]. In the study, it was indicated that internalized MWCNTs were placed in the lysosome, vacuole, endosome, mitochondria, multivesicular body and perinuclear region in *Saccharomyces cerevisiae*. It was also found that maximum MWCNT concentration inside the yeast cells was obtained after 3 hour of exposure with a value of 209.61 mg/g and MWCNT concentration reached the steady state condition after 18 h. Transmission electron microscope (TEM) was used and the endocytosis inhibition study was carried out by setting

the conditions at 4°C and 5% ethanol in which the endocytosis is inhibited. Also, the genes related to the endocytosis were investigated. Overexpression of the endocytosis related genes, END3, END6, Sla2 and Rsp5, has indicated that the uptake occurs by endocytosis. On the other hand, overexpression of these genes was found in MWCNT concentration greater than 200 mg/L, which was explained by the formation of aggregates in higher concentrations. MWCNT concentration lower than 100 mg/L showed no toxicity on the *Saccharomyces cerevisiae* cells. Three possible uptake mechanisms were found: (1) direct penetration of single MWCNTs, (2) endocytosis of single MWCNTs, and (3) endocytosis of the aggregated MWCNTs. Mainly the single MWCNTs were taken up by the cells via direct penetration and MWCNT aggregates were internalized by endocytosis [10].

In the yeast and mammalian cells, the substance uptake into the cell through the cell membrane is mainly carried out by the process of Clathrin-mediated endocytosis (CME). Although various endocytic pathways have been described in mammalian cells, there is only one pathway, which is clathrin-mediated pathway, identified for the yeast cell. Nevertheless, the construction of various mutant strains that inhibits the present pathway can lead different uptake mechanisms to occur for the uptake of bulk lipid and fluid substances in the yeast. Aghamohammadzadeh *et al*. (2014) have determined a new pathway for the material uptake in the yeast cell. This new pathway that is different from dynamin function, has been obtained by the inhibitor actin-disrupting drug Latrunculin-A (Lat-A), which prohibited the motion of Sla1, Sla2, and Sac6 proteins. It has been shown that the presence of actin binding protein Abp1 was crucial for the endocytosis if the original pathway did not exist. The overexpression of ABP1 gene has been shown to be fatal for the cell, whereas the deletion of Abp1 has caused a decreased invagination in the process of endocytosis. If low amount of Lat-A has been added to the system, Sla-GFP, which is an endocytic reporter, and GFP-Snc1, which is a transporter, have been suppressed in the internalization. Although the original pathway was interrupted, the uptake of bulk lipid and fluid substances were not inhibited and cortical F-actin structures were not segregated. In conclusion, an Abp1-dependent internalization mechanism has been identified in *S. cerevisiae* cells [30].

2.6. Uptake Mechanism of Polystyrene Latex Nanoparticles in Different Cells Types

The mechanism of uptake and the governing factors of polystyrene latex nanoparticles with 20 nm, 100 nm, 200 nm, 500 nm, 1 µm and 2 µm diameter were investigated by targeting NPs to bone marrow-derived macrophages (BMDM), 293T kidney epithelial cells and L929 fibroblasts [1]. The mechanism for the uptake of nanoparticles was driven mostly by endocytosis and NPs aggregated in intracellular vesicles. It was identified that the nanoparticles aggregated in the endosomal parts, which showed the capability of internalization in different cell types. The nanoparticles passed through the organelles in acidic conditions. The uptake mechanisms for the particles with few micrometers in size were by phagocytosis or micropinocytosis. Smaller nanoparticles were internalized by the cells via different pathways such as macropinocytosis, phagocytosis, clathrin-mediated endocytosis, caveolae-mediated endocytosis, and clathrin- and caveolae-independent pathways. It was also found that the characteristic properties of the nanoparticle affected the type of uptake mechanism. According to the ultrastructural morphology analysis, there were various uptake mechanisms for a certain nanoparticle in mammalian cells, pointing out the complexity of the interactions. The nanoparticle internalization path varied according to the type and the size of the nanoparticles as well as the cells, time and energy availability. Furthermore, in bone marrow-derived macrophages, the infection and activation conditions also affected the uptake mechanism, which required the comprehension of the pathogenesis of certain diseases in order to achieve efficient applications [1].

A study was carried out by Lunov *et al*. (2011) to understand the uptake mechanism of the nanoparticles (NPs) with carboxyl (PS-COOH) and amino functionalized (PS-NH_2) polystyrene (PS) groups by the human macrophage cells, undifferentiated monocytic THP-1 cells and PMA differentiated monocytic THP-1 cells using different media, buffer (HBSS) or human serum. The size of NPs was about 100 nm in diameter. The characterization of the NPs by their physicochemical properties was performed by dynamic light scattering (DLS) and UV/vis absorption spectroscopy. Physical properties of these nanoparticles were found to be similar in terms of the hydrodynamic diameter, surface density, and the quantity of the fluorescent dye PMI. But there were differences in the value of zeta potentials, which represent the surface charge of these nanoparticles. The effect of surface charge on the

internalization kinetics and mechanisms of these nanoparticles by macrophages and THP-1 cells was investigated. Most of the NPs were found to be taken by macrophages. THP-1 cells showed lower phagocytic capacity compared to those of macrophages. In the toxicity analysis, a critical change in cell viability that might be caused by NPs was not observed. Macrophages internalized PS-COOH four times more than THP1 cells, in serum-containing medium. On the contrary, THP-1 cells internalized PS-NH_2 faster than macrophages in both media. The uptake of PS-NH_2 nanoparticles was similar among three different cells in serum containing medium. Macropinocytosis was employed in the internalization of PSNH_2 nanoparticles by both macrophages and differentiated THP-1 cells, whereas THP-1 cells internalized nanoparticles by dynamin-dependent endocytosis [31].

2.7. Material Characterization and Analysis Techniques

2.7.1. Dynamic Light Scattering (DLS) Analysis

Dynamic light scattering (DLS) is an analytical analysis technique to determine the diffusion coefficients and hydrodynamic diameter of the molecules and particles in the solution. The size of the particles ranging from the nanometer to micrometer can be characterized by DLS method and this makes it highly preferable in the field of biotechnology. Hydrodynamic size analysis provides the information of the particle about its aggregation state, crystal formation, association reactions, etc. [32].

DLS measures Brownian motion and associated to this, particle sizes are measured. Brownian motion is the random motion of the particles resulting from the solvent molecules present in the particle solution. If the particle is large, the Brownian motion is slower and vice versa. The samples are usually in liquid form for DLS analysis. Also, the temperature of the solution is important to be known, because the viscosity of a liquid changes with the temperature. The velocity of the Brownian motion is specified by the term translational diffusion coefficient [33].

The size of the particles is obtained from the translational diffusion coefficient by applying the Stokes-Einstein equation as follows:

$$d(H) = \frac{kT}{3\pi\eta D} \tag{2.1}$$

Where,
d(H) is the hydrodynamic diameter,
D is the translational diffusion coefficient,
k is the Boltzmann's constant,
T is the temperature of the sample,
η is the viscosity of the dispersion medium.

The hydrodynamic diameter calculated by DLS method refers to the diffusion of the particles within the fluid. The value of the hydrodynamic diameter equals to the diameter of the sphere which has the same translational diffusion coefficient as the particle. Also, the translational diffusion coefficient depends on the structure of the surface, the concentration and the ion types present in the solution [33].

2.7.2. Electrophoretic Light Scattering (ELS) Analysis

Determination of the zeta potential is carried out by using Electrophoretic Light Scattering (ELS) analysis device. Electrophoretic Mobility (EPM) and the zeta potential values are obtained by ELS analysis. Zeta potential is an important parameter which shows the electrostatic interactions in particle solutions and it is significant to analyze the stability of the colloidal solutions. In general, colloidal solutions present in an aqueous medium contains an electrical charge and this charge at the surface of the particles has an impact on the distribution of the ions in the surrounding interfacial area. When the concentration of the opposite ions raises near to the surface of the particle, an electrical double layer (liquid layer around the particle) is formed. There are two regions of electrical double layer: an inner region (Stern layer) and outer layer (diffuse layer), in the first one the ions are strongly bound whereas in the latter one the ions are combined weakly compared to the inner region. There is a conceptional boundary within the diffuse layer inside this boundary the particles and the ions are stable. The ions inside this boundary move with the movement of the particle. The ions which present at the outside of this boundary are placed with the bulk solution. The zeta

potential is the electrical potential between the stern layer and the diffuse layer, which is called as slipping plane [34].

Zeta potential of the nanoparticles is calculated based on their electrophoretic mobility (EPM) values by using Henry's equation using the Smoluchowski approximation. This equation is generally valid for colloidal particles with structured surfaces which are known as hard particles/surfaces [34].

Henry's Equation is expressed as follows:

$$\mu_{ep} = \frac{2\varepsilon\zeta f(\kappa a)}{3\eta} \tag{2.2}$$

$$\frac{1}{\kappa} = \frac{\epsilon_0 . \varepsilon . k . T}{2000 . e^2 . I . N_{Av}} \tag{2.3}$$

Where,

μ_{ep} is the electrophoretic mobility,

ε is the dielectric constant,

ζ is the zeta potential,

κ is the Debye parameter, which represents electrical double layer thickness

a is the radius of the particle,

f(κa) is Henry's function,

e is the electronic charge constant,

N_{Av} is the Avogadro's number,

I is the ionic strength of the dispersion medium.

For the nanocarriers in a polar media with the ion concentration larger than 10 mM, Henry's function, $f(\kappa a)$, takes approximately its maximum value which is 1.5. This is known as Smoluchowski approximation. For non-polar media $f(\kappa a)$ is approximated to its minimum value which is 1. This is known as Huckel approximation. The most suitable approximation for $f(\kappa a)$ in water based medium related to biological applications is 1.5 [35].

Smoluchowski equation which is used to calculate the zeta potential of the nanoparticles is as follows [29]:

$$\zeta = (\frac{\mu_{ep}\eta}{\varepsilon_{\mathrm{r}}\varepsilon_0}) \tag{2.4}$$

Where,

ε_{r} is the relative permittivity of the medium,

ε_0 is the permittivity of the vacuum,

2.7.3. Transmission Electron Microscopy (TEM) Analysis

Transmission electron microscopy (TEM) technique has been widely used in characterization of the nanoscale structures in biological and material science and engineering. TEM analysis provides to be informed about the structure, morphology (size and shape) and crystallographic properties of the sample. In TEM, the electron beams are focused by metal apertures and electromagnetic lens and this process is grounded on the wavelike property of the electrons which act as negatively charged particles. Then the electrons which have a small range of energy can pass through and, are deflected by magnetic or electric fields. The transmitted electrons are applied to the sample of thickness within 100 nm that is located in the TEM column. Condenser lens is used to obtain the crystal structure information of a sample by the paralleled electrons beams. After passing the sample, the electromagnetic lens system with two lenses refocuses and magnifies the transmitted electrons and they are reflected to a phosphor screen. This process enables to turn the images of the electrons into a visible organization. With TEM imaging, high resolution of the images is provided and even the fine structure of the crystals can be obtained by using the electrons having short wavelength. Moreover, the TEM column should be kept in extremely high vacuum to prevent the movement of the electrons to the atmosphere, thus the mean free path of the electrons in TEM column is improved [36].

2.7.4. Scanning Transmission Electron Microscopy (STEM)

The scanning transmission electron microscope (STEM) is a type of characterization technique for the nanostructures in which the principles of both transmission electron microscopy (TEM) and scanning electron microscopy (SEM) are used in combination. In STEM, very small diameter of electron beam is used to form a transmission image of a thin specimen similar to TEM. There are some differences in the images obtained by the STEM imaging from TEM imaging. In STEM, multiple signals can be obtained to generate bright field, annular dark field (ADF) and spectroscopic images obtained by the electrons which have lost their energy after excitement of particular inner shell or band levels or by the determination of the emitted characteristic X-rays [37]. STEM has some advantages over TEM in allowing the use of the signals that cannot be spatially correlated with TEM such as secondary and scattered beam electrons, characteristic X-rays and electron energy loss [38]. In STEM, a very delicately focused beam of electrons around the sample are scanned as in the SEM analysis [38]. The working principle of STEM is similar to the scanning electron microscope (SEM) in which a focused electron beams, that are scanned over the sample, are formed and the images are generated by the collection of the specific signals. A serial signal stream is generated by the interaction between the beam electrons and the sample atoms. The difference of the STEM over SEM technique is the usage of thin samples which allows the imaging of the specimens in transmission mode [39]. The one of the advantage of the STEM imaging over the SEM imaging is the enhancement of spatial resolution [38].

2.7.5. Confocal Laser Scanning Microscopy (CLSM)

Confocal Laser Scanning Microscopy (CLSM) is a microscopic device that provides improved optical resolution and contrasted images. A spatial pinhole which is placed to the confocal plane of the lens is used to remove the images coming from out of focus plane. In this way, the out-of-focus light rays are eliminated. In conventional microscope, the lights coming from out-of-focus plane lead to a blurred image. In confocal microscopy, the light coming from the in-focus plane is visualized by the objective of the microscope in a way that the light passes through the pinhole, that out-of-focus plane is obstructed by the pinhole [40], [41]. Three dimensional (3-D) image of the samples is constructed by the special design of the confocal microscopy which eliminates the response of the sample that comes from the

out-of-focus plane and it is very sensitive to the responses obtained from in-focus plane [40]. The set of images is taken at different depths with the help of optical sectioning and these images constitute 3-D image which gives improved structural information of the specimen [41].

In the confocal microscope, the sample to be imaged is excited by the laser. The term excitation means that the fluorophores (dyes) are excited by absorption which results in a detectable fluorescence. The light which comes from the laser goes through the pinhole. The light is reflected by the dichroic mirror and focalized by the objective of the microscope to a small point in the sample. After the fluorescence which is emitted by the fluorophores (dyes) in the specimen is assembled by the microscope objective, the sample is visualized onto the detection pinhole which is ahead of the photo-detector. The dichroic mirror reflects the light which has shorter wavelength such as 488 nm from an Argon-ion laser and it transmits the light of a longer wavelength such as the fluorescence which has larger wavelength than 510 nm from fluorescein [40].

In recent years, confocal microscopy has attracted great attention owing to its great properties of providing high quality images of the samples compared to the conventional optical microscopes. It provides enhanced investigation of the nanostructures in intracellular trafficking. In confocal microscopy, a technique called as Z-stacking (focus stacking) has been used to constitute several images taken at several focal distances. This technique provides to the formation of a composite image of larger depth of field. In this way high magnification in-focus images are obtained as the field depth is reduced with the magnification. Thus, the visualization of the nanostructures regarding their intracellular localization can be improved by the confocal microscopy imaging [41].

3. MATERIALS AND METHODS

3.1. Chemicals and Reagents Used in the Experiments

The chemical materials used in the experiments in this study were given in Table 3.1.

Table 3.1. The properties of the Chemical and Reagents Used in the Experiments.

No	Material	Manufacturer	Form
2810305 Cas. 7447-40-7	Phosphate Buffered Saline (PBS) tablets	MP Biomedicals	Tablet
Cas. 3326-32-7	Fluorescein	Alfa Aesar	Powder
Cas. 25535-16-4	Propidium Iodide (PI)	BioFroxx	Powder
Cas. 8012-01-2	Yeast Extract	Merck	Powder
Product no. 411030	Agar Bios Special LL	Biolife Italiana	Powder
Cas. 50-99-7	Glucose	Merck	Powder
Avanti# 850375	DOPC (1,2-Dioleoyl-sn-glycero-3-phosphocholine)	Avanti Polat Lipids, Inc.	Powder
Cas. 67-66-3	Chloroform	Merck, EMSURE® ACS,ISO,Reag. Ph Eur	Liquid
Cas. 50-00-0	Formaldehyde	Merck, stabilized with about 10% methanol Ph Eur,BP,USP	Liquid
Cas. 67-68-5	Dimethyl sulfoxide (DMSO)	Merck, EMPLURA®	Liquid
Cas. 76343-93-6	Latrunculin-A (Lat-A)	Sigma-Aldrich	Waxy Solid
Cas. 31430-18-9	Nocodazole	Carbosynth	Powder

In the experiments, polystyrene latex nanoparticles (PSL NPs) in the form of aqueous suspensions, having different sizes (between 20 nm to 200 nm), surface functionalization groups (amine or carboxyl) and surface charges (positive or negative) are used. Detailed information on the properties of the nanoparticles and the supplier are given in Table 3.2.

Table 3.2. Properties of Polystyrene Latex Nanoparticles (PSL NPs) Used in This Study.

No	NPs and Yeast	Manufacturer	Nominal Diameter (nm)	Fluorescence	Composition
C37261	Carboxyl	Molecular Probes by Life Technologies	20	-	4.00 % solids
L5155-1ml	Carboxyl	Sigma	30	+ (Ex: 470 nm, Em: 505 nm)	2.50 % solids
C37263	Carboxyl	Molecular Probes by Life Technologies	60	-	4.00 % solids
L0780-1ml (Positively charged)	Amine	Sigma	50	+ (Ex: 360 nm, Em: 420 nm)	2.50 % solids
L0780-1ml (Negatively charged)	Amine	Sigma	50	+ (Ex: 360 nm, Em: 420 nm)	2.50 % solids
L9904-1ml	Amine	Sigma	100	+ (Ex: 475 nm, Em: 540 nm)	2.50 % solids
Cat# 16586	Amine	Polysciences	100	-	2.60 % solids
Cat# 15699	Amine	Polysciences	200	-	2.60 % solids

3.2. Methods

3.2.1. Liposomes

3.2.1.1. DOPC Liposome Preparation. Liposomes were produced from phospholipid DOPC (1,2-Dioleoyl-sn-glycero-3-phosphocholine) which was purchased from Avanti Polar Lipids Inc. (850375, 18:1 (Δ9-Cis) PC (DOPC)). Stock DOPC solution was prepared at 5 mg lipid (DOPC)/ml chloroform concentration and kept in the refrigerator at -20°C. Liposomes were synthesized by thin-film hydration method. 500 µl of stock solution was mixed with 5ml chloroform. The nitrogen gas was blown on the lipid solution to evaporate the chloroform and let the thin lipid film form on the surface of the glass. 10 ml 1XPBS solution was added on to the lipid film. The final concentration of the lipid solution was 0.25 mg DOPC lipid/ ml of PBS solution.

The sonication was carried out for 150 seconds (5 cycles of 30 seconds sonication) using a probe type sonicator, Branson Sonifier 450. After each of the cycle, cooling process was applied to eliminate the heating effect of sonication and keep the solution temperature constant. The solution was kept in shaker for 1 hour at 100 rpm agitation and room temperature. The solution was filtered with 0.2 µm syringe filter to obtain liposomes with uniform size distribution. FEI-Philips XL30 Environmental Scanning Electron Microscope with Field Emission Gun (Equipped with EDAX-Energy Dispersive X-ray Analysis Unit) was used in STEM (Scanning Transmission Electron Microscope) mode to characterize the synthesized liposomes.

3.2.1.2. Fluorescein Encapsulation into DOPC Liposomes. Fluorescein dye loaded DOPC liposomes were synthesized by adding fluorescein dye during the self-assembly process to visualize the liposomes in confocal microscopy. 0.1 mg/ml concentration of fluorescein dye in 1XPBS solution was added onto the thin lipid film which was formed after drying process with nitrogen gas. During the self-assembly of liposome formation via sonication, the dye molecules were incorporated inside the liposomes. The solution was shaken at 100 rpm and 24.5°C for 1 hour, then filtered using 0.2 µm syringe filter to homogenize the liposomes in terms of size distribution To remove the excess fluorescein dye which was not incorporated within the liposomes, Amicon Ultra-15 Centrifugal Filter Units with Molecular Weight Cut

Off (MWCO) value of 30,000 was used in the ultrafiltration process. The liposome solution was centrifuged at 5000 rpm and room temperature for 1 hour using Sigma 2-16PK centrifuge. After centrifugation, the content of the filtrate was the unloaded fluorescein dye in 1XPBS solution and the residue was the fluorescein loaded liposomes. Finally, fresh 1XPBS solution was added to the residue and the solution was kept in the refrigerator at 4°C until the time of usage.

3.2.2. PSL NP Encapsulated Liposomes (Hybrid Nanoparticles)

Hybrid nanoparticles were synthesized by encapsulating PSL NPs inside the empty DOPC liposomes during the formation process of liposomes. Required concentration of nanoparticle solution was prepared in 1XPBS solution. After thin film formation, this solution was added. The same procedure as in the liposome preparation described in the section 3.2.1.1 was applied. The synthesized hybrid nanoparticles and their PSL NP counterparts were characterized with TEM (Transmission Electron Microscopy) analysis using Delong Instrument, LVEM 5.

3.2.3. Dynamic Light Scattering (DLS) and Zeta Potential Analyses

The mean diameter, Polydispersity Index (PDI), electrophoretic mobility and the zeta potential of the PSL NPs, liposomes, hybrid nanoparticles and the yeast cells, which were in 1XPBS solution dispersion medium, were measured by particle size and zeta potential analyzer (Brookhaven Instruments 90Plus Particle Size/Zeta Analyzer).

3.2.4. Construction of Growth Curve Experiments for Sac6:RFP tagged *S. cerevisiae* Cells

3.2.4.1.Yeast Solution Preparation for Growth Curve Experiment. Two empty bottles, two 250 ml erlenmeyer flasks, pipette tips and graduated cylinders were autoclaved at 121°C for 15 minutes. For 100 ml yeast broth medium 3 g glucose was mixed with 30 ml distilled water in one bottle. In another bottle 0.5 g yeast extract was mixed with 70 ml distilled water. The containing glucose solution (30 g/L concentration) was autoclaved at 121°C for 3 minutes. The containing yeast extract solution (5 g/L concentration) was autoclaved at 121°C for 15

minutes. After the autoclave process was completed, the solutions were mixed and waited to be cooled. At this time Sac6:RFP tagged *S. cerevisiae* cells were taken from the refrigerator at -80°C. 50 ml yeast broth medium was taken into the 250 ml erlenmeyer flask. 400 µl of yeast cells were added to this medium. Yeast cell solution (µl) divided by yeast broth medium (ml) ratio was arranged to become less than 10:1.

3.2.4.2. Yeast Pre-culture Preparation and Optical Density (OD) Measurement. The yeast solution was taken into the shaker at 28°C and 180 rpm for 16 hours. After 16 hours pre-culture was obtained. 50 ml yeast broth medium was taken into the empty flask. 400 µl yeast pre-culture was added to the flask. This solution was taken into the shaker at 28 °C and 180 rpm for 1 hour. After 1 hour the optical density of the yeast solution was measured in UV Spectrophotometer. Optical Density (OD) measurements were taken according to 600 nm wavelength. When the value of Optical Density (OD) exceeded 0.8, the sample solution was diluted 1:1 with yeast broth medium and the measurements were carried out according to this dilution. The solution was taken into the shaker again and the optical density measurement was carried out in each hour for 22 times.

3.2.5. Cytotoxicity Experiments

3.2.5.1. Sterilization. All the necessary apparatus for the cytotoxicity experiments such as pipette tips, glass inoculating L-shaped spreaders erlenmeyer flasks, beakers, schott bottles microcentrifuge tubes and racks, which were used in the cytotoxicity experiments, were sterilized in autoclave at 121°C for 15 min. The laminar flow hood and the necessary equipments were sterilized with technical grade ethanol. Also, the liquid components of the yeast medium (yeast extract solution or yeast extract+agar solution) were sterilized in the autoclave at 121°C for 15 min. Glucose and PBS solutions were sterilized in the autoclave for 3 min and 10 min, respectively, at 121°C. The PBS solution was sterilized in the autoclave at 115°C for 10 min.

3.2.5.2. Yeast Strain and Growth in Liquid Medium. In the experiments wild type haploid Sac6:RFP (Red Fluorescent Protein) tagged Saccharomyces cerevisiae strain (EY0987; ATCC 201389: MATα his3Δ1 leu2Δ0 lys2Δ0 ura3Δ0 [42], [43]) was used as a unicellular

eukaryotic model organism. The Sac6:RFP tagged strain was kindly provided by Peter Arvidson.

The stock yeast culture was prepared by mixing 500 µl of yeast solution, 0.1 g/L peptone, 0.2 g/L yeast extract, and 0.2g/L glucose medium with 30% v/v glycerol solution. The stock solution was stored in the refrigerator at -80°C. Before the usage, the stock yeast solution was taken out of the refrigerator and defrosted at room temperature. The solution was mixed by a vortex mixer to ensure homogeneity. 500 µl of the stock solution was added to 20 ml of the yeast growth media containing 0.05 g/L yeast extract and 0.3 g/L glucose in distilled water.

The optical density (OD) measurement was carried out under 600 nm wavelength using SOIF UV-5100 UV/VIS spectrophotometer to determine the phase of growth of the cells in a given period of time. The cells were grown in sterilized liquid yeast extract and glucose medium under 180 rpm agitation for 14-18 hours to reach their late exponential phase of growth.

3.2.5.3. Solid Medium Preparation for Yeast Culture. The solid medium was prepared using 5 g/L yeast extract, 20 g/L agar and 30 g/L glucose in distilled water. Inside the sterilized fume hood, the sterilized solid medium at 70°C was poured into the petri dishes in 30 ml proportions. Once the solid medium was cooled to the room temperature, the petri dishes were wrapped with parafilm to avoid contamination from air and stored in the refrigerator upside down at 4°C.

3.2.5.4. Dispersion Solution Preparation. Phosphate Buffered Saline (PBS) tablets, which were purchased from MP Biomedicals, were used in the experiments to prepare PBS solution, which was used as dispersion medium. 1 PBS tablet was dissolved in 100 ml distilled water and the solution was autoclaved. The resultant concentration of the solution was 1XPBS, which contains 200 mg/L KCl, 200 mg/L KH_2PO_4, 8000 mg/L NaCl and 1150 mg/L Na_2HPO_4. 1XPBS solution, which was used to dilute the yeast solution, contains the essential inorganic ions to maintain the normal cell metabolism, helps sustaining the intracellular and extracellular osmotic balance and provides a buffering environment to keep the physiological pH range of the cell solution which is between 7.2 - 7.6.

3.2.5.5. Nanoparticle Exposure to the *S. cerevisiae* Cells. 1 ml of *S. cerevisiae* cell solution in the growth medium was transferred to a microcentrifuge tube when the cells reached their late exponential growth phase. The cells were centrifuged using Microfuge 22R Centrifuge at 8400 × g (9000 rpm) and 4 °C for 10 min. The cells were precipitated in the bottom of the tubes after centrifugation. The yeast medium containing yeast extract and glucose was taken with the help of micropipette and the tube was filled with 1ml of 1XPBS solution. The mixture was centrifuged again at 8400 × g (9000 rpm) and 4 °C for 1 min. This process was repeated 3 times. After the last step of centrifugation, fresh 1XPBS solution was added to the precipitated yeast cells and the solution was mixed with a vortex mixer.

1 µl of the yeast solution was dropped onto a glass slide and it was covered with a cover slip. The number of yeast cells were counted from Nikon Eclipse E200 inverted fluorescence microscopy images on 4908x3264 px^2 screen. The dimension of the wetted slide was measured, and the wetted area was found and the average number of yeast cells in 1 µl of the solution was calculated. The yeast suspension was diluted with 1XPBS solution to become 1 million cells per 1 ml solution. Different nanoparticle types (PSL NPs of different characteristics, DOPC liposomes and hybrid nanoparticles) with different concentrations (5-800 mg/L) were used in the cytotoxicity experiments to determine the effect of NP type and concentration on the cell viability. The nanoparticle exposed yeast cell solution and the control yeast solution, which did not contain any nanoparticles, were shaken at 60 rpm for 1 hour at room temperature. After shaking, the solutions were further diluted with dilution factors of 1/100 and 1/200 for CFU analysis.

3.2.5.6. Determination of the Nanoparticle Cytotoxicity by CFU Analysis. The nanoparticle exposed cells and the control group cells, which were diluted further, were spread on to the agar plates each containing 100 µl of the cell solution. For each of the dilution ratio, two petri dishes were prepared to increase the accuracy. The cells were incubated in Memmert oven at 30°C for 3 days. After incubation, the number of yeast colony forming units (CFUs) were counted on the petri dishes containing yeast extract agar medium. The toxicity of the nanoparticles on *S. cerevisiae* cells was obtained by comparing the culture not exposed to nanoparticles with the culture exposed to nanoparticles.

The viability percentage of the yeast cells under nanoparticle exposure was calculated according to the following equation:

$$Viability\ \% = \frac{CFU's\ of\ NP\ Group}{CFU's\ of\ Control\ Group} \times 100 \quad (3.1)$$

After finding the viability percentage for each of the dilution ratio, the average viability percentage was calculated as follows:

$$Avg.Viability\ \% = \frac{Viability\%\ for\ \frac{1}{100}\ ratio + Viability\%\ for\ \frac{1}{200}\ ratio}{2} \quad (3.2)$$

The average viability percentage results were obtained by the exposure of the yeast cells to different types and characteristics of nanoparticles and the possible reasons that induced these results were discussed along with the microscopic visualizations.

3.2.5.7. Microscopic Visualization of Nanoparticle Exposed *S. cerevisiae* Cells. Sac6:RFP *S. cerevisiae* cells after different types and characteristics of nanoparticle exposure were visualized with different microscopes to observe the location and distribution of the nanoparticles at the intracellular and extracellular environment of the cell. The confocal microscopes used in the experiments were Leica SP5-AOBS and Zeiss LSM 800 40x/1.3 Oil DICIII Confocal Laser Scanning Microscope (CLSM). The images were processed using image processing and analysis software Fiji-ImageJ to arrange the brightness and contrast, and to set scale bar on the images.

Propidium Iodide (PI), which is a membrane impermeable dye, was added to the yeast solution just after the nanoparticle addition. The dead cells after PI addition were stained in red fluorescence as the dye molecules passed through the cell membrane. For microscopic visualizations fluorescently labelled nanoparticles were used to observe the location of the nanoparticles under fluorescence.

For the cell fixation, 37% paraformaldehyde was diluted with 1XPBS to obtain 3.7% paraformaldehyde solution. The nanoparticle added cell solution was centrifuged and the

solution above the precipitated cell was taken with the help of micropipette. 3.7% paraformaldehyde solution was added on to the cells and the solution was mixed in a vortex. The cells were incubated at room temperature for 15-20 minutes. The cells were centrifuged at 8000 rpm for 5 min. 1XPBS solution was added and the cells were collected by centrifugation at 8000 rpm for 1 min. This process was repeated 3 times. The fixed cells were kept in the refrigerator at 4°C until the time of microscopic analysis.

3.2.5.8. Long-term Nanoparticle Exposure Experiments. The long-term effect of the PSL nanoparticle exposure to the *S. cerevisiae* cells was investigated by incorporating different types and concentrations of PSL NPs, which were not found to be toxic in cytotoxicity experiments, to determine their effects on the next generations. PSL nanoparticles having a concentration in the range between 0-200 mg/L were added to the fresh yeast solution in liquid media. The nanoparticle added yeast solution and control yeast solution were incubated overnight and the OD of the cells were measured to determine the cell intensity after incubation under nanoparticle exposure. Also, the cells were spread onto the agar plates with the same dilution procedures as the cytotoxicity experiments. The cells in the solid medium were incubated in the oven at 30°C for 3 days. The CFU analysis was carried out to determine the toxicity. The inoculating wire loop was sterilized with the flame of the Bunsen burner. The loop was cooled with the colony free side of the agar plate then one yeast colony was taken gently with the help of the loop. This colony was placed into the fresh liquid yeast medium containing nanoparticle group and control group for the growth of the next generation. This procedure was repeated until 15^{th} generation of the yeasts was obtained. According to the results of both OD measurements and CFU analysis, the long-term PSL NP exposure effect was obtained.

3.2.6. Uptake Inhibition Experiments

Lat-A (Latrunculin A), which is an efficient inhibitor of actin polymerization, was used in the inhibition studies to determine whether the nanocarriers are internalized by the yeast cells via endocytosis or diffusion. 100µg of Lat-A, which was purchased from Sigma-Aldrich (L5163), was dissolved in 250µl DMSO (Dimethyl sulfoxide) and 1 mM Lat-A stock solution was obtained. The yeast cells in their culture medium were treated with

different Lat-A concentrations (1 µM and 200 µM Lat-A) for 1 hour at 28°C to investigate the effect of inhibitor concentration on the uptake of PSL nanoparticles by *S. cerevisiae* cells.

Nocodazole is an endocytosis inhibitor which is used as a microtubule disruptor as microtubules are involved in the endocytic processes [44]. In this study, nocodazole, which was purchased from Carbosynth, was used as an endocytosis inhibitor to determine the uptake mechanism of nanoparticles inside the yeast cells. Nocodazole stock solution was prepared by dissolving 5mg of Nocodazole in 3.33 ml of DMSO. The concentration of the stock solution was obtained as 15 mg/L. In the inhibition studies, 15 µg/ml nocodazole solution was used by diluting the stock solution 100 times. The cells were treated with nocodazole for 28°C in the incubator. Different incubation times (1 hour and 2 hours) are used to investigate the effect of inhibitor incubation time on the uptake of PSL nanoparticles by *S. cerevisiae* cells.

It has been reported that ethanol shows inhibitory effect to the endocytosis between 2 to 6% (v/v) concentrations [45]. In this study, to investigate the mechanism of nanoparticle internalization 5% (v/v) ethanol [10] was used. The yeast cells were treated with 5% v/v ethanol for 1 hour at 28°C in the incubator. Then, the cell solution was centrifuged, and the same procedures applied for the other inhibitors in this study were performed for confocal microscopy imaging.

The cell solution treated with inhibitors was centrifuged for 10 minutes at 9000 rpm agitation speed at 4°C. The yeast cells were harvested and washed 3 times with 1XPBS solution along with centrifugation. After cells were diluted, the nanocarrier solution was prepared at the required concentration and added to the cell solution. After the cells were exposed to the nanoparticles for 1 hour at 60 rpm agitation and room temperature, they were diluted again, spread on the agar plates and placed at oven for 3 days at 30°C for CFU analysis. Also, for confocal microscopy analysis, the nanoparticle exposed cells were stained with propidium iodide (PI) solution and fixed with paraformaldehyde and kept in refrigerator at 4°C until the time of analysis.

4. RESULTS AND DISCUSSION

In this study, nanocarriers having different size, charge and functional groups are introduced to *S. cerevisiae* cells at different concentrations to determine their effects on viability and cellular internalization mechanisms. The nanocarriers used in the experiments can be divided into three main groups: Polystyrene Latex Nanoparticles (PSL NPs), DOPC liposomes and liposome encapsulated PSL NPs (hybrid nanoparticles). The first group of nanoparticles have been purchased from different companies and they have different sizes (20 to 200 nm), charges (positive and negative) and surface functional groups (carboxyl and amine). The liposomes are synthesized from DOPC (1,2-Dioleoyl-sn-glycero-3-phosphocholine) lipid by thin-film evaporation method. The hybrid nanoparticles are synthesized by encapsulating the PSL NPs with DOPC phospholipid during the formation of liposomes by applying the same method. The purchased and synthesized nanoparticles are characterized by different analyses which are DLS, zeta potential, STEM and TEM.

In this section, first the results from characterization studies of nanocarriers are given and discussed accordingly. Next, the growth curve construction experiment of the Sac6:RFP tagged *S. cerevisiae* cells is explained**.** The results obtained from Colony Forming Unit (CFU) analysis and the microscopic visualizations attained by confocal laser scanning microscopy (CLSM) analysis are demonstrated and discussed. Then, the results of the toxicity experiments belonging to DOPC liposome and hybrid nanoparticle exposure to the yeast cells are shown and discussed. The differences in the viability results between the PSL nanoparticles and their hybrid configurations are explained and the possible reasons underlying the toxicology results are discussed. The consequences of the experiments investigating the long-term PSL nanoparticle exposure effects for consecutive 15 yeast generations are shown and discussed. Also, the uptake mechanism of Sac6:RFP tagged *S. cerevisiae* cells is investigated by applying different endocytosis inhibitors to see whether the nanocarrier internalization occurs via an energy dependent mechanism or diffusion.

4.1. Nanoparticle Characterization Studies

In this section, the results from the characterization of the nanoparticles, i.e., Polystyrene Latex Nanoparticles (PSL NPs), DOPC liposomes and hybrid nanoparticles, as well as Sac6:RFP tagged *S. cerevisiae* cells are shown and discussed. The characterization studies include Dynamic Light Scattering (DLS) analysis to determine the size distribution and the uniformity of the particles, Electrophoretic Light Scattering Analysis (ELS) analysis to determine the zeta potential and the electrophoretic mobility of the particles, Scanning Transmission Electron Microscopy (STEM) and Transmission Electron Microscopy (TEM) analyses to determine the morphological structure and the size of the nanoparticles.

4.1.1. Characterization of Polystyrene Latex Nanoparticles (PSL NPs) and Sac6:RFP *S. cerevisiae* Cells

Polystyrene latex nanoparticles (PSL NPs) having different sizes, surface functionalization groups, and charges as well as Sac6:RFP tagged *S. cerevisiae* cells are characterized by Dynamic Light Scattering (DLS) analysis to determine the mean diameter and Polydispersity Index (PDI value of the particles and Electrophoretic Light Scattering (ELS) analysis to determine the zeta potential and electrophoretic mobility values of the particles. The characterization results for PSL nanoparticles and Sac6: RFP tagged *S. cerevisiae* cells are shown in Table 4.1.

Table 4.1. Mean Diameter and Zeta Potential Values of PSL Nanoparticles and Sac6:RFP *S. cerevisiae* Cells.

Name of NPs	**Surface Functionalization**	**Nominal Diameter (nm)**	**Mean Diameter (nm)**	**PDI**	**Electrophoretic Mobility ($m^2s^{-1}V^{-1}$)**	**Surface Charge**	**Zeta Potential (mV)**
20nm-C-n	Carboxyl	20	49.4	0.094	-3.09	Negative	-39.55
30nm-C-n	Carboxyl	30	33.0	0.160	-3.02	Negative	-38.64
60nm-C-n	Carboxyl	60	80.3	0.145	-3.34	Negative	-42.72
50nm-A-p	Amine	50	45.9	0.122	1.85	Positive	23.66
50nm-A-n	Amine	50	-	-	-1.60	Negative	-20.51
100nm-A-p	Amine	100	129.2	0.168	1.27	Positive	16.25
100nm-A-n	Amine	100	105.7	0.028	-1.17	Negative	-15.03
200nm-A-n	Amine	200	161.1	0.129	-1.96	Negative	-25.03
Sac6:RFP *S. cerevisiae*	-	-	5826.1	0.213	-0.290	Negative	-3.71

4.1.2. Characterization of DOPC Liposomes

DOPC liposomes having a concentration of 0.25 mg lipid/ml PBS solution are prepared by thin-film hydration method. According to the particle size analysis in terms of intensity, the mean diameter of the empty DOPC liposomes is 174.0 nm (Figure A.30). The synthesized liposomes have a narrow size distribution, which is in the desired range.

The Polydispersity index (PDI) is a term used in the estimation of the average size uniformity of a particle in a solution [6]. PDI changes between 0 and 1 in DLS measurements. Higher values of PDI represent larger size distribution whereas lower values (<0.1) indicate a monodisperse solution [6]. Based on DLS measurements, PDI of empty liposomes is 0.173 indicating a homogenous solution in terms of size.

Zeta potential (ζ), being a measure of surface charge, is related to the particle stability along with the cellular uptake and intracellular trafficking [46]. High absolute value of zeta potential indicates good particle stability where low absolute values represent low stability [46]. The zeta potential of low values show that the particles tend to aggregate more frequently, whereas that of high values indicate a good degree of colloidal stability [46]. Electrophoretic mobility value is another indication of liposome stability [47]. The high value of the electrophoretic mobility indicates the degree of repulsion between the liposomes and vice versa [47]. If the repulsion forces between the liposomes are high, the tendency of agglomeration is low, which shows that the liposomes are stable [47]. The electrophoretic mobility and the zeta potential values of DOPC liposomes are obtained as -1.13 $m^2s^{-1}V^{-1}$ and -14.5 mV, respectively (Figure A.33).

STEM analysis is carried out to determine the structure of the synthesized liposomes. STEM images confirm the size homogeneity of synthesized liposomes (Figure 4.1). Although agglomerated liposomes are observed in STEM imaging due to the spread of the liposomes in drying process before imaging, in general, the sizes of the liposomes synthesized in this study are in agreement with the DLS measurements.

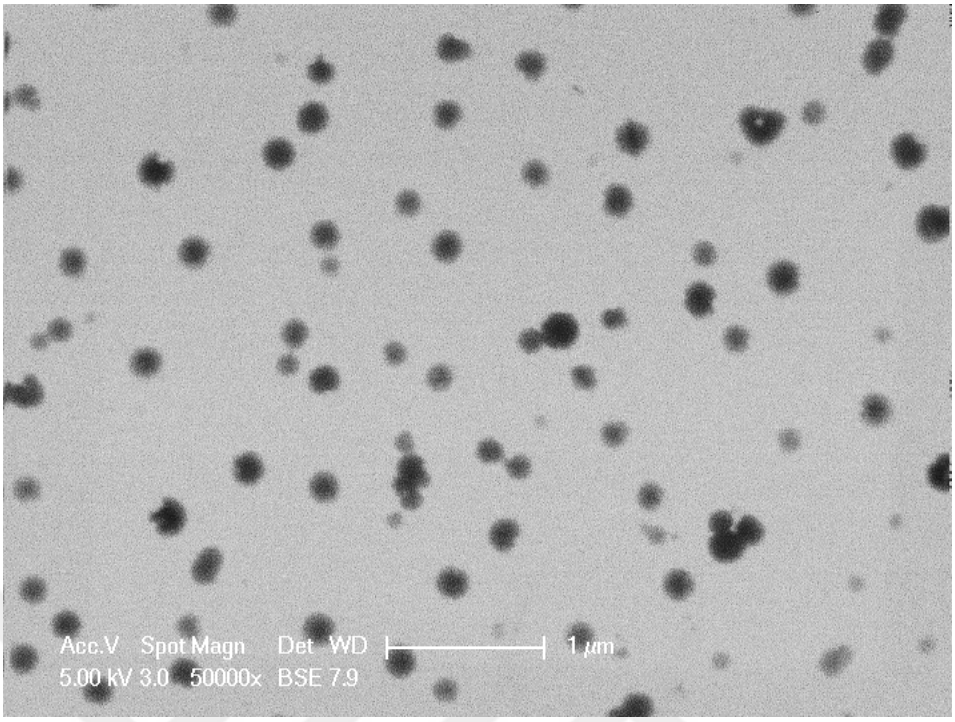

Figure 4.1. STEM image of DOPC liposomes.

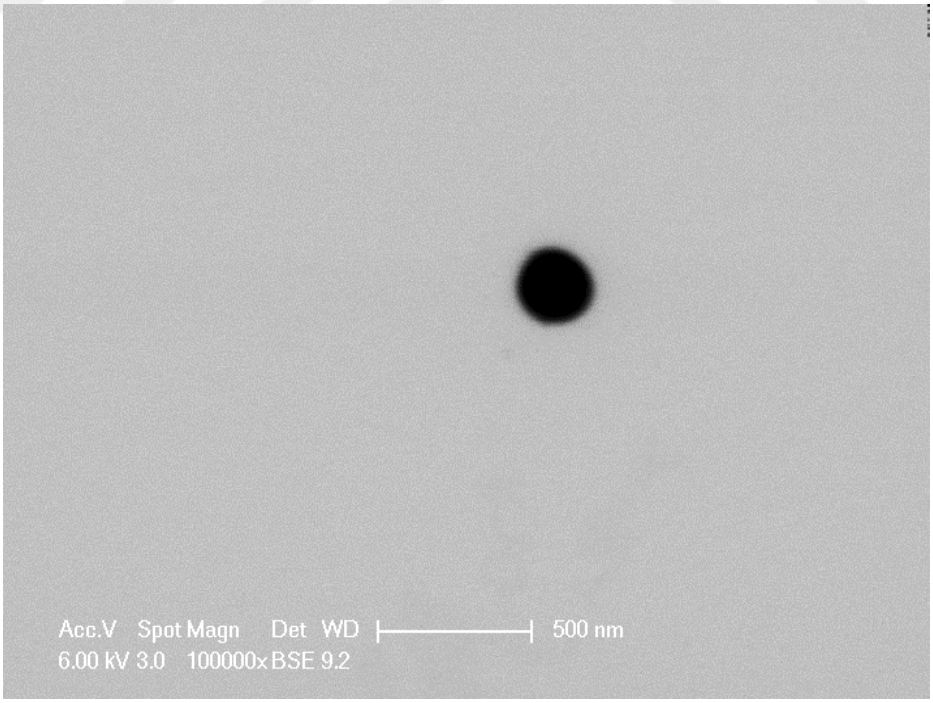

Figure 4.2. Magnifed STEM image of DOPC liposome.

4.1.3. Characterization of Hybrid Nanoparticles

Hybrid nanoparticles are synthesized by adding the nanoparticle containing PBS solution onto the lipid film formed by organic solvent evaporation under nitrogen gas. In the process of self-assembly, nanoparticles in PBS solution are encapsulated by the DOPC phospholipid bilayer and hybrid nanoparticles are formed. The characteristics of the hybrid nanoparticles are determined by particle size and zeta potential analyses. Also, TEM analyses is performed to reveal the structural differences between the bare PSL nanoparticles and liposome encapsulated nanoparticles. The properties of hybrid nanoparticles are listed in Table 4.2. Detailed discussion on the findings is given below.

Table 4.2. Comparison of the Properties of Empty DOPC Liposome, PSL and Hybrid Nanoparticles.

Nanoparticle name	**Size (nm)**	**PDI**	**Electrophoretic Mobility ($m^2s^{-1}V^{-1}$)**	**Zeta Potential (mV)**
20nm-C-n PSL NP	49.4	0.089	-3.09	-39.55
20nm-C-n Hybrid NP	199.7	0.208	-1.79	-22.94
30nm-C-n PSL NP	33.0	0.196	-3.02	-38.64
30nm-C-n Hybrid NP	155.3	0.160	-1.72	-22.0
50nm-A-p PSL NP	45.9	0.122	1.85	23.66
50nm-A-p Hybrid NP	289.5	0.251	0.66	8.48
100nm-A-n PSL NP	105.7	0.028	-1.17	-15.03
100nm-A-n Hybrid NP	165.2	0.098	-1.04	-13.3
100nm-A-p PSL NP	145.0	0.168	1.27	16.25
100nm-A-p Hybrid NP	192.3	0.179	0.56	7.14
Empty DOPC Liposome	174.0	0.173	-1.13	-14.5

4.1.3.1. 20nm-C-n Hybrid Nanoparticle Characterization. The particle size distribution analysis in terms of intensity measurement for 20nm-C-n hybrid nanoparticles shows that the diameter of the nanoparticles is 199.7 nm (Table 4.2 and Figure A.38). Also, around 60 nm, another peak is observed with a slightly lower intensity that cannot be neglected (G(d)=100 for 199.7nm, G(d)~50 for ~60nm). The PDI value is 0.208 which is much higher than the value of 0.089 belonging to 20nm-C-n PSL nanoparticles and a little higher than the value of 0.173 belonging to empty DOPC liposomes (Table 4.2 and Figure A.40). These results indicate that along with 200 nm hybrid nanoparticles, nonencapsulated nanoparticles around 60 nm also exist. The electrophoretic mobility and zeta potential of 20nm-C-n hybrid nanoparticles are found as -1.79 $m^2s^{-1}V^{-1}$ and -22.94 mV, whereas those of 20nm-C-n PSL NPs are -3.09 $m^2s^{-1}V^{-1}$ and -39.55 mV, respectively (Table 4.2 and Figure A.41). These results show that the stability of the 20nm-C-n hybrid nanoparticles are lower than 20nm-C-n PSL nanoparticles, but higher than empty DOPC liposomes.

STEM results show that a single hybrid nanoparticle consists of a single 20nm-C-n PSL nanoparticle (Figure 4.3). However, some of the hybrid nanoparticles may attach to each other that causes the hybrid nanoparticle size to increase. The sizes of the 20nm-C-n hybrid nanoparticles obtained from STEM imaging are smaller than the values measured in DLS analysis results ad DLS gives the hydrodynamic diameter of the particles.

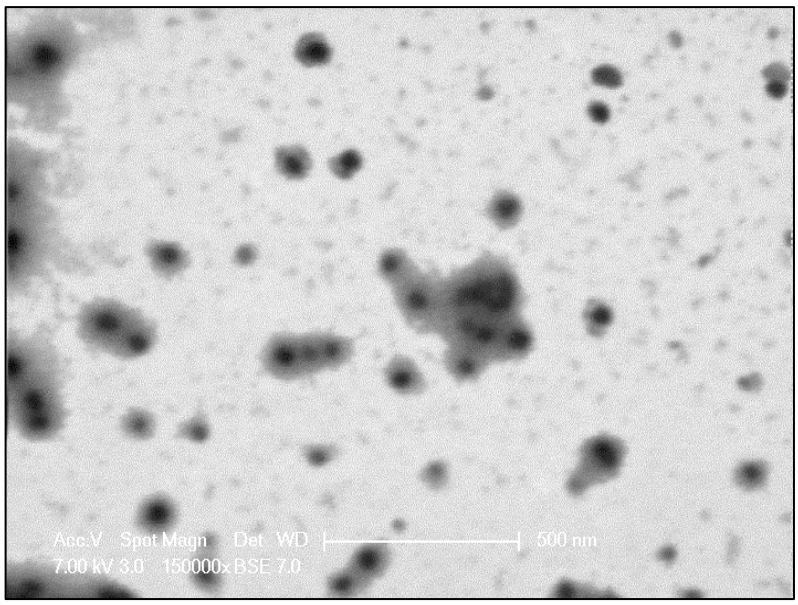

Figure 4.3. STEM image of 20nm-C-n hybrid nanoparticles.

TEM analysis has been carried out for both 20nm-C-n PSL nanoparticles and hybrid nanoparticles. It is seen that PSL nanoparticles have smooth surfaces and they have perfectly round shape (Figure 4.4). On the contrary, 20nm-C-n hybrid nanoparticles have indented surface morphology and the shape of the nanoparticles are not perfectly round (Figure 4.5). This morphological feature is expected because, the phospholipid layer is not smooth.

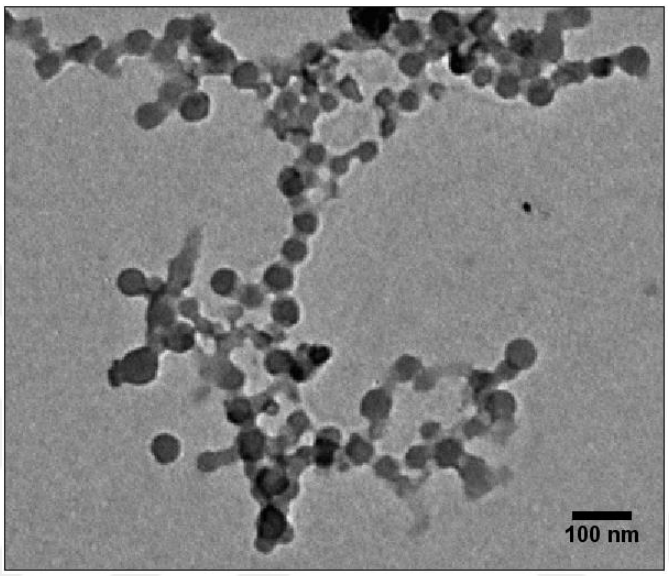

Figure 4.4. TEM image of 20nm-C-n PSL NPs.

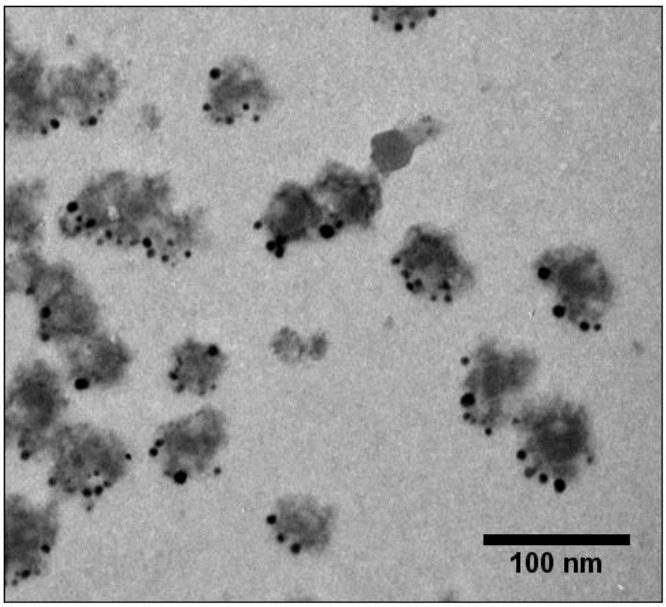

Figure 4.5. TEM image of 20nm-C-n hybrid NPs.

4.1.3.2. 30nm-C-n Hybrid Nanoparticle Characterization. The particle size distribution in terms of intensity measurement belonging to 30nm-C-n hybrid nanoparticles shows that the mean diameter is 155.3 nm, whereas the mean diameter of 30nm-C-n PSL NPs has been measured as 33.0 nm (Table 4.2 and Figure A.42). The PDI value of 30nm-C-n hybrid nanoparticles has been obtained as 0.160 whereas that of empty liposomes and 30nm-C-n PSL nanoparticles are 0.173 and 0.196, respectively (Table 4.2 and Figure A.43). This shows that the degree of size uniformity in the solution is very slightly lower in hybrid nanoparticle than the PSL nanoparticle. This is an expected result because hybrid particle solution may contain both capsulated and non-capsulated nanoparticles. Still, it can be interpreted that the synthesized hybrid nanoparticles are uniform and stable enough when PDI values of PSL nanoparticles are considered.

The electrophoretic mobility and the zeta potential of the hybrid nanoparticles have been measured as -1.72 $m^2s^{-1}V^{-1}$ and -22.0 mV, whereas those of PSL nanoparticles are -3.02 $m^2s^{-1}V^{-1}$ and -38.64 mV, respectively (Table 4.2 and Figure A.45). With lower absolute values of electrophoretic mobility and zeta potential, hybrid nanoparticles are less stable. However, when the values of empty DOPC liposomes are considered, an increase in the absolute value is observed. Part of this increase results from the presence of non-encapsulated PSL nanoparticles. In general, however, it can be concluded that the stability of the empty DOPC liposomes increases when PSL nanoparticles are encapsulated inside them.

4.1.3.3. 50nm-A-p Hybrid Nanoparticle Characterization. The particle size distribution analysis in terms of intensity for 50nm-A-p hybrid nanoparticles shows that the diameter and PDI values are 289.5 nm and 0.251, whereas these values for 50nm-A-p PSL nanoparticles are 45.9 nm and 0.122, respectively (Table 4.2, Figure A.46) and Figure A.48). For 50nm-A-p hybrid nanoparticles, particle uniformity was lower than 50nm-A-p PSL nanoparticles. When these results are compared with those of empty DOPC liposomes, the size of the synthesized hybrid nanoparticles is found to be higher and the uniformity value is lower.

The electrophoretic mobility and the zeta potential values belonging to 50nm-A-p hybrid nanoparticles are found as 0.66 $m^2s^{-1}V^{-1}$ and 8.48 mV, whereas the values for 50nm-A-p PSL nanoparticles are measured as 1.85 $m^2s^{-1}V^{-1}$ and 23.66 mV, respectively (Table 4.2

and Figure 49). The values of electrophoretic mobility and zeta potential are both decreased with hybrid nanoparticles, thus the stability of the hybrid nanoparticles is lower than PSL nanoparticles. Although the electrophoretic mobility and the zeta potential values of empty DOPC liposomes are negative, the values of the 50nm-A-p hybrid nanoparticles are positive similar to 50nm-A-p PSL nanoparticles. However, the lowest absolute values of electrophoretic mobility and zeta potential are obtained with hybrid nanoparticles.

TEM analysis is carried out to compare the morphologies of 50nm-A-p hybrid nanoparticles and PSL nanoparticles. According to the results, 50nm-A-p PSL nanoparticles have perfectly round shape and a smooth surface. On the contrary, hybrid nanoparticles have near round shapes and indented surfaces (Figure 4.6 and 4.7). The size of the 50nm-A-p hybrid nanoparticles obtained from the TEM images is in agreement with the size measurements carried out in DLS analysis.

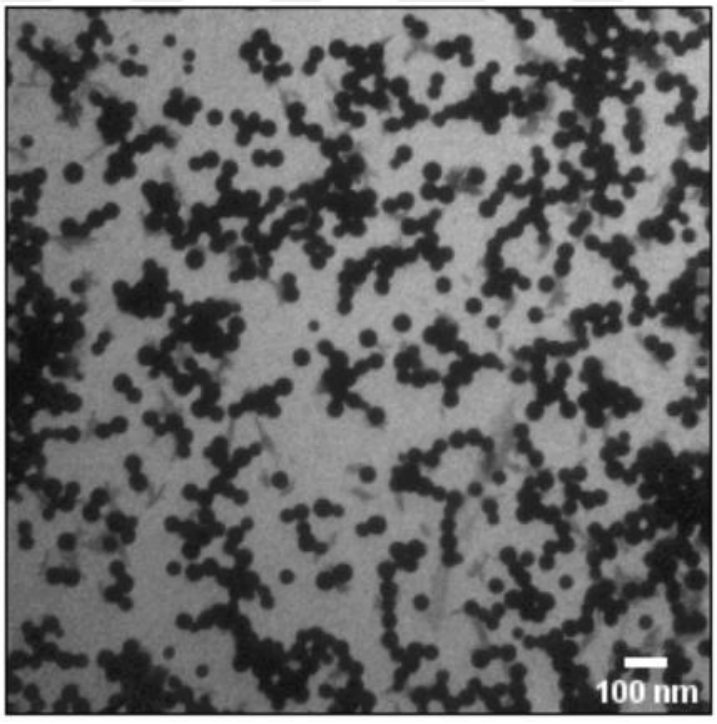

Figure 4.6. TEM image of 50nm-A-p PSL NPs.

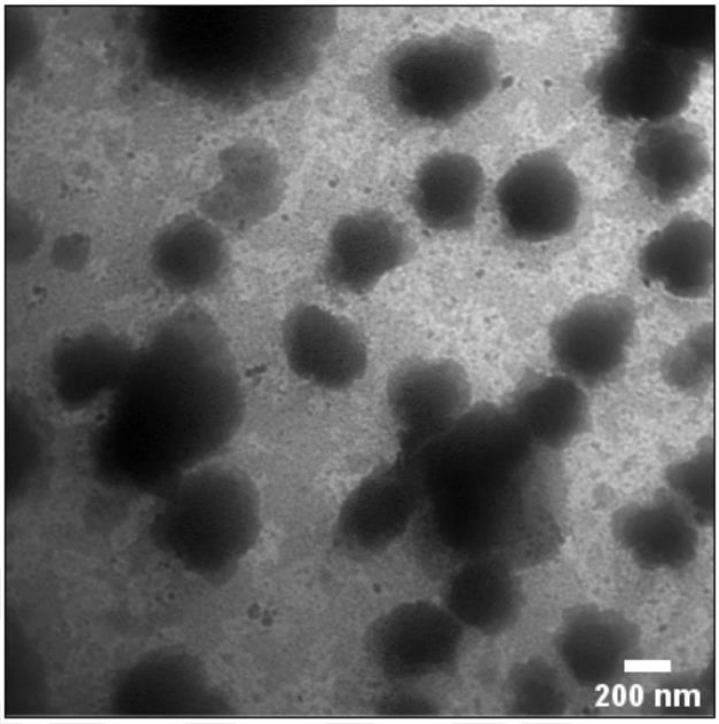

Figure 4.7. TEM image of 50nm-A-p hybrid NPs.

4.1.3.4. 100nm-A-p Hybrid Nanoparticle Characterization. The particle size distribution analysis in terms of intensity measurement for 100nm-C-n hybrid nanoparticles shows that diameter and PDI values are 192.3 nm and 0.179, whereas these values for 100nm-A-p PSL nanoparticles are 145 nm and 0.168, respectively (Table 4.2, Figure A.50 and Figure A.52). A slight increase of PDI value is observed with hybrid nanoparticles, indicating that the size uniformity of 100nm-A-p hybrid nanoparticles is lower than that of 100nm-A-p PSL nanoparticles. This slight increase in the PDI value can be explained by the presence of nonencapsulated nanoparticles and/or empty DOPC liposomes.

The electrophoretic mobility and the zeta potential values for 100nm-A-p hybrid nanoparticles are found as 0.56 $m^2s^{-1}V^{-1}$ and 7.14 mV, whereas these values for 100nm-A-p PSL nanoparticles are measured as 1.27 $m^2s^{-1}V^{-1}$ and 16.25 mV, respectively (Table 4.2 and Figure 53). The decrease in electrophoretic mobility and the zeta potential values with hybrid nanoparticles is expected because of the presence of the phospholipid molecules which come from the structure of the liposomes. The surface charge of the 100nm-A-p PSL nanoparticles is found to be positive and their hybrid counterparts obtained by liposome encapsulation are also positively charged.

4.1.3.5. 100nm-A-n Hybrid Nanoparticle Characterization. According to the particle size distribution analysis in terms of intensity for 100nm-A-n hybrid nanoparticles, the diameter and PDI values are found as 165.2 nm and 0.098, whereas these values for 100nm-A-p PSL nanoparticles are 105.7 nm and 0.028, respectively (Table 4.2, Figure A.54 and Figure A.56), it can be interpreted that 100nm-A-n hybrid nanoparticles are much more uniform in terms of size distribution with respect to empty DOPC liposomes.

The electrophoretic mobility and the zeta potential values for 100nm-A-n hybrid nanoparticles are found as -1.04 $m^2s^{-1}V^{-1}$ and -13.3 mV, and these values for 100nm-A-n PSL nanoparticles are -1.17 $m^2s^{-1}V^{-1}$ and -15.03 mV, respectively (Table 4.2 and Figure A.57). The values show that the stability of the hybrid nanoparticles is very similar to PSL nanoparticles. Also, the electrophoretic mobility and the zeta potential values are similar to empty DOPC liposomes' values.

TEM analysis is performed to compare the characteristics of 100nm-A-n PSL nanoparticles and hybrid nanoparticles. PSL nanoparticles have perfectly round shape and their surfaces are smooth similar to other PSL nanoparticles. In contrast to other synthesized hybrid nanoparticles in this study, 100nm-A-n hybrid nanoparticles are also round shape.

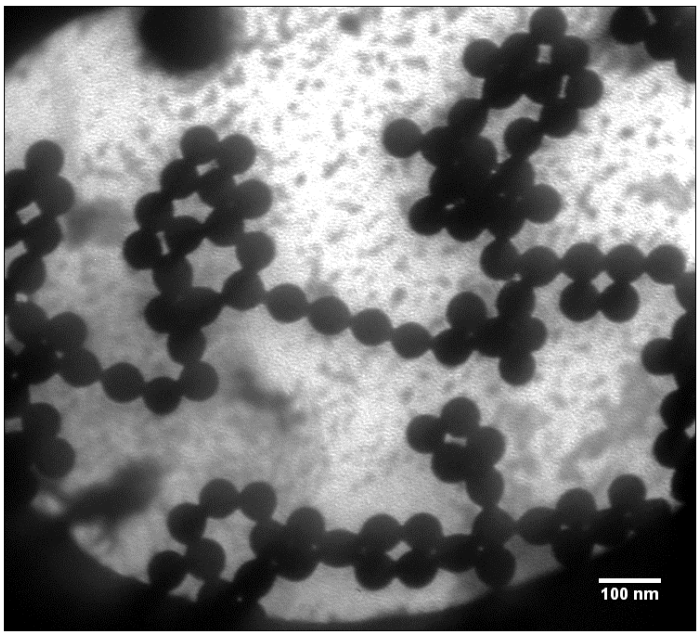

Figure 4.8. TEM image of 100nm-A-n PSL NPs.

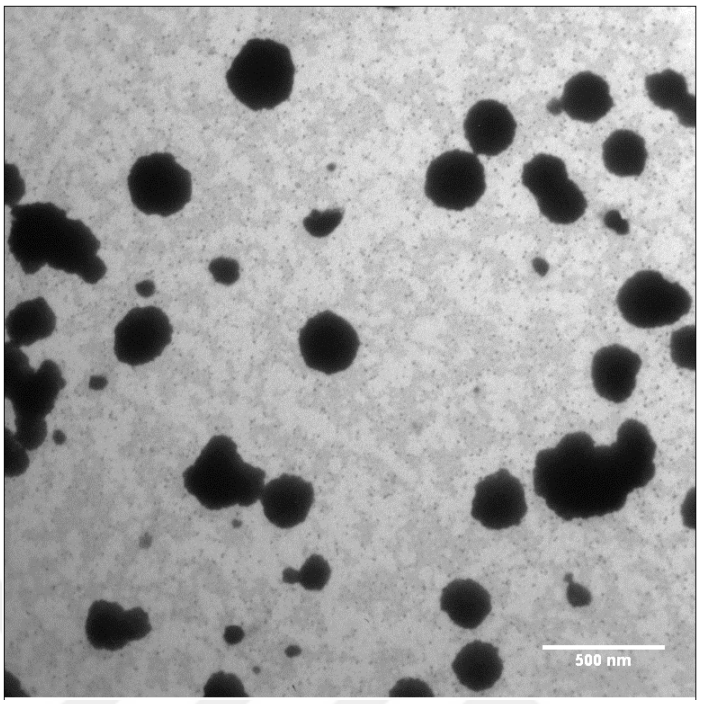

Figure 4.9. TEM image of 100nm-A-n hybrid NPs.

4.1.4. Characterization of Fluorescein Dye Loaded DOPC Liposomes

To be able to see the interaction of the DOPC liposomes and hybrid nanoparticles with the *S. cerevisiae* cells in confocal microscopy, fluorescein dye has been added to the dispersion medium during the self-assembly of liposomes. The excess fluorescein is ultrafiltrated, the nanoparticle solution is washed with fresh PBS solution and fluorescently labelled DOPC liposomes and hybrid nanoparticle are obtained.

4.1.4.1. Determination of Fluorescein Encapsulation Efficiency into DOPC-Liposomes. Fluorescence spectroscopy analysis is carried out using UV–VIS spectrophotometer to determine the fluorescein dye encapsulation efficiency inside the DOPC-liposomes. The maximum absorbance wavelength of 15 µg/ml fluorescein solution in 1XPBS is measured at wavelengths between 250 nm and 600 nm. The maximum dye absorbance is recorded as 2.475 at 494 nm in accordance with the literature [48]. The absorbance values of fluorescein at different wavelengths are shown in Table C.1, absorbance versus wavelength graph is shown in Figure 4.10.

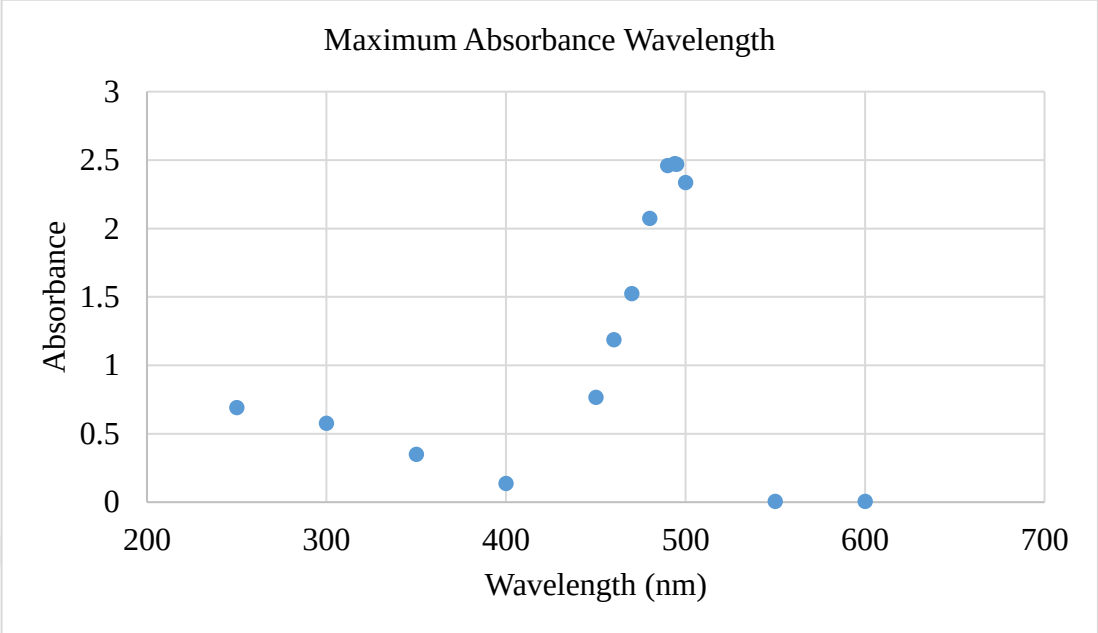

Figure 4.10. Absorbance spectra of fluorescein.

The calibration curve is obtained by recording the absorbance values at 494 nm for various concentration of fluorescein, in the range between 0 and 12 µg/ml using fluorescence spectroscopy. The absorbance versus concentration curve is given in Figure 4.11.

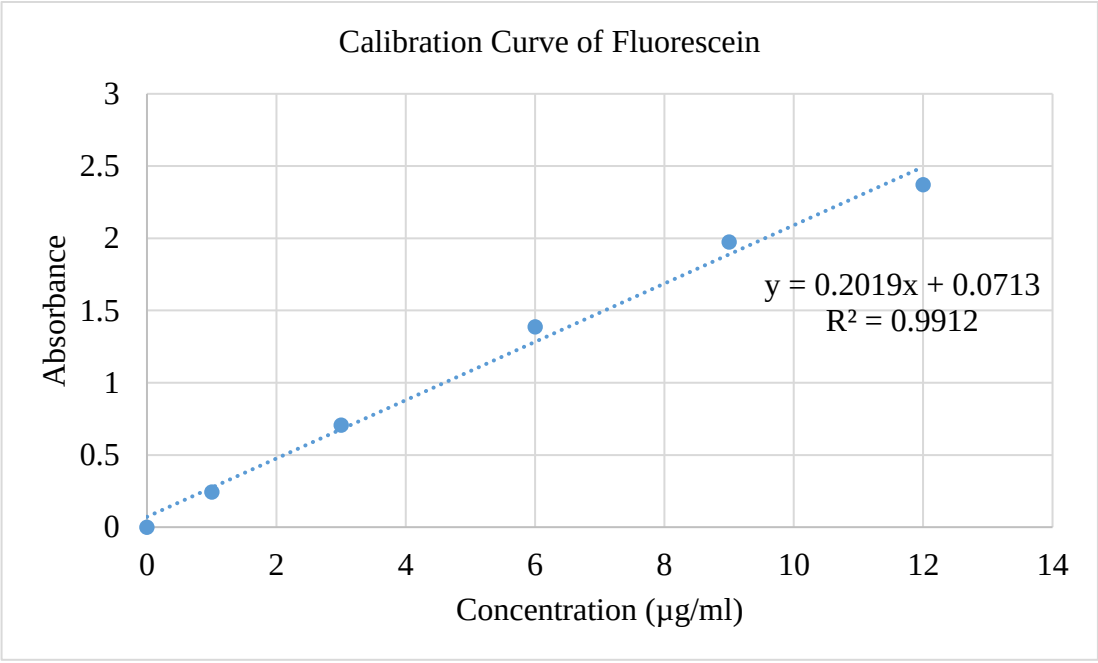

Figure 4.11. Calibration curve of fluorescein.

The linear equation obtained from the calibration curve data is as follows:

$$y = 0.2019x + 0.0713 \quad (4.1)$$

Excess amount of fluorescein, which is not encapsulated, is removed by ultrafiltration using Amicon Ultra-15 Centrifugal Filter Units with Molecular Weight Cut Off (MWCO) value of 30,000. For this purpose, centrifugation for 1 hour at 5000 rpm and room temperature has been performed. As the concentration of the solution is high to be analyzed in the spectrophotometer, it is diluted with 1XPBS solution to result in 1:10 dye solution to PBS solution ratio. The absorbance of the dye solution is recorded as 1.146. The equation 4.1 is solved for this absorbance value to determine the concentration of the excess dye solution.

$$1.146 = 0.2019x + 0.0713$$

$$x = 5.323$$

$$Concentration\ of\ the\ excess\ dye\ solution = 5.323\ \mu g/ml\ \ (for\ 1{:}10\ dilution)$$

$$Concentration\ of\ the\ excess\ dye\ solution = 53.23\ \mu g/ml\ \ (no\ diluton)$$

The encapsulation percentage of fluorescein inside the liposomes is calculated according to the equation 4.2.

$$\%\ Fluorescein\ encapsulation = \left(\frac{C_0 - C_t}{C_0}\right) * 100 \quad (4.2)$$

Where,

C_0 is the initial fluorescein concentration (µg/ml),

C_t is the fluorescein concentration in the solution (µg/ml).

The starting concentration of the fluorescein solution (C_0) is 100 µg/ml. The percentage of fluorescein encapsulation is calculated as follows:

$$\%\ Fluorescein\ encapsulation = \left(\frac{100 - 53.23}{100}\right) * 100 = 46.77\%$$

The absorbed fluorescein dye amount inside the liposomes is calculated by the equation 4.3.

$$q_f = (C_0 - C_t) * V \tag{4.3}$$

Where,
q_f is the amount of fluorescein encapsulated (µg),
V is the volume of the solution (ml),

The volume of the solution used in the preparation of the fluorescein loaded liposomes is 10 ml. The amount of the fluorescein loaded inside the liposomes is calculated as follows:

$$q_f = (100 - 53.23) * 10 = 467.7\ \mu g$$

4.1.4.2. Comparison of DOPC Liposomes and Fluorescently Labelled DOPC Liposomes in terms of Characteristic Properties. The mean diameter of fluorescein dye loaded liposomes is found as 170.4 nm which is near to the value of empty liposomes (174.0 nm) and the PDI value is 0.172 indicating narrow particle size distribution (Table 4.3, Figure A.34 and Figure A.36). Hence, fluorescein loaded liposomes are homogeneous similar to the empty liposomes.

According to the zeta potential analysis measurements, the zeta potential values for empty and fluorescein loaded liposomes are -14.5 mV and -4.96 mV, respectively. (Table 4.3 and Figure A.37). Hence, empty DOPC liposomes have higher colloidal stability and less tendency for agglomeration than fluorescently labelled liposomes. The difference between the zeta potentials of empty liposomes and fluorescein loaded liposomes indicates that the addition of fluorescein has a neutralizing effect on the surface charge of the liposomes. In the study of Yang H. *et al*. (2013), the addition of fluorescein in Fe_2O_4@SiO_2 nanoparticles has resulted in a decrease in the value of the zeta potential towards neutral state [49]. Sun D. *et al*. (2014) have shown in their study that while Mesoporous Silica

Nanoparticles (MSNs) have zeta potential of -25.9 mV, the zeta potential of fluorescently labelled MSNs is -15.2 mV [50]. Ge Y. *et al*. (2009) have found that the absolute value of the zeta potentials belonging to FITC added Magnetic Nanoparticles (MNPs) are lower than the naked MNPs [51]. The electrophoretic mobility values for empty and fluorescently labelled DOPC liposomes are found as -1.13 $m^2s^{-1}V^{-1}$ and -0.39 $m^2s^{-1}V^{-1}$, respectively. (Table 4.3 and Figure A.37). The fact that empty liposomes have higher absolute value of electrophoretic mobility value compared to fluorescein loaded liposomes supports the finding of higher colloidal stability.

Table 4.3. DLS and Zeta Potential Analysis Results for DOPC Liposomes.

Name of Nanoparticle	**Mean Diameter (nm)**	**Surface Charge**	**Zeta Potential (mV)**	**Electrophoretic mobility ($m^2s^{-1}V^{-1}$)**
DOPC Liposome	174.0	Negative	-14.5	-1.13
DOPC Liposome with Fluorescein	170.4	Negative	-4.96	-0.39

4.1.5. Comparison of the Hybrid NPs and Fluorescently Labelled Hybrid NPs in terms of Characteristic Properties

The zeta potential and the electrophoretic mobility of the fluorescently labelled hybrid nanoparticles are lower than unlabeled hybrid nanoparticles when the absolute values are considered (Table 4.4). It can be interpreted that the addition of fluorescein dye results in neutralizing/diminishing effect on the zeta potential/electrophoretic mobility values, respectively, in hybrid nanoparticles as well as empty DOPC liposomes. The mean diameter of the fluorescently labelled hybrid nanoparticles is generally similar to the corresponding hybrid nanoparticles without fluorescein as expected (Table 4.4). However, for 50nm-A-p hybrid nanoparticles, the mean diameter increases from 289.5 nm to 406.8 nm when the nanoparticles are fluorescently labelled with fluorescein dye. This result can be explained by the reduction in stability of the nanoparticles after fluorescein dye addition. In 50nm-A-p hybrid nanoparticle case, the addition of fluorescein dye has resulted in the zeta potential value to decrease from 8.48 mV to 0.70 mV. Since the zeta potential values near to zero

indicates the instability of the nanoparticle, this effect is found much more prominent in 50nm-A-p-Fl hybrid nanoparticle case. The nanoparticles tend to agglomerate more when they are instable, so the increase in the mean diameter of 50nm-A-p-Fl nanoparticle stems from the fact that they cluster and form larger particles after they are labelled with fluorescein dye.

It is observed that as the size of the PSL nanoparticles increases, the change in the absolute values of zeta potential value decreases. For example, for 30nm-C-n hybrid nanoparticles, the absolute value of zeta potential decreases from -22.00 mV to -11.48 mV, whereas for 100nm-A-n hybrid nanoparticle, the reduction of zeta potential is from -13.30 mV to -12.00 mV. There exist more space inside the hybrid liposomes with smaller PSL NPs allowing for higher loading of fluorescein. More amount of fluorescein results in higher changes in zeta potential values.

Table 4.4. DLS and Zeta Potential Results for Liposome Encapsulated Hybrid Nanoparticles and Their Fluorescein Dye Loaded Counterparts.

Name of Nanoparticle	**Mean Diameter (nm)**	**Surface Charge**	**Zeta Potential (mV)**	**Electrophoretic mobility ($m^2s^{-1}V^{-1}$)**
30nm-C-n Hybrid NP	155.3	Negative	-22.00	-1.72
30nm-C-n-Fl Hybrid NP	165.4	Negative	-11.48	-0.900
50nm-A-p Hybrid NP	289.5	Positive	8.480	0.660
50nm-A-p-Fl Hybrid NP	406.8	Positive	0.7000	0.0500
100nm-A-n Hybrid NP	165.2	Negative	-13.30	-1.04
100nm-A-n-Fl Hybrid NP	155.4	Negative	-12.00	-0.940

4.2. Construction of Growth Curve for Sac6:RFP Tagged *S. cerevisiae* Cells

Yeast cell growth curve experiments are carried out to obtain the time required to reach the late exponential growth phase of Sac6:RFP tagged *S. cerevisiae* cells. The average values of the OD measurements corresponding to each of the time interval are shown in Table D.1. All experiments are carried out twice.

The growth curve representing the optical density versus time graph for Sac6:RFP tagged *S. cerevisiae* cells was obtained as shown in Figure 4.12.

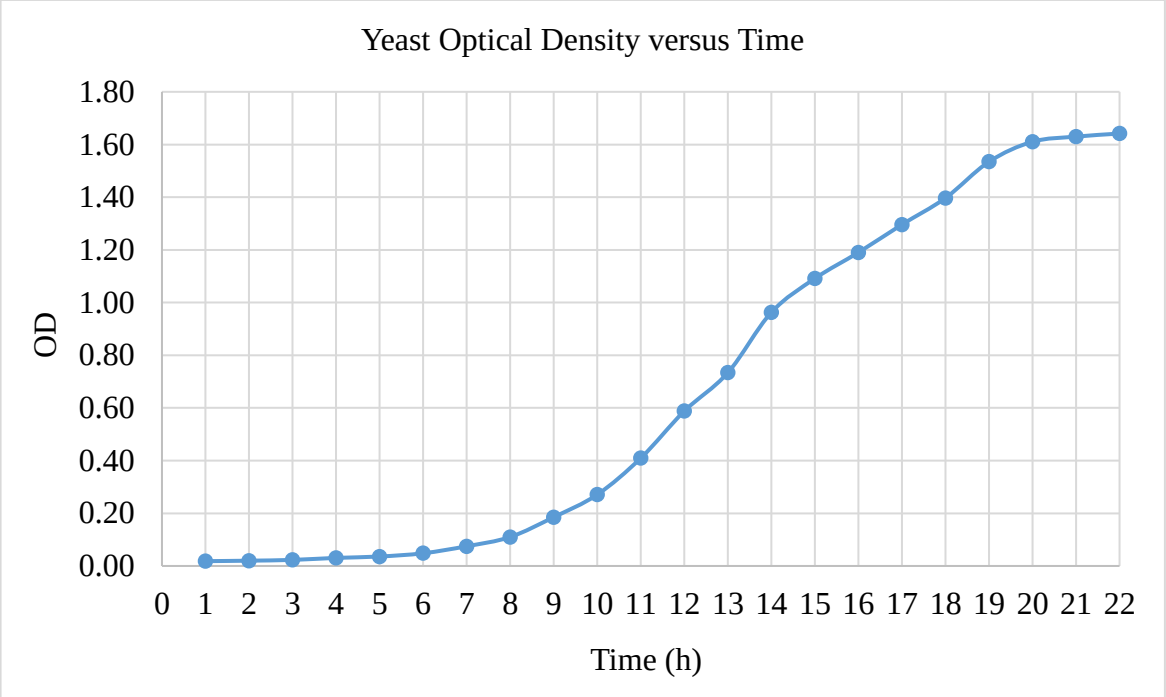

Figure 4.12. Growth curve for Sac6:RFP tagged *S. cerevisiae* for 22 hour incubation time.

Exponential growth phase refers to a period in which the growth rate of the cells increases gradually, the cells grow at a constant and a maximum rate. The increase in the biomass concentration is proportional to the initial biomass concentration in this growth period [52].

$$r_x = \frac{dx}{dt} = \mu x = \mu_{max} x \tag{4.4}$$

$$In\ this\ phase;\ \mu = \mu_{max} = constant$$

Where,

r_x is the net rate of cell mass growth (OD value/hour)

x is the yeast cell mass per unit culture volume (OD value)

μ is the specific growth rate of yeast cells $(hour)^{-1}$

μ_{max} is the maximum specific growth rate of yeast cells $(hour)^{-1}$

In order to calculate the specific growth rate, the above equation is linearized by taking integral of the equation and setting the boundary conditions as follows:

$$Boundary\ conditions:$$

$$x_{initial} = x_0, \qquad t_{initial} = t_0$$

$$x_{final} = x, \qquad t_{final} = t$$

$$\int_{x_0}^{x} \frac{1}{x} dx = \int_{t_0}^{t} \mu_{max}\, dt$$

$$\ln x - \ln x_0 = \mu_{max}(t - t_0)$$

$$\ln x = \mu_{max}(t - t_0) + \ln x_0 \tag{4.5}$$

Where, t_0 is taken as zero.

The lnOD values for each of the time interval have been recorded as shown in Table D.1. $\ln x$ versus $(t - t_0)$ graph of the corresponding measurements is given in Figure 4.13.

The following figure shows lnOD versus time graph for 22 hours of growth measurement.

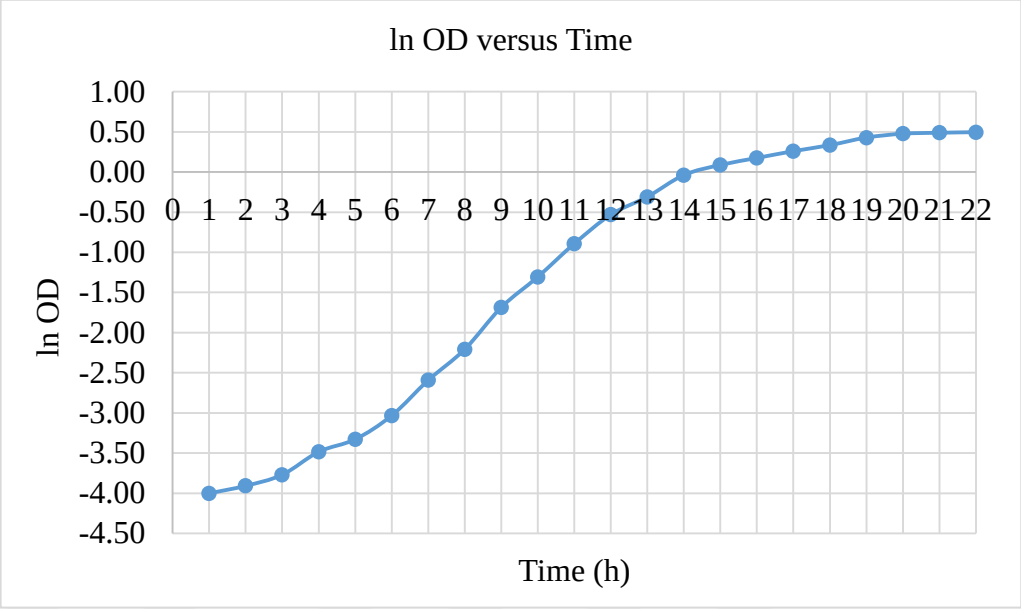

Figure 4.13. lnOD versus time curve of Sac6 tagged *S. cerevisiae* for 22 hour incubation time.

The linear part of the lnOD versus time graph represents constant growth rate of the cells, which is the exponential growth phase. This region of the graph obeys to the linearized equation represented above (eqn.4.5). The slope of the equation gives the maximum specific growth rate (μ_{max}) and the intercept gives ln x_0.

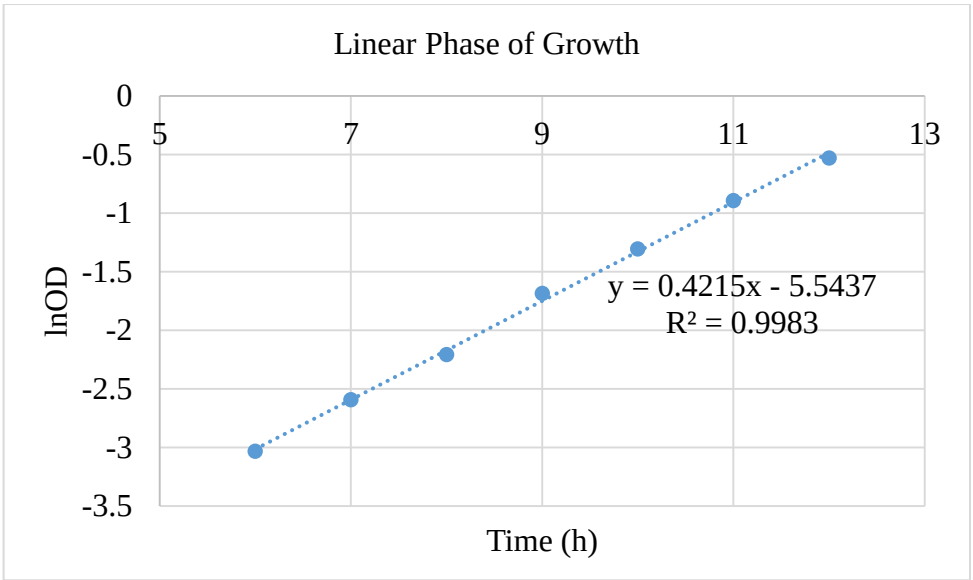

Figure 4.14. lnOD versus time graph representing exponential phase of growth.

According to the fitted linear trendline between the hours 6 to 12 as shown in Figure 4.14, the following equation is found:

$$y = 0.4215x - 5.5437$$

The slope of the equation gives the specific growth rate (μ_{max}) which is 0.4215 h^{-1}.

The cell doubling time is calculated using the following equation:

$$t_d = \frac{\ln 2}{\mu_{max}} \tag{4.6}$$

Where,
t_d is the doubling time of the yeast cells (min)

The doubling time of the Sac6:RFP *S. cerevisiae* cells is calculated as follows:

$$t_d = \frac{\ln 2}{0.4215} = 1.644\ hours = 98.67\ minutes$$

The cell doubling time of the Sac6:RFP tagged EY0987 *S. cerevisiae* cells is calculated as 98.67 minutes. In the literature, it has been reported that the cell doubling time of the *S. cerevisiae* cells are approximately 90 minutes [53]. Thus, it can be interpreted that the results obtained by the growth time analysis for Sac6:RFP tagged EY0987 *S. cerevisiae* cells coincide with the literature.

4.3. Size and Concentration Effects of Polystyrene Latex Nanoparticles (PSL NPs) on *S. cerevisiae* Cells in terms of Cytotoxicity and Internalization

The effects of nanoparticle size and concentration on the toxicity behavior of nanoparticles on *S. cerevisiae* cells are analyzed for negatively charged 20 nm, 30 nm, and 60 nm diameter, carboxyl functionalized PSL nanoparticles (20nm-C-n, 30nm-C-n and 60nm-C-n), negatively charged 50 nm, 100 nm and 200 nm diameter amine functionalized

PSL nanoparticles (50nm-A-n, 100nm-A-n and 200nm-A-n), as well as positively charged 50 nm and 100 nm amine functionalized PSL nanoparticles (50nm-A-p and 1000nm-A-p).

In order to determine the effect of nanoparticle concentration on the viability of the yeast cells, different nanoparticle concentrations in a range between 25 and 800 mg/L are used. CFU results show that for all type of nanoparticles used in this study, as the nanoparticle concentration increases, the viability of the yeast cells decreases accordingly. However, the differences in the level of the viability response appear with the concentration changes in accordance with the size, functional group and surface charge of the nanoparticles.

4.3.1. Size and Concentration Effect of Negatively Charged and Carboxyl Modified PSL NPs on *S. cerevisiae*

Colony Forming Unit (CFU) analysis shows that for each of the nanoparticle concentration used in the study, the viability percentages of different sized negatively charged and carboxyl functionalized nanoparticles are relatively similar to each other (Figure 4.15). Small amount of deviation in all viability percentages resulting from the size differences is found for carboxyl functionalized nanoparticles. For all of the nanoparticle concentrations applied in this study (50-800 mg/L), the calculated average viability of the yeast cells exposed to different sized carboxyl modified PSL nanoparticles (20nm-C-n, 30nm-C-n and 60nm-C-n) varies slightly. However, when the error bound is taken into consideration, the change in viability with respect to the size of the PSL nanoparticles is minimal. For 800 mg/L, which is the highest experimental nanoparticle concentration, it is found from the average viability calculations that as the nanoparticle size increases, the viability percentage decreases accordingly, but according to the error bound, this effect is also negligible. Consequently, it can be interpreted that the size effect of the negatively charged carboxyl functionalized PSL nanoparticles on yeast cell toxicity is insignificant in the range of 20 to 60 nm according to the experimental results.

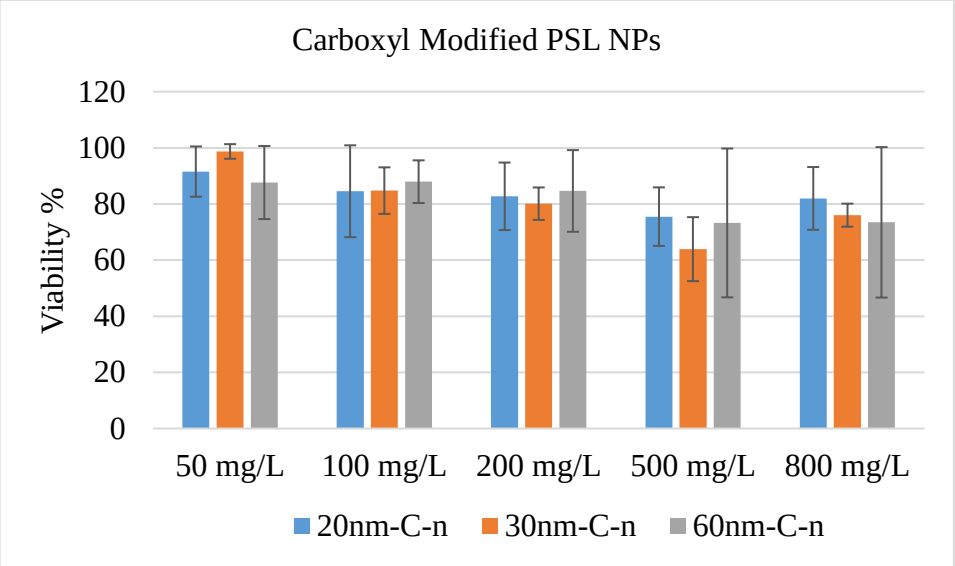

Figure 4.15. Viability percentage of *S. cerevisiae* cells showing the size effect of negatively charged and carboxyl functionalized PSL NPs after exposure for 3 days at 30°C.

Concentration effect of carboxyl functionalized nanoparticles on the yeast cells is analyzed for 20nm-C-n, 30nm-C-n and 60nm-C-n PSL nanoparticles. 50 mg/L nanoparticle concentration causes little or no toxicity towards the yeast cell. However, as the nanoparticle concentration increases up to 500 mg/L, the viability starts to decrease gradually according to CFU analysis. Interestingly, at the nanoparticle concentration of 800 mg/L, a slight degree of increment in the viability percentage of the yeast cells is observed. This can be explained as follows: when the concentration increases, the possibility of interaction between the nanoparticles increases and the particles form clusters. If the agglomeration of the nanoparticles occurs in the dispersion medium before their uptake by the yeast cells, it may prevent the occurrence of the endocytosis. In this way, the nanoparticle concentration inside the cells cannot easily increase and the nanoparticles cannot show toxic effect.

4.3.2. Size and Concentration Effect of Negatively Charged and Amine Modified PSL NPs on *S. cerevisiae*

The size effect for negatively charged amine functionalized nanoparticles is also investigated by CFU analysis. The viability percentages of *S. cerevisiae* cells exposed to 50,

100 and 200 nm of negatively charged amine functionalized nanoparticles having different concentrations are given in Figure 4.16

The viability percentages are found similar for 50nm-A-n, 100nm-A-n and 200nm-A-n PSL nanoparticles for the 0-500 mg/L concentration range considering the standard deviation results. The decrease in viability with increasing nanoparticle size is prominent for 800 mg/L concentration, i.e., the average viability percentages are 95.5%, 73.2% and 59.5%, for 50nm-A-n, 100nm-A-n and 200nm-A-n PSL nanoparticles, respectively. This can be the result of cell membrane damage during the endocytosis of nanoparticles. Since the higher sized materials require larger vacuoles to be encapsulated, they may cause damage to the cellular membrane structure more presumably than the smaller materials. In general, as the size of the negatively charged and amine functionalized nanoparticles increases the viability of the yeast cells decreases.

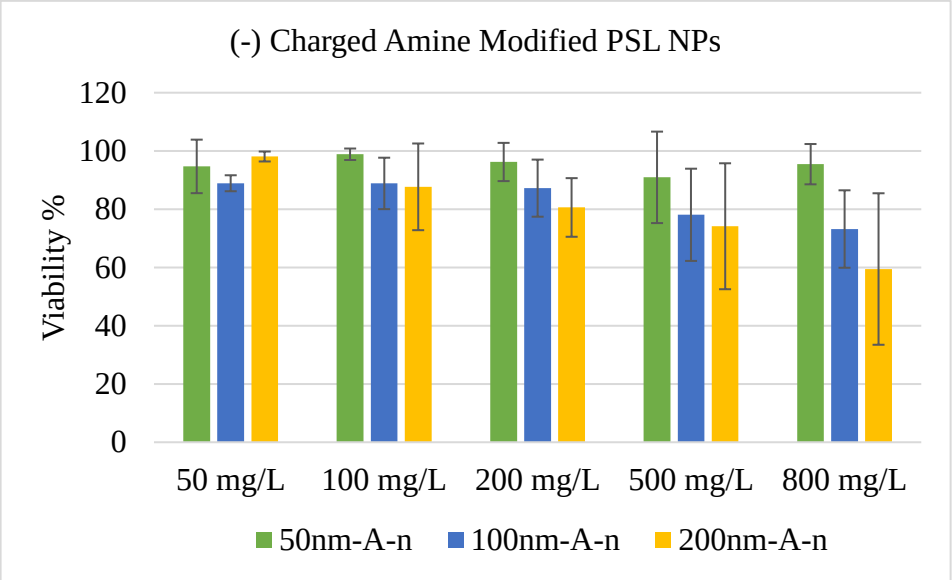

Figure 4.16. Viability percentage of *S. cerevisiae* cells showing the size effect of negatively charged and amine functionalized PSL NPs after exposure for 3 days at 30°C.

The concentration effect of negatively charged amine functionalized nanoparticles on the yeast cells is analyzed for 50nm-A-n, 100nm-A-n and 200nm-A-n PSL nanoparticles (Figure 4.16). 50 mg/L nanoparticle concentration causes little or no toxicity towards the yeast cell, which is similar to the negatively charged and carboxyl modified PSL

nanoparticles. For 50nm-A-n PSL nanoparticles, the effect of the concentration increase is not found significant for 50-800 mg/L concentration range. However, a gradual decrease in viability is observed as a result of concentration increase from 50 mg/L to 800 mg/L for 100nm-A-n and 200 nm-A-n PSL nanoparticles.

4.3.3. Size and Concentration Effect of Positively Charged and Amine Modified PSL NPs on *S. cerevisiae*

The size effect for positively charged and amine functionalized PSL nanoparticles on the toxicity of *S. cerevisiae* cells is investigated by CFU analysis. The viability percentages of *S. cerevisiae* cells exposed to 50nm-A-p and 100nm-A-p PSL nanoparticles of different concentrations are shown in Figure 4.17. The cell viability has been observed only at 50 and 100 mg/L concentrations. At higher concentrations these nanoparticles have shown fully toxic effect towards *S. cerevisiae* cells. At both nanoparticle concentrations (50 and 100 mg/L), 50nm-A-p is slightly more toxic than 100nm-A-p, but when the standard deviations are considered this effect is found minimal. These results are in accordance with the literature. Miyazaki *et al.* (2014) stated that the toxicity results of the 50 nm and 100 nm PSL nanoparticles are similar, which shows that the effect of nanoparticle size on the viability of the yeast cells is minimal. However, slight increase in the viability percentages of *S. Cerevisiae* cells is observed as the size of the positively charged and amine functionalized PSL nanoparticles increases from 50 nm to 100 nm at 50 mg/L nanoparticle concentration. One reason for this outcome can be the higher impact of the surface accumulation of smaller nanoparticles compared to larger ones that may result in more severe effects on the *S. cerevisiae* cells to sustain their viability. It may be suggested that if the smaller nanoparticles agglomerate on the cell surface and constitute clusters, there exists less space on the cell surface uncovered by the nanoparticles to continue the transportation processes between the intracellular and extracellular environment of the cell. Hence, the probability of the cell death because of the nanoparticle coverage on the cell surface becomes higher for smaller nanoparticles.

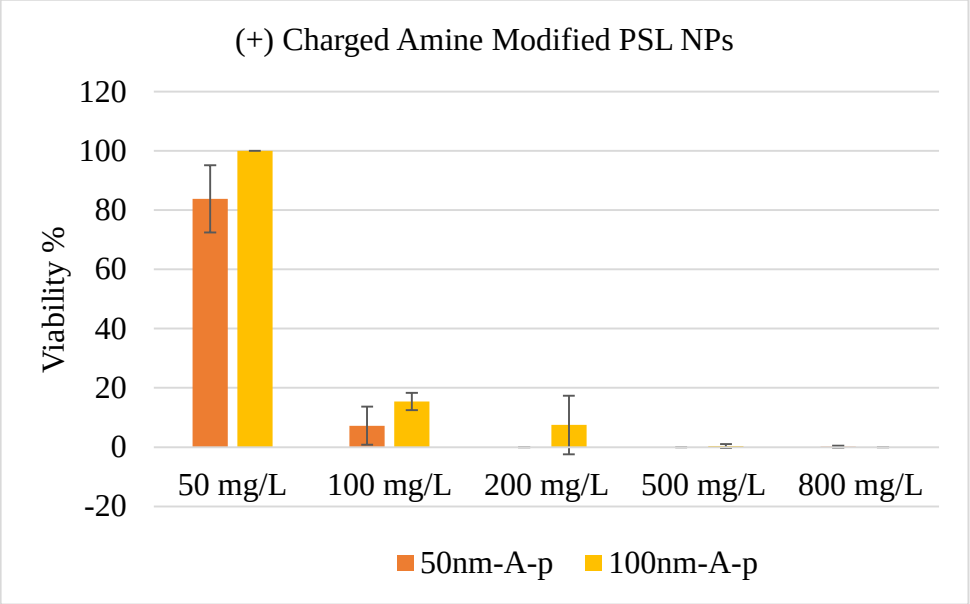

Figure 4.17. Viability percentage of *S. cerevisiae* cells showing the size effect of positively charged and amine functionalized PSL NPs after exposure for 3 days at 30°C.

The concentration effect of positively charged amine functionalized nanoparticles on the yeast cells is analyzed for 50nm-A-p and 100nm-A-p (Figure 4.17). 50 mg/L concentration causes little or no toxic effect towards the yeast cells for both of the nanoparticles, whereas starting with 100 mg/L concentration, the viability percentages decrease very sharply such that only 7.2% and 15.43% of the cells are viable after 50nm-A-p and 100nm-A-p PSL nanoparticle exposure, respectively. Starting with 200 mg/L up to 800 mg/L concentration, very little or no cells are found viable after positively charged amine functionalized nanoparticle concentrations. Consequently, it is determined from the experimental studies that positively charged and amine functionalized PSL nanoparticles show toxic effect towards the yeast cell starting with 100 mg/L concentration.

4.3.4. Charge Effect of Polystyrene Latex Nanoparticles (PSL NPs) on *S. cerevisiae*

The charge effect of the nanoparticles on the viability of the *S. cerevisiae* cells has been analyzed using amine functionalized PSL nanoparticles, 50nm-A-n, 50nm-A-p, 100nm-A-n, 100nm-A-p (Figure 4.18). Amine functionalized nanoparticles can possess negative or positive surface potentials according to their molecular arrangements. Here, the positively charged amine functionalized nanoparticles are observed to cause fully toxic

effect at concentrations higher than 100 mg/L, whereas at low concentrations, (50 mg/L) the toxicity effect is not observed.

With 50nm-A-p PSL nanoparticles, the viability of the yeast cells decreases when the nanoparticle concentration increases. However, the viability percentage does not fall below 80% at 50 mg/L nanoparticle concentration (Figure 4.18). When the nanoparticle concentration is 50 mg/L the viability percentage is 83.8%. Interestingly, further increase in the concentration (from 100 to 800 mg/L) has caused a rapid reduction in the viability percentages. In other words, the positively charged nanoparticles have shown fully toxic effect on the yeast cells at concentrations higher than 100 mg/L. On the contrary, the exposure of 50nm-A-n PSL nanoparticles towards *S. cerevisiae* cells even at high concentrations does not cause any toxic effect, such that at 800 mg/L nanoparticle concentration, the viability percentage of the cells is 95.5%.

With 100nm-A-p PSL nanoparticles, 50 mg/L concentration is not found toxic towards the yeast cell. But at 100 mg/L concentration, the viability percentages decrease significantly. At 500 mg/L and higher nanoparticle concentrations, no viable cells are observed with CFU analysis. With 100nm-A-n PSL nanoparticles, 0-200 mg/L nanoparticle concentrations are little or none toxic towards the yeast cell. At concentrations higher than 200 mg/L the viability percentages decrease slightly with increasing concentration values. Although the increase in nanoparticle concentration results in lower viability percentages, this reduction is negligible compared to 100nm-A-p. The viability percentages after exposing the yeast cells with 800 mg/L 100nm-A-n and 800 mg/L 100nm-A-p PSL nanoparticles are 73.2% and 0.00%, respectively. It was reported that the positively charged nanoparticles result in more toxic effect than the anionic nanoparticles because they cause the cell membrane disruption and damages on mitochondria and lysosome of the cells [54].

The effect of oppositely charged nanoparticles on *S. cerevisiae* can be investigated through their zeta potentials together with the electrostatic attraction forces. A strong electrostatic attraction force exists between the negatively charged EY0987 *S. cerevisiae* cell (zeta-potential: -3.71 mV) and positively charged PSL nanoparticles: 50nm-A-p and 100nm-A-p (zeta-potentials: 23.66 mV and 16.25 mV, respectively). As a result of the attraction forces, more nanoparticles are pulled towards cell; but they may be agglomerated on the

membrane surface or transported through it. Since the absolute zeta potential value of 100nm-A-p is lower than that of 50nm-A-p PSL nanoparticles, the effects of attraction forces may become less significant which leads to the lower amount of nanoparticle related toxicity with 100nm-A-p PSL nanoparticles.

In the study of Miyazaki *et al*. (2014), amine functionalized and positively charged 50 nm PSL nanoparticles were found to be fully toxic towards the *S. cerevisiae* cells at 80 mg/L concentration when 5mM NaCl was used as dispersion medium and the nanoparticles were observed on the cell surface. However, when 154 mM NaCl solution was used, the cells internalized the PSL nanoparticles and the viability of the yeast cells was around 80%. This was explained that because of strong electrostatic attraction forces between the yeast cell and PSL nanoparticles surface accumulation of the PSL nanoparticles was occurred when 5 mM NaCl solution was used. But with 154 mM NaCl solution, there was less electrostatic interaction between the PSL nanoparticles and the yeast cells and the nanoparticles were internalized inside the cells. Similarly, in the study of Nomura *et al*. (2013), positively charged and amine functionalized PSL nanoparticles at 40 mg/L concentration showed fully toxic effect towards the *S. cerevisiae* cells when 5 mM NaCl solution was used as dispersion medium. But the viability of the yeast cells was around 80% when 154 mM NaCl solution was used. In the present study, according to the CFU analyses, at 50 mg/L 50nm-A-p and 100nm-A-p PSL nanoparticle concentration, the cells are around 90% viable but starting with 100 mg/L PSL nanoparticle concentration significant reduction in the cell viability is observed and after 200 mg/L PSL nanoparticle concentration, the nanoparticles show fully toxic effect towards the *S. cerevisiae* cells when 1XPBS solution is used as the dispersion medium.

In spite of the electrostatic attraction forces between the positively charged PSL nanoparticles (50nm-A-p and 100nm-A-p) and slightly negatively charged yeast cells, the PSL nanoparticles tend to accumulate on the cell surface rather than to be internalized inside the cell. In this aspect, the presence of other parameters than the charge effects can be considered such as nanoparticle-protein corona formation [55]. When nanoparticles are introduced in biological medium, the biomolecules bind on the surface of the nanoparticles and formation of nanoparticle-corona occurs [55]. This means that the strength of the electrostatic attraction forces between the nanoparticles and the yeast cells does not always

result in nanoparticle uptake inside the cells. In the present study, the positively charged nanoparticles cover the cell surface and do not enter inside the cell. This may be explained by the nanoparticle-protein corona formation and thus the alteration of interactions between the nanoparticles and the yeast cells as a result of new configuration.

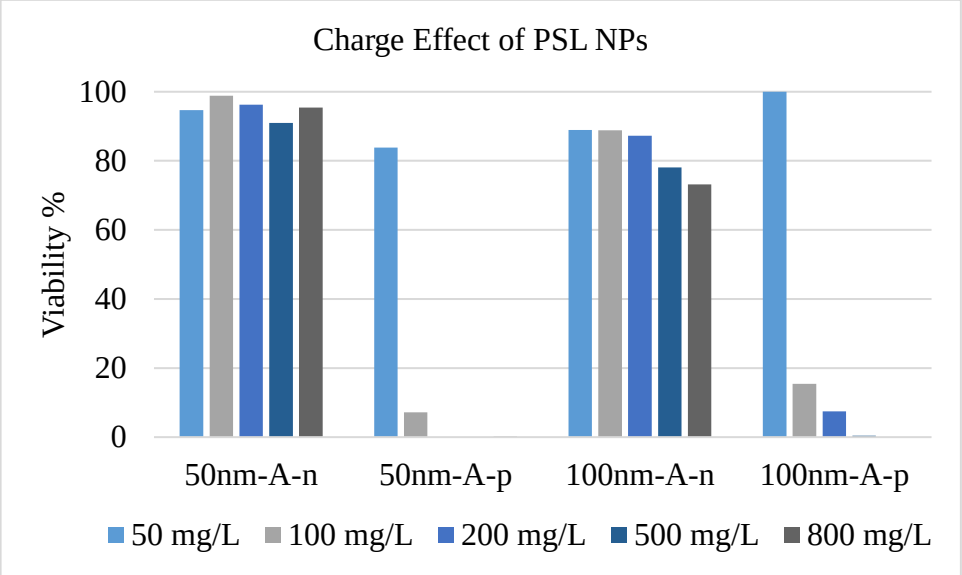

Figure 4.18. Viability percentage of *S. cerevisiae* cells showing the charge effect of amine functionalized PSL NPs after exposure for 3 days at 30°C.

4.4. Confocal Microscopy Analyses of *S. cerevisiae* Cells Exposed to Polystyrene Latex Nanoparticles (PSL NPs)

Confocal microscopy analysis is carried out to obtain the microscopic visualizations of the *S. cerevisiae* cells under different concentrations of 30nm-C-n PSL nanoparticles (50 mg/L and 100 mg/L). By this analysis the viability of the yeast cell under nanoparticle exposure is determined by PI staining and also the location of the nanoparticles inside the cells or on the cell surface is determined. These results enable better understanding of the possible reasons behind the toxicity behavior of these nanoparticles on the yeast cells.

In Figure 4.19., the location of 30nm-C-n PSL nanoparticles at 50 mg/L concentration inside the *S. cerevisiae* cells is seen. The nanoparticles inside the cells make clusters and they have round shapes. From this image, it can also be seen that the cell is viable as it is not

stained by PI, which is a membrane impermeable dye (Figure 4.20). It can be interpreted that this concentration of nanoparticle accumulation inside the cells does not show a toxic effect for this cell. This result is also confirmed by the CFU analysis carried out for 50 mg/L 30nm-C-n PSL nanoparticle exposure in which the viability percentage of the cells is found as 98.7%. As a result, confocal analysis shows that when the nanoparticle concentration inside the cells is low, it does not affect the viability. But when the nanoparticle concentration increases, the nanoparticles begin to show toxic effect towards the yeast cell.

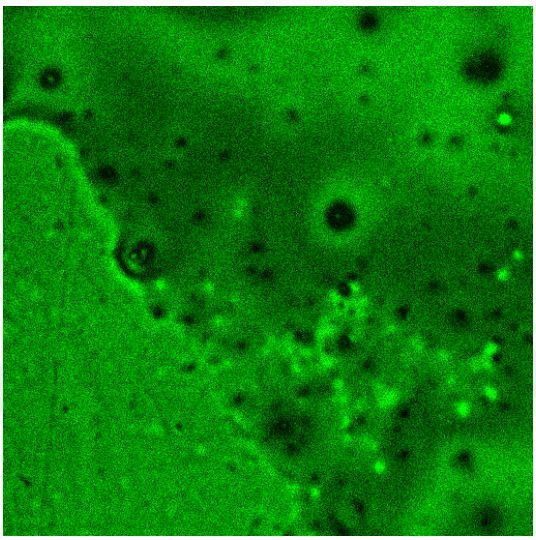

Figure 4.19. CLSM image of 50 mg/L 30nm-C-n PSL NP exposed yeast cell, FITC filter.

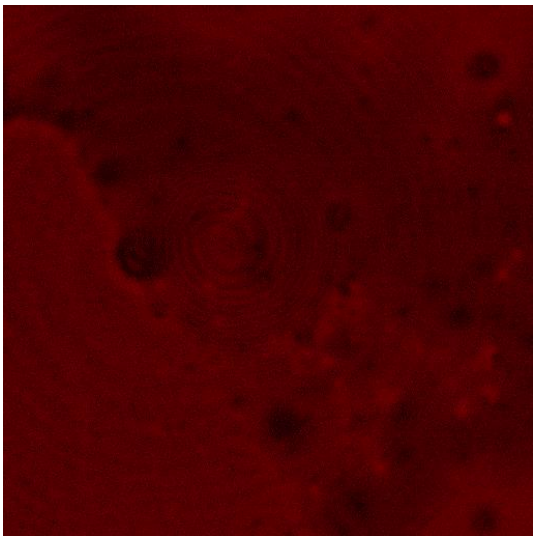

Figure 4.20. CLSM image of 50 mg/L 30nm-C-n PSL NP exposed yeast cell, PI filter.

In Figure 4.21, the confocal microscopy images of *S. cerevisiae* cells under 100 mg/L of 30nm-C-n PSL nanoparticle exposure can be seen. For 100 mg/L concentration, the nanoparticle accumulation inside the cells is observed and it is confirmed by the 3-D projection image of these cells (Figure 4.22). The agglomerated nanoparticles inside the cells are more visible for 100 mg/L than 50 mg/L concentration of nanoparticles. Confocal analysis results show that when the nanoparticle concentration inside the cell is low, it does not affect the viability. But when the concentration increases, the nanoparticles begin to show toxic effect towards the yeast cell. Fluorescence exerted by 30nm-C-n PSL nanoparticles shows that the cells, in which the nanoparticles agglomerate in the cell cytoplasm, are viable, but when the nanoparticles pass to the inside of the nucleus, they show toxic effect, that is observed by the PI staining (Figure F.4 and Figure F.5)

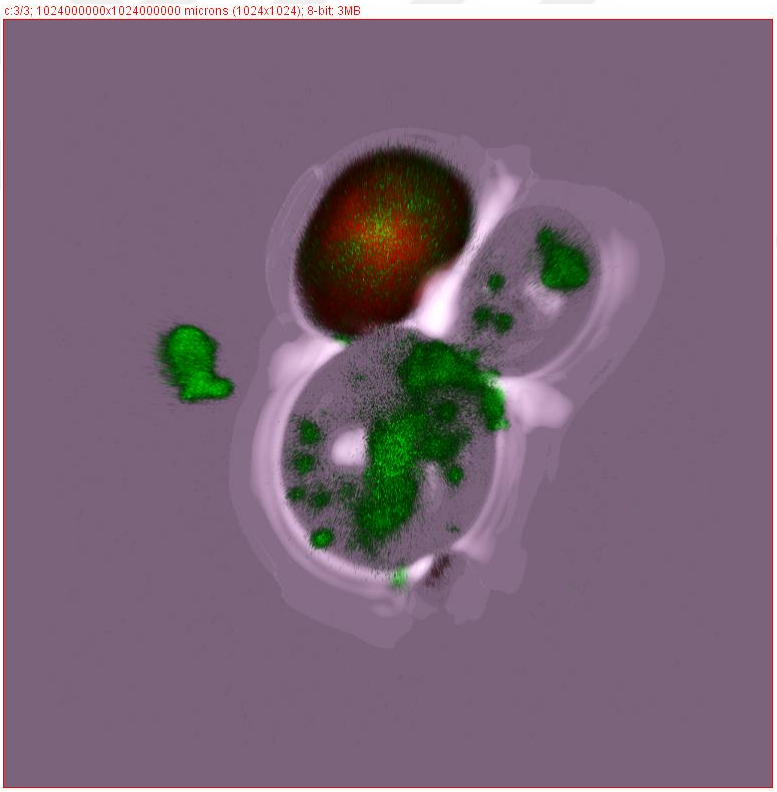

Figure 4.21. CLSM merged image of 100 mg/L 30nm-C-n PSL NP exposed yeast cells.

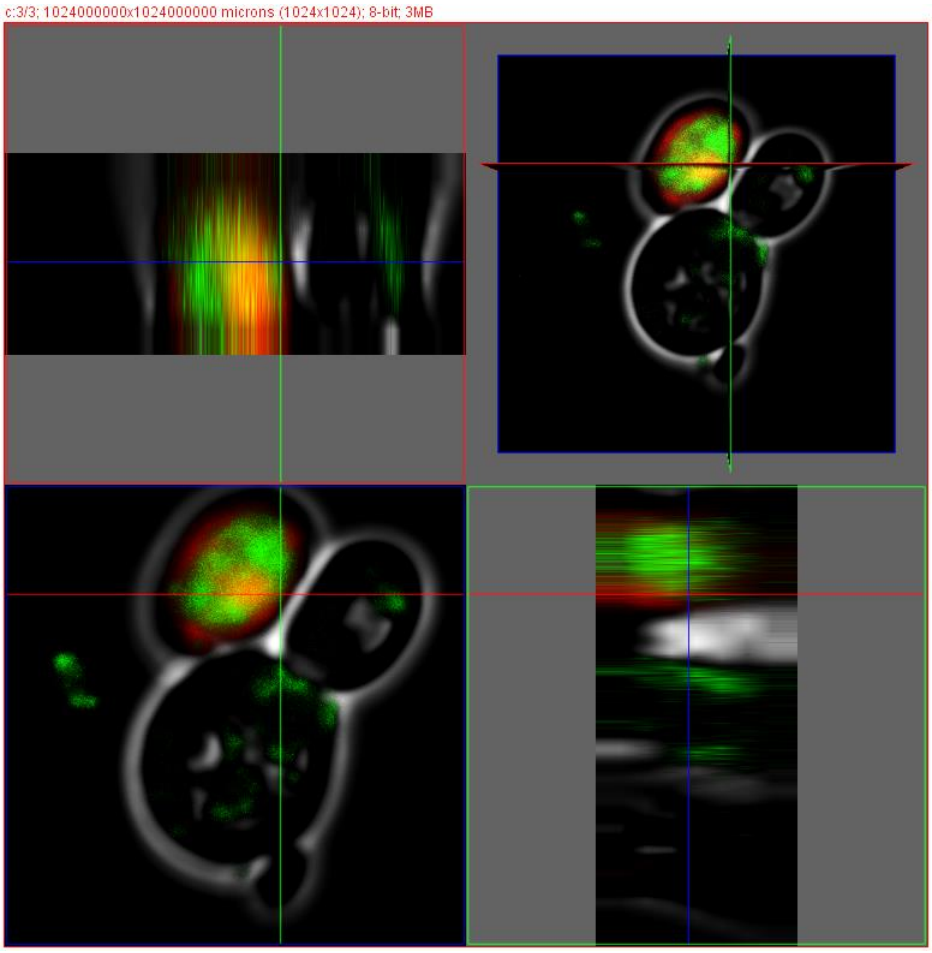

Figure 4.22. 3-D projection image of 100 mg/L 30nm-C-n PSL NP exposed yeast cells.

The confocal analysis is performed to visualize the effects of different concentrations of 100nm-A-p PSL nanoparticles on *S. cerevisiae* cells. Four different concentrations, which are 50, 100, 500 and 800 mg/L, were used to observe the concentration effect of 100nm-A-p PSL nanoparticles. According to the microscopic visualizations of 50 mg/L 100nm-A-p PSL nanoparticle exposed yeast cells, in accordance with the CFU analysis results, most of the cells are viable, i.e. they are not stained with PI, which is a membrane impermeable dye (Figure 4.23).

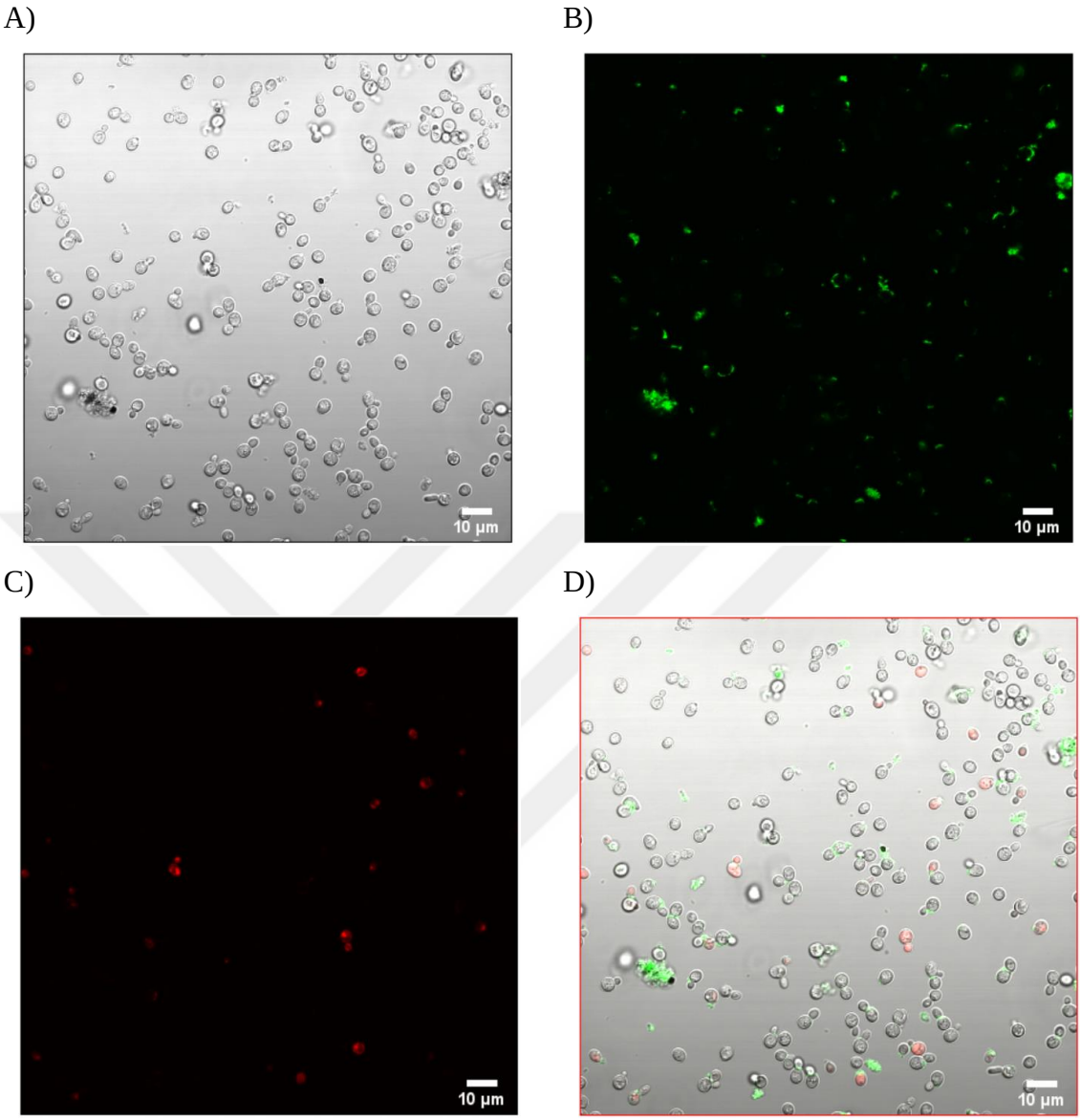

Figure 4.23. CLSM images of 50 mg/L 100nm-A-p PSL NP exposed yeast cells A) Bright field B) FITC C) PI D) Merged image.

As the nanoparticle concentration increases to 100 mg/L, the amount of inviable cells increase and for the concentrations starting with 500 mg/L (up to 800 mg/L) almost all of the cells observed are found dead because of the high concentration of nanoparticle exposure (Figure 4.24, Figure 4.25 and Figure 4.26). The fluorescence emitted from the nanoparticles shows their location in the yeast suspension. For all of the concentrations (50, 100, 500 and 800 mg/L), it is observed that 100nm-A-p nanoparticles tend to accumulate on the cell surface in spite of the electrostatic attraction forces between the slightly negatively charged

yeast cells and positively charged 100nm-A-p PSL nanoparticles. Although the accumulation of the nanoparticles on the cell surface is observable for all of the concentrations, the toxicity effect of them is apparent at higher concentrations. At 50 mg/L NP concentration, there are still viable cells, whose surfaces are partly covered by the 100nm-A-p PSL nanoparticles (Figure F.6). At 100 mg/L NP concentration, the surface coverage of the 100nm-A-p PSL nanoparticles becomes more prominent (Figure 4.24).

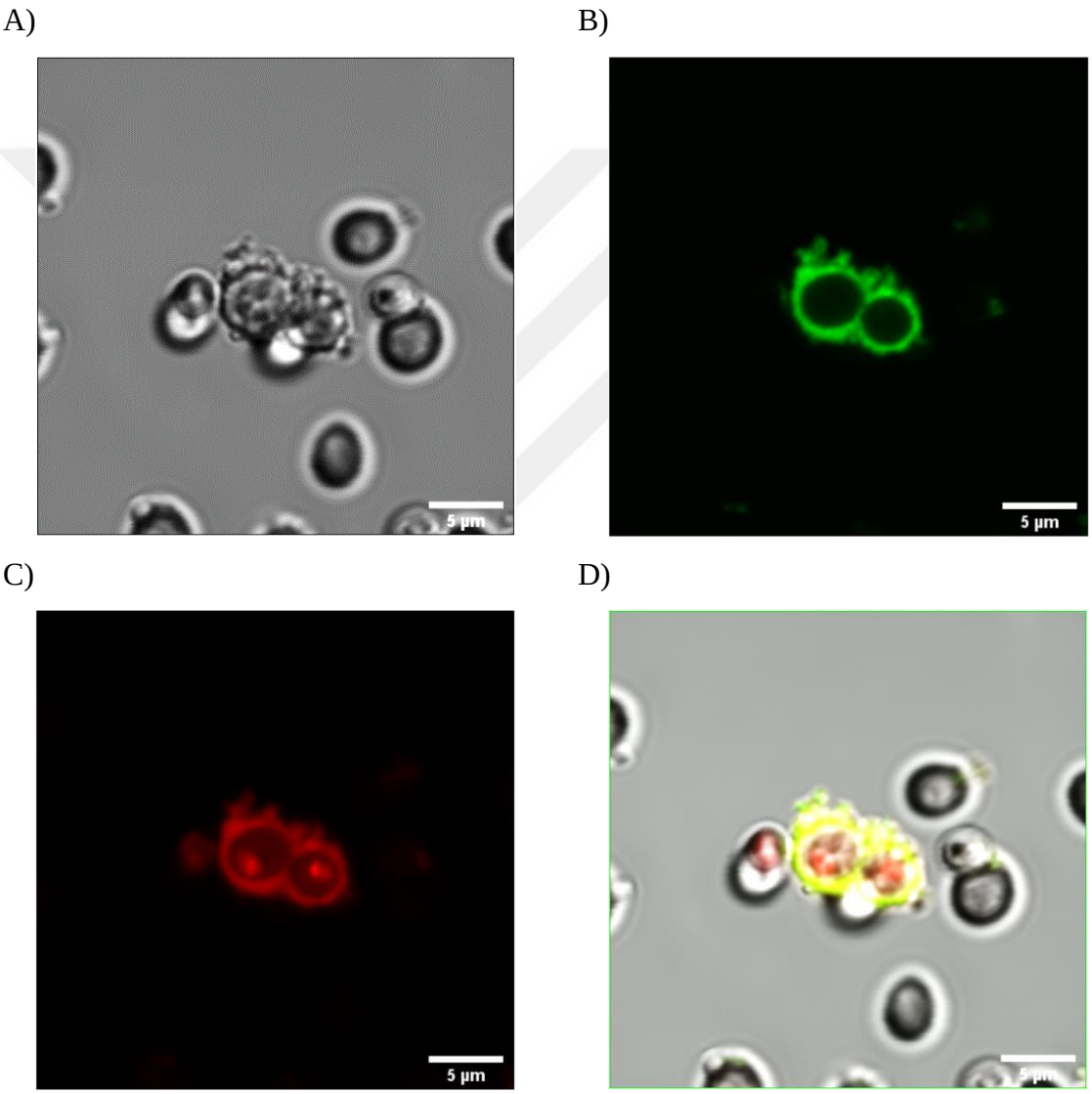

Figure 4.24. CLSM images of 100 mg/L 100nm-A-p PSL NP exposed yeast cells A) Bright field B) FITC C) PI D) Merged image.

The intense clustering of the nanoparticles is observable especially from 500 mg/L nanoparticle concentration onwards, in which there is huge amount of nanoparticle aggregation. Also, at high nanoparticle concentrations, the *S. cerevisiae* cells are clustered to each other and seen as stuck on these nanoparticle aggregates (Figure 4.26). It can be suggested that the reason why almost all the cells are found inviable at high concentrations, may be the insufficient transportation through the cell membrane because of the large amount of nanoparticle agglomeration.

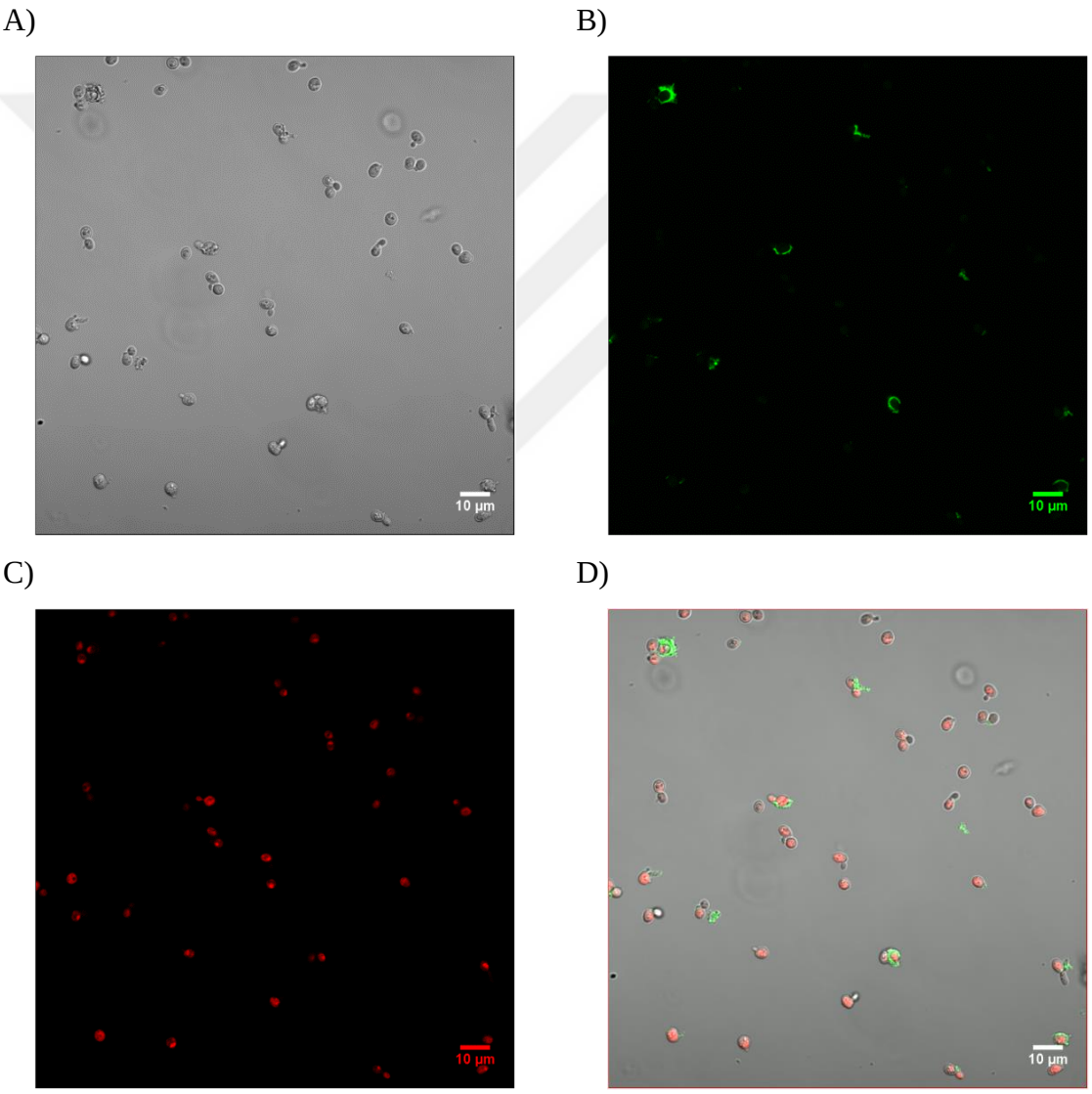

Figure 4.25. CLSM images of 500 mg/L 100nm-A-p PSL NP exposed yeast cells A) Bright field B) FITC C) PI D) Merged image.

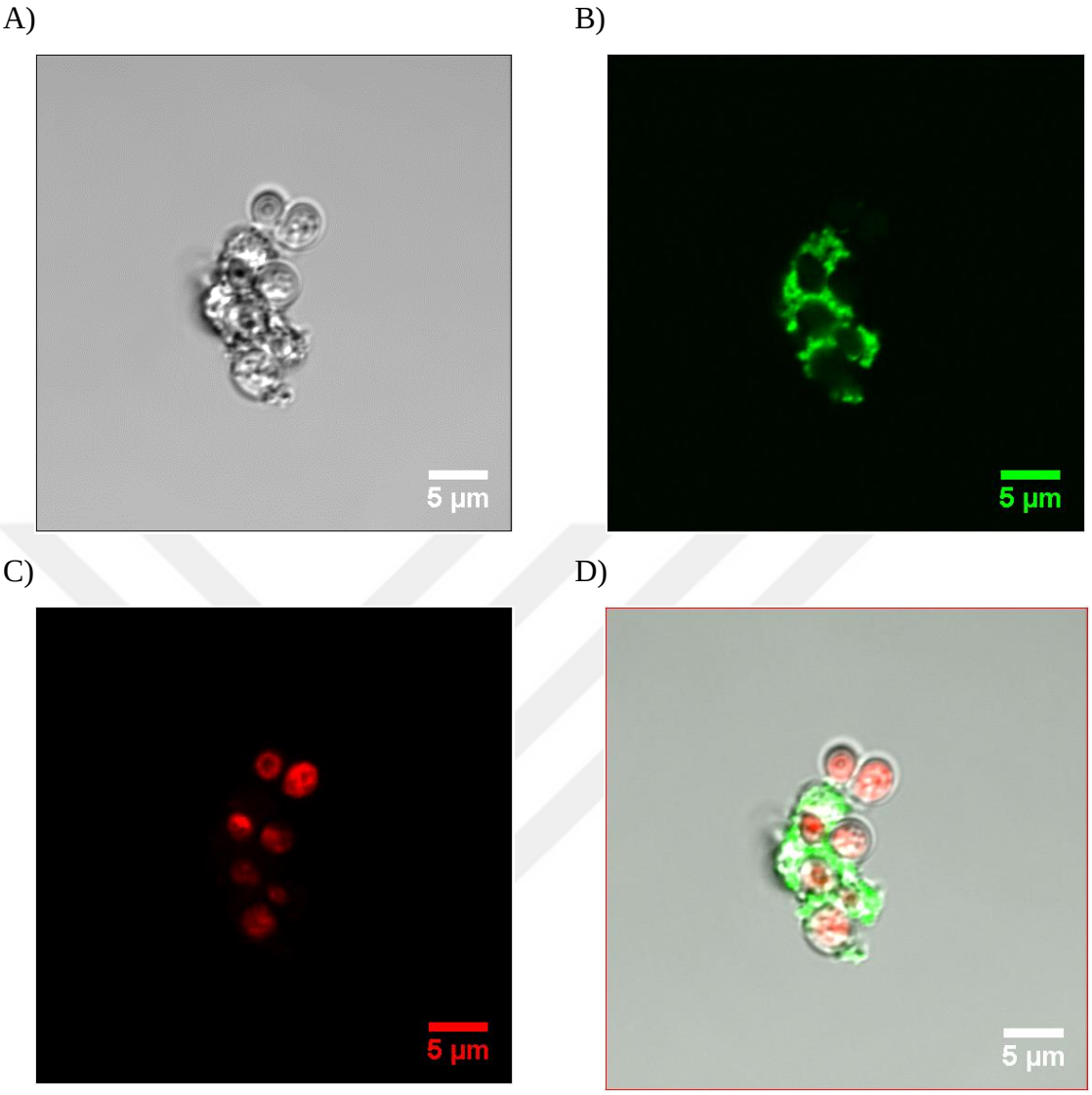

Figure 4.26. CLSM images of 800 mg/L 100nm-A-p PSL NP exposed yeast cells A) Bright field B) FITC C) PI D) Merged image.

4.5. Long-Time Effects of Polystyrene Latex Nanoparticle (PSL NP) Exposure on *S. cerevisiae* Cells

The investigation of the possible effects of PSL nanoparticles towards the living organisms with short-term toxicological analysis is important to observe the behavior of these nanoparticles. However, the prolonged exposure of these nanoparticles should also be investigated in long-term to elucidate toxic impacts of the PSL nanoparticles on the next generations of these organisms. In the present study, the effects of PSL nanoparticle

exposure towards the *S. cerevisiae* cells are investigated in long-term to observe their potential effects on the next generations. For the long-time exposure experiments, the PSL nanoparticles, which are not found toxic towards the yeast cell in short-term experiments, are opted to determine whether the non-toxic nanoparticles exert a degree of toxicity on the next generations or not. For this purpose, 100 mg/L 20nm-C-n, 200 mg/L 20nm-C-n and 100 mg/L 60nm-C-n PSL nanoparticles have been selected since these types and concentrations of nanoparticles are found little or no toxic towards the yeast cells after CFU analysis carried out for 3 days at 30°C of incubation. It is aimed to see both the concentration effect by carrying out the experiment with two different concentrations (100 mg/L and 200 mg/L) and also the size effect by using two different sized nanoparticles (20nm and 60nm).

The yeast cells are grown in liquid yeast extract and glucose medium with the addition of the specified type and concentration of PSL nanoparticles. The incubated yeast cells at their exponential phase of growth are spread on the agar plates after the dilution process. The nanoparticle exposed yeast cells are grown also in solid medium at 30°C for 3 days. One of the colonies on the agar plates are placed inside the fresh liquid yeast extract and glucose medium containing nanoparticles with the help of the inoculating wire loop. These processes are repeated until 15^{th} generation of the yeast strain is obtained. The effects of the nanoparticles on *S. cerevisiae* cells are investigated both by CFU analysis and OD measurements. OD measurements are carried out by diluting the yeast solution and recording the optical density values. OD measurements for 15 generation of the yeast cells exposed to different size and concentrations of PSL nanoparticles are shown in Table 4.5. CFU analysis is carried out and the viability percentages of the yeast cells are calculated with respect to the control group that does not contain nanoparticles and the results are shown in Table 4.6. The results obtained by the OD measurements and CFU analysis confirm each other. According to the findings in the present study, although some fluctuation is observed in the viability percentages of the subsequent yeast generations, in overall the yeast cells are viable after 100 mg/L 20nm-C-n, 200 mg/L 20nm-C-n and 100 mg/L 60nm-C-n PSL nanoparticle exposure in long-term exposure experiments. One can conclude that after 15 yeast generations the nontoxic PSL NPs in short-term do not cause any toxicity to the yeast cells.

Table 4.5. OD Measurements of the PSL NP Exposed Yeast Cells for 15 Generations.

	500/500 Dilution (Yeast/Medium)				250/750 Dilution (Yeast/Medium)			
OD	**Control**	**20nm 100 mg/L**	**20nm 200 mg/L**	**60nm 100 mg/L**	**Control**	**20nm 100 mg/L**	**20nm 200 mg/L**	**60nm 100 mg/L**
1st generation	1.003	1.134	-	-	0.615	-	-	-
2nd generation	1.026	1.034	-	-	0.665	0.687	-	-
3rd generation	1.076	1.046	1.033	-	0.673	0.643	0.690	-
4th generation	1.143	1.240	1.264	1.162	0.745	0.855	0.775	0.737
5th generation	1.075	1.069	1.021	1.217	0.693	0.676	0.654	0.824
6th generation	1.212	1.091	1.123	1.066	0.808	0.727	0.740	0.693
7th generation	1.593	1.458	1.441	1.460	1.144	0.950	0.981	1.001
8th generation	1.119	1.132	1.145	1.106	0.691	0.727	0.704	0.651
9th generation	0.986	1.046	0.988	1.022	0.595	0.622	0.590	0.630
10th generation	1.239	1.305	1.260	1.211	0.780	0.831	0.809	0.753
11th generation	0.858	1.074	1.017	0.905	0.484	0.671	0.626	0.533
12th generation	1.095	1.124	1.095	1.076	0.693	0.705	0.670	0.674
13th generation	1.082	1.072	1.060	1.020	0.676	0.683	0.669	0.636
14th generation	1.121	1.160	1.080	1.098	0.727	0.742	0.661	0.679
15th generation	1.046	1.039	1.092	0.960	0.596	0.642	0.687	0.586

Table 4.6. Viability Percentages of the PSL NP Exposed Yeast Cells for 15 Generations.

Viability (%)	20nm-C-n 100 mg/L	20nm-C-n 200 mg/L	60nm-C-n 100 mg/L
1st generation	100.0	-	-
2nd generation	90.1	-	-
3rd generation	96.0	76.7	-
4th generation	100.0	100.0	100.0
5th generation	82.6	84.0	100.0
6th generation	95.2	98.2	81.5
7th generation	85.2	94.6	97.7
8th generation	87.3	71.0	92.8
9th generation	88.8	96.7	100.0
10th generation	74.5	57.7	98.1
11th generation	100.0	77.3	87.6
12th generation	75.0	100.0	74.7
13th generation	94.5	93.0	90.0
14th generation	83.3	97.9	74.5
15th generation	68.9	84.5	83.8
Average	88.1	87.0	90.1

4.6. Effects of DOPC Liposomes on *S. cerevisiae* in terms of Cytotoxicity

Phosphatidylcholines (PCs) are the major components of the phospholipid bilayer of cellular membranes and they constitute almost half of the membrane lipids [56]. The liposomes made by DOPC phospholipids have been widely used in the therapeutic studies [57]. DOPC liposomes have been found as highly efficient *in vivo* siRNA delivery. It has been reported that siRNA incorporated and nanometer sized liposomes made by DOPC phospholipid can penetrate into the tumors deeply *in vivo* meanwhile preventing the phagocytosis [57]. In the present study, the phospholipid 1,2-Dioleoyl-sn-glycero-3-phosphocholine (DOPC) is used to generate liposomes.

CFU analysis is carried out to determine the effects of DOPC liposomes on *S. cerevisiae*. Synthesized liposomes at different concentrations, which are 0.25 mg lipid/ml 1XPBS solution (1:0 dilution liposome solution:PBS solution), 0.125 mg lipid/ml 1XPBS solution (1:1 dilution liposome solution:PBS solution), 0.025 mg lipid/ml 1XPBS solution (1:9 dilution liposome solution:PBS solution) and 0.0025 mg lipid/ml 1XPBS solution (1:99 dilution liposome solution:PBS solution), are used to treat the yeast cells, and the viability percentages are calculated after 3 days at 30°C incubation. It can be concluded from the CFU results that the DOPC liposomes possess little or no inhibitory effect on the viability of the yeast cells. According to the results, even for the most concentrated case, the DOPC liposomes cause little or no toxicity towards the yeast cell (Figure 4.27). This result is important to investigate the cellular uptake analysis of PSL NP encapsulated hybrid nanoparticles on the yeast cells. Since any significant viability decrease is not found after the liposome exposure, the effects that may stem from the usage of liposomes as PSL NP encapsulating agents in further investigation, can be analyzed effectively.

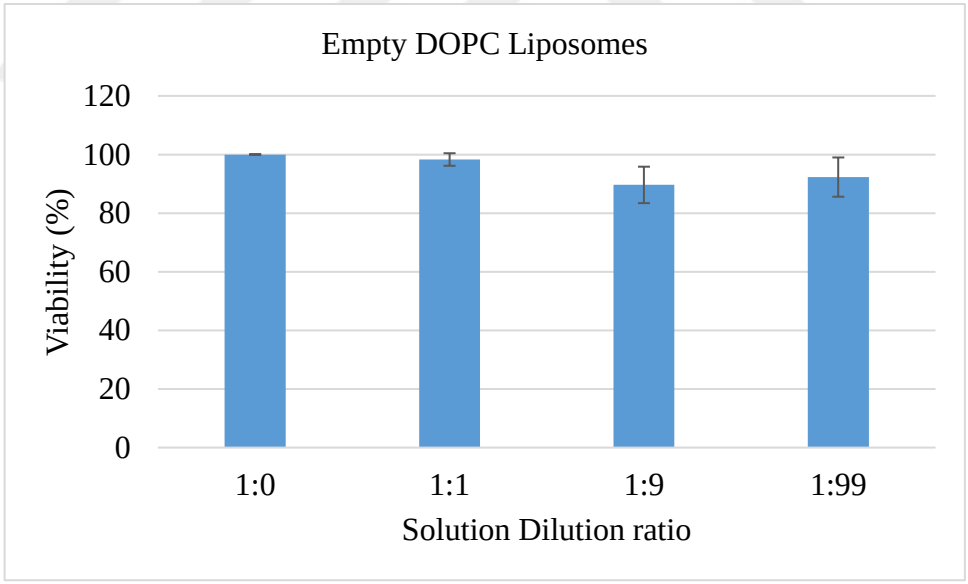

Figure 4.27. Viability percentage of *S. cerevisiae* cells exposed to different concentrations of empty DOPC liposome.

4.7. Effects of Hybrid Nanoparticles on *S. cerevisiae* Cells in terms of Cytotoxicity and Internalization

Hybrid nanoparticles were synthesized by encapsulating different type of PSL nanoparticles (30nm-C-n, 50nm-A-p, 100nm-A-n and 100nm-A-p) with DOPC liposomes during self-assembly process of liposome formation. Different concentrations of hybrid nanoparticles in the range of 50-800 mg/L were prepared and they were exposed to *S. cerevisiae* cells. The possible toxicity effects caused by the exposure of the synthesized hybrid nanoparticles in terms of toxicity and cellular internalization on the yeast cells were analyzed by CFU method and confocal microscopy analyses. Also, the response of the yeast cells to different concentrations of hybrid nanoparticles were investigated. The viability percentages of *S. cerevisiae* cells under different types and concentrations of hybrid nanoparticle exposure after 3 days and 30°C of incubation are shown in Figure 4.28.

According to the CFU analysis results, it has been found out that 30nm-C-n and 100nm-A-n hybrid nanoparticles show significant toxic effect towards the *S. Cerevisiae* cells even at low concentrations (50 mg/L), such that the average viability percentage is found as 71.0% and 61.1% for 30nm-C-n and 100nm-A-n PSL nanoparticles, respectively. On the contrary, the viability percentage of 50nm-A-p hybrid nanoparticles has been found to be very low or non-toxic towards the yeast cell for all of the concentrations (50-800 mg/L) (Figure 4.28). These results are completely opposite from the findings obtained from PSL nanoparticle exposure, namely, the positively charged amine functionalized PSL nanoparticles (50nm-A-p) are found to be fully toxic to the yeast cells even at low concentrations (starting with 100 mg/L), whereas negatively charged carboxyl functionalized PSL nanoparticles are found to be non-toxic even at high concentrations. For 100nm-A-p hybrid nanoparticles, 50mg/L concentration causes little toxicity towards the yeast cells, such that the viability percentage is 83.4%. For 100 g/L and 200 mg/L concentrations, the viability percentages are found as 92.5% and 95.4%, respectively (Figure 4.28). Thus, it can be interpreted that the viability results belonging to the hybrid nanoparticles containing negatively charged nanoparticles are in accordance with each other. Similarly, the viability results of the yeast cells under hybrid nanoparticle exposure containing positively charged nanoparticles coincide with each other.

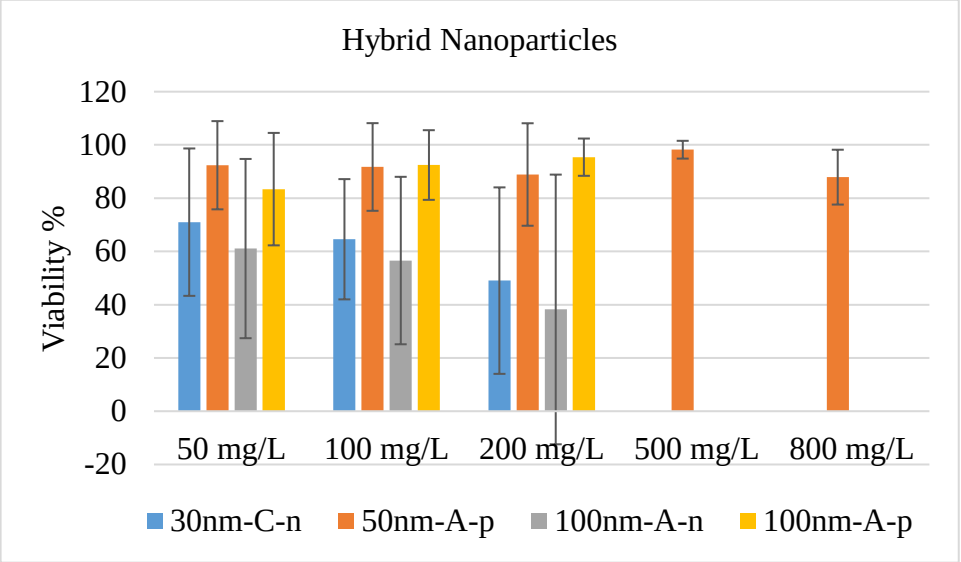

Figure 4.28. Viability percentage of *S. cerevisiae* cells exposed to different type and concentrations of hybrid nanoparticle for 3 days at 30°C.

4.7.1. Effects of Negatively Charged Hybrid Nanoparticles on *S. cerevisiae* in terms of Cytotoxicity and Internalization

For the hybrid nanoparticles synthesized from the phospholipid bilayer encapsulation of the negatively charged and carboxyl functionalized PSL nanoparticles (30nm-C-n), the viability percentages at all concentrations (0-200 mg/L) are found much lower than those obtained with PSL nanoparticle exposure at the corresponding concentrations. The yeast cells exposed to 50 mg/L 30nm-C-n hybrid nanoparticles are 71.0% viable, whereas the viability percentage for the same concentration of PSL nanoparticle exposure is 98.7%, showing significant reduction in the viability (Figure 4.29). Similarly, at 100 mg/L concentration the viability percentage decreases from 84.8% to 64.6%. When the 30nm-C-n hybrid nanoparticle concentration reaches 200 mg/L, the viability percentage becomes 49.0% whereas the viability percentage obtained with 200 mg/L 30nm-C-n PSL nanoparticle exposure is 80.1%.

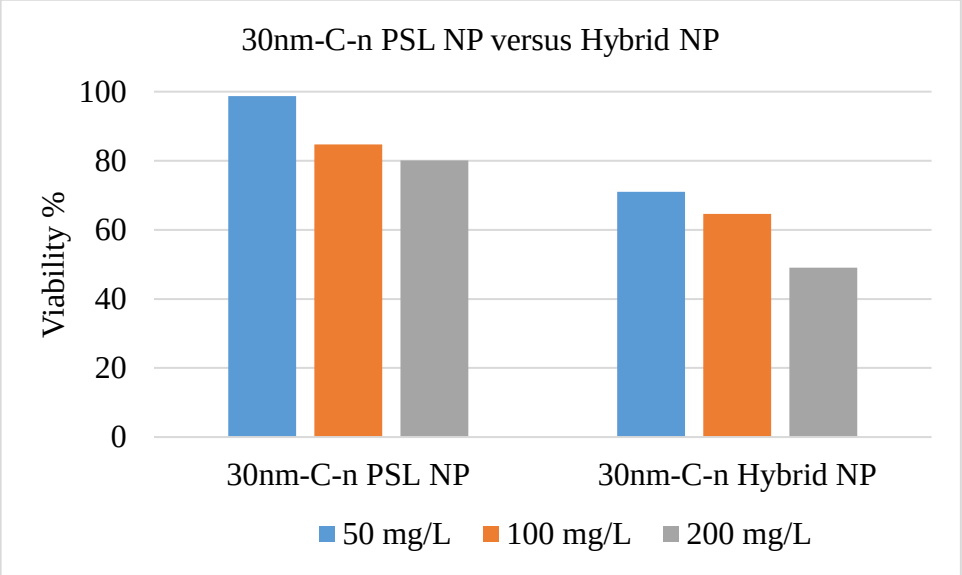

Figure 4.29. Viability percentages of *S. cerevisiae* cells exposed to different concentrations of 30nm-C-n PSL and hybrid nanoparticle for 3 days at 30°C.

For the hybrid nanoparticles synthesized from the phospholipid bilayer encapsulation of the negatively charged and amine functionalized PSL nanoparticles (100nm-A-n), the same cytotoxicity trend as with 30nm-C-n hybrid nanoparticles has been observed. Even at low concentrations (50 mg/L), the viability percentage decreases from 88.9% to 61.1% when the 100nm-A-n PSL nanoparticles are encapsulated by liposomes. (Figure 4.30). The increase in 100nm-A-n hybrid nanoparticle concentration to 100 mg/L leads further decrease in the viability percentage such that it is calculated as 56.6% whereas for 100nm-A-n PSL nanoparticle it is 88.9%. At 200 mg/L 100nm-A-n hybrid nanoparticle concentration, the viability percentage of the yeast cells is calculated as 38.2% which is significantly lower than the viability obtained at the same concentration of PSL nanoparticle exposure, i.e, 87.2%.

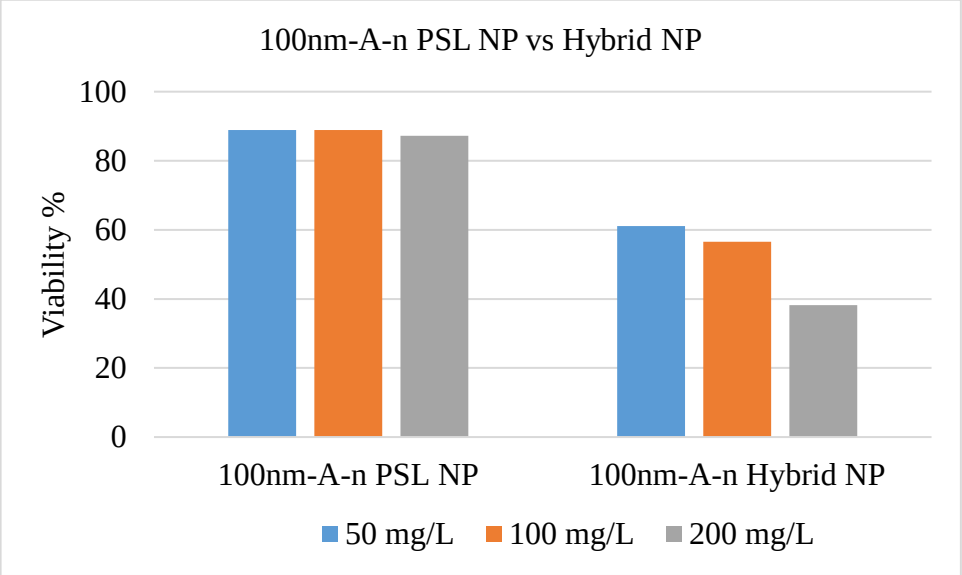

Figure 4.30. Viability percentages of *S. cerevisiae* cells exposed to different concentrations of 100nm-A-n PSL and hybrid nanoparticle for 3 days at 30°C.

4.7.2. Effects of Positively Charged Hybrid Nanoparticles on *S. cerevisiae* in terms of Cytotoxicity and Internalization

CFU analysis results of the yeast cells exposed to the hybrid nanoparticles, which are synthesized by the phospholipid bilayer encapsulation of the positively charged and amine functionalized PSL nanoparticles (50nm-A-p), show that, 50nm-A-p hybrid nanoparticle exposure results in significant increase in the viability of *S. cerevisiae* cells. 50nm-A-p PSL nanoparticles show fully toxic effect at the concentrations higher than 100 mg/L. Conversely, the hybrid nanoparticles are non-toxic towards the yeast cells even at 800 mg/L concentration, i.e. the viability percentage increases from 0.16% to 87.9% (Figure 4.31). The reason behind this may be the larger size of the 50nm-A-p hybrid nanoparticles (~290 nm). As the diameter of the nanoparticles increases, the cellular internalization may become difficult to take place and the possibility of interaction between the nanoparticles and the yeast cells decreases.

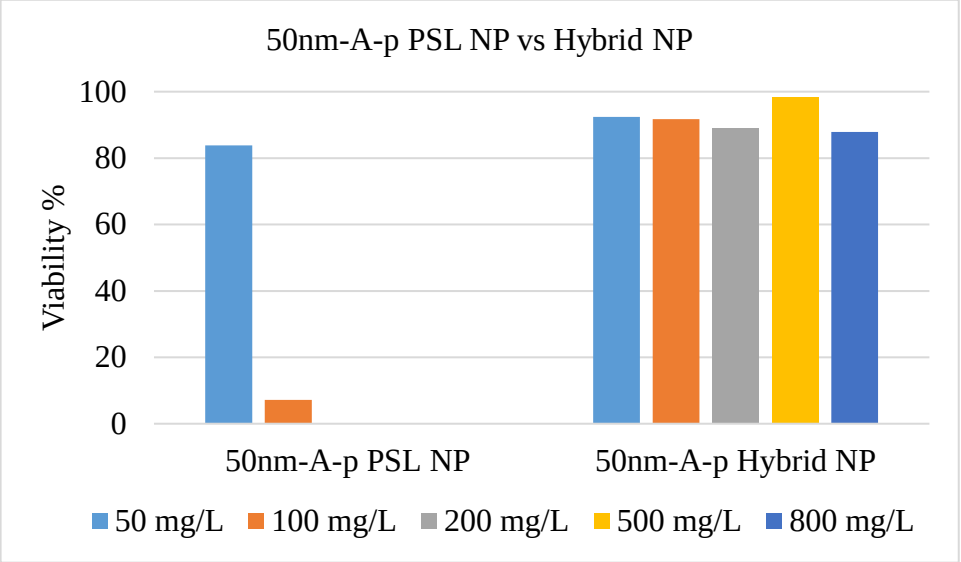

Figure 4.31. Viability percentages of *S. cerevisiae* cells exposed to different concentrations of 50nm-A-p PSL and hybrid nanoparticle for 3 days at 30°C.

CFU analysis is performed to assess the viability percentage of the yeast cells exposed to different concentrations of (50, 100 and 200 mg/L) 100nm-A-p hybrid nanoparticles. The results are compared with the findings of the same concentration of 100nm-A-p PSL nanoparticles. At 50 mg/L 100nm-A-p hybrid nanoparticle concentration, the viability percentage of the yeast cells is found as 83.4% whereas the result with 100nm-A-p PSL nanoparticles is 100.0%. When the concentration increases to 100 mg/L, the viability of the yeast cells is calculated as 92.5% with 100nm-A-p hybrid nanoparticles, whereas the viability is 15.4% with 100nm-A-p PSL nanoparticles (Figure 4.32). Similar trend can be seen when the nanoparticle concentration is 200 mg/L. In this case, the viability is 95.4% with the hybrid nanoparticles and 7.5% with PSL nanoparticles (Figure 4.32). A rapid increase in the viability of the yeast cells is observed for 100nm-A-p hybrid nanoparticles compared to 100nm-A-p PSL nanoparticles for the 100 mg/L and 200 mg/L nanoparticle concentrations. These results are also in agreement with the results obtained with 50nm-A-p hybrid nanoparticles. From these consequences, it can be interpreted that although the positively charged and amine functionalized PSL nanoparticles show toxic effect starting with 100 mg/L concentration, the hybrid forms of the same nanoparticles do not affect the viability of the yeast cells.

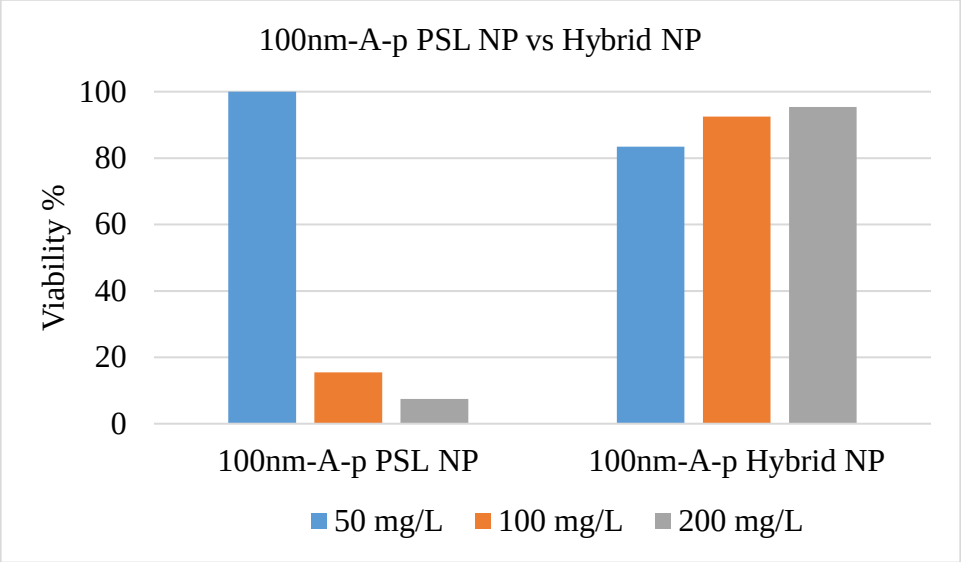

Figure 4.32. Viability percentages of *S. cerevisiae* cells exposed to different concentrations of 100nm-A-p PSL and hybrid nanoparticle for 3 days at 30°C.

4.7.3. Confocal Microscopy Analyses of *S. cerevisiae* Cells Exposed to Hybrid Nanoparticles

Confocal microscopy analysis is carried out for the 100 mg/L 30nm-C-n and 100 mg/L 100nm-A-n-Fl hybrid nanoparticle exposed *S. cerevisiae* cells to observe the location of the hybrid nanoparticles in the yeast suspension. The images for 100 mg/L concentration of 30nm-C-n hybrid and 100nm-A-n-Fl hybrid nanoparticles show that these nanoparticles are mainly accumulated on the cell surface, but not taken up by the cells into their cytoplasm. However, the cells, which internalize hybrid nanoparticles, are also observed (Figure 4.33 and Figure 4.34). These results are opposite of the confocal microscopy images obtained with 30nm-C-n PSL nanoparticles. In that case, most of the nanoparticles are internalized by the yeast cells, and the fluorescence exerted by the agglomerated nanoparticles can easily be seen inside the cells (Figure 4.21 and Figure 4.22). The viability decrease caused by the negatively charged hybrid nanoparticle exposure (30nm-C-n and 100nm-A-n-Fl) of the yeast cells can be explained by the surface accumulation of hybrid nanoparticles. The surface accumulation of hybrid NPs possibly inhibits the interaction of the yeast cell with its environment and the molecules that need to be internalized by the cells cannot pass through

the cell membrane. Also, the waste materials cannot be disposed from the intracellular environment to the outside of the cell.

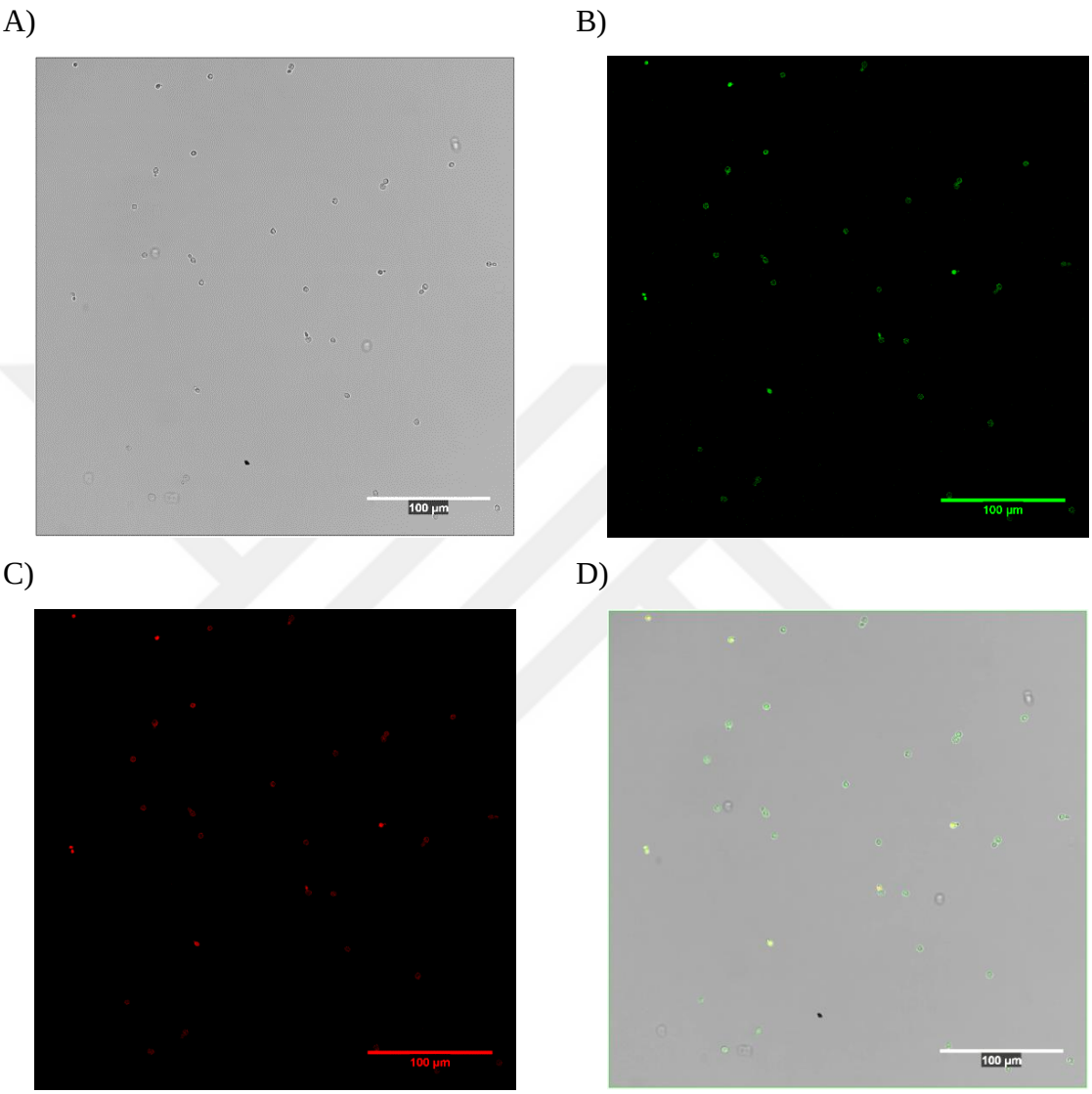

Figure 4.33. CLSM Images of the 100 mg/L 30nm-C-n hybrid nanoparticle exposed yeast cells A) Bright field B) FITC C) PI D) Merged image.

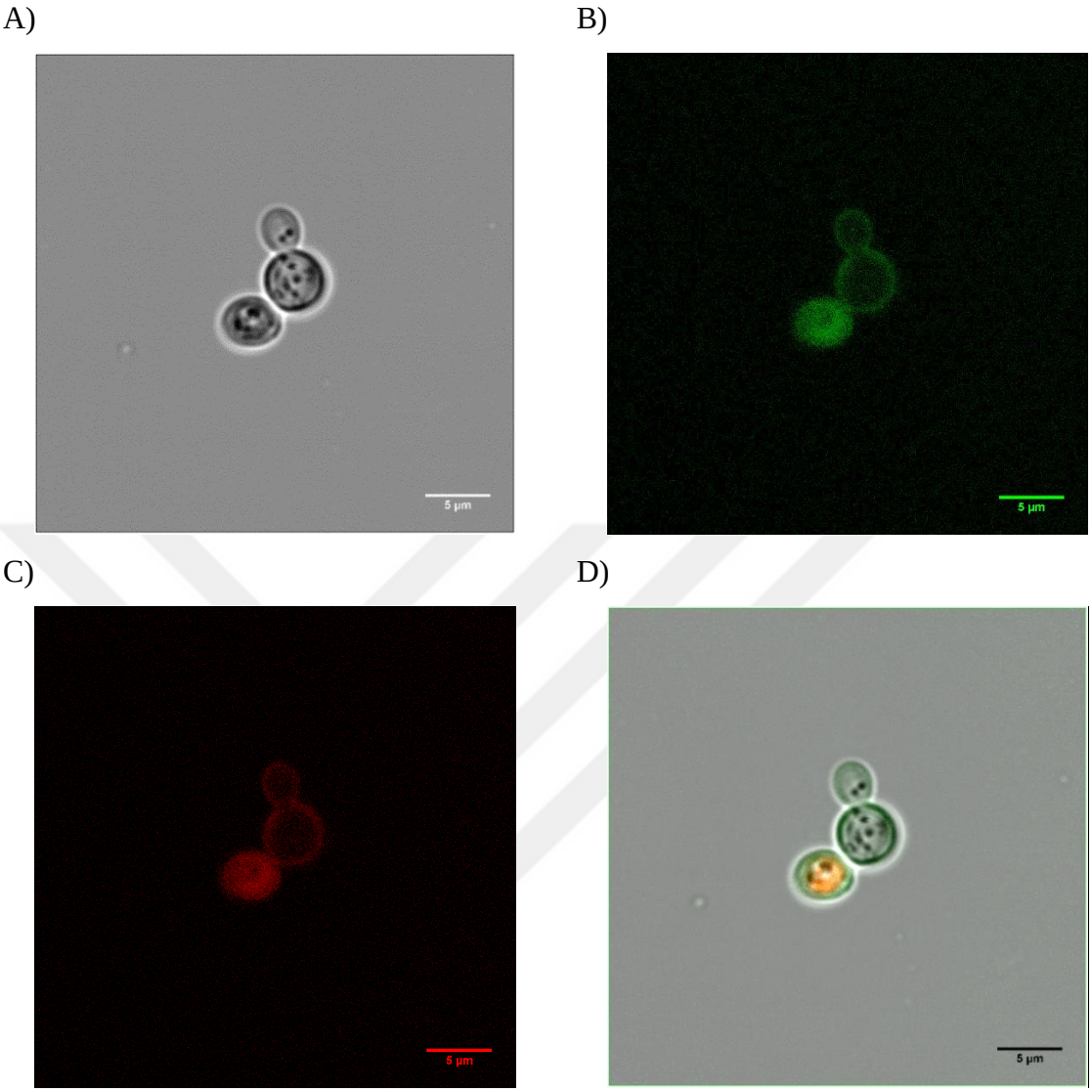

Figure 4.34. CLSM Images of the 100 mg/L 100nm-A-n hybrid NP exposed yeast cells A) Bright field B) FITC C) PI D) Merged image.

4.8. Effect of Uptake Inhibitors on Polystyrene Latex Nanoparticle (PSL NP) Exposed *S. cerevisiae* Cells

4.8.1. Latrunculin-A (Lat-A) Treatment on *S. cerevisiae* Cells

4.8.1.1. Effect of Latrunculin-A on the Control Groups. Endocytosis is an energy dependent process in which proteins and lipids are internalized by the cell from the plasma membrane and some molecules are taken up by the cell from the surrounding environment [58]. It has been shown that the endocytosis is primarily related to the actin filaments according to the genetic screening studies in which end (endocytosis) mutants are isolated [59]. The inhibitor Latrunculin-A (Lat-A) is used to depolymerize the actin filaments to inhibit endocytosis. Various studies have been conducted showing the effective inhibitory effect of Lat-A on the yeast *S. cerevisiae*. 200 μM Lat-A treatment for 10 min has been found to depolymerize all the detachable actin filaments in the yeast cell [60]. 50 μM Lat-A has been shown to inhibit the movement of the patches partially, whereas treatment by 100-200 μM Lat-A has resulted in complete inhibition [61]. It has been pointed out that after 200 μM Lat-A treatment, actin monomers are separated and cortical actin patches are disassembled [62].

In the present study, 200 μM Lat-A is used to depolymerize actin filaments and inhibit endocytosis to see whether the uptake of polystyrene latex nanoparticles (PSL NPs) by the yeast cell occurs via endocytosis or diffusion which are energy dependent and independent mechanisms, respectively. The yeast cells in their liquid growth culture (5.0 g/L yeast extract and 30 g/L glucose) are treated with the 200 μM Lat-A, which depolymerizes actin filaments, for 1 hour at 28°C.

When the number of colonies are counted for the control groups, which are non-treated and treated with inhibitor, 200 μM Lat-A treatment is observed to cause very little toxicity towards the yeast cell. When the control group without inhibitor treatment and with 200 μM Lat-A for 1 hour is compared after 3 days of incubation, the viability of the yeast cells is calculated as 90.2%. The inhibition of endocytosis may cause the prevention of some of the metabolic activities that the yeast must implement throughout its lifecycle as certain substances are taken via the process of endocytosis inside the cytoplasm of the yeast cell and

this may cause the reduction of the cell viability as a result of the endocytosis inhibitor treatment.

4.8.1.2. Effect of Latrunculin-A on Nanoparticle Exposed Groups. To determine the effect of Latrunculin-A (Lat-A) endocytosis inhibitor treatment on the yeast cells, the viability of the nanoparticle added groups with and without inhibitor addition has been analyzed. The yeast cells are treated with 200 µM Lat-A solution, which is dissolved in DMSO, for 1 hour at 28°C. The yeast cells are exposed to different types and concentrations of PSL nanoparticles. CFU and confocal microscopy analyses are performed to determine the effects of Lat-A treatment on the toxicity as well as the uptake of the PSL nanoparticles by *S. cerevisiae* cells.

CFU analysis has been carried out to determine the viability percentages of 200 µM Lat-A treated and PSL nanoparticle exposed yeast cells with respect to only PSL nanoparticle exposed yeast cells. The toxicity behavior of 100 mg/L 30nm-C-n and 100 mg/L 50nm-A-p PSL nanoparticles towards the Lat-A treated yeast cells is found to be similar to the non-inhibitor included PSL nanoparticle exposed yeast cells. The viability percentages are found as 84.8% and 7.20% for inhibitor treated cells, and 100.0% and 5.1% for non-inhibitor included cells for 100 mg/L 30nm-C-n and 100 mg/L 50nm-A-p PSL nanoparticles, respectively (Table 4.7). However, the viability percentages of Lat-A treated and non-inhibitor included cells after the exposure of 50 mg/L 50nm-A-p PSL nanoparticles are found as 71.1% and 83.8%, respectively (Table 4.7). These results show that, 50 mg/L 50nm-A-p PSL nanoparticles do not show significant toxicity towards the yeast cell. The toxic behavior of these nanoparticles is observed after 100 mg/L nanoparticle concentration. The presence of Lat-A treatment causes little toxicity at lower concentrations (50 mg/L) compared to non-inhibitor included cells. This may stem from the slightly toxic effect of the inhibitor Lat-A alone or from the accumulation of the nanoparticles on the cell surface as a result of the endocytosis inhibition.

Table 4.7. Viability Percentages of Non-Inhibitor Included and 200 µM Lat-A Treated Cells Exposed to Different Type and Concentrations of PSL Nanoparticles.

PSL NPs			**200 µM Lat-A treated PSL NPs**		
30nm-C-n	**50nm-A-p**		**30nm-C-n**	**50nm-A-p**	
100 mg/L	**50 mg/L**	**100 mg/L**	**100 mg/L**	**50 mg/L**	**100 mg/L**
84.8	83.8	7.20	100.0	71.1	5.1

Confocal analysis for Lat-A treated and 30nm-C-n and 50nm-A-p PSL nanoparticle exposed yeast cells has been carried out for 100 mg/L nanoparticle concentration. The inhibitor concentrations and the treatment time applied for confocal microscopy analyses are 1 µM Lat-A for 1 hour and 200 µM Lat-A for 1 hour. For 100 mg/L concentration of 30nm-C-n PSL nanoparticle exposed cells after 1 µM Lat-A treatment for 1 hour, the nanoparticles are seen inside the cells, which shows that in spite of 1 µM Lat-A treatment, the cells internalize the 30nm-C-n PSL nanoparticles (Figure 4.35). After 1 µM Lat-A treatment, the nanoparticles are clustered and constitute agglomerates similarly in the case of non-inhibitor included 30nm-C-n nanoparticle exposure. The 3-D projection image confirms the uptake of 30nm-C-n PSL nanoparticles of these yeast cells (Figure 4.35).

50nm-A-p PSL nanoparticles are fluorescently labelled with blue color, it is very difficult to see the fluorescence exerted by these nanoparticles since they have excitation wavelength of 360 nm and emission wavelength of 420 nm. It can be suggested from the confocal microscopy images obtained for 100 mg/L 50nm-A-p PSL nanoparticle exposed yeast cells after 1 µM Lat-A treatment for 1 hour that, the nanoparticles accumulate as clusters on the surfaces of the yeast cells (Figure 4.36). Although the internalization of these nanoparticles is not observed clearly, very slight amount of fluorescence inside the cells is seen.

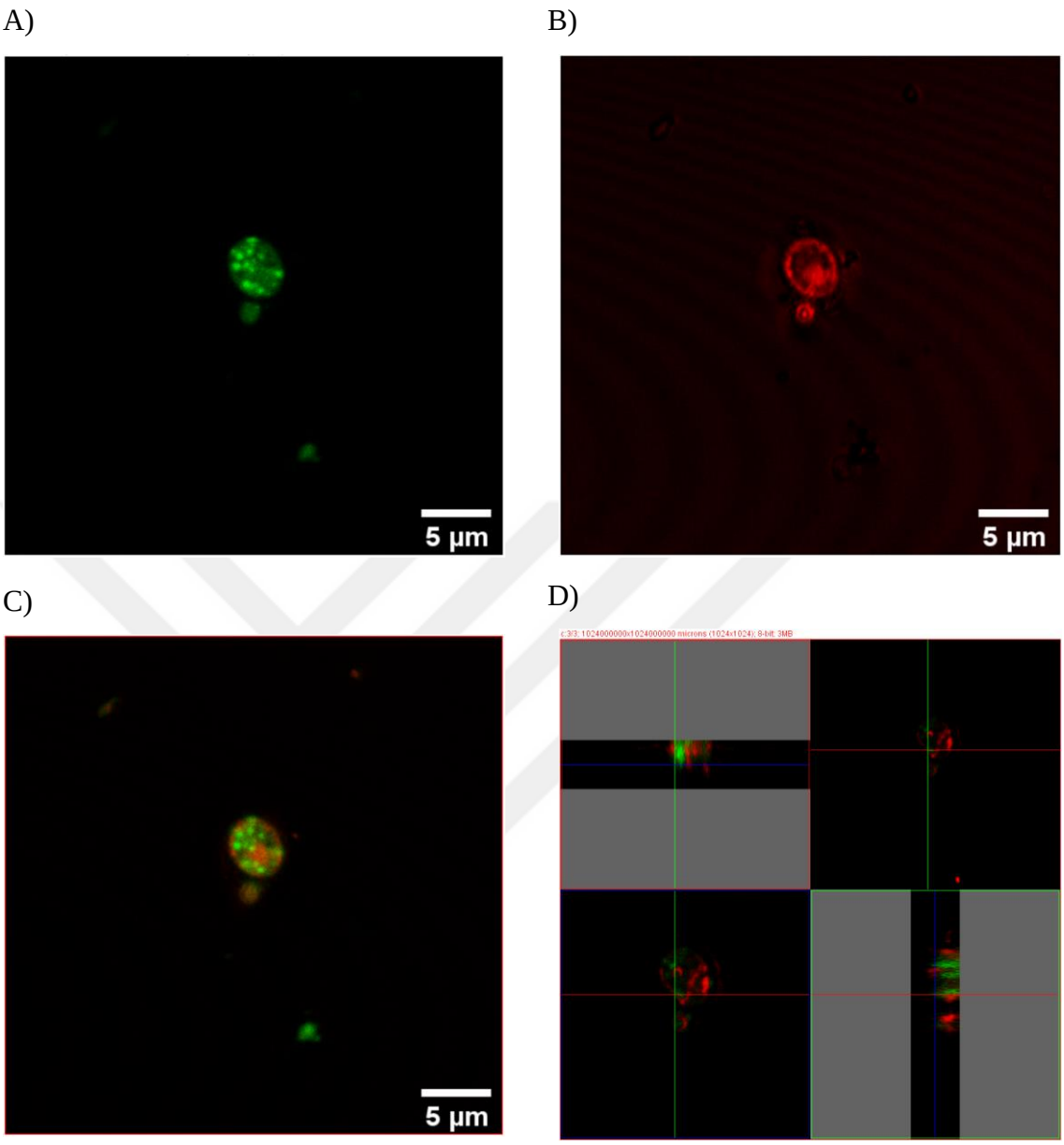

Figure 4.35. CLSM images of 100 mg/L 30nm-C-n PSL NP exposed yeast cells after 1 µM Lat-A treatment A) FITC B) PI C) Merged image D) 3-D projection image.

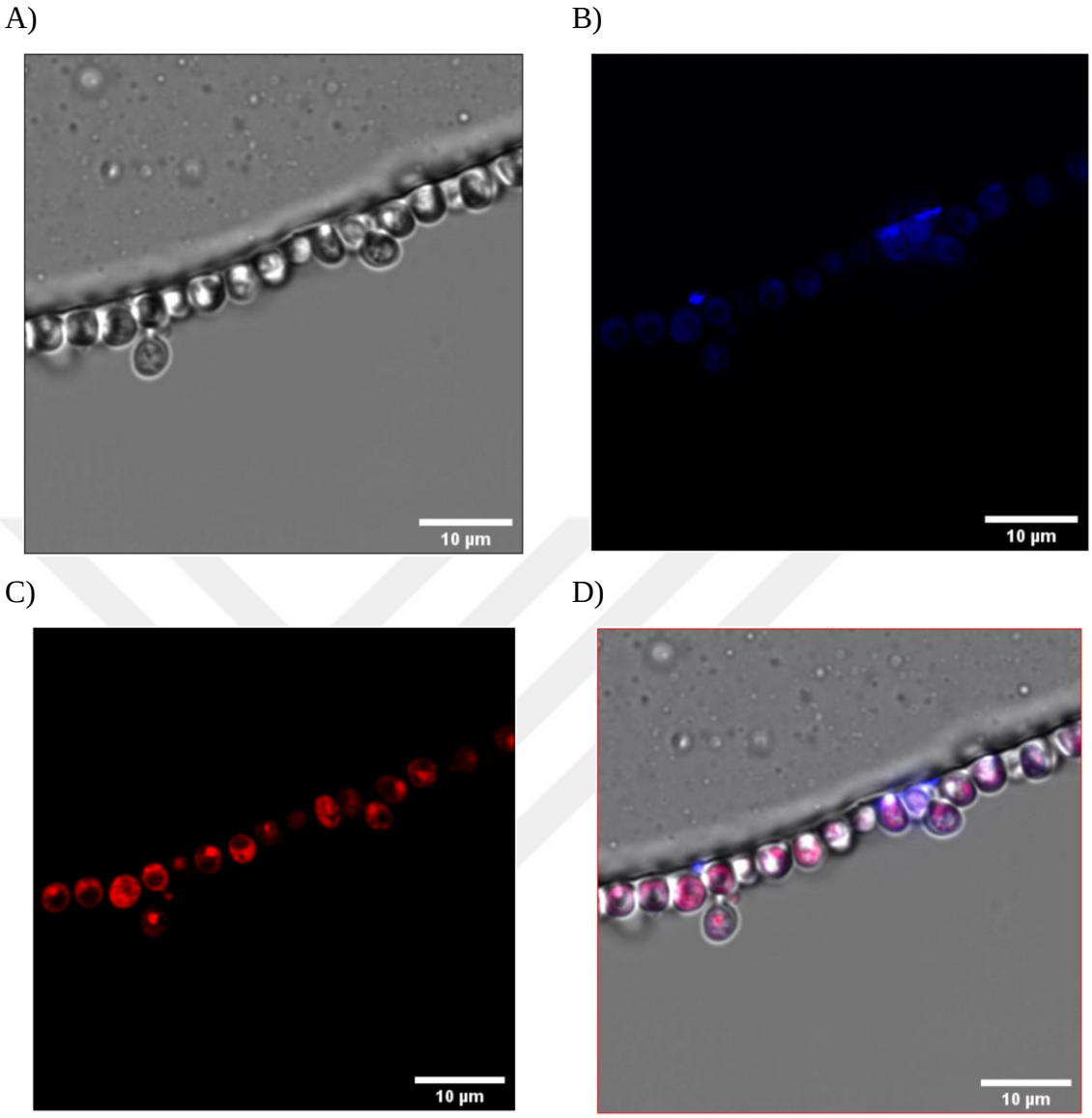

Figure 4.36. CLSM images of 100 mg/L 50nm-A-p PSL NP exposed yeast cells after 1 µM Lat-A treatment A) Bright field B) FITC C) PI D) Merged image.

For 100 mg/L concentration of 30nm-C-n PSL nanoparticle exposed cells after 200 µM Lat-A treatment for 1 hour, the nanoparticles are observed inside the cells similar to the case of 1 µM Lat-A treatment (Figure 4.37). From the 3-D projection image obtained for these nanoparticles, the location of the 30nm-C-n PSL nanoparticles inside the yeast cells after 200 µM Lat-A treatment for 1 hour is confirmed (Figure 4.38). This result shows that the uptake of 30nm-C-n PSL nanoparticles is independent of actin filaments as Lat-A is used to depolymerize the actin filaments. There are two possible reasons suggested to explain the 30nm-C-n PSL nanoparticle internalization through the cell membrane in the presence of

Lat-A inhibitor: (1) by an energy independent mechanism which is diffusion process, or (2) by a different mechanism of endocytosis.

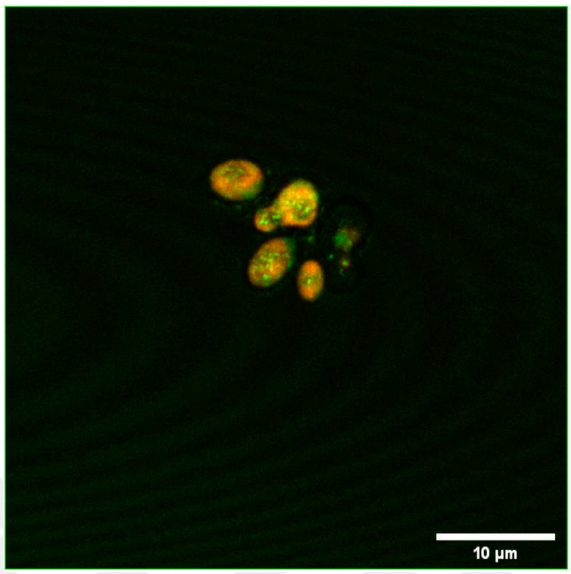

Figure 4.37. Merged CLSM image of 100 mg/L 30nm-C-n PSL NP exposed yeast cells after 1hour of 200 µM Lat-A treatment.

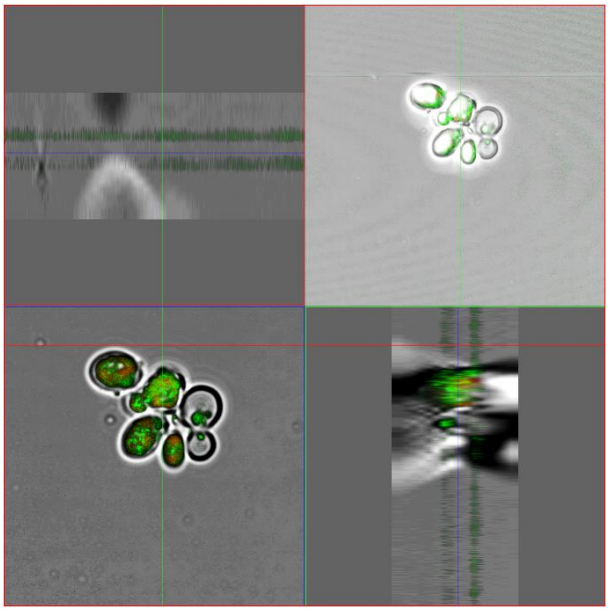

Figure 4.38. 3-D Projection image of 100 mg/L 30nm-C-n PSL NP exposed yeast cells after 1 hour of 200 µM Lat-A treatment.

At 100 mg/L 50nm-A-p PSL nanoparticle exposure to the yeast cells along with 200 µM Lat-A treatment, large clusters of nanoparticles are accumulated on the surfaces of the cells similar to the inhibitor excluded and positively charged PSL nanoparticle exposed yeast cells (Figure 4.39). Also, inside the yeast cells, slight fluorescence due to the presence of nanoparticles is observed, which is in accordance with the results of 30nm-C-n PSL nanoparticles where the cellular uptake is not inhibited after 200 µM Lat-A treatment (Figure F.17).

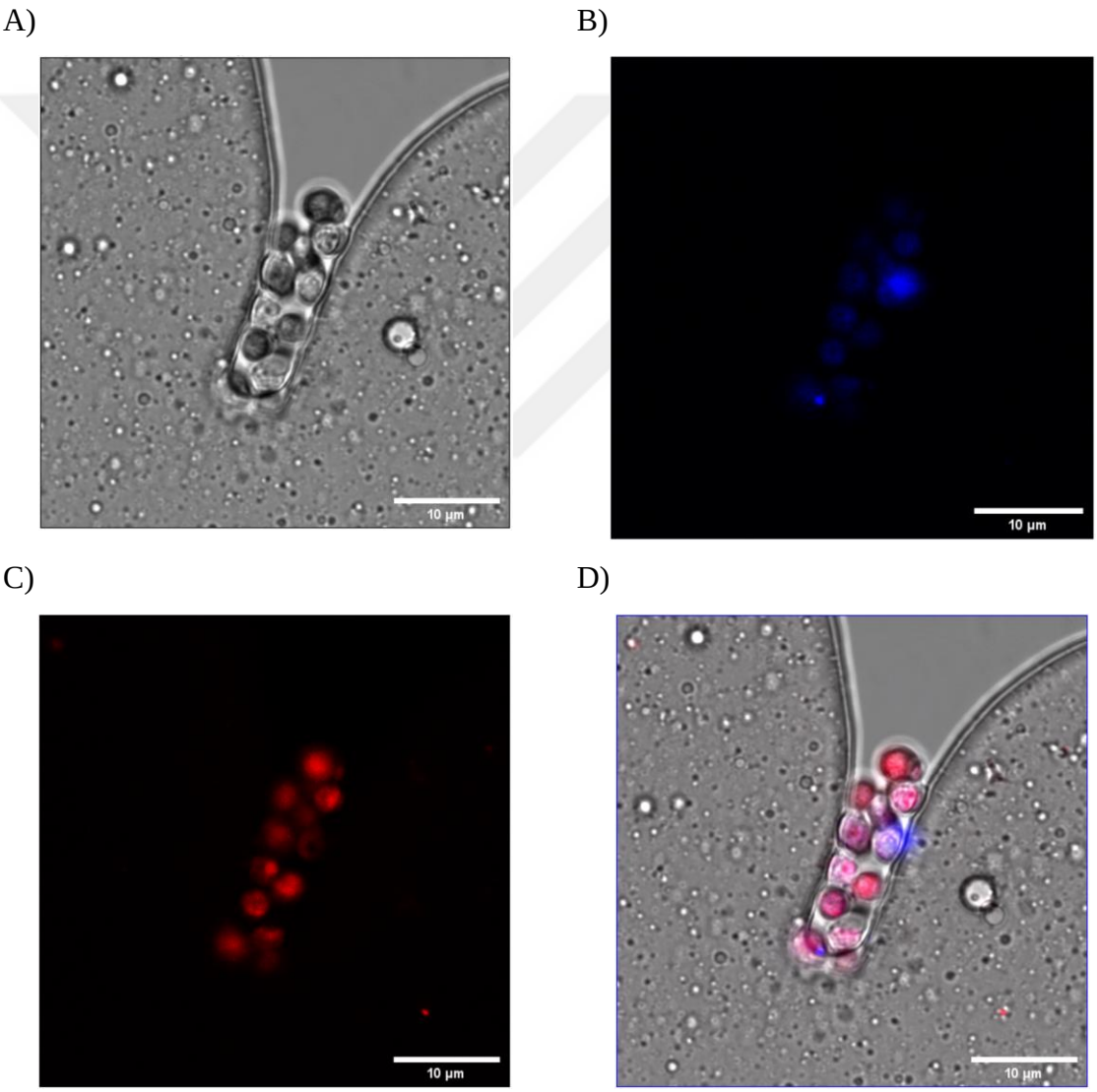

Figure 4.39. CLSM images of 100 mg/L 50nm-A-p PSL NP exposed yeast cells after 200 µM Lat-A treatment A) Bright field B) FITC C) PI D) Merged image

4.8.2. Nocodazole Treatment on *S. cerevisiae* Cells

4.8.2.1. Effect of Nocodazole on the Control Groups. The function of the cytoskeleton in endocytosis has been studied widely to understand its role in intracellular transportation processes. It has been recently shown that actin cytoskeleton has a role in the process of endocytosis at certain steps in the yeast cells. The microtubules, which are the component of the cytoskeleton, participate in the process of endocytosis at its late steps. The disruption of the microtubules results in the translocation inhibition of the endosomes and the lysosomes [63]. Nocodazole is a cell cycle disturbing agent which disrupts microtubules and locks cells in mitosis [64]. Nocodazole inhibits microtubule polymerization and leads to checkpoint arrest at the metaphase to anaphase transition during the process of mitosis [65].

In the study of Andrews *et al*. (2005), the yeast cells have been treated with 15 µg/ml of nocodazole to investigate the cell cycle progression in the presence of endocytosis inhibitor [66]. Also, in the study of Torres *et al*. (2011), 15 µg/ml of nocodazole has been used to arrest the *S. cerevisiae* cells in G2/M phase [65]. Nakashima *et al*. (2008) and Bryan *et al*. (2010) have used 15 µg/ml of nocodazole to arrest the *S. cerevisiae* cells in metaphase [62,63]. In the study of Santos *et al*. (2011), 20 µM nocodazole has been used to inhibit microtubule polymerization to see the effect of microtubules in nanoparticle internalization [44]. The nanoparticles are carboxylate modified polystyrene nanoparticles in 40 nm and 200 nm diameters and the cell types are human cervix epithelium HeLa, human lung epithelium A549 and human glial astrocytoma 1321N1 cells [44]. Nocodazole has been found to inhibit the uptake of larger particles (200 nm carboxylate modified polystyrene nanoparticle) in which the endocytosis is inhibited by 40% in A549 cell line and by 20% in HeLa and 1321N1 cells with respect to the control groups [44]. However, for 40 nm carboxylate modified polystyrene nanoparticles, this inhibition effect has been significantly reduced. The endocytosis is inhibited 5-10% in A549 and 1321N1 cells with respect to the control cells and no endocytosis inhibition has been observed in HeLa cells. Thus, the influence of microtubules in the uptake of smaller particles (40nm) is not prominent, but for larger particles (200nm) the involvement of the microtubules in the endocytosis is observed in A549 cells [44]. Also, Dausend *et al*. (2008) have shown that the uptake of 120 nm negatively charged and carboxylate modified polystyrene nanoparticles are not inhibited by 10 µg/ml of nocodazole treatment to HeLa cells [69].

In this section, the effect of 15 µg/ml of nocodazole treatment of the *S. cerevisiae* cells in terms of toxicity with respect to the control cells, which do not contain any inhibitor, is investigated to determine whether the applied inhibitor concentration affects the viability of the yeast cells. When the CFU analysis is carried out after 3 days at 30°C incubation on the nocodazole treated groups and non-treated groups, nocodazole is found not to have any toxic effect towards the yeast cells. The viability percentage of the nocodazole treated groups with respect to the control groups, which do not contain inhibitor, is found as 100% after 1 hour of 15 µg/ml nocodazole treatment. Thus, it can be interpreted that the viability of the *S. cerevisiae* cells is not affected after the treatment with 15 µg/ml nocodazole for 1 hour at 28°C. With this result, the PSL nanoparticle exposure experiments towards the yeast cells in the presence of nocodazole treatment are performed to determine the uptake mechanism of these nanoparticles.

4.8.2.2. Effect of Nocodazole on the Nanoparticle Exposed Groups. In the present study, nocodazole, which is a microtubule disrupting agent, is used as an endocytosis inhibitor to evaluate the effect of microtubules in the internalization of 30nm-C-n and 50nm-A-p PSL nanoparticles by the *S. cerevisiae* cells. The yeast cells at the late exponential growth phase are treated with 15 µg/ml of nocodazole in DMSO for 1 hour at 28°C. After the inhibition process *S. cerevisiae* cells are exposed to different types and concentrations of PSL nanoparticles. CFU and confocal microscopy analyses are performed to determine the effects nocodazole on the toxicity and the uptake of PSL nanoparticles by *S. cerevisiae* cells.

The viability percentages of 15 µg/ml nocodazole treated and PSL nanoparticle exposed yeast cells are compared with the viability non-inhibitor treated PSL nanoparticles to determine whether there is a change in the toxicity behavior of the PSL nanoparticles towards the yeast cells. According to the CFU results, after 15 µg/ml nocodazole treatment, 100 mg/L 30nm-C-n and 50 mg/L 50nm-A-p PSL nanoparticle exposures do not result in toxic effect towards the yeast cells as the viability percentages are 100%. The viability results are higher than those of the inhibitor excluded and PSL nanoparticle exposed yeast cells, in which the viability percentages are found as 84.75% and 83.83% for 100 mg/L 30nm-C-n and 50 mg/L 50nm-A-p PSL NPs, respectively (Table 4.8). For 15 µg/ml nocodazole treated cells after 100 mg/L 50nm-A-p PSL nanoparticle exposure, the viability percentage is calculated as 9.96% whereas for non-inhibitor control yeast cells it is found as 7.20%

showing no significant change in viability due to the nocodazole treatment. (Table 4.8). In the light of these results, it can be interpreted that 15 µg/ml nocodazole treatment of the *S. cerevisiae* cells do not show toxic effect compared to non-inhibitor treated cells. After nocodozole treatment, the effects of both 30nm-C-n PSL NPs (100 mg/L) and 50nm-A-p PSL NPs (50 mg/L and 100 mg/L) are not changed significantly which shows that the these nanoparticles are taken up by cells through energy independent mechanism or microtubule independent endocytosis mechanism.

Table 4.8. Viability Percentages of Non-Inhibitor Included and 15 µg/ml Nocodazole Treated Cells Exposed to Different Type and Concentrations of PSL Nanoparticles.

PSL NPs			**15 µg/ml Nocodazole treated PSL NPs**		
30nm-C-n	**50nm-A-p**		**30nm-C-n**	**50nm-A-p**	
100 mg/L	**50 mg/L**	**100 mg/L**	**100 mg/L**	**50 mg/L**	**100 mg/L**
84.75	83.83	7.20	100.0	100.0	9.96

Confocal analysis is carried out for nocodazole treated and 30nm-C-n and 100 nm-A-p PSL nanoparticle exposed yeast cells. The concentrations of the nanoparticles used in the confocal analysis are 100 mg/L for 30nm-C-n PSL nanoparticle and 100 mg/L and 500 mg/L for 100nm-A-p PSL nanoparticles. The inhibitor concentration and the treatment time are 15 µg/ml nocodazole for 1 hour and 15 µg/ml nocodazole for 2 hours, respectively. According to the confocal microscopy images, for the yeast cells treated with 15 µg/ml nocodazole for 1 hour and exposed to 100 mg/L 30nm-C-n PSL nanoparticles, the nanoparticles enter the cell cytoplasm but nanoparticles are not observed inside the cell nucleus (Figure 4.40). Most of the cells are viable after nanoparticle exposure since the nanoparticles are not taken up by the nucleus. However, there are also some cells, in which nanoparticles enter inside their nucleus and these cells are found to be dead through staining by PI dye.

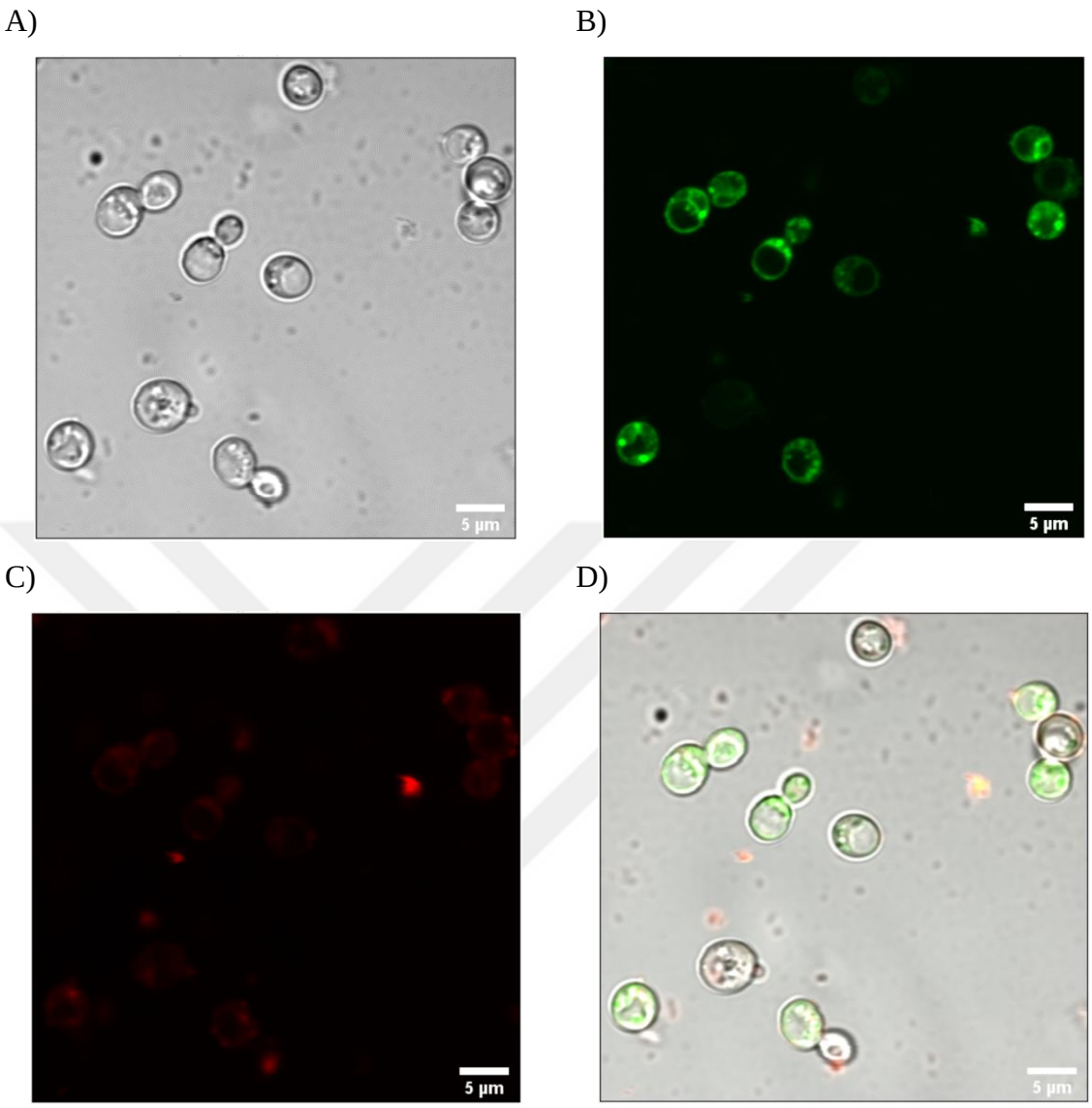

Figure 4.40. CLSM images of 100 mg/L 30nm-C-n PSL NP exposed yeast cells after 1 hour of 15 µg/ml nocodazole treatment) Bright field B) FITC C) PI D) Merged image.

For 100 mg/L 100nm-A-p PSL nanoparticle exposure to the yeast cells after 15 µg/ml nocodazole treatment for 1 hour, the location of the nanoparticles do not change with respect to the yeast cells compared to non-inhibitor included cells. The nanoparticles are generally on the surface of the yeast cells and little amount of nanoparticle aggregates are seen inside the cytoplasm of some of the cells (Figure 4.41).

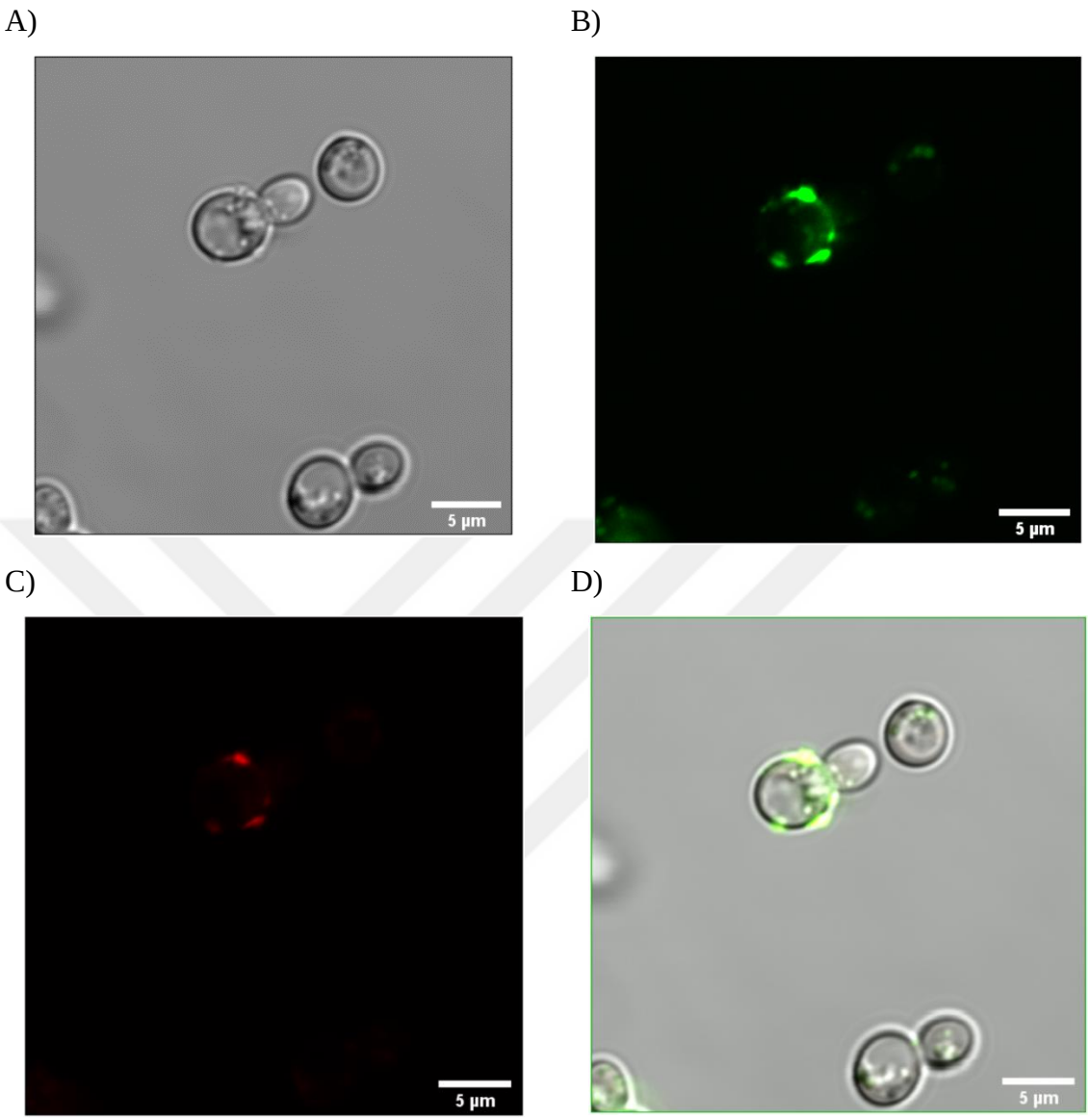

Figure 4.41. CLSM images of 100 mg/L 100nm-A-P PSL NP exposed yeast cells after 1 hour of 15 µg/ml nocodazole treatment A) Bright field B) FITC C) PI D) Merged image.

When the 15 µg/ml nocodazole treatment time is increased from 1 hour to 2 hours, for 100 mg/L 30nm-C-n PSL nanoparticle exposed yeast cells, in spite of endocytosis being inhibited, agglomerated nanoparticles are observed inside of the yeast cells similar to the 15 µg/ml nocodazole treatment for 1 hour (Figure 4.42). It has been reported that blockage of one endocytosis pathway may result in the activation of another pathway and thus the increase of the inhibitor treatment time may induce another uptake mechanisms to take place [44]. Thus, the 30nm-C-n PSL nanoparticle uptake after 2 hours of nocodazole treatment may be explained by the inducement of other endocytosis mechanisms in the yeast cells.

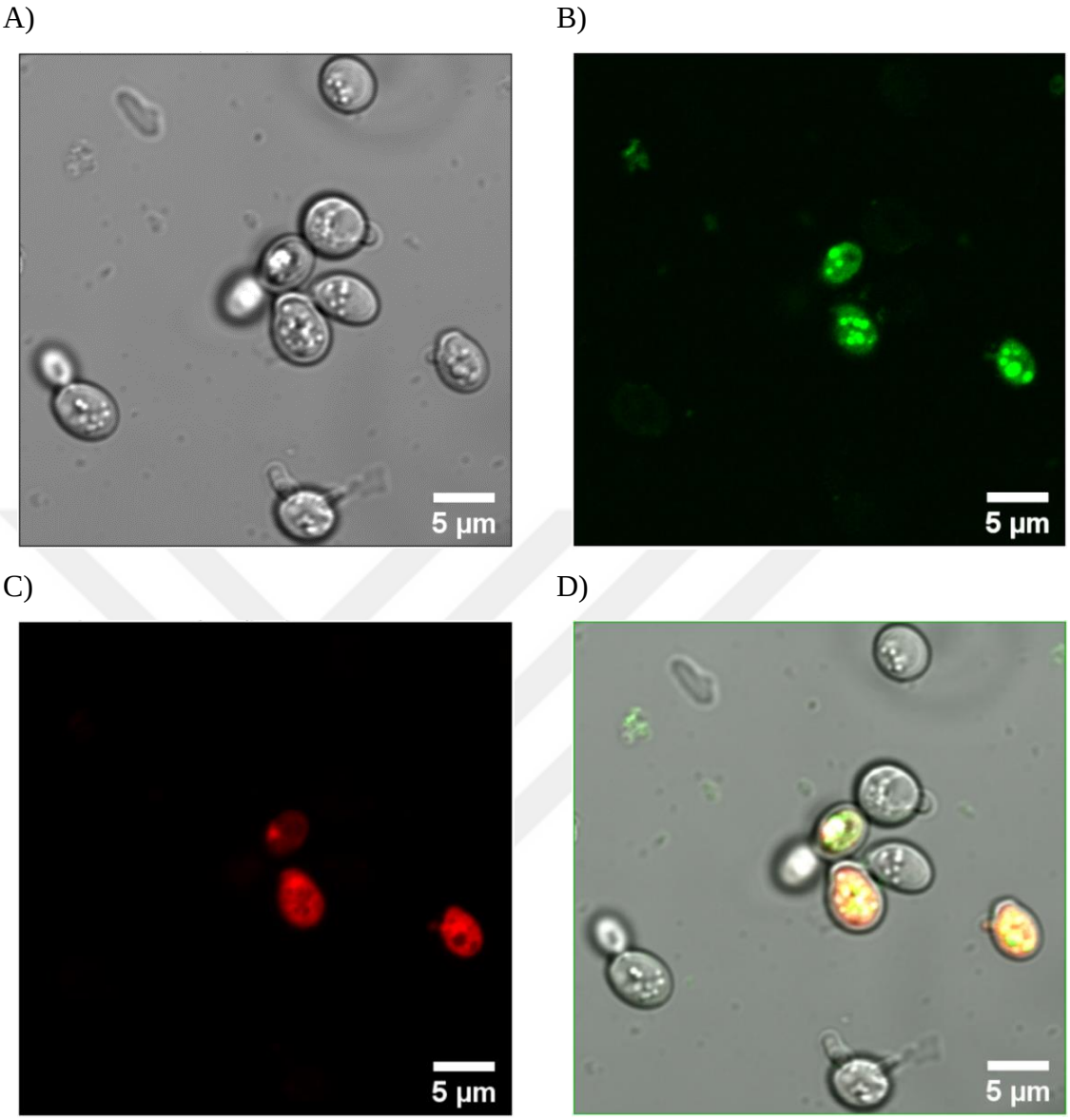

Figure 4.42. CLSM images of 100 mg/L 30nm-C-n PSL NP exposed yeast cells after 2 hours of 15 µg/ml nocodazole treatment A) Bright field B) FITC C) PI D) Merged image.

For 500 mg/L 100nm-A-p PSL nanoparticle exposed yeast cells, after 2 hours of 15 µg/ml nocodazole treatment, there is no change observed in terms of the location of the nanoparticles such that they are still on the surface of the yeast cells which is an expected result because for the inhibitor excluded and 100nm-A-p PSL nanoparticle exposed yeast cells, the nanoparticles were also on the surface of the cells (Figure 4.43).

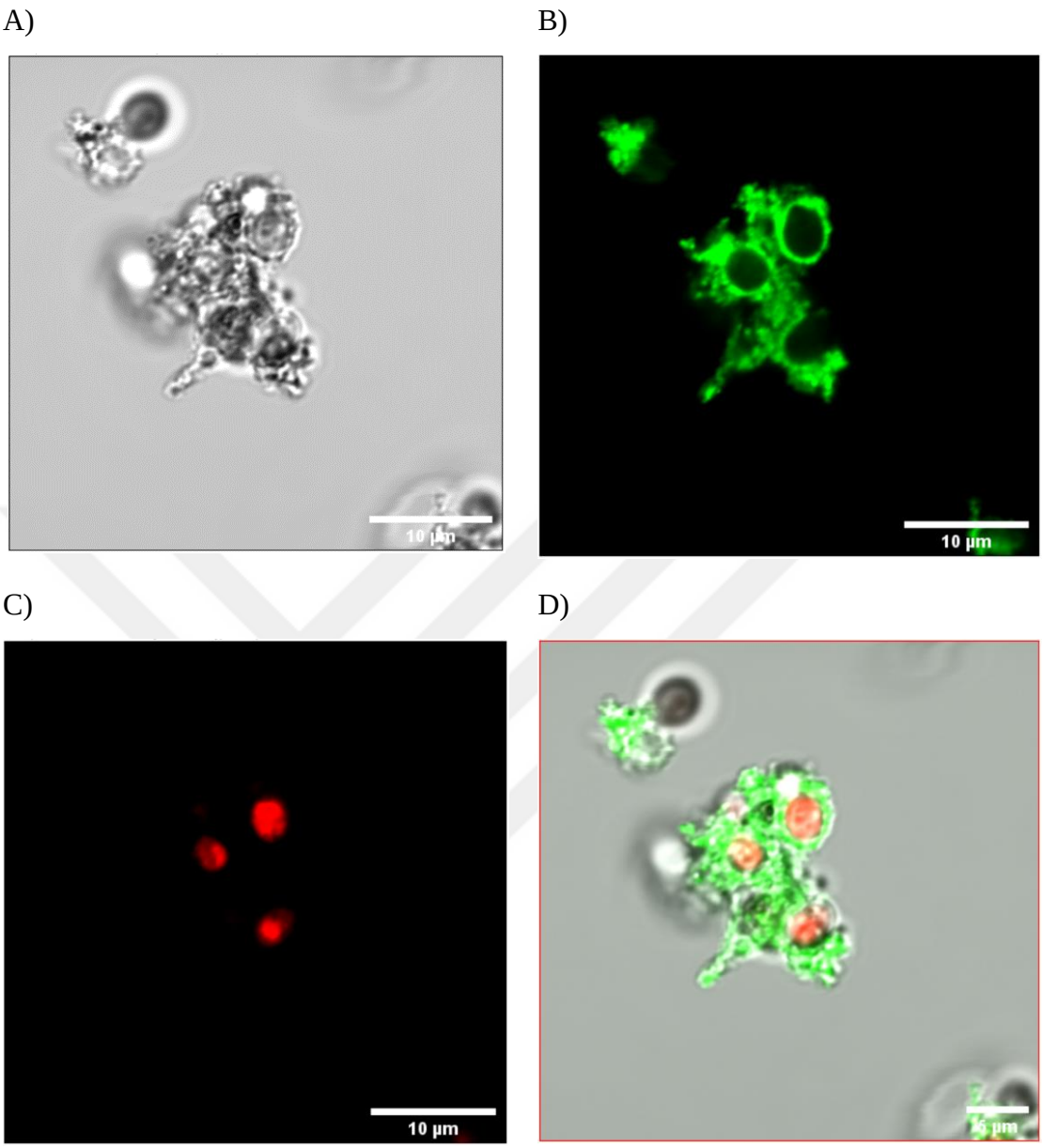

Figure 4.43. CLSM images of 500 mg/L 100nm-A-p PSL NP exposed yeast cells after 2 hours of 15 µg/ml nocodazole treatment A) Bright field B) FITC C) PI D) Merged image.

It has been reported that the nocodazole, which is a microtubule depolymerizing drug, treatment may cause haploid cells to delay their cell division progression [70],[71]. The prolonged treatment time of the yeast cells with the inhibitor nocodazole causes the cells to arrest in mitosis with large buds [72]. In the present study, the increase of 15 µg/ml nocodazole treatment time from 1 hour to 2 hours resulted in the abnormal growth of the

yeast cells and it causes cell death for both 30nm-C-n and 100nm-A-p PSL nanoparticle exposed yeast cells (Figure 4.44).

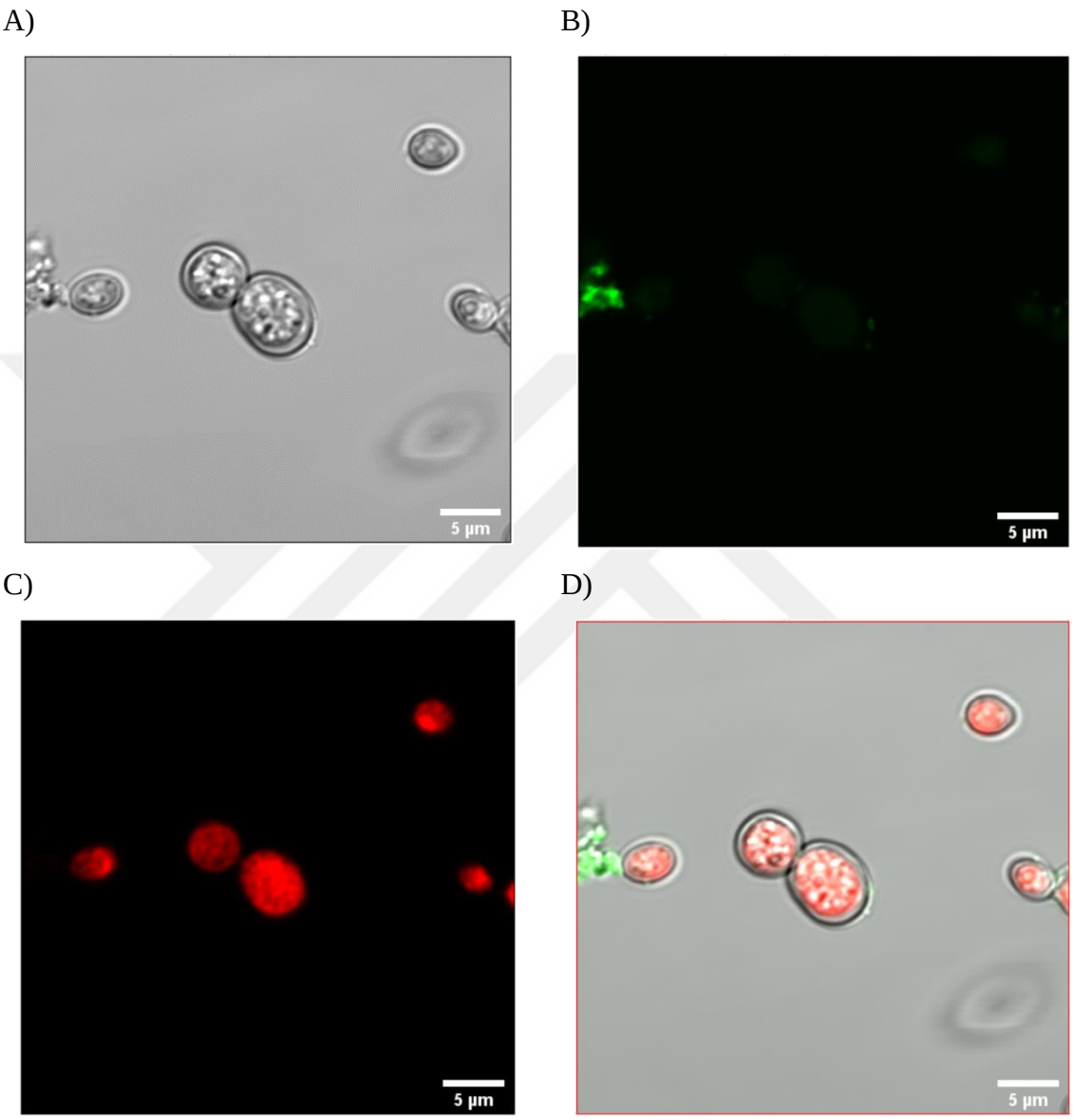

Figure 4.44. CLSM images showing abnormal growth of the yeast cells exposed to 500 mg/L 100nm-A-p PSL NP after 2 hours of 15 µg/ml nocodazole treatment A) Bright field B) FITC C) PI D) Merged image.

4.8.2.3. Fluorescence Intensity Analysis inside the S. cerevisiae Cells under 30nm-C-n PSL NP Exposure with or without Nocodazole Treatment. To determine the degree of nanoparticle internalization into the *S. cerevisiae* cells, the fluorescence intensity analysis is carried out for the 100 mg/L 30nm-C-n PSL NPs for three different cases: (1) no inhibitor treatment, (2) 1 hour of 15 µg/ml nocodazole treatment and (3) 2 hours of 15 µg/ml nocodazole treatment. Image J program is used to obtain the fluorescently labeled area stemmed from the nanoparticle agglomeration inside the cells and the integrated density (IntDen) value, which is the summation of the pixels in the selected area of the image, in order to investigate the integrated fluorescence intensity of the nanoparticles inside the cells. Also, the integrated fluorescence intensity values of the inhibitor treated cells at different drug exposure times are compared with those of the inhibitor excluded cells by carrying out percentage of error analysis.

The Image J processing results show that after 100 mg/L 30nm-C-n PSL NP exposure, the fluorescently labeled area, which is the area covered by the agglomerated nanoparticles in the *S. cerevisiae* cells, is found as 8.404 μm^2, whereas for the 15 µg/ml nocodazole treated cells this area is calculated as 8.089 μm^2 and 4.516 μm^2, after 1 hour and 2 hours of treatment, respectively (Table 4.9). As the nocodazole treatment time increases, the area exerted by the agglomerated fluorescent nanoparticles inside the yeast cells decreases. The similar situation can be observed for the IntDen value representing the integrated density of the fluorescence inside the cells. When there is no inhibitor treatment, the IntDen value is found as 2142.9, whereas those values corresponding to 15 µg/ml nocodazole treatment after 1 hour and 2 hours are found as 2062.7 and 1151.5, respectively (Table 4.9). When the IntDen values after nocodazole treatment are compared with the values of non-inhibitor included cells, the percentage of the integrated fluorescence intensity inside the yeast cells is found as 96.3% and 53.7% for 1 hour and 2 hours of 15 µg/ml nocodazole treatment, respectively. Hence, it can be interpreted that 15 µg/ml nocodazole inhibits the 30nm-C-n PSL NP internalization up to 3.74% after 1 hour of treatment, and 46.3% after 2 hours of treatment.

Table 4.9. Fluorescence Intensity Analysis inside the *S. cerevisiae* Cells Exposed to 30nm-C-n PSL NP in the Presence and Absences of Inhibitor.

	30nm-C-n PSL NP Exposure (100 mg/L)		
	No inhibitor	**1 hour of 15 µg/ml Nocodazole**	**2 hours of 15 µg/ml Nocodazole**
Fluorescently labelled area in the cell (µm^2)	8.404	8.089	4.516
Integrated Density (IntDen)	2142.9	2062.7	1151.5
% Decrease in Fluorescence Intensity	-	3.74 %	46.3 %

4.8.3. Ethanol Treatment on *S. cerevisiae* Cells

4.8.3.1. Effect of Ethanol on the Control Groups. It has been shown that *Saccharomyces* species are resistant to alcohols such that they can grow in the presence of 8% to 12% (v/v) alcohol. They can also continue living up to 15% concentrations of alcohol exposure. Although the *Saccharomyces* species show high resistivity towards ethanol exposure, some processes like endocytosis are affected by the presence of ethanol at certain concentrations. The yeast cells are sensitive to the ethanol in terms of endocytosis process in which it is strongly inhibited between 2% to 6% (v/v) concentrations of ethanol [73]. It has been found that the presence of 6% (v/v) ethanol inhibits the endocytosis of the maltose and galactose transporters for more than 90% of the cells, which are grown in glucose medium. But, when the cells are grown in only ethanol or glycerol included media, the inhibition of endocytosis is not observed [73].

In the study of Zhu *et al*. (2016), the effect of endocytosis on the internalization of multi-walled carbon nanotubes (MWCNTs), which have average length of 190-210 nm, by the *S. cerevisiae* cells has been investigated by 5% (v/v) ethanol treatment [10]. According to the results, it is reported that the uptake of MWCNTs decreases significantly after the

treatment with ethanol compared to control groups in which the uptake decreases from 209.61 mg/g to 65.40 mg/g [10].

CFU analysis is carried out to determine whether 5% (v/v) ethanol treatment causes toxicity towards the yeast cells. The viability percentages belonging to ethanol treated and non-inhibitor included cells are calculated after 3 days of incubation at 30°C. The viability percentage of the ethanol treated cells with respect to control group is found as 100% which shows that 5% (v/v) ethanol treatment does not show any toxic effect towards the *S. cerevisiae* cells. Based on this, the effect of ethanol as an endocytosis inhibitor is studied using the PSL nanoparticle exposed *S. cerevisiae* cells.

4.8.3.2. Effect of Ethanol on the Nanoparticle Exposed Groups. In the present study, 5% (v/v) ethanol is used as an endocytosis inhibitor towards the yeast cells. The *S. cerevisiae* cells are treated with 5% (v/v) ethanol for 1 hour at 28°C. *S. cerevisiae* cells are exposed to different types and concentrations of PSL NPs to determine whether the effects of these nanoparticles change after the addition of ethanol as endocytosis inhibitor and to see whether the uptake behavior of these nanoparticles is affected or not. CFU and confocal microscopy analyses are carried out to investigate the effects of ethanol on the toxicity and the uptake of PSL nanoparticles by *S. cerevisiae* cells.

The viability percentages of the 5% (v/v) ethanol treated and PSL nanoparticle exposed yeast cells with respect to only PSL nanoparticle exposed yeast cells are compared through the CFU analysis. The viability results belonging to inhibitor treated and non-treated PSL nanoparticle exposed yeast cells show that the toxicity behavior of the nanoparticles (100 mg/L 30nm-C-n, 50 mg/L and 100 mg/L 50nm-A-p PSL NPs) does not change as the viability percentages are very similar (Table 4.10).

After 1 hour of 5% (v/v) ethanol treatment, the viability of 100 mg/L 30nm-C-n PSL nanoparticle exposed yeast cells is calculated as 80.5%, whereas without ethanol treatment it is found as 84.8%. For the ethanol treated and 50 mg/L and 100 mg/L 50nm-A-p PSL nanoparticle exposed cells, the viability percentages are found as 100.0% and 15.9%, respectively. For the inhibitor excluded and 50 mg/L 50nm-A-p and 100 mg/L 50nm-A-p PSL nanoparticle exposed cells, the viability percentages are calculated as 83.8% and 7.20%,

respectively (Table 4.10). These results indicate that although the fundamental toxicity pattern of the nanoparticles does not change, ethanol treatment induces the cell viability to increase slightly.

Table 4.10. Viability Percentages of Non-Inhibitor Included and 5 % (v/v) Ethanol Treated Cells Exposed to Different Type and Concentrations of PSL Nanoparticles.

PSL NPs			**5 % v/v ethanol treated PSL NPs**		
30nm-C-n	**50nm-A-p**		**30nm-C-n**	**50nm-A-p**	
100 mg/L	**50 mg/L**	**100 mg/L**	**100 mg/L**	**50 mg/L**	**100 mg/L**
84.8	83.8	7.20	80.5	100.0	15.9

Confocal microscopy analysis is carried out for the yeast cells, which are treated with 5% (v/v) ethanol for 1 hour to inhibit the process of endocytosis and exposed to 100 mg/L 30nm-C-n and 100 mg/L 100nm-A-p PSL nanoparticles. In Figure 4.45, it is seen that after ethanol treatment, 30nm-C-n PSL nanoparticles are taken up by the cells and they agglomerate in the cell cytoplasm. Most of the 30nm-C-n PSL nanoparticles do not enter to the cell nucleus and in general the yeast cells are viable. However, the yeast cells, whose nucleus include nanoparticles, are not viable.

Confocal microscopy results show that 5% (v/v) ethanol treatment for 1 hour does not inhibit the internalization of the 30nm-C-n PSL nanoparticles (Figure 4.45). After ethanol treatment, the response of the yeast cells to the exposure of 100 mg/L 100nm-A-p PSL nanoparticles does not change as they are located on the surface of the yeast cells in the form of clusters (Figure 4.46).

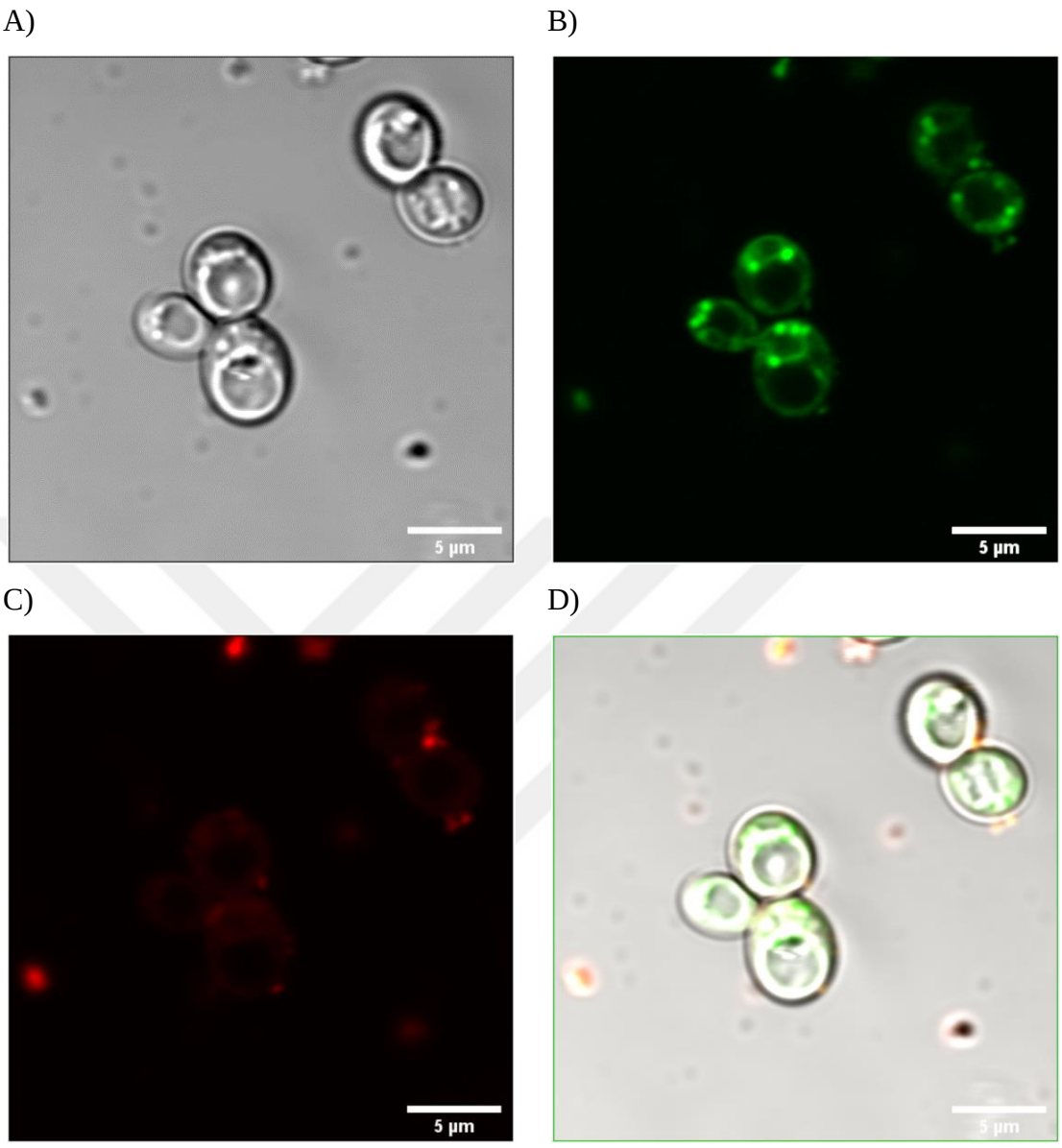

Figure 4.45. CLSM images of 100 mg/L 30nm-C-n PSL NP exposed yeast cells after 1 hour of 5% (v/v) ethanol treatment A) Bright field B) FITC C) PI D) Merged image.

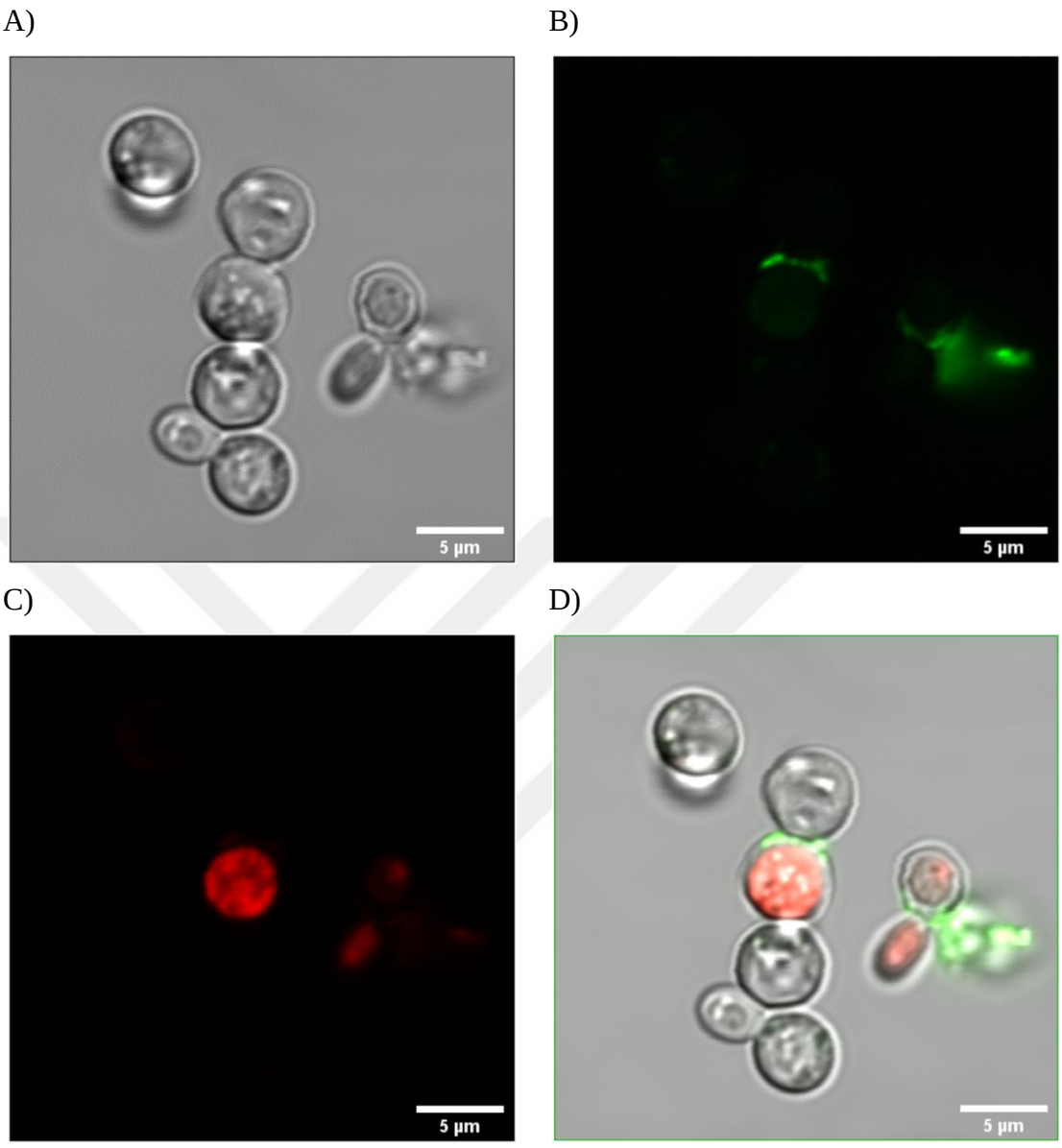

Figure 4.46. CLSM images of 100 mg/L 100nm-A-p PSL NP exposed yeast cells after 1 hour of 5% (v/v) ethanol treatment A) Bright field B) FITC C) PI D) Merged image.

5. CONCLUSIONS AND RECOMMENDATIONS

5.1. Conclusions

In the present study, the aim was to determine the short- and long-term exposure effects of nanoparticles having different size, charge, and functional groups on Sac6:RFP tagged *S. cerevisiae* cells and to investigate the uptake mechanism of the nanoparticles by the yeast cells after treatment with different endocytosis inhibitors. The nanoparticles used in the study were: positively and negatively charged, carboxyl and amine functionalized Polystyrene Latex Nanoparticles (PSL NPs) in the size and concentration range between 20-200 nm and 50-800 mg/L, respectively; DOPC liposomes; and DOPC liposome encapsulated PSL NPs having different concentrations, sizes and surface charges.

Experimental studies were performed to characterize the nanoparticles and to assess the outcomes after exposing *S. cerevisiae* cells to different types of nanoparticles. For that purpose, the PSL NPs, DOPC liposomes and the hybrid DOPC-PSL nanoparticles were characterized via Dynamic Light Scattering (DLS) analysis to determine the mean hydrodynamic radius and size distribution of the nanoparticles, Electrophoretic Light Scattering (ELS) analysis was performed to assess the surface charge and the zeta potentials of the nanoparticles, Scanning Transmission Electron Microscopy (STEM) and Transmission Electron Microscopy (TEM) techniques were used to determine the average size, size distribution and the morphology of the nanoparticles. Colony Forming Unit (CFU) analysis was carried out for the yeast cells exposed to PSL NPs, DOPC liposomes and hybrid nanoparticles after 3 days of incubation at 30°C for short term cytotoxicity analyses. To obtain the long-term nanoparticle toxicity effects, the yeast cells were grown for 15 generations under different size and concentrations of PSL NP exposure that were found to be non-toxic in short term toxicity analyses. Confocal Laser Scanning Microscopy (CLSM) analyses were carried out to reveal the localizations of the nanoparticles within the yeast cells and to determine their toxicities in terms of viability after applying Propidium Iodide (PI) dye. To investigate the uptake mechanism of the nanoparticles into the yeast cells, several endocytosis inhibitors were applied with different concentrations and treatment times.

5.1.1. Effects of Polystyrene Latex Nanoparticles (PSL NPs) on *S. cerevisiae* Cells

According to the CFU analysis results, negatively charged and carboxyl functionalized PSL nanoparticles, (20nm-C-n, 30nm-C-n and 60nm-C-n), were found to be non-toxic towards the yeast cells at low concentrations (50 mg/L). As the nanoparticle concentration increased (50-800 mg/L), the viability percentage of the yeast cells decreased accordingly. The viability percentage for negatively charged and carboxyl functionalized PSL nanoparticles did not fall below 80% and 60% at 100-200 mg/L and 500-800 mg/L concentration ranges, respectively. Overall, it can be interpreted that these nanoparticles show non-toxic effect at 50 mg/L, and show low toxicity at 100-200 mg/L and moderate toxicity at 500-800 mg/L concentrations towards the yeast cell. The effect of nanoparticle size (20, 30 and 60 nm) on the viability of the yeast cells was not found significant considering the error bound for negatively charged and carboxyl functionalized PSL nanoparticles.

According to the CFU results, negatively charged and amine functionalized PSL nanoparticles, (50nm-A-n, 100nm-A-n and 200nm-A-n) were found to be non-toxic at low concentrations (50 mg/L). As the concentrations of the nanoparticles increased, the viability percentages decreased except for 50nm-A-n PSL nanoparticles. The viability of the yeast cells did not fall below 90% for all studied concentrations (50-800 mg/L) for 50nm-A-n PSL nanoparticles. A gradual decrease in viability was observed in the yeast cell after exposing 100nm-A-n and 200nm-A-n PSL nanoparticles in a concentration range between 100 to 800 mg/L. For 100nm-A-n, the lowest viability was obtained as 73.2%, and for 200nm-A-n it was 59.5%, both at 800 mg/L nanoparticle concentration. While 50nm-A-n did not cause toxicity, with negatively charged and amine functionalized nanoparticles the increase in nanoparticle size induced toxic behavior.

Positively charged and amine functionalized PSL nanoparticles, (50nm-A-p and 100nm-A-n), caused low amount of toxicity towards the yeast cells at low concentrations (50 mg/L), i.e. the viability percentages did not fall below 80%. At 100 mg/L nanoparticle concentration, a sharp reduction in the viability of the yeast cells was observed, i.e. the viability percentages were 7.20% and 15.4% for 50nm-A-n and 100nm-A-n PSL nanoparticles, respectively. Further increase (500-800 mg/L) in the concentrations resulted

in fully toxic effect towards the yeast cells. Cytotoxicity of the positively charged and amine functionalized nanoparticles was insignificant within the error bounds considering the size of the nanoparticles. While negatively charged and amine functionalized PSL nanoparticles (50nm-A-n and 100nm-A-n) did not show a significant toxic effect, the same sizes of positively charged and amine functionalized PSL nanoparticles (50nm-A-p and 100nm-A-p) exhibited high toxicity towards the yeast cells at concentrations between 100-800 mg/L.

Confocal microscopy analysis showed that 30nm-C-n PSL nanoparticles (50 and 100 mg/L concentration) were internalized by the yeast cells. The nanoparticles were agglomerated inside the yeast cells but in general, they did not show toxic effect until they entered to the cell nucleus. Moreover, it was observed that when the nanoparticle accumulation was dominant in the cell cytoplasm, the nanoparticles did not cause toxicity in general. On the other hand, the occurrence of cell death was more common when the nanoparticles were inside the cell nucleus. 100nm-A-p PSL nanoparticles (50-800 mg/L concentrations) were observed to accumulate on the membrane surface of the yeast cells in the confocal microscopy images. The results were in accordance with the CFU analyses, such that for 50 mg/L most of the cells were observed as viable, on the contrary after 100 mg/L concentration most of the cells were stained with PI which shows the cells are not viable. At higher nanoparticles concentrations, the nanoparticles agglomerated and formed clusters. Moreover, the surface coverage of the nanoparticles became more significant. Consequently, greater amount of nanoparticles on the cell surface inhibited the interaction of the cells with their environment and caused toxic effect.

5.1.2. Effects of DOPC Liposomes on *S. cerevisiae* Cells

The liposomes synthesized from DOPC phospholipid by thin-film hydration method were characterized via DLS, ELS and STEM analyses. According to the DLS results, the mean diameter of the DOPC liposomes was obtained as 174.0 nm and PDI value was 0.173, which demonstrated the size uniformity of the liposomes in the solution. ELS results showed that the surface charge of the DOPC liposomes was negative with a zeta potential value of -14.5 mV. STEM analysis results were also in accordance with the DLS results.

In order to determine toxicity behavior of the DOPC liposomes, CFU analysis was carried out after exposing the yeast cells to different liposome concentrations (0.25, 0.125, 0.025 and 0.0025 mg lipid/ml 1XPBS solution) for 3 days at 30°C. DOPC liposomes were found to be non-toxic towards the yeast cells i.e. the viability percentages of the yeast cells were found as 100.0% even at the highest liposome concentration, which was 0.25 mg lipid /ml 1XPBS solution.

5.1.3. Effects of Hybrid Nanoparticles on *S. cerevisiae* Cells

Hybrid nanoparticles were synthesized by encapsulating the PSL NPs (20nm-C-n, 30nm-C-n, 50nm-A-p, 100nm-A-n and 100nm-A-p) with DOPC phospholipids by thin film hydration method. The hydrodynamic diameter values were measured as 199.7 nm, 155.3 nm, 289.5 nm, 165.2 nm and 192.3 nm, for 20nm-C-n, 30nm-C-n, 50nm-A-p, 100nm-A-n and 100nm-A-p hybrid nanoparticles, respectively. The zeta potentials were found as -22.94 mV, -22.0 mV, 8.48 mV, -13.3 mV and 7.14 mV, for 20nm-C-n, 30nm-C-n, 50nm-A-p, 100nm-A-n and 100nm-A-p hybrid nanoparticles, respectively. TEM analysis results for 20nm-C-n, 50nm-A-n and 100nm-A-n hybrid nanoparticles were compared with the corresponding results of PSL nanoparticles. Hybrid nanoparticles had indented surface morphology, and the shapes of the nanoparticles were not perfectly round whereas the surfaces of the PSL nanoparticles were smooth and the shapes were perfectly round.

CFU analysis was carried out for hybrid nanoparticles, (30nm-C-n, 50nm-A-p, 100nm-A-n and 100nm-A-p), at 50-800 mg/L NP concentrations. Exposure of 30nm-C-n and 100nm-A-n hybrid nanoparticles between 50 to 200 mg/L resulted in the viability percentages that were completely different from those of the PSL nanoparticles. Even at the lowest nanoparticle concentration (50 mg/L), the average viability percentages were found as 71.0% and 61.1% for 30nm-C-n and 100nm-A-n hybrid nanoparticles respectively. With increasing hybrid nanoparticle concentrations, the viabilities decreased, i.e. the viability percentages were 64.6% and 49.0% for 100 and 200 mg/L 30nm-C-n hybrid and 56.6% and 38.2% for 100 mg/L and 200 mg/L 100nm-A-n hybrid nanoparticles, respectively. In other words, negatively charged hybrid nanoparticles showed moderate toxicity at 50 mg/L and high toxicity between 100-200 mg/L NP concentration. Confocal microscopy analysis of 100 mg/L 30nm-C-n and 100 mg/L 100nm-A-n-Fl hybrid nanoparticle exposed yeast cells

showed that most of these nanoparticles accumulated on the cell surface instead of being internalized.

CFU analysis results for positively charged hybrid nanoparticles (50-800 mg/L 50nm-A-p and 50-200 mg/L 100nm-A-p hybrid NP) revealed that 50nm-A-p hybrid nanoparticles were non-toxic even at the highest experimental concentration (800 mg/L). Similarly, 100nm-A-p hybrid nanoparticles were found to be non-toxic between 100-200 mg/L NP concentrations, i.e. the viability percentages were 92.4% and 94.9%, respectively, but low toxicity was observed at 50 mg/L, where the viability was found as 80.4%. The viability results for positively charged hybrid nanoparticles were completely opposite of the viability results of their PSL NP counterparts in which 50nm-A-p and 100nm-A-p PSL NPs caused fully toxic effect towards the yeast cells after 100 mg/L concentration. The significant increase in the viability percentages of the yeast cells exposed to positively charged hybrid nanoparticles may be explained by the size increment of the hybrid nanoparticles with respect to their PSL nanoparticle counterparts particularly for 50nm-A-p hybrid nanoparticles. The nanoparticle sizes increased from 45.9 nm to 289.5 nm for 50nm-A-p hybrid and from 129.2 nm to 192.3 nm for 100nm-A-p hybrid nanoparticles compared to their PSL nanoparticle counterparts. Also, the molecular interactions between the hybrid nanoparticles and the yeast cell surface changed after the positively charged PSL nanoparticles were encapsulated by the DOPC phospholipid bilayer. As the cell surface comes across to the phospholipid structure first in the hybrid configuration, the effects of the positively charged PSL nanoparticles on the yeast cells are not prominent.

5.1.4. Long Term Effects of Polystyrene Latex Nanoparticles (PSL NPs) on *S. cerevisiae* Cells

Long-term effects of the PSL nanoparticles were investigated by exposing 100 mg/L and 200 mg/L 20nm-C-n and 100 mg/L 60nm-C-n PSL nanoparticles to the yeast cells for 15 generations. Although fluctuations in the viability percentages of the yeast cells from one generation to the subsequent generation were observed, in general the results showed that the nanoparticles did not show toxic effect in the long-term. A very slight decrease in the average viability percentage was observed when 20nm-C-n PSL NP concentration was increased from 100 mg/L to 200 mg/L, i.e. the average viability percentages were 88.1% and

87.0%, respectively. The increase in the size of the nanoparticle from 100 mg/L 20nm-C-n to 60nm-C-n did not affect the yeast viability, as the average viability percentage after 15 generations of 100 mg/L 60nm-C-n PSL nanoparticle exposure was found as 90.1%.

5.1.5. Uptake Mechanism Studies of Polystyrene Latex Nanoparticles (PSL NPs) on *S. cerevisiae*

In order to investigate the uptake mechanism of the PSL NPs by *S. cerevisiae*, three different endocytosis inhibitors were used: (i) Latrunculin-A, which depolymerizes actin filaments, (ii) Nocodazole, which disrupts the microtubules and (iii) ethanol, which has been shown to inhibit endocytosis between 2-6 % (v/v) concentrations. 100 mg/L 30nm-C-n and 50 mg/L and 100 mg/L 50nm-A-p PSL nanoparticles were exposed to the yeast cells after inhibitor treatment.

CFU analysis of 200 µM Lat-A treated yeast cells for 1 hour showed that the viability percentage with respect to inhibitor excluded control group was 90.2%, which showed that it did not cause toxicity. 200 µM Lat-A treated yeast cells were exposed to 100 mg/L of 30nm-C-n and 50 mg/L and 100 mg/L of 50nm-A-p PSL nanoparticles. The viability percentages of the yeast cells were similar with 30nm-C-n, but very slight decrease in viability was observed with 50 and 100 mg/L 50nm-A-p PSL nanoparticles compared to the inhibitor excluded PSL NP group. 15 µg/ml nocodazole treated yeast cells for 1 hour were found as 100.0% viable, which indicated that the inhibitor did not cause any toxicity. When the yeast cells were exposed to PSL NPs after 15 µg/ml nocodazole treatment, the viability of the yeast cells were not affected compared to inhibitor excluded control group. The yeast cells treated with 5 % (v/v) ethanol for 1 hour were found 100.0% viable showing the non-toxic effect of the inhibitor. After PSL NP exposure, the viability of 100 mg/L 30nm-C-n exposed yeast cells decreased very slightly, whereas those exposed to 50 and 100 mg/L 50nm-A-p PSL nanoparticles, the viability was not affected.

Confocal analysis was carried out at different concentrations, types and times of inhibitor treatments: 1 µM Lat-A for1 hour, 200 µM Lat-A for 1 hour, 15 µg/ml nocodazole for 1 hour, 15 µg/ml nocodazole for 2 hours and 5 % (v/v) ethanol for 1 hour. With all

inhibitors, 30nm-C-n nanoparticles were found to enter into the cells, which indicated that the uptake of the nanoparticles was not inhibited.

The integrated fluorescence intensity decreased by 3.7% after 15 µg/ml nocodazole treatment for 1 hour compared to the inhibitor excluded cells according to the results of Image J processing. When the 15 µg/ml nocodazole inhibitor treatment time was increased from 1 hour to 2 hours, it resulted in the decrease of the 100 mg/L of 30nm-C-n PSL nanoparticle internalization by 46.3%, which showed that as the inhibitor treatment increased, the uptake of the 30nm-C-n PSL nanoparticles decreased. However, the internalization process was not fully inhibited, which can be explained by the possibility of the activation of other endocytosis mechanisms by inhibiting the other one. Moreover, it is observed that 30nm-C-n PSL nanoparticles, which located in the cell cytoplasm, generally did not exert toxicity whereas the nanoparticles, which enter the cell nucleus, showed toxic effect towards the yeast cells. Finally, it can be suggested that the uptake of 30nm-C-n PSL nanoparticles by the yeast cells occurs via energy independent mechanism, i.e. diffusion or different mechanism mediated endocytosis.

5.2. Recommendations

The aim of this study was to characterize and investigate the effects of Polystyrene Latex Nanoparticles (PSL NPs), DOPC liposomes and hybrid nanoparticles which consist of DOPC liposome encapsulated PSL NPs as well as to analyze the uptake mechanism of the PSL NPs by Sac6:RFP tagged *S. cerevisiae* cells. The following recommendations may be applied to improve the experimental studies in the future.

- The yeast cells may be grown in different medium to determine the response of the yeast cells to the nanoparticles in case of changed growing medium or environmental stress.
- Different inhibitors that affect different endocytosis pathways may be implemented to further analyze the uptake mechanism of the PSL NPs by the *S. cerevisiae* cells.
- Different type of yeast strains or different organisms may be used to analyze the response of the other living organisms to the PSL NPs, DOPC liposomes and hybrid nanoparticles.

- Defined minimal yeast medium may be implemented in the toxicity studies. By the determination of the exact chemical formula of each component in the yeast medium, the charge effect of the PSL and hybrid nanoparticles on the yeast cells can be identified clearly.
- To wash the excess nanoparticles on the surface of the yeast cells and to determine the surface adhesion or the internalization of the nanoparticles more clearly, Sodium dodecyl sulfate (SDS), which is an anionic surfactant, or Tween-20, which is nonionic detergent widely used in biochemical applications, can be used.

REFERENCES

1. R. Firdessa, T. A. Oelschlaeger, and H. Moll, “Identification of multiple cellular uptake pathways of polystyrene nanoparticles and factors affecting the uptake: Relevance for drug delivery systems”, *Eur. J. Cell Biol.*, vol. 93, no. 8, pp. 323–337, 2014.

2. S. Mura, J. Nicolas, and P. Couvreur, “Stimuli-responsive nanocarriers for drug delivery”, *Nat. Mater.*, vol. 12, p. 991, Oct. 2013.

3. M. Massignani *et al.*, “Controlling Cellular Uptake by Surface Chemistry, Size, and Surface Topology at the Nanoscale”, *Small*, vol. 5, no. 21, pp. 2424–2432, Nov. 2009.

4. T. M. Fahmy, P. M. Fong, A. Goyal, and W. M. Saltzman, “Targeted for drug delivery”, *Mater. Today*, vol. 8, no. 8, Supplement, pp. 18–26, 2005.

5. Y. Malam, M. Loizidou, and A. M. Seifalian, “Liposomes and nanoparticles: nanosized vehicles for drug delivery in cancer”, *Trends Pharmacol. Sci.*, vol. 30, no. 11, pp. 592–599, 2009.

6. J. Miyazaki, Y. Kuriyama, A. Miyamoto, H. Tokumoto, Y. Konishi, and T. Nomura, “Adhesion and internalization of functionalized polystyrene latex nanoparticles toward the yeast Saccharomyces cerevisiae”, *Adv. Powder Technol.*, vol. 25, no. 4, pp. 1394–1397, 2014.

7. S. Haque and E. Chowdhury, “Recent Progress in Delivery of Therapeutic and Imaging Agents Utilizing Organic-Inorganic Hybrid Nanoparticles”, *Curr. Drug Deliv.*, vol. 14, Nov. 2017.

8. V. Colapicchioni *et al.*, “Killing cancer cells using nanotechnology: novel poly(I:C) loaded liposome-silica hybrid nanoparticles”, *J. Mater. Chem. B*, vol. 3, no. 37, pp. 7408–7416, 2015.

9. T. Wang, J. Bai, X. Jiang, and G. U. Nienhaus, “Cellular Uptake of Nanoparticles by Membrane Penetration: A Study Combining Confocal Microscopy with FTIR Spectroelectrochemistry”, *ACS Nano*, vol. 6, no. 2, pp. 1251–1259, Feb. 2012.

10. S. Zhu, B. Zhu, A. Huang, Y. Hu, G. Wang, and F. Ling, “Toxicological effects of multi-walled carbon nanotubes on Saccharomyces cerevisiae: The uptake kinetics and mechanisms and the toxic responses”, *J. Hazard. Mater.*, vol. 318, pp. 650–662, 2016.

11. C. Cordon, M. Piva, C. Melo, M. Pinhal, and E. R. Suarez, “Nanoparticles as platforms of molecular delivery in diagnosis and therapy”, *OA Cancer*, vol. 1, Dec. 2013.

12. D. A. Richards, A. Maruani, and V. Chudasama, “Antibody fragments as nanoparticle targeting ligands: a step in the right direction”, *Chem. Sci.*, vol. 8, no. 1, pp. 63–77, Jan. 2017.

13. A. Z. Wilczewska, K. Niemirowicz, K. H. Markiewicz, and H. Car, “Nanoparticles as drug delivery systems”, *Pharmacol. Reports*, vol. 64, no. 5, pp. 1020–1037, 2012.

14. A. Akbarzadeh *et al.*, “Liposome: classification, preparation, and applications”, *Nanoscale Res. Lett.*, vol. 8, no. 1, p. 102, 2013.

15. W. H. De Jong and P. J. A. Borm, “Drug delivery and nanoparticles: Applications and hazards”, *Int. J. Nanomedicine*, vol. 3, no. 2, pp. 133–149, Jun. 2008.

16. V. Guida, “Thermodynamics and kinetics of vesicles formation processes”, *Adv. Colloid Interface Sci.*, vol. 161, no. 1, pp. 77–88, 2010.

17. J. Zhang, “Amphiphilic Molecules BT - Encyclopedia of Membranes”, E. Drioli and L. Giorno, Eds. Berlin, Heidelberg: Springer Berlin Heidelberg, 2015, pp. 1–4.

18. C. Huang, D. Quinn, Y. Sadovsky, S. Suresh, and K. J. Hsia, “Formation and size distribution of self-assembled vesicles”, *Proc. Natl. Acad. Sci. U. S. A.*, vol. 114, no.

11, pp. 2910–2915, Mar. 2017.

19. A. Laouini, C. Jaafar-Maalej, I. Limayem Blouza, S. Sfar, C. Charcosset, and H. Fessi, "*Preparation, Characterization and Applications of Liposomes: State of the Art*", vol. 1. 2012.

20. C. Nkanga, A. Bapolisi, N. Ikemefuna, and R. Krause, "General Perception of Liposomes: Formation, Manufacturing and Application", 2019.

21. W. Gao, C.-M. J. Hu, R. H. Fang, and L. Zhang, "Liposome-like Nanostructures for Drug Delivery", *J. Mater. Chem. B. Mater. Biol. Med.*, vol. 1, no. 48, p. 10.1039/C3TB21238F, Dec. 2013.

22. M. Mathiyazhakan, C. Wiraja, and C. Xu, "A Concise Review of Gold Nanoparticles-Based Photo-Responsive Liposomes for Controlled Drug Delivery", *Nano-Micro Lett.*, vol. 10, no. 1, p. 10, 2017.

23. A.-L. Troutier, T. Delair, C. Pichot, and C. Ladavière, "Physicochemical and Interfacial Investigation of Lipid/Polymer Particle Assemblies", *Langmuir*, vol. 21, no. 4, pp. 1305–1313, Feb. 2005.

24. A. M. Carmona-Ribeiro and B. R. Midmore, "Synthetic bilayer adsorption onto polystyrene microspheres", *Langmuir*, vol. 8, no. 3, pp. 801–806, Mar. 1992.

25. L. Zhang and S. Granick, "How to Stabilize Phospholipid Liposomes (Using Nanoparticles)", *Nano Lett.*, vol. 6, no. 4, pp. 694–698, Apr. 2006.

26. D. Distler, W. S. Neto, and F. B. T.-R. M. in M. S. and M. E. Machado, "Emulsion Polymerization", Elsevier, 2017.

27. Ran Hao, "Encapsulation of Biological Nanoparticles — Virus Coating and Drug Nanoparticulation", Queen Mary, University of London, 2016.

28. G. Libralato, E. Galdiero, A. Falanga, R. Carotenuto, E. de Alteriis, and M. Guida, “Toxicity Effects of Functionalized Quantum Dots, Gold and Polystyrene Nanoparticles on Target Aquatic Biological Models: A Review”, *Molecules*, vol. 22, no. 9, p. 1439, Aug. 2017.

29. T. Nomura, J. Miyazaki, A. Miyamoto, Y. Kuriyama, H. Tokumoto, and Y. Konishi, “Exposure of the Yeast Saccharomyces cerevisiae to Functionalized Polystyrene Latex Nanoparticles: Influence of Surface Charge on Toxicity”, *Environ. Sci. Technol.*, vol. 47, no. 7, pp. 3417–3423, Apr. 2013.

30. S. Aghamohammadzadeh, I. I. Smaczynska-de Rooij, and K. R. Ayscough, “An Abp1-Dependent Route of Endocytosis Functions when the Classical Endocytic Pathway in Yeast Is Inhibited”, *PLoS One*, vol. 9, no. 7, p. e103311, Jul. 2014.

31. O. Lunov *et al.*, “Differential Uptake of Functionalized Polystyrene Nanoparticles by Human Macrophages and a Monocytic Cell Line”, *ACS Nano*, vol. 5, no. 3, pp. 1657–1669, Mar. 2011.

32. R. Schmidt, “Dynamic Light Scattering for Protein Characterization”, *Encyclopedia of Analytical Chemistry*. 15-Dec-2010.

33. Warwick.ac.uk, *Dynamic Light Scattering: An Introduction in 30 Minutes*., https://warwick.ac.uk/fac/cross_fac/sciencecity/programmes/internal/themes/am2/booking/particlesize/intro_to_dls.pdf, accessed in June 2019.

34. M. Kaszuba, J. Corbett, F. M. Watson, and A. Jones, “High-concentration zeta potential measurements using light-scattering techniques”, *Philos. Trans. A. Math. Phys. Eng. Sci.*, vol. 368, no. 1927, pp. 4439–4451, Sep. 2010.

35. Warwick.ac.uk, *Zeta Potential An Introduction in 30 Minutes*., https://warwick.ac.uk/fac/cross_fac/sciencecity/programmes/internal/themes/am2/booking/particlesize/mrk654-01_an_introduction_to_zeta_potential_v3.pdf., accessed in June 2019.

36. C. Y. Tang and Z. Yang, “Chapter 8 - Transmission Electron Microscopy (TEM)”, N. Hilal, A. F. Ismail, T. Matsuura, and D. B. T.-M. C. Oatley-Radcliffe, Eds. Elsevier, 2017, pp. 145–159.

37. S. J. Pennycook, “Scanning Transmission Electron Microscopy: Z-Contrast Imaging”, *Characterization of Materials*. 12-Oct-2012.

38. Thermo Fisher Scientific, *An Introduction to Electron Microscopy - STEM.*, https://www.fei.com/introduction-to-electron-microscopy/stem/, accessed in June 2019.

39. S. J. Pennycook *et al.*, *6 Scanning Transmission Electron Microscopy for Nanostructure Characterization*, vol. 2. 2006.

40. Michiel Mueller, “Chapter 1- Confocal Fluorescence Microscopy”, in *Introduction to Confocal Fluorescence Microscopy*, 2005.

41. A. Ray and A. K. Mitra, “Chapter 8 - Nanotechnology in Intracellular Trafficking, Imaging, and Delivery of Therapeutic Agents”, in *Micro and Nano Technologies*, A. K. Mitra, K. Cholkar, and A. B. T.-E. N. for D. Mandal Drug Delivery and Medical Devices, Eds. Boston: Elsevier, 2017, pp. 169–188.

42. W.-K. Huh *et al.*, “Global analysis of protein localization in budding yeast”, *Nature*, vol. 425, no. 6959, pp. 686–691, 2003.

43. R. Narayanaswamy *et al.*, “Systematic definition of protein constituents along the major polarization axis reveals an adaptive reuse of the polarization machinery in pheromone-treated budding yeast”, *J. Proteome Res.*, vol. 8, no. 1, pp. 6–19, Jan. 2009.

44. T. dos Santos, J. Varela, I. Lynch, A. Salvati, and K. A. Dawson, “Effects of Transport Inhibitors on the Cellular Uptake of Carboxylated Polystyrene Nanoparticles in Different Cell Lines”, *PLoS One*, vol. 6, no. 9, p. e24438, Sep. 2011.

45. P. Lucero, E. Peñalver, E. Moreno, and R. Lagunas, “Moderate concentrations of ethanol inhibit endocytosis of the yeast maltose transporter”, *Appl. Environ. Microbiol.*, vol. 63, no. 10, pp. 3831–3836, Oct. 1997.

46. M. Gumustas, C. T. Sengel-Turk, A. Gumustas, S. A. Ozkan, and B. Uslu, “Chapter 5 - Effect of Polymer-Based Nanoparticles on the Assay of Antimicrobial Drug Delivery Systems”, A. M. B. T.-M. S. for C. D. Grumezescu Biosensing and Diagnostics, Ed. Elsevier, 2017, pp. 67–108.

47. A. Jacquot *et al.*, “Morphological and Physical Analysis of Natural Phospholipids-Based Biomembranes,”, *PLoS One*, vol. 9, no. 9, p. e107435, Sep. 2014.

48. E. Oliveira *et al.*, “Green and Red Fluorescent Dyes for Translational Applications in Imaging and Sensing Analytes: A Dual-Color Flag”, *ChemistryOpen*, vol. 7, no. 1, pp. 9–52, Nov. 2017.

49. H. Yang *et al.*, “VCAM-1-targeted core/shell nanoparticles for selective adhesion and delivery to endothelial cells with lipopolysaccharide-induced inflammation under shear flow and cellular magnetic resonance imaging in vitro”, *Int. J. Nanomedicine*, vol. 8, pp. 1897–1906, 2013.

50. D. Sun *et al.*, “Uptake and cellular distribution, in four plant species, of fluorescently labeled mesoporous silica nanoparticles”, *Plant Cell Rep.*, vol. 33, no. 8, pp. 1389–1402, 2014.

51. Y. Ge, Y. Zhang, S. He, F. Nie, G. Teng, and N. Gu, “Fluorescence Modified Chitosan-Coated Magnetic Nanoparticles for High-Efficient Cellular Imaging”, *Nanoscale Res. Lett.*, vol. 4, no. 4, pp. 287–295, Jan. 2009.

52. P. F. Stanbury, A. Whitaker, and S. J. Hall, “Chapter 2 - Microbial growth kinetics”, P. F. Stanbury, A. Whitaker, and S. J. B. T.-P. of F. T. (Third E. Hall, Eds. Oxford: Butterworth-Heinemann, 2017, pp. 21–74.

53. R. Salari and R. Salari, “Investigation of the Best Saccharomyces cerevisiae Growth Condition”, *Electron. physician*, vol. 9, no. 1, pp. 3592–3597, Jan. 2017.

54. Z. Xia, A. Woods, A. Quirk, I. J. Burgess, and B. L. T. Lau, “Interactions between polystyrene nanoparticles and supported lipid bilayers: impact of charge and hydrophobicity modification by specific anions”, *Environ. Sci. Nano*, 2019.

55. V. Forest and J. Pourchez, “*Preferential binding of positive nanoparticles on cell membranes is due to electrostatic interactions: A too simplistic explanation that does not take into account the nanoparticle protein corona*”, vol. 70. 2016.

56. A. M. Crane, H.-U. Hua, A. D. Coggin, B. G. Gugiu, B. L. Lam, and S. K. Bhattacharya, “Mass Spectrometric Analyses of Phosphatidylcholines in Alkali-Exposed Corneal TissuePhosphatidylcholines in Alkali-Exposed Corneas”, *Invest. Ophthalmol. Vis. Sci.*, vol. 53, no. 11, pp. 7122–7130, Oct. 2012.

57. L. S. Mangala, H. D. Han, G. Lopez-Berestein, and A. K. Sood, “Liposomal siRNA for Ovarian Cancer BT - Therapeutic Applications of RNAi: Methods and Protocols”, C. M. Rondinone and J. F. Reidhaar-Olson, Eds. Totowa, NJ: Humana Press, 2009, pp. 29–42.

58. S. Y. Carroll, H. E. M. Stimpson, J. Weinberg, C. P. Toret, Y. Sun, and D. G. Drubin, “Analysis of yeast endocytic site formation and maturation through a regulatory transition point”, *Mol. Biol. Cell*, vol. 23, no. 4, pp. 657–668, Feb. 2012.

59. S. Feyder, J.-O. De Craene, S. Bär, D. L. Bertazzi, and S. Friant, “Membrane Trafficking in the Yeast Saccharomyces cerevisiae Model”, *Int. J. Mol. Sci.*, vol. 16, no. 1, pp. 1509–1525, Jan. 2015.

60. R. Basu, E. L. Munteanu, and F. Chang, “Role of turgor pressure in endocytosis in fission yeast”, *Mol. Biol. Cell*, vol. 25, no. 5, pp. 679–687, Mar. 2014.

61. K. Kim, B. J. Galletta, K. O. Schmidt, F. S. Chang, K. J. Blumer, and J. A. Cooper,

"Actin-based motility during endocytosis in budding yeast", *Mol. Biol. Cell*, vol. 17, no. 3, pp. 1354–1363, Mar. 2006.

62. M. Kaksonen, Y. Sun, and D. G. Drubin, "A Pathway for Association of Receptors, Adaptors, and Actin during Endocytic Internalization", *Cell*, vol. 115, no. 4, pp. 475–487, 2003.

63. A. Subtil and A. Dautry-Varsat, "Microtubule depolymerization inhibits clathrin coated-pit internalization in non-adherent cell lines while interleukin 2 endocytosis is not affected", *J. Cell Sci.*, vol. 110, no. 19, pp. 2441 LP – 2447, Oct. 1997.

64. J. Shareck and P. Belhumeur, "Modulation of morphogenesis in Candida albicans by various small molecules", *Eukaryot. Cell*, vol. 10, no. 8, pp. 1004–1012, Aug. 2011.

65. M. P. Torres, S. T. Clement, S. D. Cappell, and H. G. Dohlman, "Cell cycle-dependent phosphorylation and ubiquitination of a G protein alpha subunit", *J. Biol. Chem.*, vol. 286, no. 23, pp. 20208–20216, Jun. 2011.

66. C. A. Andrews, L. A. Díaz-Martínez, J. F. Gimenez-Abian, and D. J. Clarke, "Evidence That the Yeast Spindle Assembly Checkpoint Has a Target Other Than the Anaphase Promoting Complex", *Cell Cycle*, vol. 4, no. 11, pp. 1555–1557, Nov. 2005.

67. A. Nakashima *et al.*, "The yeast Tor signaling pathway is involved in G2/M transition via polo-kinase", *PLoS One*, vol. 3, no. 5, pp. e2223–e2223, May 2008.

68. A. K. Bryan, A. Goranov, A. Amon, and S. R. Manalis, "Measurement of mass, density, and volume during the cell cycle of yeast", *Proc. Natl. Acad. Sci.*, vol. 107, no. 3, pp. 999 LP – 1004, Jan. 2010.

69. J. Dausend *et al.*, "Uptake Mechanism of Oppositely Charged Fluorescent Nanoparticles in HeLa Cells", *Macromol. Biosci.*, vol. 8, no. 12, pp. 1135–1143, Dec. 2008.

70. Y. Wang and D. J. Burke, “Checkpoint genes required to delay cell division in response to nocodazole respond to impaired kinetochore function in the yeast Saccharomyces cerevisiae”, *Mol. Cell. Biol.*, vol. 15, no. 12, pp. 6838–6844, Dec. 1995.

71. H. Song *et al.*, “Overexpression of DRG2 Increases G_2/M Phase Cells and Decreases Sensitivity to Nocodazole-Induced Apoptosis”, *J. Biochem.*, vol. 135, no. 3, pp. 331–335, 2004.

72. K. Endo, M. Mizuguchi, A. Harata, G. Itoh, and K. Tanaka, “Nocodazole induces mitotic cell death with apoptotic-like features in Saccharomyces cerevisiae”, *FEBS Lett.*, vol. 584, no. 11, pp. 2387–2392, 2010.

73. P. Lucero, E. Peñalver, E. Moreno, and R. Lagunas, “Internal trehalose protects endocytosis from inhibition by ethanol in Saccharomyces cerevisiae”, *Appl. Environ. Microbiol.*, vol. 66, no. 10, pp. 4456–4461, Oct. 2000.

APPENDIX A: RESULTS OF DLS AND ZETA POTENTIAL ANALYSES MEASUREMENTS

A.1. Results of DLS and Zeta Potential Analyses for 20nm-C-n PSL NPs

Sample ID	20nm-C-n PSL NP (Combined)
Operator ID	BBGU
Elapsed Time	00:08:00
Mean Diam.	60.1 nm
Rel. Var.	5.052
Skew	7.301

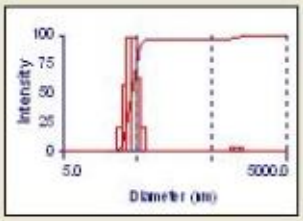

d(nm)	G(d)	C(d)	d(nm)	G(d)	C(d)	d(nm)	G(d)	C(d)
21.2	0	0	105.4	0	98	523.5	0	98
24.6	0	0	122.0	0	98	605.6	0	98
28.4	20	5	141.1	0	98	715.2	0	98
32.9	57	21	163.2	0	98	810.3	0	98
38.0	99	48	188.8	0	98	918.0	2	99
44.0	100	75	218.4	0	98	1040.1	2	99
50.9	64	93	252.7	0	98	1178.4	2	100
58.9	20	98	292.3	0	98	1335.2	0	100
68.1	0	98	338.2	0	98	1512.7	0	100
78.8	0	98	391.2	0	98	1942.1	0	100
91.2	0	98	452.5	0	98	2246.7	0	100

Figure A.1. Intensity distribution of 20nm-C-n PSL NPs obtained from DLS analysis.

Sample ID	20nm-C-n PSL NP (Combined)
Operator ID	BBGU
Elapsed Time	00:08:00
Mean Diam.	34.7 nm
Rel. Var.	0.028
Skew	1.221

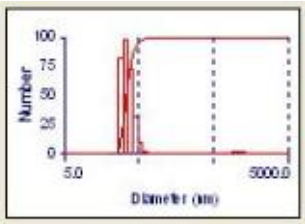

d(nm)	G(d)	C(d)	d(nm)	G(d)	C(d)	d(nm)	G(d)	C(d)
21.2	0	0	105.4	0	100	523.5	0	100
24.6	0	0	122.0	0	100	605.6	0	100
28.4	82	28	141.1	0	100	715.2	0	100
32.9	100	62	163.2	0	100	810.3	0	100
38.0	73	86	188.8	0	100	918.0	0	100
44.0	31	97	218.4	0	100	1040.1	0	100
50.9	8	100	252.7	0	100	1178.4	0	100
58.9	1	100	292.3	0	100	1335.2	0	100
68.1	0	100	338.2	0	100	1512.7	0	100
78.8	0	100	391.2	0	100	1942.1	0	100
91.2	0	100	452.5	0	100	2246.7	0	100

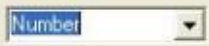

Figure A.2. Number distribution of 20nm-C-n PSL NPs obtained from DLS analysis.

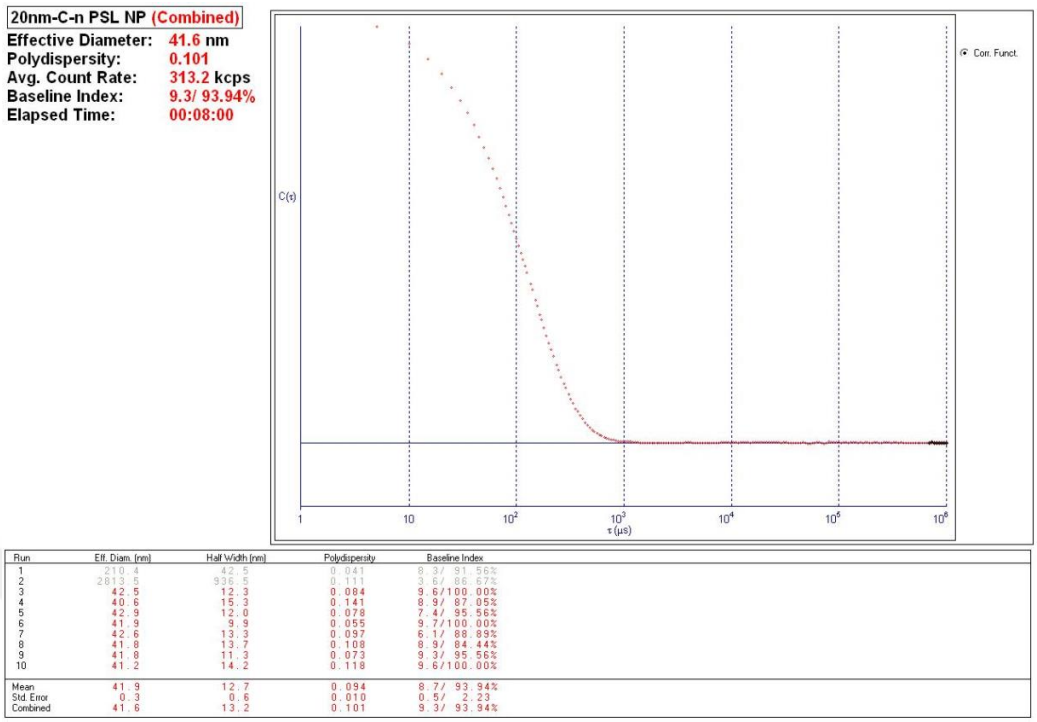

Figure A.3. Effective diameter and polydispersity values of 20nm-C-n PSL NPs obtained from DLS analysis.

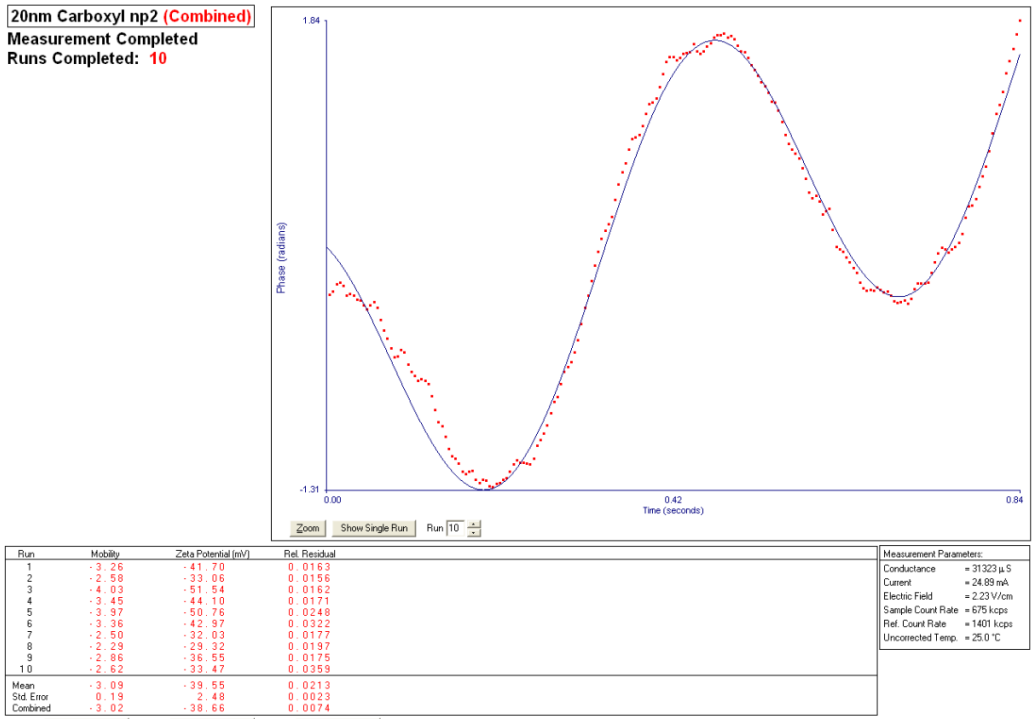

Figure A.4. Zeta potential of 20nm-C-n PSL NPs obtained from ELS analysis.

A.2. Results of DLS and Zeta Potential Analyses for 30nm-C-n PSL NPs

Sample ID	30nm Carboxyl np--new (Combined)
Operator ID	BBGU
Elapsed Time	00:08:00
Mean Diam.	435.6 nm
Rel. Var.	13.082
Skew	4.780

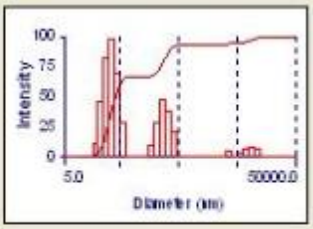

d(nm)	G(d)	C(d)	d(nm)	G(d)	C(d)	d(nm)	G(d)	C(d)
8.8	0	0	99.1	0	67	1110.9	0	95
11.0	0	0	123.4	0	67	1383.9	0	95
13.7	0	0	153.7	9	69	1724.0	0	95
17.1	10	2	191.5	29	74	2147.6	0	95
21.3	46	11	238.6	48	84	2675.4	0	95
26.5	84	28	297.2	38	91	3333.0	4	96
33.0	100	47	370.2	20	95	4152.1	0	96
41.1	69	61	461.2	0	95	5172.5	2	96
51.2	29	67	574.6	0	95	6443.6	5	97
63.8	0	67	715.8	0	95	8027.2	7	99
79.5	0	67	891.7	0	95	10000.0	6	100

Intensity

Figure A.5. Intensity distribution of 30nm-C-n PSL NPs obtained from DLS analysis.

Sample ID	30nm Carboxyl np--new (Combined)
Operator ID	BBGU
Elapsed Time	00:08:00
Mean Diam.	21.9 nm
Rel. Var.	0.053
Skew	1.650

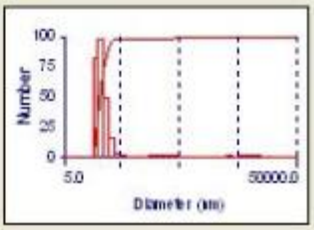

d(nm)	G(d)	C(d)	d(nm)	G(d)	C(d)	d(nm)	G(d)	C(d)
8.8	0	0	99.1	0	100	1110.9	0	100
11.0	0	0	123.4	0	100	1383.9	0	100
13.7	0	0	153.7	0	100	1724.0	0	100
17.1	82	33	191.5	0	100	2147.6	0	100
21.3	100	73	238.6	0	100	2675.4	0	100
26.5	49	92	297.2	0	100	3333.0	0	100
33.0	16	99	370.2	0	100	4152.1	0	100
41.1	3	100	461.2	0	100	5172.5	0	100
51.2	0	100	574.6	0	100	6443.6	0	100
63.8	0	100	715.8	0	100	8027.2	0	100
79.5	0	100	891.7	0	100	10000.0	0	100

Number

Figure A.6. Number distribution of 30nm-C-n PSL NPs obtained from DLS analysis.

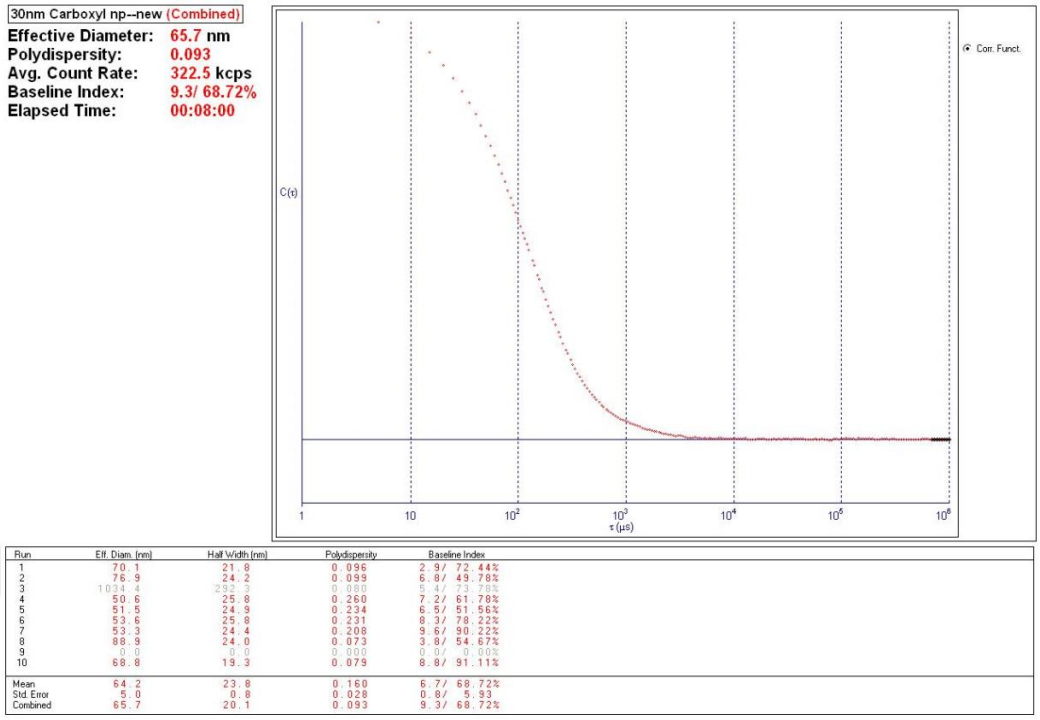

Figure A.7. Effective diameter and polydispersity values of 30nm-C-n PSL NPs obtained from DLS analysis.

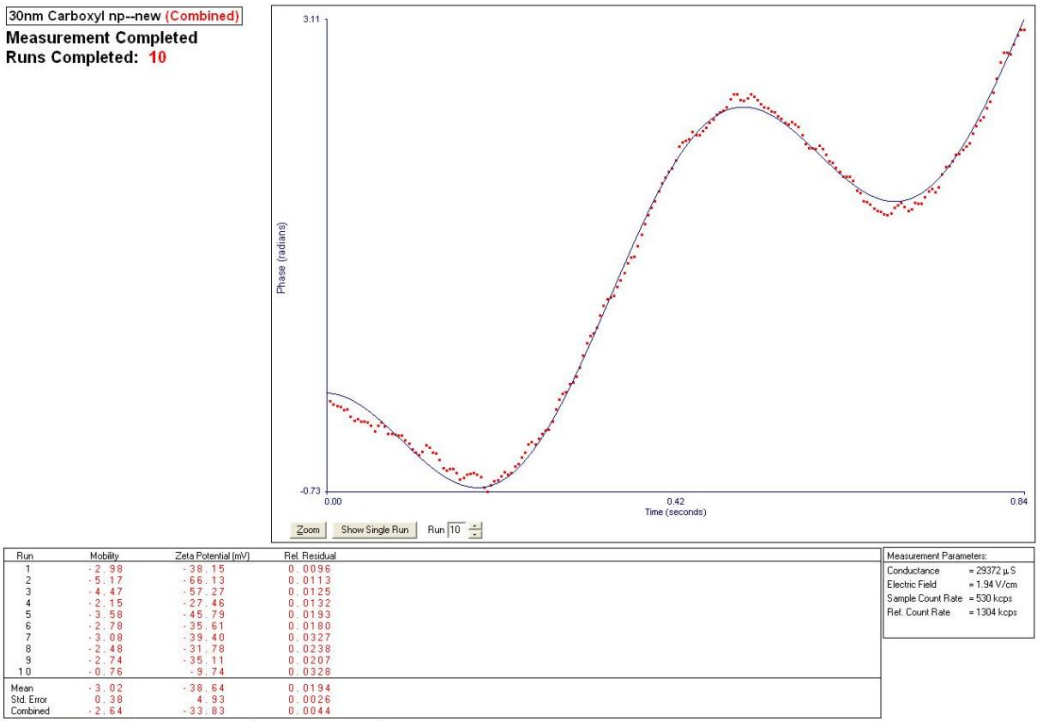

Figure A.8. Zeta potential of 30nm-C-n PSL NPs obtained from ELS analysis.

A.3. Results of DLS and Zeta Potential Analyses for 60nm-C-n PSL NPs

Sample ID	60nm Karboksil (Combined)
Operator ID	BBGU
Elapsed Time	00:09:00
Mean Diam.	106.9 nm
Rel. Var.	0.250
Skew	1.566

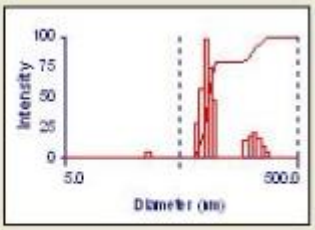

d(nm)	G(d)	C(d)	d(nm)	G(d)	C(d)	d(nm)	G(d)	C(d)
21.9	0	0	56.8	0	1	147.2	0	80
23.9	0	0	61.9	0	1	160.5	0	80
26.0	4	1	67.5	29	8	175.1	14	84
28.4	0	1	73.6	58	23	190.9	16	88
30.9	0	1	80.3	100	49	208.2	20	93
33.7	0	1	87.5	75	68	227.0	15	97
36.8	0	1	95.4	48	80	247.6	9	99
40.1	0	1	104.1	0	80	270.0	4	100
43.8	0	1	113.5	0	80	294.4	0	100
47.7	0	1	123.8	0	80	321.1	0	100
52.0	0	1	135.0	0	80	350.1	0	100

Figure A.9. Intensity distribution of 60nm-C-n PSL NPs obtained from DLS analysis.

Sample ID	60nm Karboksil (Combined)
Operator ID	BBGU
Elapsed Time	00:09:00
Mean Diam.	31.2 nm
Rel. Var.	0.254
Skew	2.930

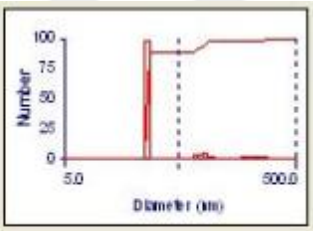

d(nm)	G(d)	C(d)	d(nm)	G(d)	C(d)	d(nm)	G(d)	C(d)
21.9	0	0	56.8	0	90	147.2	0	100
23.9	0	0	61.9	0	90	160.5	0	100
26.0	100	90	67.5	3	92	175.1	0	100
28.4	0	90	73.6	3	95	190.9	0	100
30.9	0	90	80.3	3	98	208.2	0	100
33.7	0	90	87.5	2	99	227.0	0	100
36.8	0	90	95.4	1	100	247.6	0	100
40.1	0	90	104.1	0	100	270.0	0	100
43.8	0	90	113.5	0	100	294.4	0	100
47.7	0	90	123.8	0	100	321.1	0	100
52.0	0	90	135.0	0	100	350.1	0	100

Figure A.10. Number distribution of 60nm-C-n PSL NPs obtained from DLS analysis.

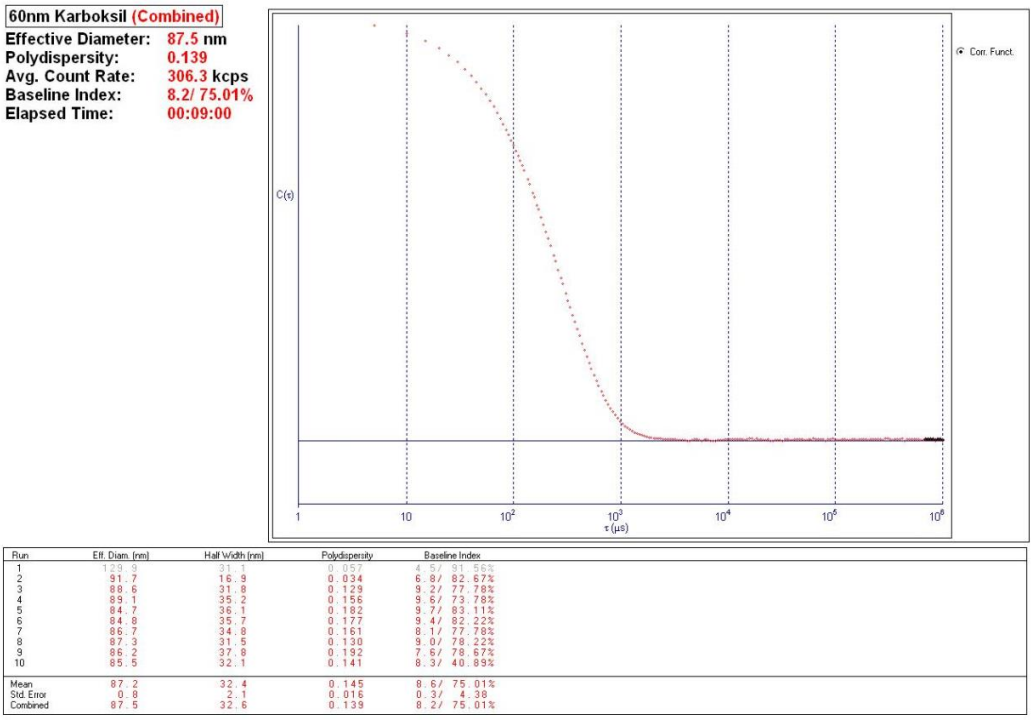

Run	Eff. Diam. [nm]	Half Width [nm]	Polydispersity	Baseline Index
1	129.9	31.1	0.057	4.5/ 91.56%
2	91.7	16.9	0.034	6.8/ 82.67%
3	88.6	31.8	0.129	9.2/ 77.78%
4	89.1	35.2	0.156	9.6/ 73.78%
5	84.7	36.1	0.182	9.7/ 83.11%
6	84.8	35.7	0.177	9.4/ 82.22%
7	86.7	34.8	0.161	8.1/ 77.78%
8	87.3	31.5	0.130	9.0/ 78.22%
9	86.2	37.8	0.192	7.6/ 78.67%
10	85.5	32.1	0.141	8.3/ 40.89%
Mean	87.2	32.4	0.145	8.6/ 75.01%
Std. Error	0.8	2.1	0.016	0.3/ 4.38
Combined	87.5	32.6	0.139	8.2/ 75.01%

Figure A.11. Effective diameter and polydispersity values of 60nm-C-n PSL NPs obtained from DLS analysis.

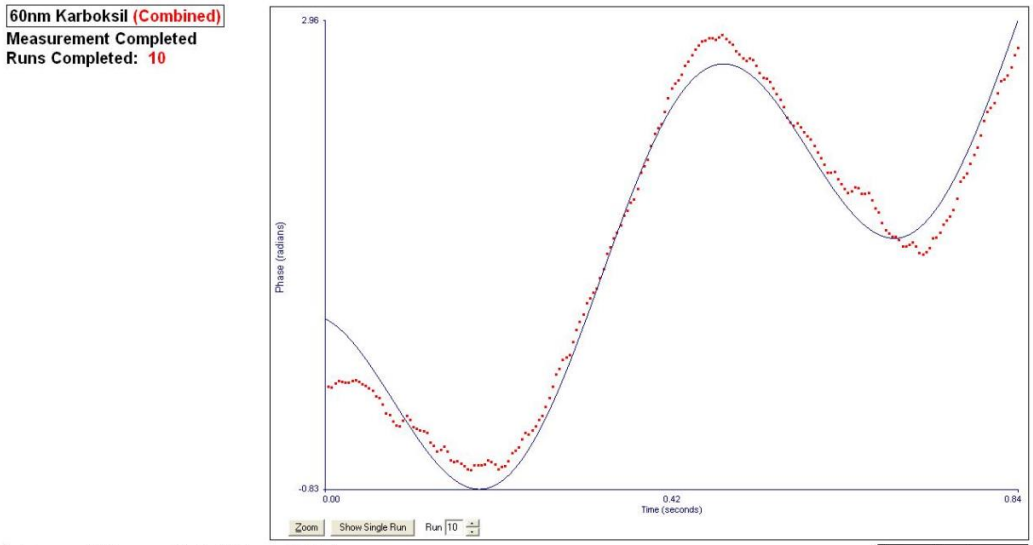

Run	Mobility	Zeta Potential (mV)	Rel. Residual
1	-4.11	-52.56	0.0200
2	-2.57	-32.90	0.0139
3	-2.86	-36.55	0.0199
4	-3.94	-50.45	0.0143
5	-1.53	-19.64	0.0343
6	-1.98	-25.33	0.0284
7	-4.03	-51.58	0.0283
8	-4.59	-58.79	0.0372
9	-4.12	-52.72	0.0147
10	-3.65	-46.70	0.0156
Mean	-3.34	-42.72	0.0227
Std. Error	0.33	4.19	0.0028
Combined	-3.24	-41.53	0.0118

Measurement Parameters:	
Conductance	= 31411 µS
Electric Field	= 2.08 V/cm
Sample Count Rate	= 276 kcps
Ref. Count Rate	= 1427 kcps

Figure A.12. Zeta potential of 60nm-C-n PSL NPs obtained from ELS analysis.

A.4. Results of DLS and Zeta Potential Analyses for 50nm-A-p PSL NPs

Sample ID	50nm Amine Fl (Combined)
Operator ID	BBGU
Elapsed Time	00:10:00
Mean Diam.	64.1 nm
Rel. Var.	0.222
Skew	0.955

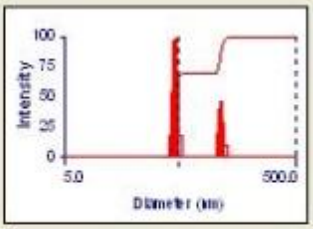

d(nm)	G(d)	C(d)	d(nm)	G(d)	C(d)	d(nm)	G(d)	C(d)
35.5	0	0	56.8	0	71	90.9	0	71
37.1	0	0	59.3	0	71	94.8	0	71
38.7	0	0	61.9	0	71	99.0	0	71
40.4	16	3	64.6	0	71	103.3	19	75
42.1	55	15	67.4	0	71	107.8	39	83
44.0	98	35	70.3	0	71	112.5	45	93
45.9	100	55	73.4	0	71	117.4	27	98
47.9	61	68	76.6	0	71	122.5	9	100
50.0	17	71	79.9	0	71	127.8	0	100
52.2	0	71	83.4	0	71	133.4	0	100
54.4	0	71	87.1	0	71	139.2	0	100

Intensity

Figure A.13. Intensity distribution of 50nm-A-p PSL NPs obtained from DLS analysis.

Sample ID	50nm Amine Fl (Combined)
Operator ID	BBGU
Elapsed Time	00:10:00
Mean Diam.	44.5 nm
Rel. Var.	0.007
Skew	11.065

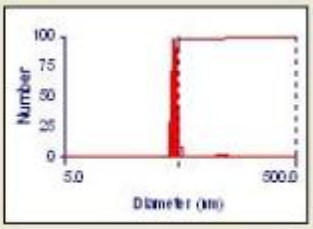

d(nm)	G(d)	C(d)	d(nm)	G(d)	C(d)	d(nm)	G(d)	C(d)
35.5	0	0	56.8	0	100	90.9	0	100
37.1	0	0	59.3	0	100	94.8	0	100
38.7	0	0	61.9	0	100	99.0	0	100
40.4	28	8	64.6	0	100	103.3	0	100
42.1	72	31	67.4	0	100	107.8	0	100
44.0	100	61	70.3	0	100	112.5	0	100
45.9	79	86	73.4	0	100	117.4	0	100
47.9	38	97	76.6	0	100	122.5	0	100
50.0	8	100	79.9	0	100	127.8	0	100
52.2	0	100	83.4	0	100	133.4	0	100
54.4	0	100	87.1	0	100	139.2	0	100

Number

Figure A.14. Number distribution of 50nm-A-p PSL NPs obtained from DLS analysis.

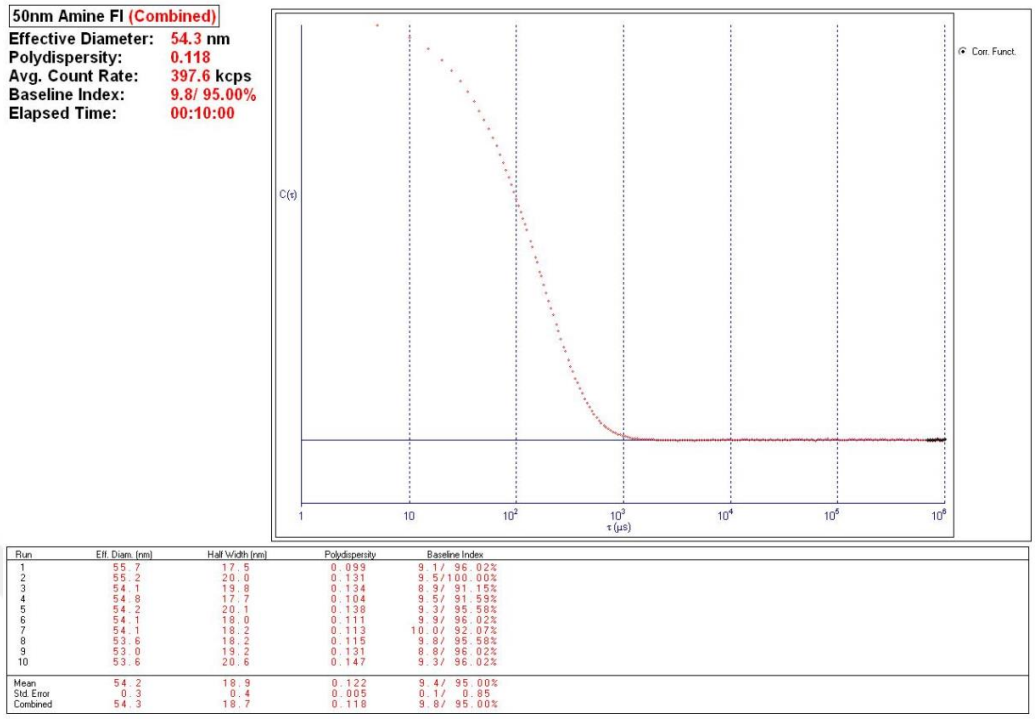

Figure A.15. Effective diameter and polydispersity values of 50nm-A-p PSL NPs obtained from DLS analysis.

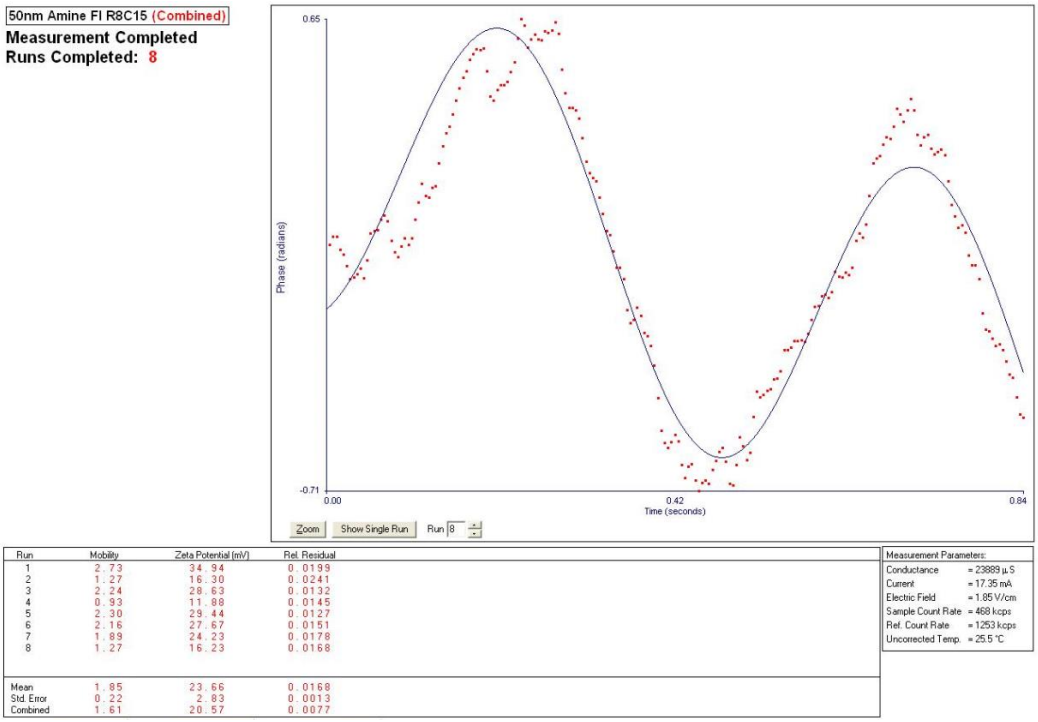

Figure A.16. Zeta potential of 50nm-A-p PSL NPs obtained from ELS analysis.

A.5. Result of Zeta Potential Analysis for 50nm-A-n PSL NPs

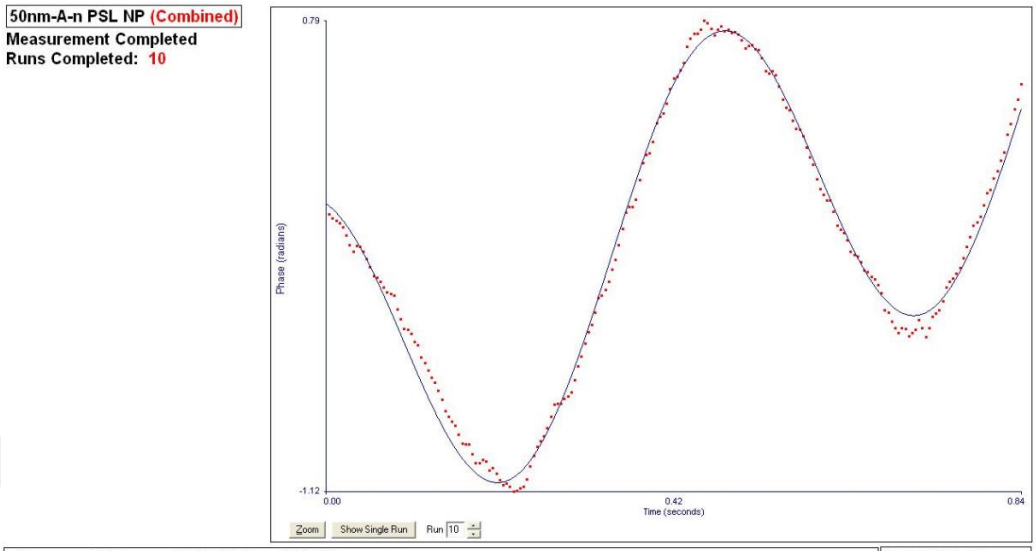

Run	Mobility	Zeta Potential (mV)	Rel. Residual
1	-2.06	-26.31	0.0083
2	-1.71	-21.91	0.0088
3	-1.62	-20.70	0.0069
4	-1.37	-17.57	0.0089
5	-1.48	-18.99	0.0098
6	-1.68	-21.44	0.0120
7	-1.16	-14.83	0.0111
8	-1.98	-25.35	0.0241
9	-1.55	-19.82	0.0280
10	-1.42	-18.16	0.0105
Mean	-1.60	-20.51	0.0128
Std. Error	0.09	1.10	0.0023
Combined	-1.59	-20.31	0.0035

Measurement Parameters:	
Conductance	= 28189 µS
Electric Field	= 2.70 V/cm
Sample Count Rate	= 305 kcps
Ref. Count Rate	= 1631 kcps

Figure A.17. Zeta potential of 50nm-A-n PSL NPs obtained from ELS analysis.

A.6. Results of DLS and Zeta Potential Analyses for 100nm-A-p PSL NPs

Sample ID	100nm-A-p PSL NP (Combined)
Operator ID	BBGU
Elapsed Time	00:10:00
Mean Diam.	129.2 nm
Rel. Var.	0.072
Skew	-1.392

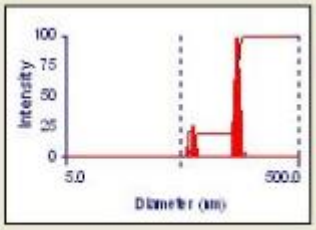

d(nm)	G(d)	C(d)	d(nm)	G(d)	C(d)	d(nm)	G(d)	C(d)
46.8	0	0	75.5	0	20	121.9	0	20
48.9	0	0	78.9	0	20	127.3	0	20
51.1	0	0	82.4	0	20	132.9	29	27
53.4	0	0	86.1	0	20	138.8	64	44
55.7	8	2	89.9	0	20	145.0	100	70
58.2	19	7	93.9	0	20	151.4	73	89
60.8	25	14	98.1	0	20	158.2	38	99
63.5	17	18	102.4	0	20	165.2	3	100
66.3	5	20	107.0	0	20	172.5	0	100
69.3	0	20	111.7	0	20	180.2	0	100
72.3	0	20	116.7	0	20	188.2	0	100

Figure A.18. Intensity distribution of 100nm-A-p PSL NPs obtained from DLS analysis.

Sample ID	100nm-A-p PSL NP (Combined)
Operator ID	BBGU
Elapsed Time	00:10:00
Mean Diam.	62.1 nm
Rel. Var.	0.051
Skew	5.505

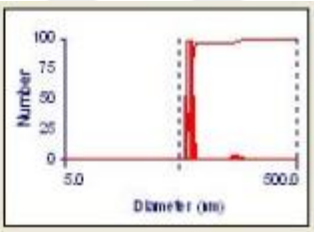

d(nm)	G(d)	C(d)	d(nm)	G(d)	C(d)	d(nm)	G(d)	C(d)
46.8	0	0	75.5	0	97	121.9	0	97
48.9	0	0	78.9	0	97	127.3	0	97
51.1	0	0	82.4	0	97	132.9	1	98
53.4	0	0	86.1	0	97	138.8	2	98
55.7	53	16	89.9	0	97	145.0	3	99
58.2	99	47	93.9	0	97	151.4	2	100
60.8	100	77	98.1	0	97	158.2	1	100
63.5	53	93	102.4	0	97	165.2	0	100
66.3	13	97	107.0	0	97	172.5	0	100
69.3	0	97	111.7	0	97	180.2	0	100
72.3	0	97	116.7	0	97	188.2	0	100

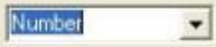

Figure A.19. Number distribution of 100nm-A-p PSL NPs obtained from DLS analysis.

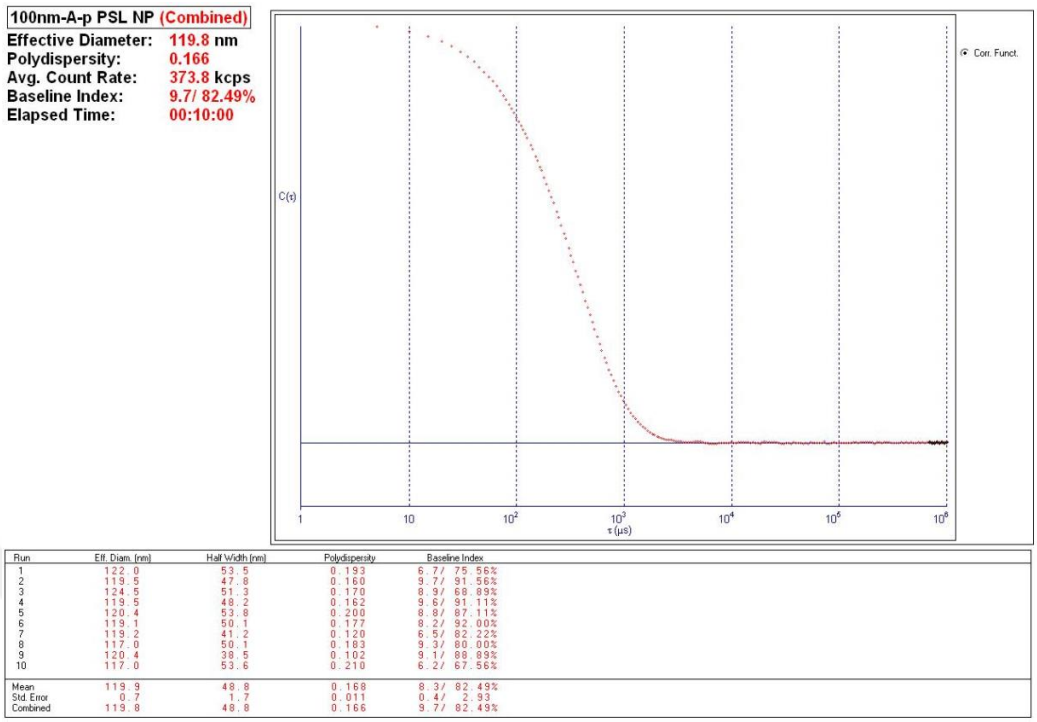

Figure A.20. Effective diameter and polydispersity values of 50nm-A-p PSL NPs obtained from DLS analysis.

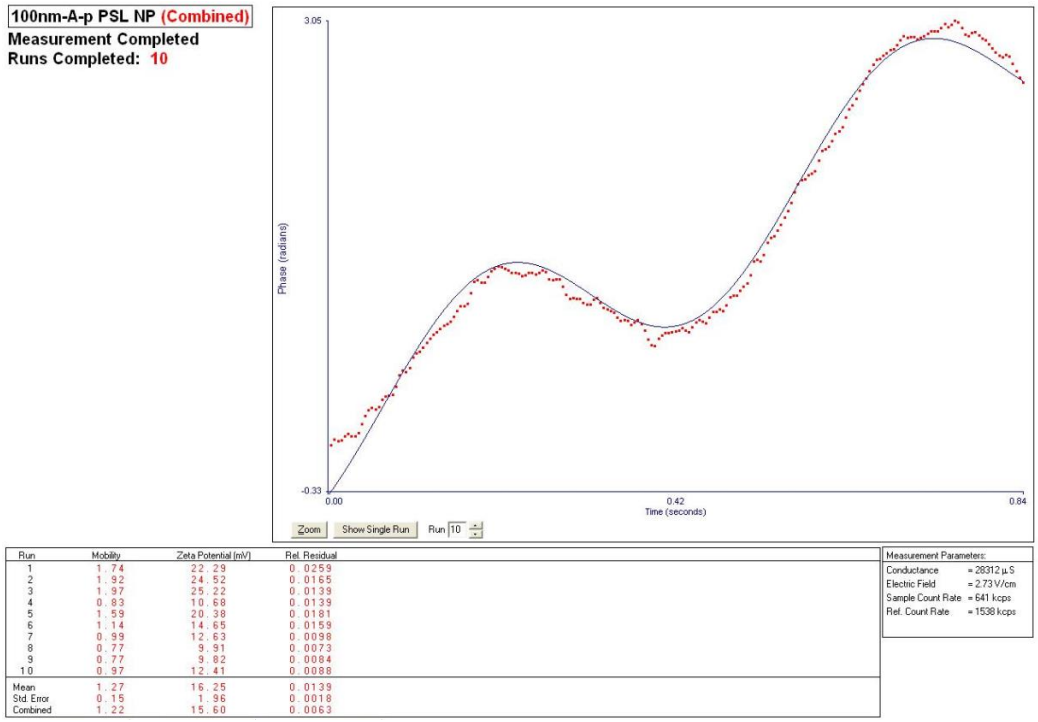

Figure A.21. Zeta potential of 100nm-A-n PSL NPs obtained from ELS analysis.

A.7. Results of DLS and Zeta Potential Analyses for 100nm-A-n PSL NPs

Sample ID	100nm Amine no FI (Combined)
Operator ID	BBGU
Elapsed Time	00:10:00
Mean Diam.	105.7 nm
Rel. Var.	0.000
Skew	-0.022

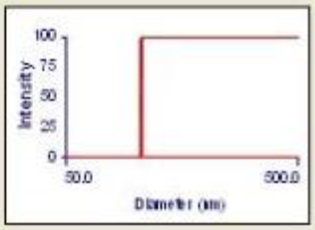

d(nm)	G(d)	C(d)	d(nm)	G(d)	C(d)	d(nm)	G(d)	C(d)
102.4	0	0	104.6	0	0	106.9	0	100
102.6	0	0	104.8	0	0	107.1	0	100
102.8	0	0	105.0	3	1	107.3	0	100
103.0	0	0	105.3	37	13	107.6	0	100
103.2	0	0	105.5	72	36	107.8	0	100
103.4	0	0	105.7	100	69	108.0	0	100
103.6	0	0	105.9	65	90	108.2	0	100
103.8	0	0	106.1	31	100	108.4	0	100
104.0	0	0	106.3	0	100	108.6	0	100
104.2	0	0	106.5	0	100	108.8	0	100
104.4	0	0	106.7	0	100	109.1	0	100

Figure A.22. Intensity distribution of 100nm-A-n PSL NPs obtained from DLS analysis.

Sample ID	100nm Amine no FI (Combined)
Operator ID	BBGU
Elapsed Time	00:10:00
Mean Diam.	105.6 nm
Rel. Var.	0.000
Skew	-0.015

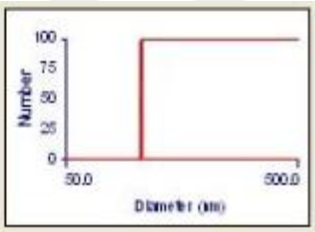

d(nm)	G(d)	C(d)	d(nm)	G(d)	C(d)	d(nm)	G(d)	C(d)
102.4	0	0	104.6	0	0	106.9	0	100
102.6	0	0	104.8	0	0	107.1	0	100
102.8	0	0	105.0	3	1	107.3	0	100
103.0	0	0	105.3	38	13	107.6	0	100
103.2	0	0	105.5	73	37	107.8	0	100
103.4	0	0	105.7	100	69	108.0	0	100
103.6	0	0	105.9	64	90	108.2	0	100
103.8	0	0	106.1	30	100	108.4	0	100
104.0	0	0	106.3	0	100	108.6	0	100
104.2	0	0	106.5	0	100	108.8	0	100
104.4	0	0	106.7	0	100	109.1	0	100

Figure A.23. Number distribution of 100nm-A-n PSL NPs obtained from DLS analysis.

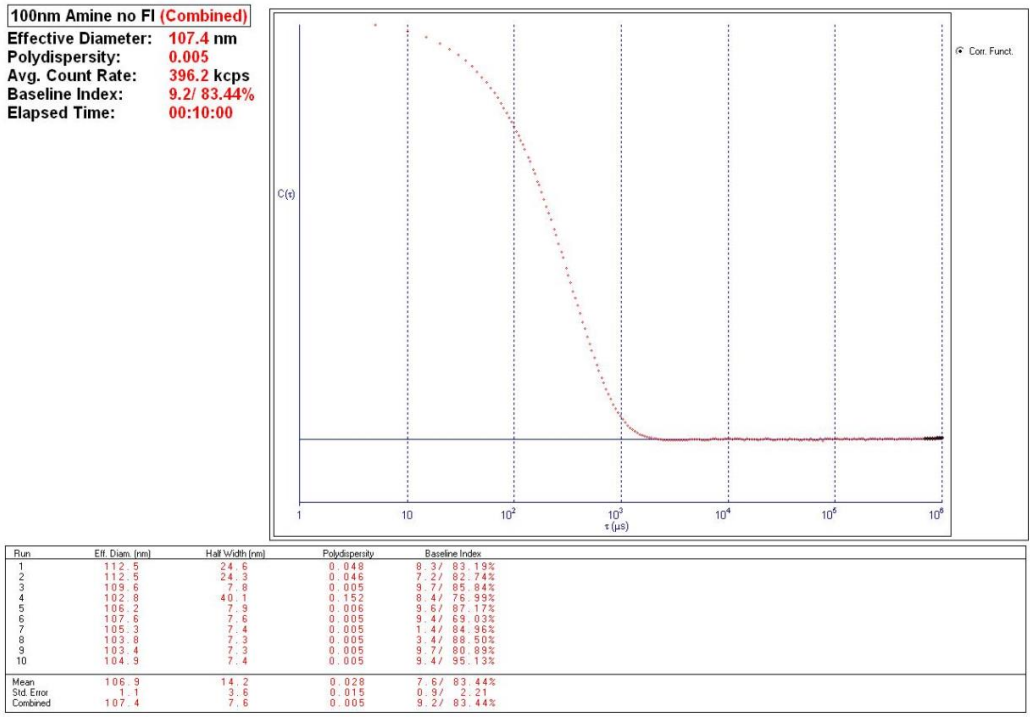

Figure A.24. Effective diameter and polydispersity values of 100nm-A-n PSL NPs obtained from DLS analysis.

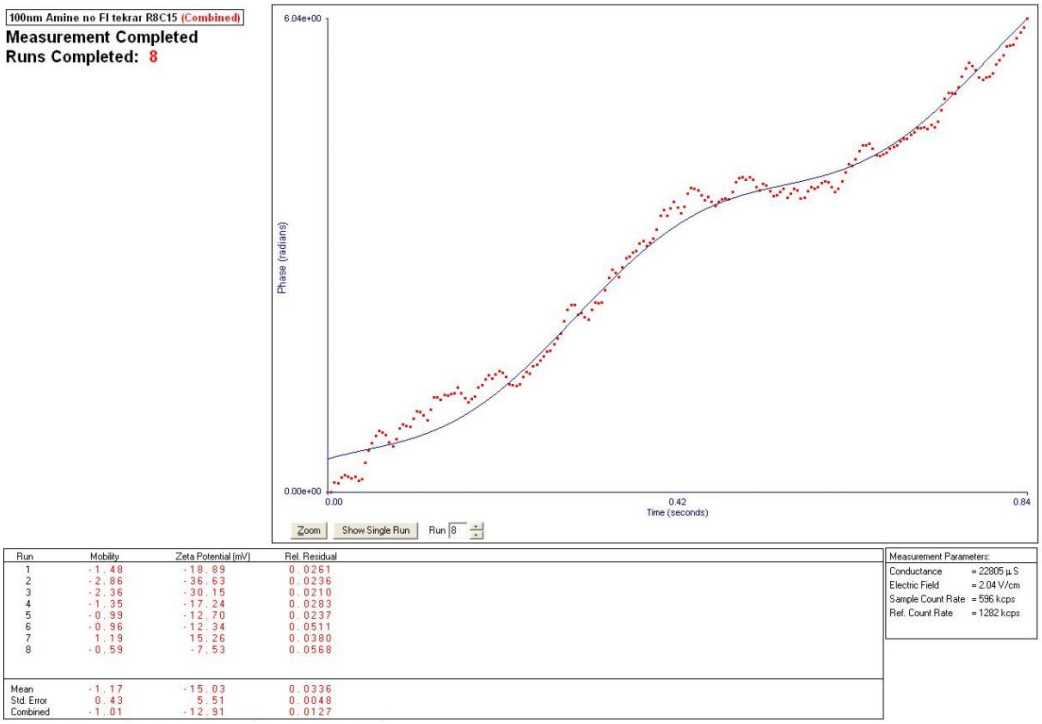

Figure A.25. Zeta potential of 100nm-A-n PSL NPs obtained from ELS analysis.

A.8. Results of DLS and Zeta Potential Analyses for 200nm-A-n PSL NPs

Sample ID	200nm Amine (Combined)
Operator ID	BBGU
Elapsed Time	00:09:00
Mean Diam.	183.1 nm
Rel. Var.	0.086
Skew	0.669

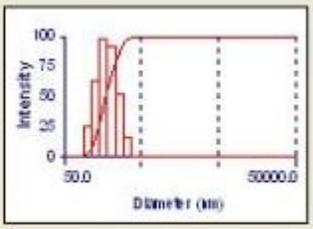

d(nm)	G(d)	C(d)	d(nm)	G(d)	C(d)	d(nm)	G(d)	C(d)
6.5	0	0	80.9	0	0	1009.0	0	100
8.2	0	0	101.8	24	7	1269.1	0	100
10.3	0	0	128.0	64	25	1596.3	0	100
12.9	0	0	161.1	100	54	2007.8	0	100
16.3	0	0	202.6	92	80	2525.4	0	100
20.4	0	0	254.8	52	95	3176.4	0	100
25.7	0	0	320.5	16	100	3995.3	0	100
32.3	0	0	403.1	0	100	5025.3	0	100
40.7	0	0	507.0	0	100	6320.9	0	100
51.2	0	0	637.8	0	100	7950.4	0	100
64.3	0	0	802.2	0	100	10000.0	0	100

Intensity

Figure A.26. Intensity distribution of 200nm-A-n PSL NPs obtained from DLS analysis.

Sample ID	200nm Amine (Combined)
Operator ID	BBGU
Elapsed Time	00:09:00
Mean Diam.	126.8 nm
Rel. Var.	0.063
Skew	1.891

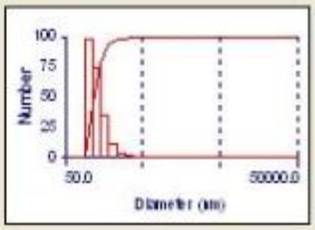

d(nm)	G(d)	C(d)	d(nm)	G(d)	C(d)	d(nm)	G(d)	C(d)
6.5	0	0	80.9	0	0	1009.0	0	100
8.2	0	0	101.8	100	45	1269.1	0	100
10.3	0	0	128.0	74	78	1596.3	0	100
12.9	0	0	161.1	34	94	2007.8	0	100
16.3	0	0	202.6	11	99	2525.4	0	100
20.4	0	0	254.8	3	100	3176.4	0	100
25.7	0	0	320.5	1	100	3995.3	0	100
32.3	0	0	403.1	0	100	5025.3	0	100
40.7	0	0	507.0	0	100	6320.9	0	100
51.2	0	0	637.8	0	100	7950.4	0	100
64.3	0	0	802.2	0	100	10000.0	0	100

Number

Figure A.27. Number distribution of 200nm-A-n PSL NPs obtained from DLS analysis.

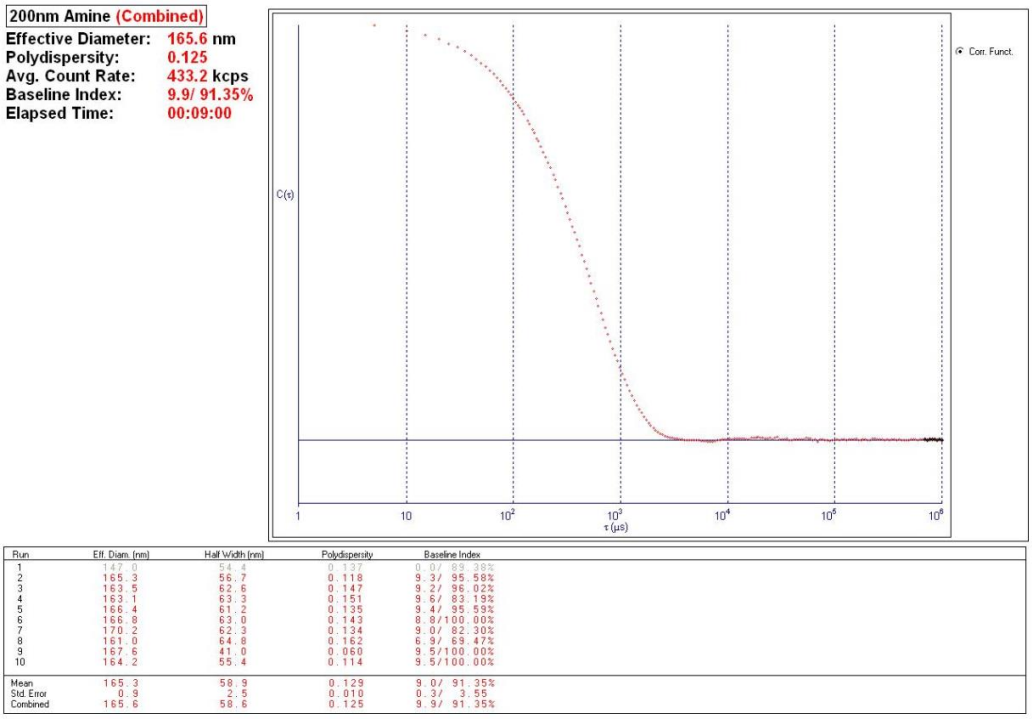

Run	Eff. Diam. (nm)	Half Width (nm)	Polydispersity	Baseline Index
1	147.0	54.4	0.137	0.0/ 89.38%
2	165.3	56.7	0.118	9.3/ 95.58%
3	163.5	62.6	0.147	9.2/ 96.02%
4	163.1	63.3	0.151	9.6/ 83.19%
5	166.4	61.2	0.135	9.4/ 95.59%
6	166.8	63.0	0.143	8.8/100.00%
7	170.2	62.3	0.134	9.0/ 82.30%
8	161.0	64.8	0.162	6.9/ 69.47%
9	167.6	41.0	0.060	9.5/100.00%
10	164.2	55.4	0.114	9.5/100.00%
Mean	165.3	58.9	0.129	9.0/ 91.35%
Std. Error	0.9	2.5	0.010	0.3/ 3.55
Combined	165.6	58.6	0.125	9.9/ 91.35%

Figure A.28. Effective diameter and polydispersity values of 200nm-A-n PSL NPs obtained from DLS analysis.

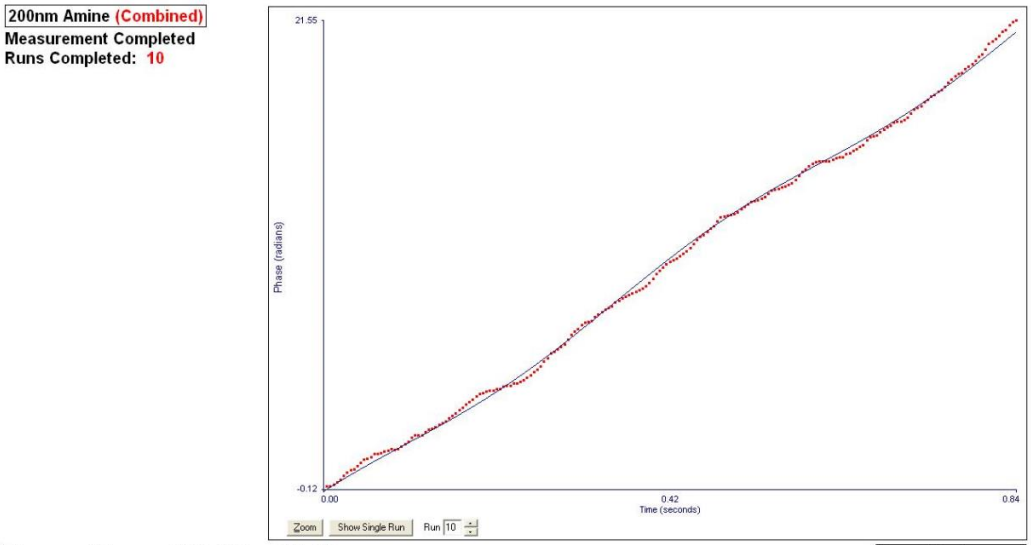

Run	Mobility	Zeta Potential (mV)	Rel. Residual
1	-2.86	-36.59	0.0458
2	1.65	21.06	0.0369
3	-2.56	-32.73	0.0444
4	-2.71	-34.68	0.0567
5	-0.26	-3.35	0.0274
6	-2.82	-36.15	0.0727
7	-3.37	-43.19	0.0295
8	-1.80	-23.07	0.0461
9	-3.74	-47.83	0.0307
10	-1.08	-13.77	0.0445
Mean	-1.96	-25.03	0.0435
Std. Error	0.52	6.65	0.0043
Combined	-1.37	-17.59	0.0143

Measurement Parameters:	
Conductance	= 30651 µS
Electric Field	= 1.79 V/cm
Sample Count Rate	= 638 kcps
Ref. Count Rate	= 1409 kcps

Figure A.29. Zeta potential of 200nm-A-n PSL NPs obtained from ELS analysis.

A.9. Results of DLS and Zeta Potential Analyses for DOPC Liposomes

Sample ID	Liposome 08/10 (Combined)
Operator ID	BBGU
Elapsed Time	00:10:00
Mean Diam.	164.8 nm
Rel. Var.	0.064
Skew	-2.223

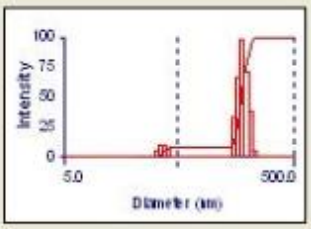

d(nm)	G(d)	C(d)	d(nm)	G(d)	C(d)	d(nm)	G(d)	C(d)
22.8	0	0	55.7	0	8	136.3	0	8
24.7	0	0	60.4	0	8	147.9	34	18
26.8	0	0	65.5	0	8	160.4	68	38
29.1	0	0	71.1	0	8	174.0	100	67
31.5	4	1	77.1	0	8	188.7	72	88
34.2	9	4	83.7	0	8	204.7	37	99
37.1	8	6	90.8	0	8	222.1	5	100
40.2	6	8	98.5	0	8	240.9	0	100
43.6	0	8	106.8	0	8	261.3	0	100
47.3	0	8	115.8	0	8	283.5	0	100
51.4	0	8	125.7	0	8	307.5	0	100

Figure A.30. Intensity distribution of DOPC liposomes obtained from DLS analysis.

Sample ID	Liposome 08/10 (Combined)
Operator ID	BBGU
Elapsed Time	00:10:00
Mean Diam.	34.8 nm
Rel. Var.	0.027
Skew	18.601

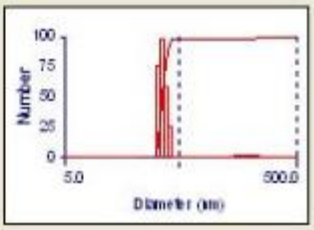

d(nm)	G(d)	C(d)	d(nm)	G(d)	C(d)	d(nm)	G(d)	C(d)
22.8	0	0	55.7	0	100	136.3	0	100
24.7	0	0	60.4	0	100	147.9	0	100
26.8	0	0	65.5	0	100	160.4	0	100
29.1	0	0	71.1	0	100	174.0	0	100
31.5	77	29	77.1	0	100	188.7	0	100
34.2	100	68	83.7	0	100	204.7	0	100
37.1	59	90	90.8	0	100	222.1	0	100
40.2	25	100	98.5	0	100	240.9	0	100
43.6	0	100	106.8	0	100	261.3	0	100
47.3	0	100	115.8	0	100	283.5	0	100
51.4	0	100	125.7	0	100	307.5	0	100

Figure A.31. Number distribution of DOPC liposomes obtained from DLS analysis.

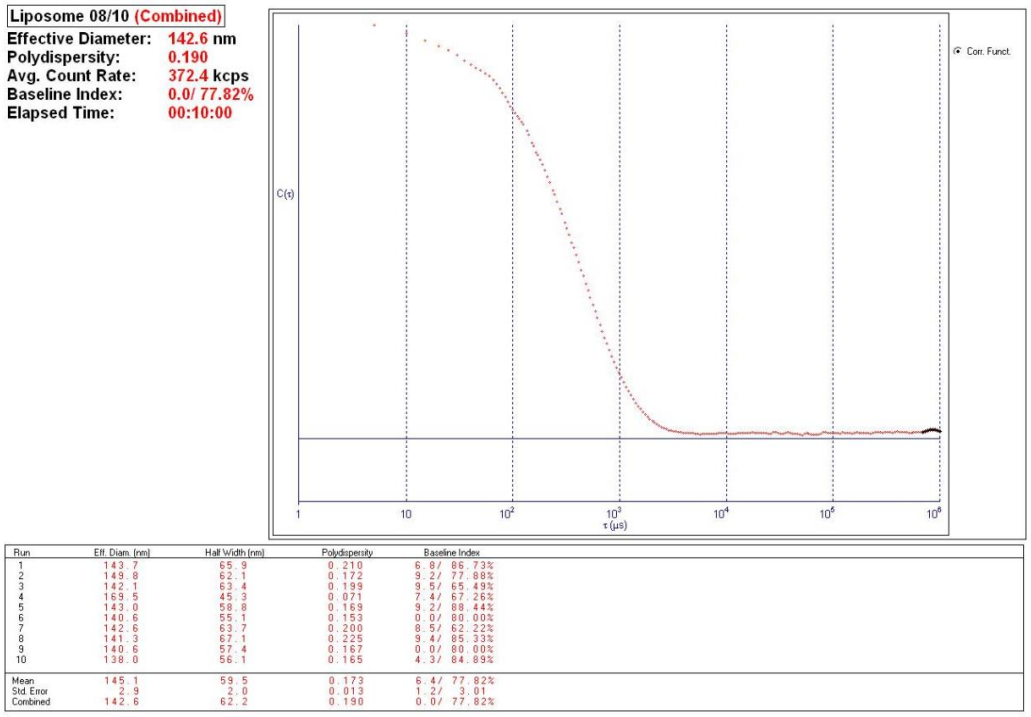

Figure A.32. Effective diameter and polydispersity values of DOPC liposomes obtained from DLS analysis.

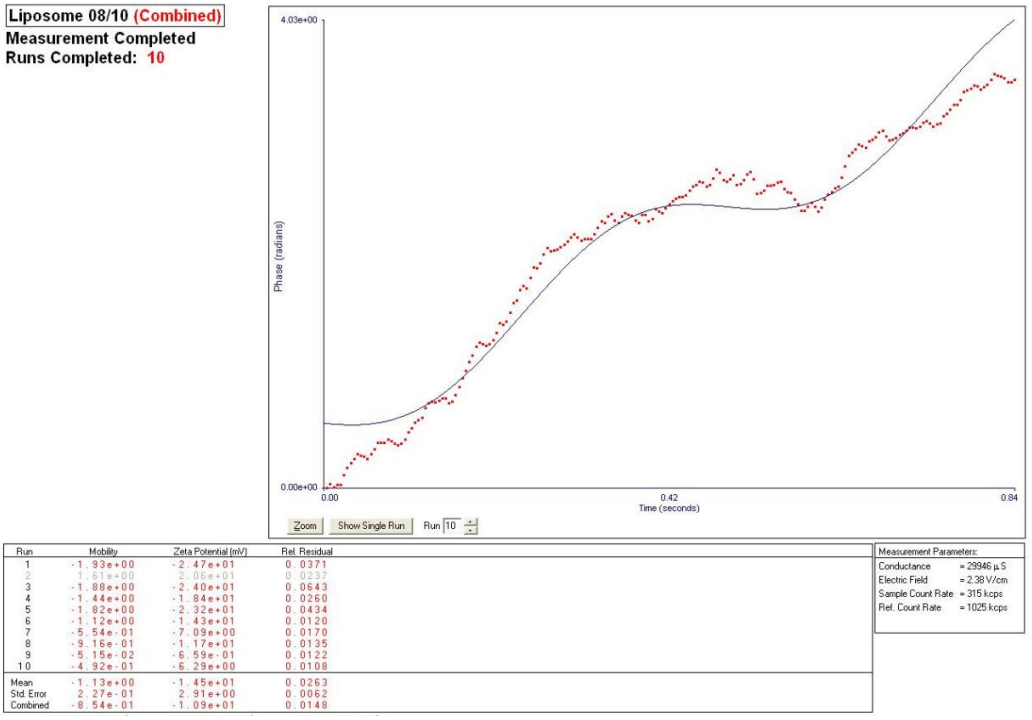

Figure A.33. Zeta potential of DOPC liposomes obtained from ELS analysis.

A.10. Results of DLS and Zeta Potential Analyses for Fluorescein Dye Loaded DOPC Liposomes

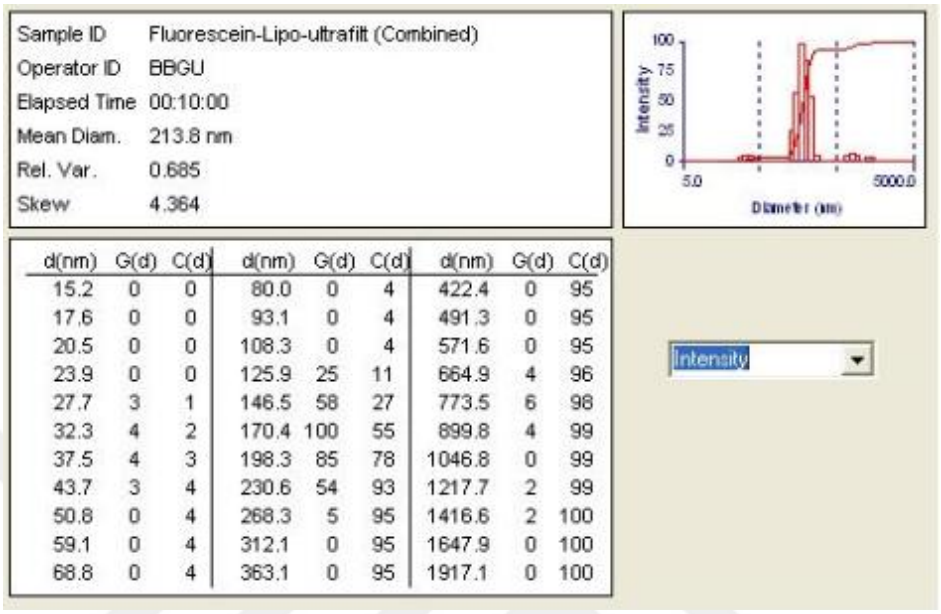

Sample ID	Fluorescein-Lipo-ultrafilt (Combined)
Operator ID	BBGU
Elapsed Time	00:10:00
Mean Diam.	213.8 nm
Rel. Var.	0.685
Skew	4.364

d(nm)	G(d)	C(d)	d(nm)	G(d)	C(d)	d(nm)	G(d)	C(d)
15.2	0	0	80.0	0	4	422.4	0	95
17.6	0	0	93.1	0	4	491.3	0	95
20.5	0	0	108.3	0	4	571.6	0	95
23.9	0	0	125.9	25	11	664.9	4	96
27.7	3	1	146.5	58	27	773.5	6	98
32.3	4	2	170.4	100	55	899.8	4	99
37.5	4	3	198.3	85	78	1046.8	0	99
43.7	3	4	230.6	54	93	1217.7	2	99
50.8	0	4	268.3	5	95	1416.6	2	100
59.1	0	4	312.1	0	95	1647.9	0	100
68.8	0	4	363.1	0	95	1917.1	0	100

Figure A.34. Intensity distribution of fluorescein loaded and ultra-filtrated DOPC liposomes obtained from DLS analysis.

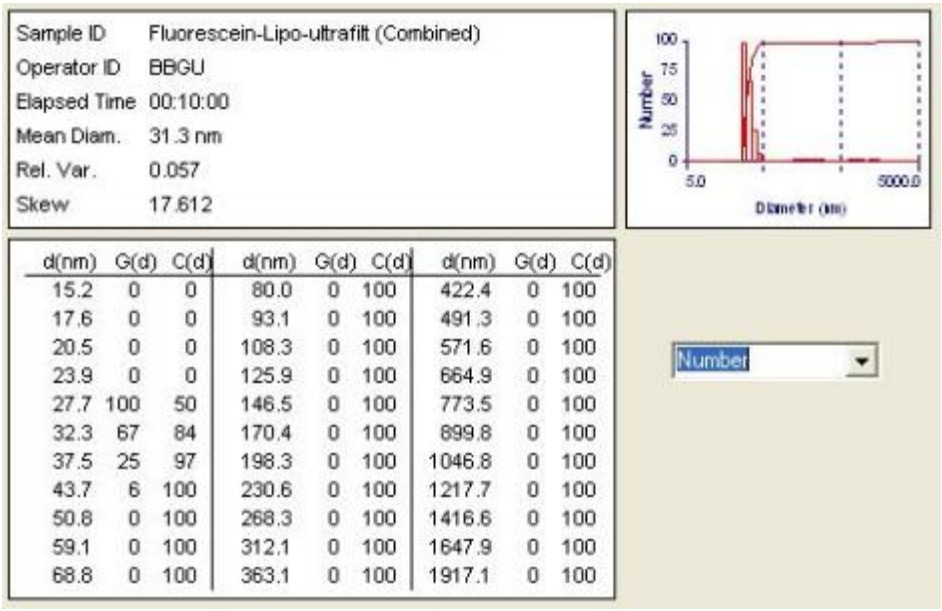

Sample ID	Fluorescein-Lipo-ultrafilt (Combined)
Operator ID	BBGU
Elapsed Time	00:10:00
Mean Diam.	31.3 nm
Rel. Var.	0.057
Skew	17.612

d(nm)	G(d)	C(d)	d(nm)	G(d)	C(d)	d(nm)	G(d)	C(d)
15.2	0	0	80.0	0	100	422.4	0	100
17.6	0	0	93.1	0	100	491.3	0	100
20.5	0	0	108.3	0	100	571.6	0	100
23.9	0	0	125.9	0	100	664.9	0	100
27.7	100	50	146.5	0	100	773.5	0	100
32.3	67	84	170.4	0	100	899.8	0	100
37.5	25	97	198.3	0	100	1046.8	0	100
43.7	6	100	230.6	0	100	1217.7	0	100
50.8	0	100	268.3	0	100	1416.6	0	100
59.1	0	100	312.1	0	100	1647.9	0	100
68.8	0	100	363.1	0	100	1917.1	0	100

Figure A.35. Number distribution of fluorescein loaded and ultra-filtrated DOPC liposomes obtained from DLS analysis.

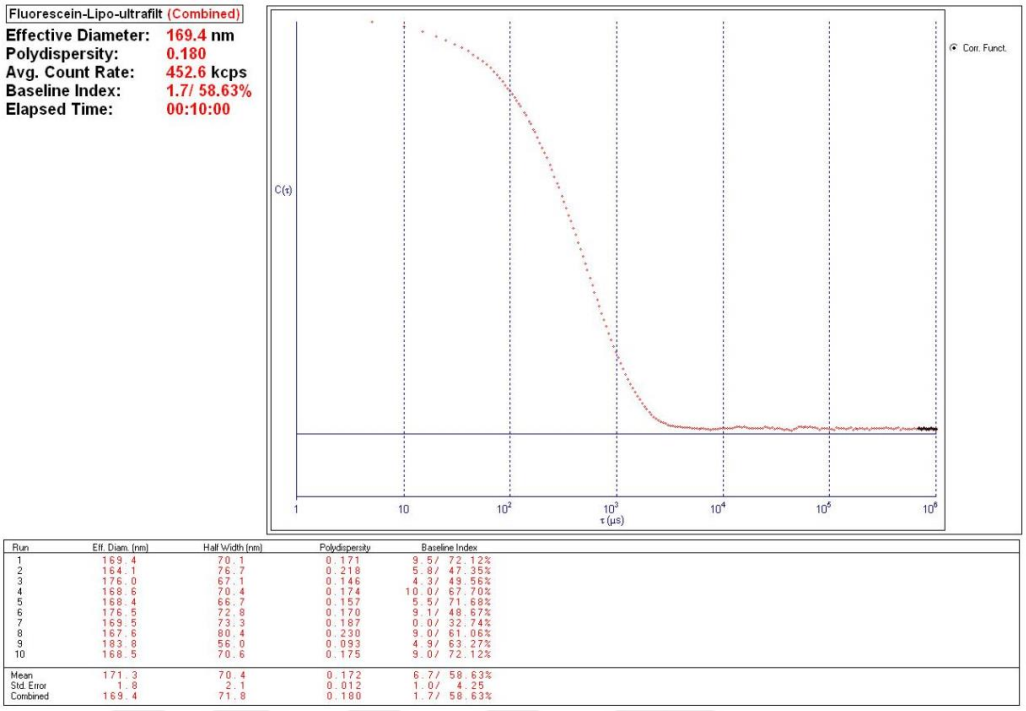

Figure A.36. Effective diameter and polydispersity values of fluorescein loaded and ultra-filtrated DOPC liposomes obtained from DLS analysis.

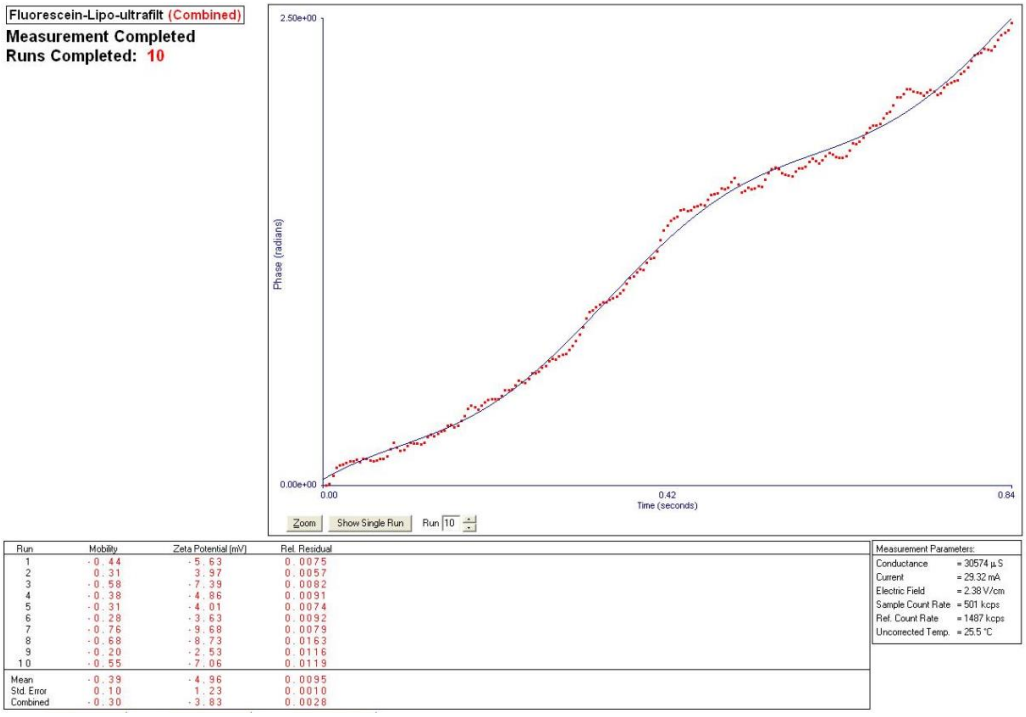

Figure A.37. Zeta potential of fluorescein loaded and ultra-filtrated DOPC liposomes obtained from ELS analysis.

A.11. Results of DLS and Zeta Potential Analyses for DOPC Liposome Encapsulated 20nm-C-n Hybrid NPs

Sample ID	Lipo-20nm carboxyl 50mgL10.05 (Combined)
Operator ID	BBGU
Elapsed Time	00:09:00
Mean Diam.	149.9 nm
Rel. Var.	0.189
Skew	-0.580

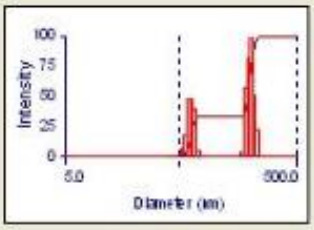

d(nm)	G(d)	C(d)	d(nm)	G(d)	C(d)	d(nm)	G(d)	C(d)
40.0	0	0	78.9	0	34	155.9	0	34
42.5	0	0	84.0	0	34	165.9	3	35
45.2	0	0	89.3	0	34	176.4	57	47
48.1	0	0	95.0	0	34	187.7	83	64
51.2	6	1	101.1	0	34	199.7	100	85
54.4	17	5	107.5	0	34	212.4	50	95
57.9	48	15	114.4	0	34	226.0	22	100
61.6	48	25	121.7	0	34	240.4	0	100
65.6	39	33	129.5	0	34	255.8	0	100
69.7	3	34	137.8	0	34	272.1	0	100
74.2	0	34	146.5	0	34	289.5	0	100

Figure A.38. Intensity distribution of liposome encapsulated 20nm-C-n hybrid NPs obtained from DLS analysis.

Sample ID	Lipo-20nm carboxyl 50mgL10.05 (Combined)
Operator ID	BBGU
Elapsed Time	00:09:00
Mean Diam.	59.1 nm
Rel. Var.	0.020
Skew	11.924

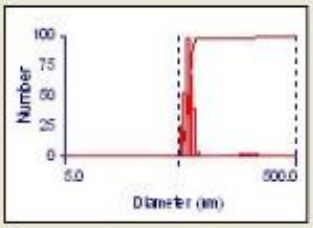

d(nm)	G(d)	C(d)	d(nm)	G(d)	C(d)	d(nm)	G(d)	C(d)
40.0	0	0	78.9	0	100	155.9	0	100
42.5	0	0	84.0	0	100	165.9	0	100
45.2	0	0	89.3	0	100	176.4	0	100
48.1	0	0	95.0	0	100	187.7	0	100
51.2	26	9	101.1	0	100	199.7	0	100
54.4	52	27	107.5	0	100	212.4	0	100
57.9	100	61	114.4	0	100	226.0	0	100
61.6	69	85	121.7	0	100	240.4	0	100
65.6	39	99	129.5	0	100	255.8	0	100
69.7	2	100	137.8	0	100	272.1	0	100
74.2	0	100	146.5	0	100	289.5	0	100

Figure A.39. Number distribution of liposome encapsulated 20nm-C-n hybrid NPs obtained from DLS analysis.

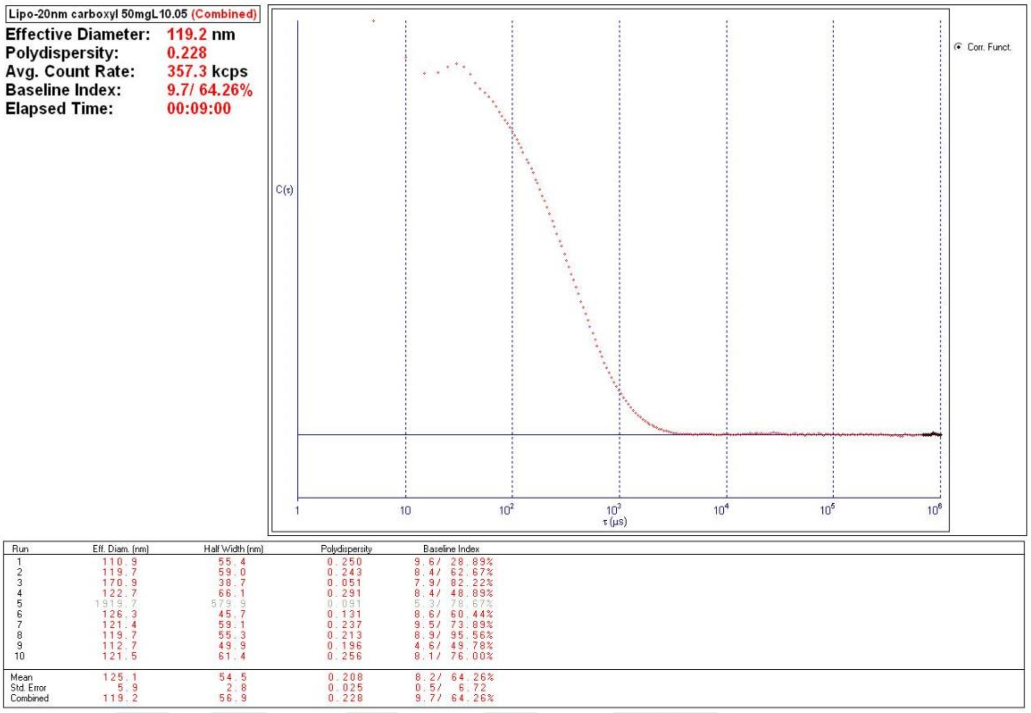

Figure A.40. Effective diameter and polydispersity values 20nm-C-n hybrid NPs obtained from DLS analysis.

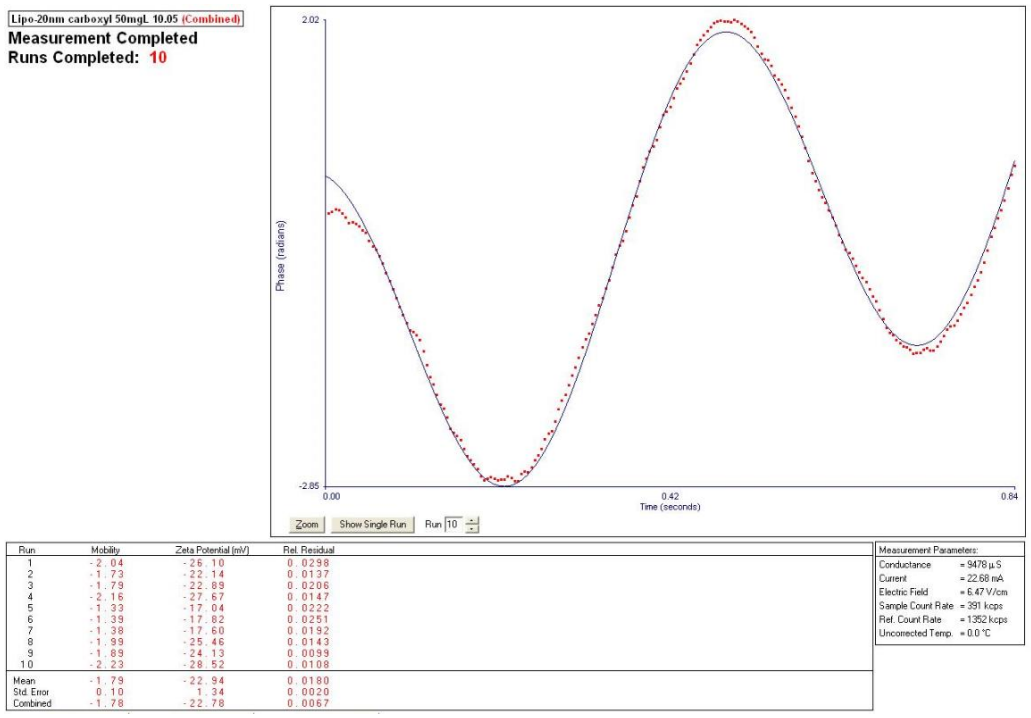

Figure A.41. Zeta potential of liposome encapsulated 20nm-C-n hybrid NPs obtained from ELS analysis.

A.12. Results of DLS and Zeta Potential Analyses for DOPC Liposome Encapsulated 30nm-C-n Hybrid NPs

Sample ID	30nm-C-Hyb (Combined)
Operator ID	BBGU
Elapsed Time	00:10:00
Mean Diam.	142.9 nm
Rel. Var.	0.093
Skew	-1.653

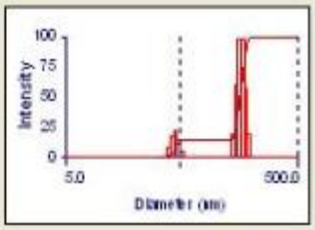

d(nm)	G(d)	C(d)	d(nm)	G(d)	C(d)	d(nm)	G(d)	C(d)
30.2	0	0	60.3	0	15	120.7	0	15
32.1	0	0	64.3	0	15	128.5	0	15
34.2	0	0	68.4	0	15	136.9	18	20
36.4	0	0	72.9	0	15	145.8	60	34
38.8	7	2	77.6	0	15	155.3	100	58
41.3	17	6	82.7	0	15	165.4	99	82
44.0	21	11	88.1	0	15	176.1	58	96
46.9	14	14	93.8	0	15	187.6	18	100
49.9	4	15	99.9	0	15	199.8	0	100
53.2	0	15	106.4	0	15	212.8	0	100
56.6	0	15	113.3	0	15	226.6	0	100

Figure A.42. Intensity distribution of liposome encapsulated 30nm-C-n hybrid NPs obtained from DLS analysis.

Sample ID	30nm-C-Hyb (Combined)
Operator ID	BBGU
Elapsed Time	00:10:00
Mean Diam.	42.9 nm
Rel. Var.	0.028
Skew	13.513

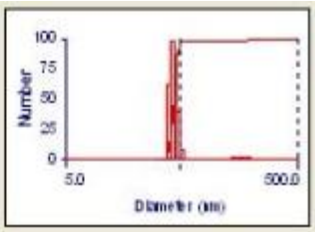

d(nm)	G(d)	C(d)	d(nm)	G(d)	C(d)	d(nm)	G(d)	C(d)
30.2	0	0	60.3	0	100	120.7	0	100
32.1	0	0	64.3	0	100	128.5	0	100
34.2	0	0	68.4	0	100	136.9	0	100
36.4	0	0	72.9	0	100	145.8	0	100
38.8	62	21	77.6	0	100	155.3	0	100
41.3	100	55	82.7	0	100	165.4	0	100
44.0	88	84	88.1	0	100	176.1	0	100
46.9	39	97	93.8	0	100	187.6	0	100
49.9	8	100	99.9	0	100	199.8	0	100
53.2	0	100	106.4	0	100	212.8	0	100
56.6	0	100	113.3	0	100	226.6	0	100

Figure A.43. Number distribution of liposome encapsulated 30nm-C-n hybrid NPs obtained from DLS analysis.

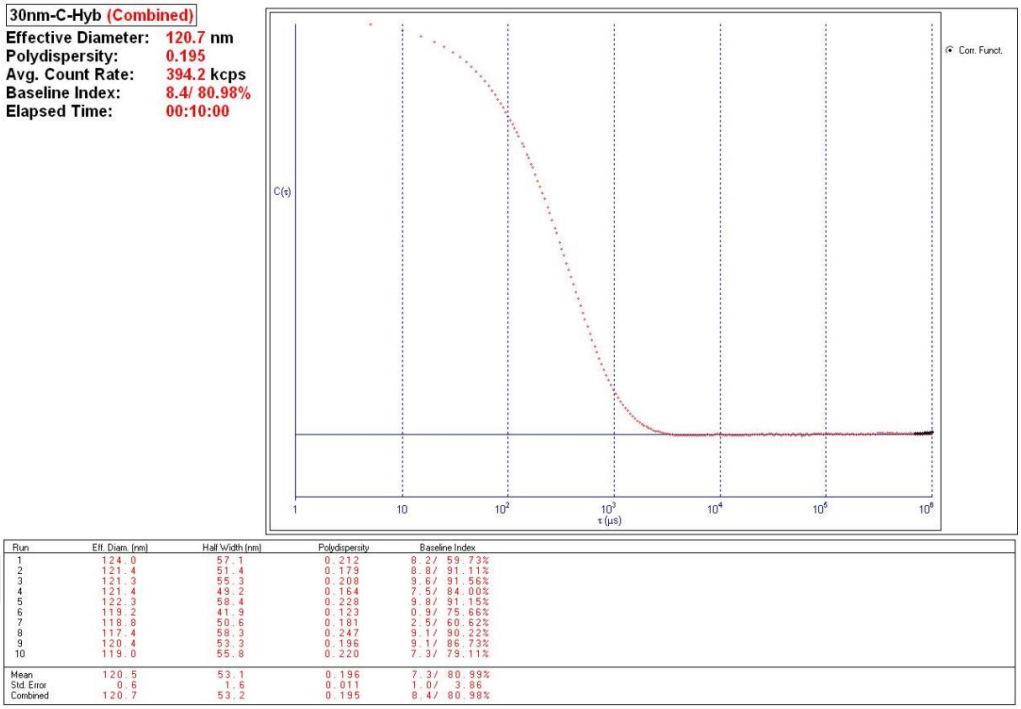

Run	Eff. Diam. (nm)	Half Width (nm)	Polydispersity	Baseline Index
1	124.0	57.1	0.212	8.2/ 59.73%
2	121.4	51.4	0.179	8.8/ 91.11%
3	121.3	55.3	0.208	9.6/ 91.56%
4	121.4	49.2	0.164	7.5/ 84.00%
5	122.3	58.4	0.228	9.8/ 91.15%
6	119.2	41.9	0.123	0.9/ 75.66%
7	118.8	50.6	0.181	2.5/ 60.62%
8	117.4	58.3	0.247	9.1/ 90.22%
9	120.4	53.3	0.196	9.1/ 86.73%
10	119.0	55.8	0.220	7.3/ 79.11%
Mean	120.5	53.1	0.196	7.3/ 80.99%
Std. Error	0.6	1.6	0.011	1.0/ 3.86
Combined	120.7	53.2	0.195	8.4/ 80.98%

Figure A.44. Effective diameter and polydispersity values 30nm-C-n hybrid NPs obtained from DLS analysis.

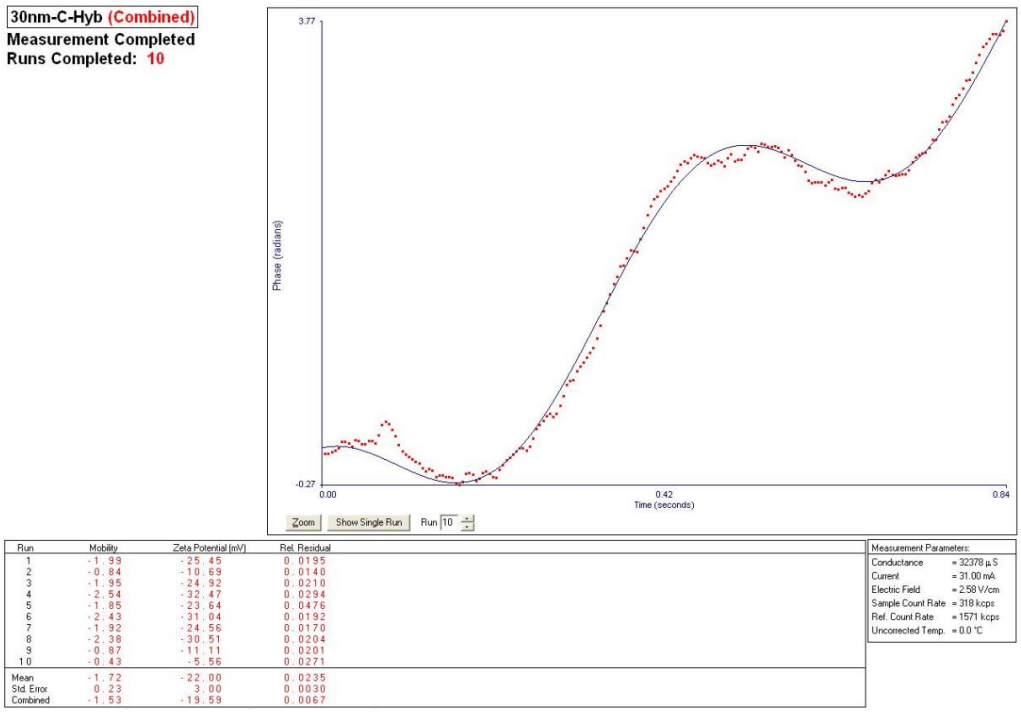

Run	Mobility	Zeta Potential (mV)	Rel. Residual
1	-1.99	-25.45	0.0195
2	-0.84	-10.69	0.0140
3	-1.95	-24.92	0.0210
4	-2.54	-32.47	0.0294
5	-1.85	-23.64	0.0476
6	-2.43	-31.04	0.0192
7	-1.92	-24.56	0.0170
8	-2.38	-30.51	0.0204
9	-0.87	-11.11	0.0201
10	-0.43	-5.56	0.0271
Mean	-1.72	-22.00	0.0235
Std. Error	0.23	3.00	0.0030
Combined	-1.53	-19.59	0.0067

Measurement Parameters:	
Conductance	= 32378 µS
Current	= 31.00 mA
Electric Field	= 2.58 V/cm
Sample Count Rate	= 318 kcps
Ref. Count Rate	= 1571 kcps
Uncorrected Temp.	= 0.0 °C

Figure A.45. Zeta potential of liposome encapsulated 30nm-C-n hybrid NPs obtained from ELS analysis.

A.13. Results of DLS and Zeta Potential Analyses for DOPC Liposome Encapsulated 50nm-A-p Hybrid NPs

Sample ID	50nm-A-Hyb (Combined)
Operator ID	BBGU
Elapsed Time	00:10:00
Mean Diam.	252.8 nm
Rel. Var.	0.106
Skew	-1.700

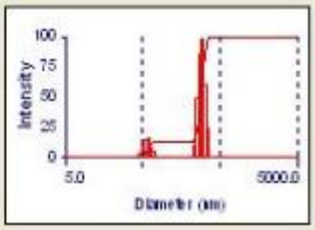

d(nm)	G(d)	C(d)	d(nm)	G(d)	C(d)	d(nm)	G(d)	C(d)
36.2	0	0	87.2	0	14	210.2	0	14
39.2	0	0	94.4	0	14	227.7	9	16
42.4	0	0	102.3	0	14	246.7	49	29
46.0	2	1	110.8	0	14	267.3	86	51
49.8	10	3	120.1	0	14	289.5	100	78
53.9	13	7	130.1	0	14	313.6	61	94
58.4	15	10	140.9	0	14	339.8	24	100
63.3	7	12	152.6	0	14	368.1	0	100
68.6	5	14	165.4	0	14	398.7	0	100
74.3	0	14	179.1	0	14	432.0	0	100
80.5	0	14	194.1	0	14	467.9	0	100

Figure A.46. Intensity distribution of liposome encapsulated 50nm-A-p hybrid NPs obtained from DLS analysis.

Sample ID	50nm-A-Hyb (Combined)
Operator ID	BBGU
Elapsed Time	00:10:00
Mean Diam.	53.8 nm
Rel. Var.	0.040
Skew	16.480

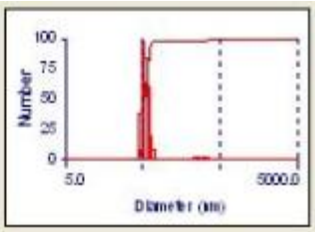

d(nm)	G(d)	C(d)	d(nm)	G(d)	C(d)	d(nm)	G(d)	C(d)
36.2	0	0	87.2	0	100	210.2	0	100
39.2	0	0	94.4	0	100	227.7	0	100
42.4	0	0	102.3	0	100	246.7	0	100
46.0	37	12	110.8	0	100	267.3	0	100
49.8	100	44	120.1	0	100	289.5	0	100
53.9	85	72	130.1	0	100	313.6	0	100
58.4	60	91	140.9	0	100	339.8	0	100
63.3	19	97	152.6	0	100	368.1	0	100
68.6	8	100	165.4	0	100	398.7	0	100
74.3	0	100	179.1	0	100	432.0	0	100
80.5	0	100	194.1	0	100	467.9	0	100

Figure A.47. Number distribution of liposome encapsulated 50nm-A-p hybrid NPs obtained from DLS analysis.

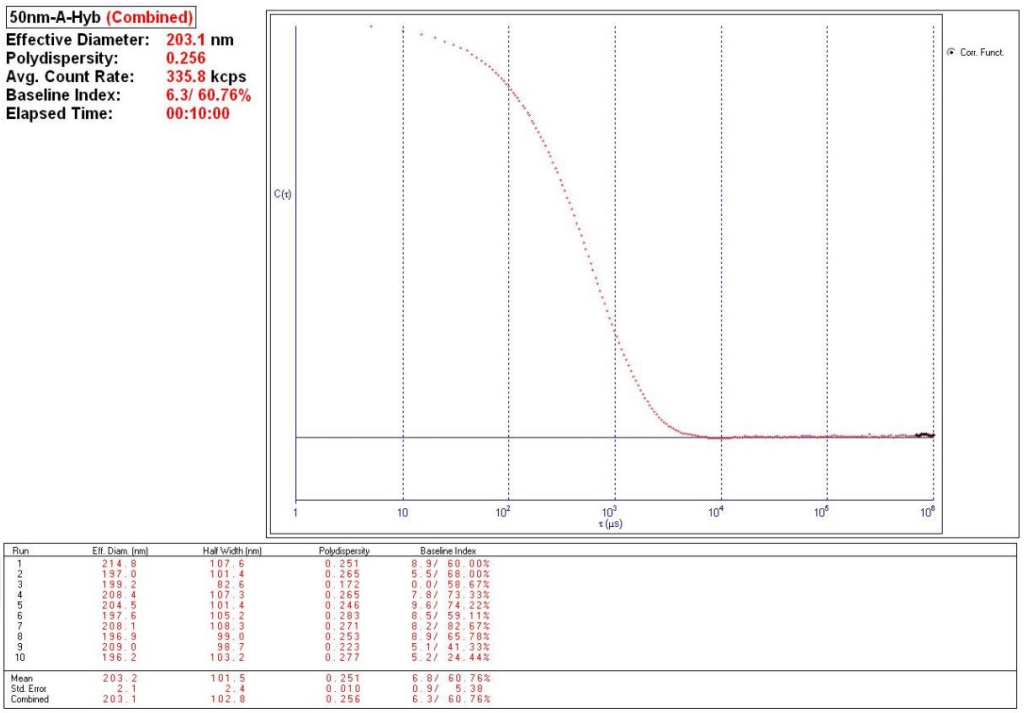

Run	Eff. Diam. (nm)	Half Width (nm)	Polydispersity	Baseline Index
1	214.8	107.6	0.251	8.9/ 60.00%
2	197.0	101.4	0.265	5.5/ 68.00%
3	199.2	82.6	0.172	0.0/ 58.67%
4	208.4	107.3	0.265	7.8/ 73.33%
5	204.5	101.4	0.246	9.6/ 74.22%
6	197.6	105.2	0.283	8.5/ 59.11%
7	208.1	108.3	0.271	8.2/ 82.67%
8	196.9	99.0	0.253	8.9/ 65.78%
9	209.0	98.7	0.223	5.1/ 41.33%
10	196.2	103.2	0.277	5.2/ 24.44%
Mean	203.2	101.5	0.251	6.8/ 60.76%
Std. Error	2.1	2.4	0.010	0.9/ 5.38
Combined	203.1	102.8	0.256	6.3/ 60.76%

Figure A.48. Effective diameter and polydispersity values of liposome encapsulated 50nm-A-p hybrid NPs obtained from DLS analysis.

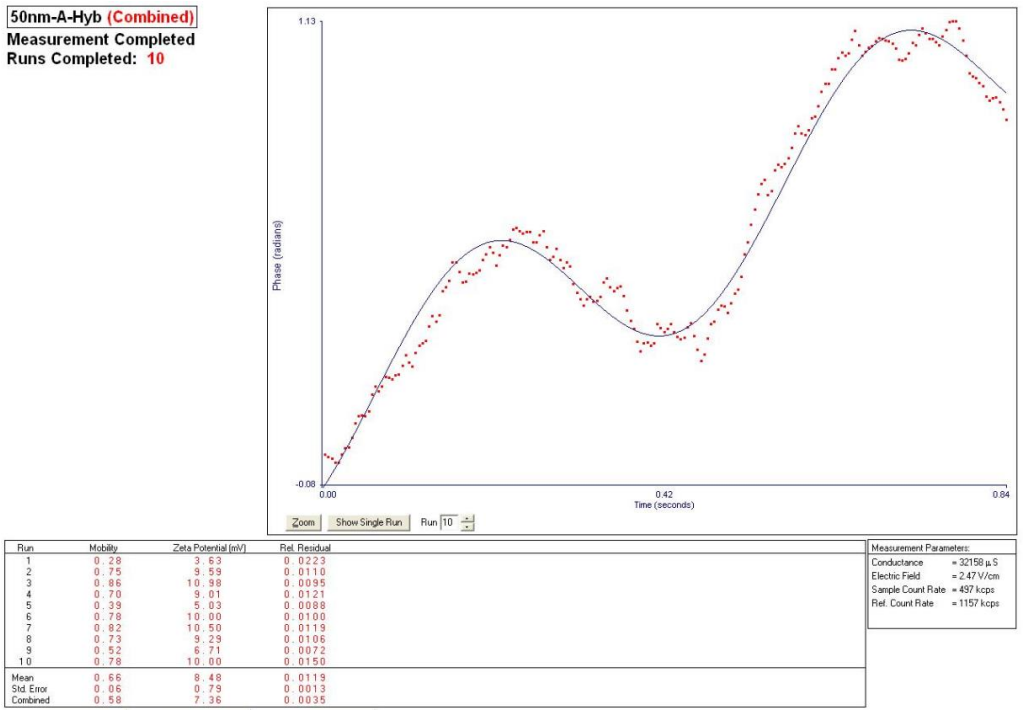

Run	Mobility	Zeta Potential (mV)	Rel. Residual
1	0.28	3.63	0.0223
2	0.75	9.59	0.0110
3	0.86	10.98	0.0095
4	0.70	9.01	0.0121
5	0.39	5.03	0.0088
6	0.78	10.00	0.0100
7	0.82	10.50	0.0119
8	0.73	9.29	0.0106
9	0.52	6.71	0.0072
10	0.78	10.00	0.0150
Mean	0.66	8.48	0.0119
Std. Error	0.06	0.79	0.0013
Combined	0.58	7.36	0.0035

Figure A.49. Zeta potential of liposome encapsulated 50nm-A-p hybrid NPs obtained from ELS analysis.

A.14. Results of DLS and Zeta Potential Analyses for DOPC Liposome Encapsulated 100nm-A-p Hybrid NPs

Sample ID	100nm-A-p Hybrid (Combined)
Operator ID	BBGU
Elapsed Time	00:10:00
Mean Diam.	183.1 nm
Rel. Var.	0.066
Skew	-2.187

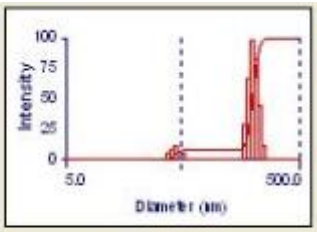

d(nm)	G(d)	C(d)	d(nm)	G(d)	C(d)	d(nm)	G(d)	C(d)
27.4	0	0	62.5	0	9	142.5	0	9
29.5	0	0	67.3	0	9	153.6	0	9
31.8	0	0	72.6	0	9	165.6	28	16
34.3	0	0	78.2	0	9	178.5	66	35
37.0	4	1	84.3	0	9	192.3	100	62
39.8	7	3	90.9	0	9	207.3	83	85
42.9	11	6	98.0	0	9	223.5	44	97
46.3	6	8	105.6	0	9	240.9	10	100
49.9	4	9	113.8	0	9	259.6	0	100
53.8	0	9	122.7	0	9	279.8	0	100
58.0	0	9	132.2	0	9	301.6	0	100

Intensity

Figure A.50. Intensity distribution of liposome encapsulated 100nm-A-p hybrid NPs obtained from DLS analysis.

Sample ID	100nm-A-p Hybrid (Combined)
Operator ID	BBGU
Elapsed Time	00:10:00
Mean Diam.	41.2 nm
Rel. Var.	0.034
Skew	15.865

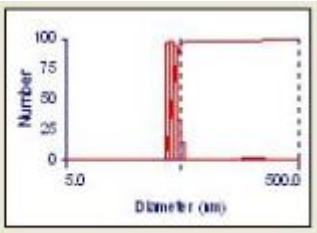

d(nm)	G(d)	C(d)	d(nm)	G(d)	C(d)	d(nm)	G(d)	C(d)
27.4	0	0	62.5	0	100	142.5	0	100
29.5	0	0	67.3	0	100	153.6	0	100
31.8	0	0	72.6	0	100	165.6	0	100
34.3	0	0	78.2	0	100	178.5	0	100
37.0	97	29	84.3	0	100	192.3	0	100
39.8	100	58	90.9	0	100	207.3	0	100
42.9	96	86	98.0	0	100	223.5	0	100
46.3	34	96	105.6	0	100	240.9	0	100
49.9	14	100	113.8	0	100	259.6	0	100
53.8	0	100	122.7	0	100	279.8	0	100
58.0	0	100	132.2	0	100	301.6	0	100

Number

Figure A.51. Number distribution of liposome encapsulated 100nm-A-p hybrid NPs obtained from DLS analysis.

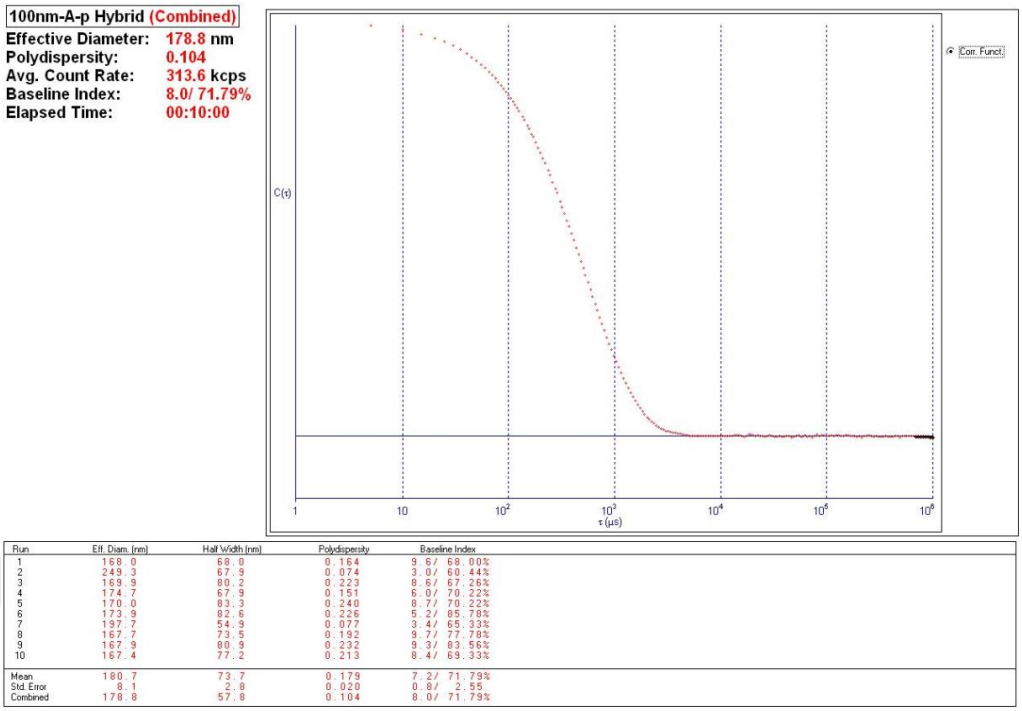

Run	Eff. Diam. (nm)	Half Width (nm)	Polydispersity	Baseline Index
1	168.0	68.0	0.164	9.6/ 68.00%
2	249.3	67.9	0.074	3.0/ 60.44%
3	169.9	80.2	0.223	8.6/ 67.26%
4	174.7	67.9	0.151	6.0/ 70.22%
5	170.0	83.3	0.240	8.7/ 70.22%
6	173.9	82.6	0.226	5.2/ 85.78%
7	197.7	54.9	0.077	3.4/ 65.33%
8	167.7	73.5	0.192	9.7/ 77.78%
9	167.9	80.9	0.232	9.3/ 83.56%
10	167.4	77.2	0.213	8.4/ 69.33%
Mean	180.7	73.7	0.179	7.2/ 71.79%
Std. Error	8.1	2.8	0.020	0.8/ 2.55
Combined	178.8	57.8	0.104	8.0/ 71.79%

Figure A.52. Effective diameter and polydispersity values of liposome encapsulated 100nm-A-p hybrid NPs obtained from DLS analysis.

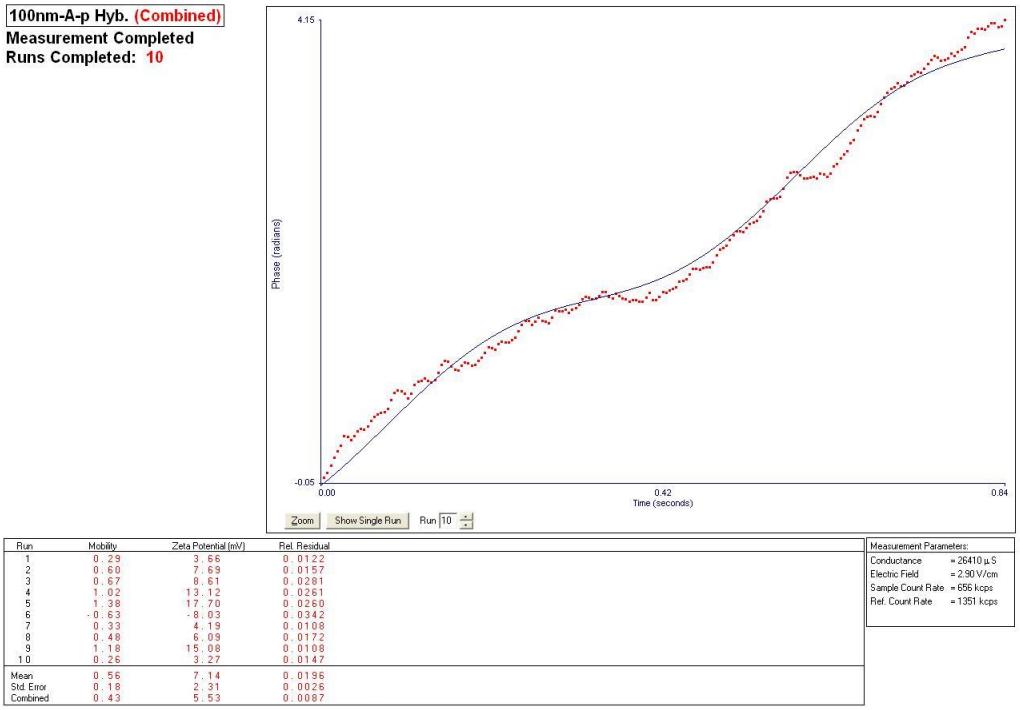

Run	Mobility	Zeta Potential (mV)	Rel. Residual
1	0.29	3.66	0.0122
2	0.60	7.69	0.0157
3	0.67	8.61	0.0281
4	1.02	13.12	0.0261
5	1.38	17.70	0.0260
6	-0.63	-8.03	0.0342
7	0.33	4.19	0.0108
8	0.48	6.09	0.0172
9	1.18	15.08	0.0108
10	0.26	3.27	0.0147
Mean	0.56	7.14	0.0196
Std. Error	0.18	2.31	0.0026
Combined	0.43	5.53	0.0087

Measurement Parameters:	
Conductance	= 26410 µS
Electric Field	= 2.90 V/cm
Sample Count Rate	= 656 kcps
Ref. Count Rate	= 1351 kcps

Figure A.53. Zeta potential of liposome encapsulated 100nm-A-p hybrid NPs obtained from ELS analysis.

A.15. Results of DLS and Zeta Potential Analyses for DOPC Liposome Encapsulated 100nm-A-n Hybrid NPs

Sample ID	100nm-A-Hyb (Combined)
Operator ID	BBGU
Elapsed Time	00:10:00
Mean Diam.	167.0 nm
Rel. Var.	0.030
Skew	-2.850

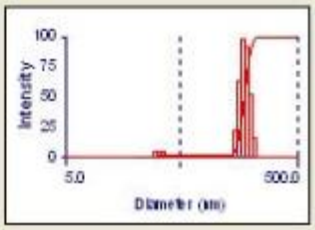

d(nm)	G(d)	C(d)	d(nm)	G(d)	C(d)	d(nm)	G(d)	C(d)
21.5	0	0	50.9	0	3	120.7	0	3
23.2	0	0	55.1	0	3	130.6	0	3
25.1	0	0	59.6	0	3	141.2	22	9
27.2	0	0	64.4	0	3	152.8	64	27
29.4	3	1	69.7	0	3	165.2	100	55
31.8	4	2	75.4	0	3	178.7	93	81
34.4	3	3	81.5	0	3	193.3	52	96
37.2	0	3	88.2	0	3	209.1	16	100
40.2	0	3	95.4	0	3	226.2	0	100
43.5	0	3	103.2	0	3	244.6	0	100
47.1	0	3	111.6	0	3	264.6	0	100

Figure A.54. Intensity distribution of liposome encapsulated 100nm-A-n hybrid NPs obtained from DLS analysis.

Sample ID	100nm-A-Hyb (Combined)
Operator ID	BBGU
Elapsed Time	00:10:00
Mean Diam.	31.5 nm
Rel. Var.	0.045
Skew	18.647

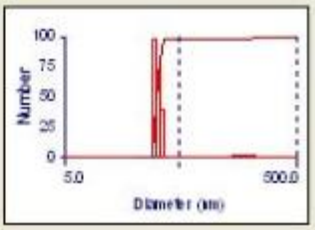

d(nm)	G(d)	C(d)	d(nm)	G(d)	C(d)	d(nm)	G(d)	C(d)
21.5	0	0	50.9	0	100	120.7	0	100
23.2	0	0	55.1	0	100	130.6	0	100
25.1	0	0	59.6	0	100	141.2	0	100
27.2	0	0	64.4	0	100	152.8	0	100
29.4	100	47	69.7	0	100	165.2	0	100
31.8	74	81	75.4	0	100	178.7	0	100
34.4	39	100	81.5	0	100	193.3	0	100
37.2	0	100	88.2	0	100	209.1	0	100
40.2	0	100	95.4	0	100	226.2	0	100
43.5	0	100	103.2	0	100	244.6	0	100
47.1	0	100	111.6	0	100	264.6	0	100

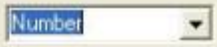

Figure A.55. Number distribution of liposome encapsulated 100nm-A-n hybrid NPs obtained from DLS analysis.

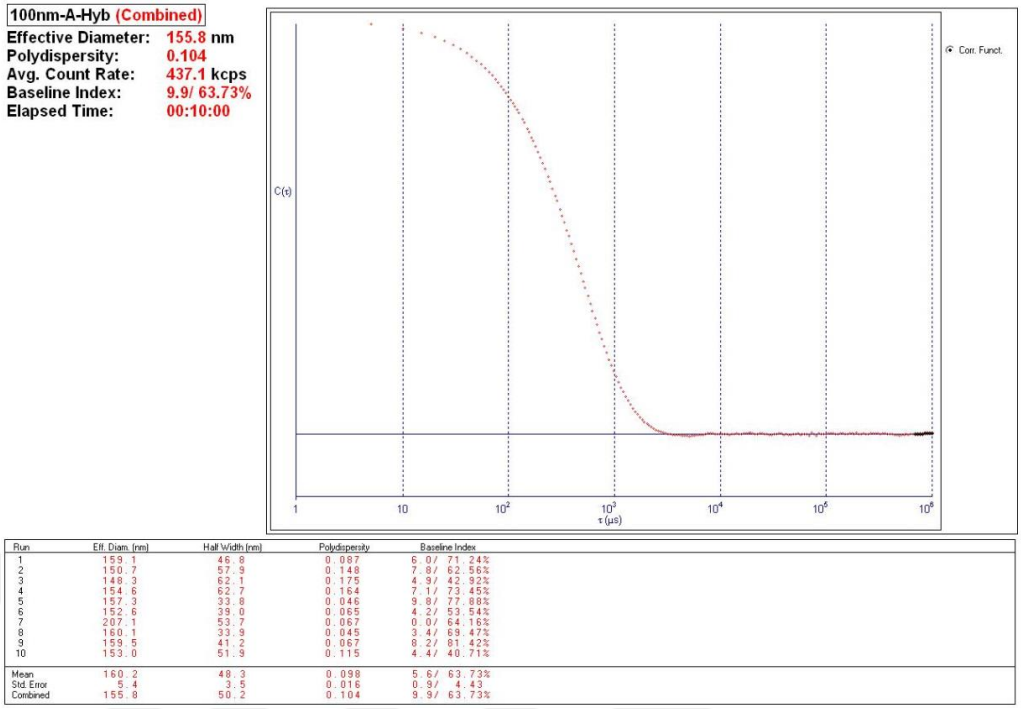

Run	Eff. Diam. (nm)	Half Width (nm)	Polydispersity	Baseline Index
1	159.1	46.8	0.087	6.0/ 71.24%
2	150.7	57.9	0.148	7.0/ 62.56%
3	148.3	62.1	0.175	4.9/ 42.92%
4	154.6	62.7	0.164	7.1/ 73.45%
5	157.3	33.8	0.046	9.8/ 77.88%
6	152.6	39.0	0.065	4.2/ 53.54%
7	207.1	53.7	0.067	0.0/ 64.16%
8	160.1	33.9	0.045	3.4/ 69.47%
9	159.5	41.2	0.067	8.2/ 81.42%
10	153.0	51.9	0.115	4.4/ 40.71%
Mean	160.2	48.3	0.098	5.6/ 63.73%
Std. Error	5.4	3.5	0.016	0.9/ 4.43
Combined	155.8	50.2	0.104	9.9/ 63.73%

Figure A.56. Effective diameter and polydispersity values of liposome encapsulated 100nm-A-n hybrid NPs obtained from DLS analysis.

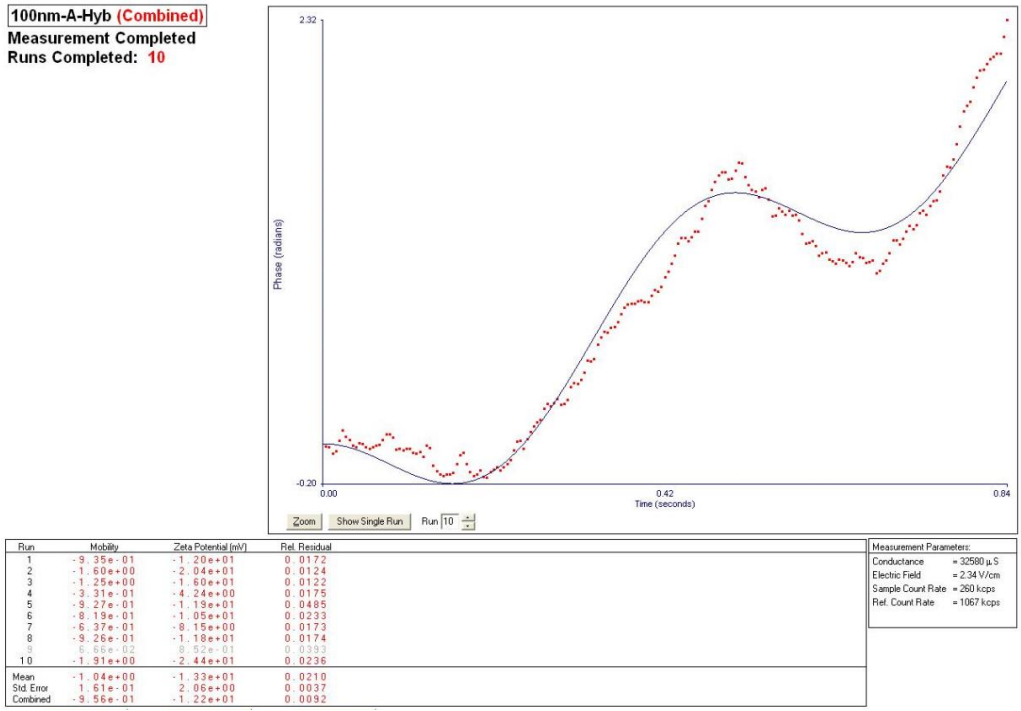

Run	Mobility	Zeta Potential (mV)	Rel. Residual
1	-9.35e-01	-1.20e+01	0.0172
2	-1.60e+00	-2.04e+01	0.0124
3	-1.25e+00	-1.60e+01	0.0122
4	-3.31e-01	-4.24e+00	0.0175
5	-9.27e-01	-1.19e+01	0.0485
6	-8.19e-01	-1.05e+01	0.0233
7	-6.37e-01	-8.15e+00	0.0173
8	-9.26e-01	-1.18e+01	0.0174
9	-6.66e-02	-8.52e-01	0.0393
10	-1.91e+00	-2.44e+01	0.0236
Mean	-1.04e+00	-1.33e+01	0.0210
Std. Error	1.61e-01	2.06e+00	0.0037
Combined	-9.56e-01	-1.22e+01	0.0092

Figure A.57. Zeta potential of liposome encapsulated 100nm-A-n hybrid NPs obtained from ELS analysis.

A.16. Results of DLS and Zeta Potential Analyses for DOPC Liposome Encapsulated and Fluorescein Loaded 30nm-C-n-Fl Hybrid NPs

Sample ID	30nm-C-n Hybrid Fl (Combined)
Operator ID	BBGU
Elapsed Time	00:10:00
Mean Diam.	149.6 nm
Rel. Var.	0.065
Skew	-2.170

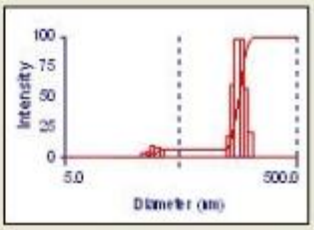

d(nm)	G(d)	C(d)	d(nm)	G(d)	C(d)	d(nm)	G(d)	C(d)
14.3	0	0	37.5	0	8	97.9	0	8
15.6	0	0	40.9	0	8	106.9	0	8
17.1	0	0	44.6	0	8	116.6	0	8
18.6	0	0	48.7	0	8	127.3	17	12
20.3	0	0	53.1	0	8	138.9	61	28
22.2	0	0	58.0	0	8	151.6	98	54
24.2	3	1	63.3	0	8	165.4	100	80
26.4	4	2	69.0	0	8	180.5	57	95
28.8	9	4	75.3	0	8	197.0	19	100
31.4	7	6	82.2	0	8	215.0	0	100
34.3	6	8	89.7	0	8	234.6	0	100

Figure A.58. Intensity distribution of liposome encapsulated 30nm-C-n-Fl hybrid NPs with fluorescein dye obtained from DLS analysis.

Sample ID	30nm-C-n Hybrid Fl (Combined)
Operator ID	BBGU
Elapsed Time	00:10:00
Mean Diam.	27.9 nm
Rel. Var.	0.027
Skew	15.689

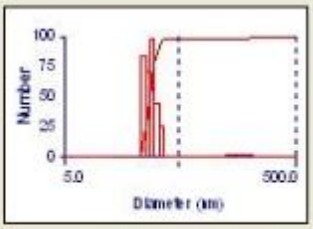

d(nm)	G(d)	C(d)	d(nm)	G(d)	C(d)	d(nm)	G(d)	C(d)
14.3	0	0	37.5	0	100	97.9	0	100
15.6	0	0	40.9	0	100	106.9	0	100
17.1	0	0	44.6	0	100	116.6	0	100
18.6	0	0	48.7	0	100	127.3	0	100
20.3	0	0	53.1	0	100	138.9	0	100
22.2	0	0	58.0	0	100	151.6	0	100
24.2	85	26	63.3	0	100	165.4	0	100
26.4	72	48	69.0	0	100	180.5	0	100
28.8	100	79	75.3	0	100	197.0	0	100
31.4	44	92	82.2	0	100	215.0	0	100
34.3	24	100	89.7	0	100	234.6	0	100

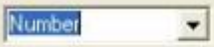

Figure A.59. Number distribution of liposome encapsulated 30nm-C-n-Fl hybrid NPs with fluorescein dye obtained from DLS analysis.

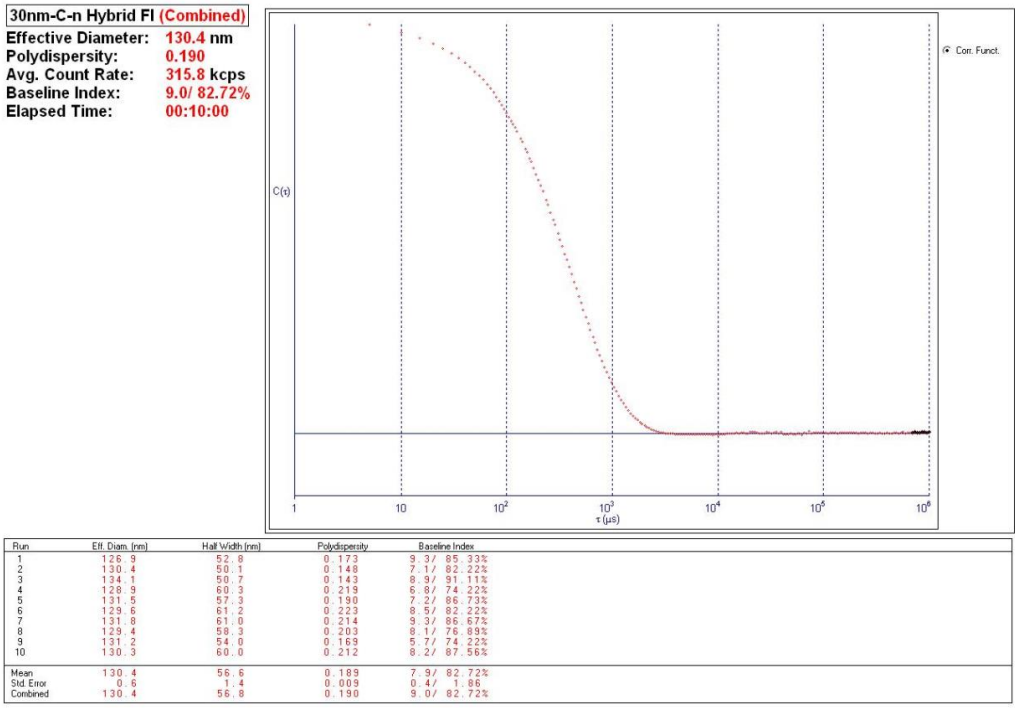

Figure A.60. Effective diameter and polydispersity values of liposome encapsulated 30nm-C-n-Fl hybrid NPs with fluorescein dye obtained from DLS analysis.

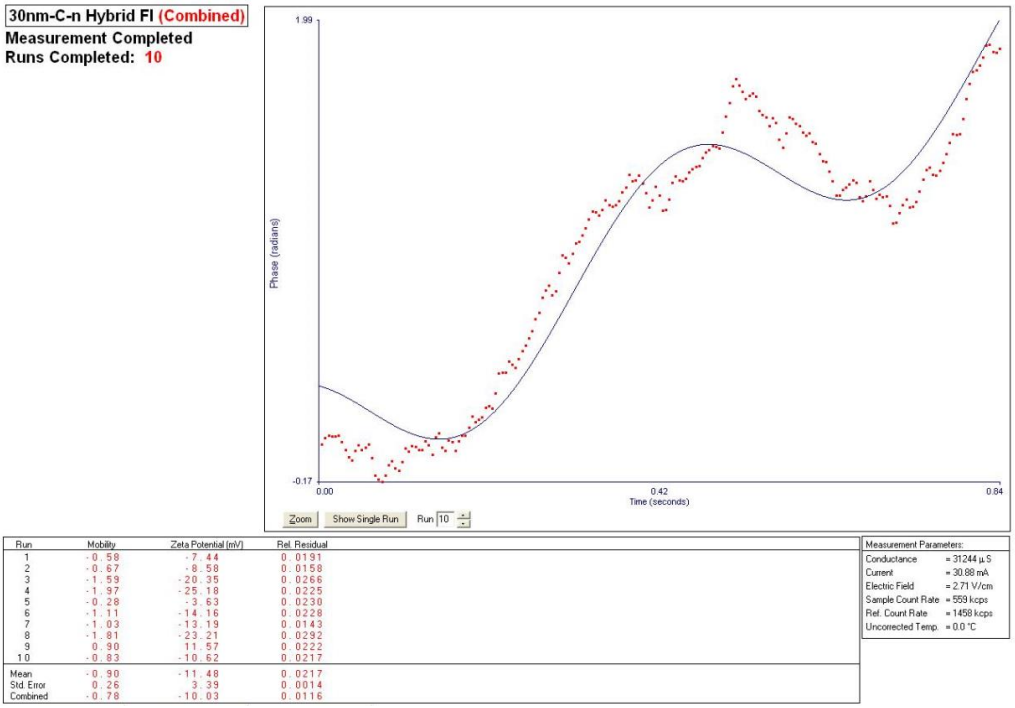

Figure A.61. Zeta potential of liposome encapsulated 30nm-C-n-Fl hybrid NPs with fluorescein dye obtained from ELS analysis.

A.17. Results of DLS and Zeta Potential Analyses for DOPC Liposome Encapsulated and Fluorescein Loaded 50nm-A-p-Fl Hybrid NPs

Sample ID	50nm-A-p Hyb. Fl. (Combined)
Operator ID	BBGU
Elapsed Time	00:10:00
Mean Diam.	315.9 nm
Rel. Var.	0.185
Skew	-0.866

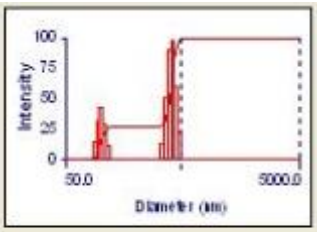

d(nm)	G(d)	C(d)	d(nm)	G(d)	C(d)	d(nm)	G(d)	C(d)
72.6	0	0	150.5	0	28	312.0	0	28
77.5	0	0	160.8	0	28	333.4	11	30
82.8	0	0	171.8	0	28	356.2	51	41
88.5	14	3	183.6	0	28	380.7	91	61
94.6	32	10	196.2	0	28	406.8	100	82
101.1	43	19	209.6	0	28	434.7	60	95
108.0	29	25	224.0	0	28	464.4	21	100
115.4	11	28	239.3	0	28	496.3	0	100
123.3	0	28	255.7	0	28	530.3	0	100
131.8	0	28	273.3	0	28	566.7	0	100
140.8	0	28	292.0	0	28	605.5	0	100

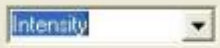

Figure A.62. Intensity distribution of liposome encapsulated 50nm-A-p-Fl hybrid NPs with fluorescein dye obtained from DLS analysis.

Sample ID	50nm-A-p Hyb. Fl. (Combined)
Operator ID	BBGU
Elapsed Time	00:10:00
Mean Diam.	113.1 nm
Rel. Var.	0.370
Skew	4.234

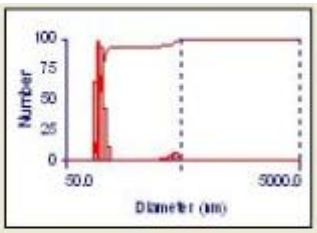

d(nm)	G(d)	C(d)	d(nm)	G(d)	C(d)	d(nm)	G(d)	C(d)
72.6	0	0	150.5	0	95	312.0	0	95
77.5	0	0	160.8	0	95	333.4	0	95
82.8	0	0	171.8	0	95	356.2	1	96
88.5	66	20	183.6	0	95	380.7	2	96
94.6	100	50	196.2	0	95	406.8	4	98
101.1	94	79	209.6	0	95	434.7	6	99
108.0	43	92	224.0	0	95	464.4	2	100
115.4	11	95	239.3	0	95	496.3	0	100
123.3	0	95	255.7	0	95	530.3	0	100
131.8	0	95	273.3	0	95	566.7	0	100
140.8	0	95	292.0	0	95	605.5	0	100

Figure A.63. Number distribution of liposome encapsulated 50nm-A-p-Fl hybrid NPs with fluorescein dye obtained from DLS analysis.

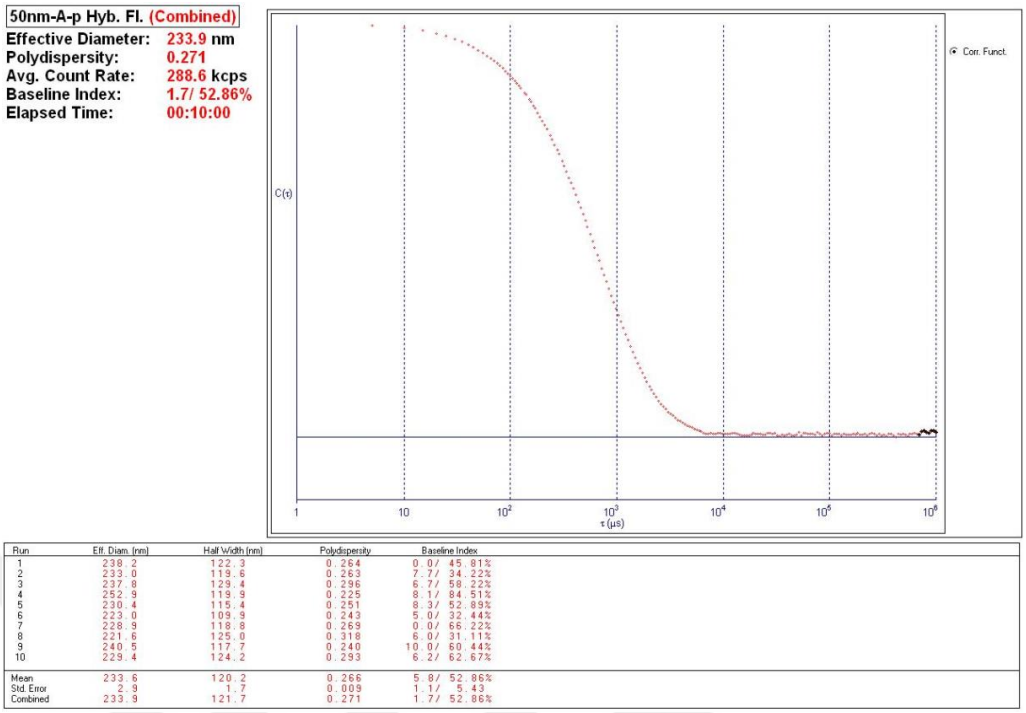

Figure A.64. Effective diameter and polydispersity values of liposome encapsulated 50nm-A-p-Fl hybrid NPs obtained from DLS analysis.

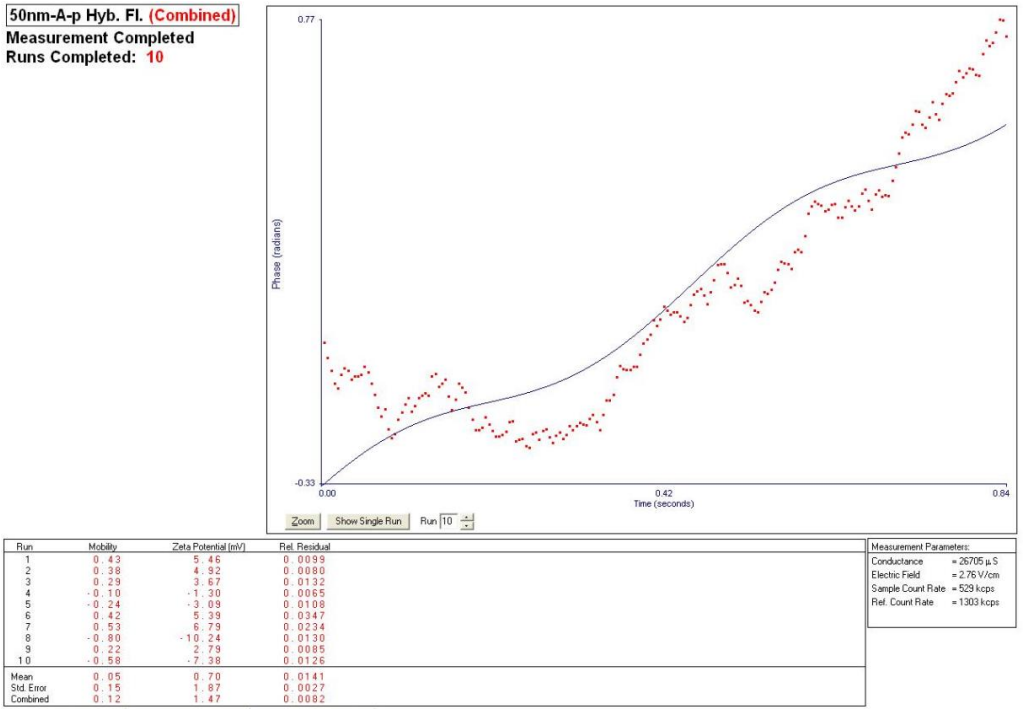

Figure A.65. Zeta potential of liposome encapsulated 50nm-A-p-Fl hybrid NPs with fluorescein dye obtained from ELS analysis.

A.18. Results of DLS and Zeta Potential Analyses for DOPC Liposome Encapsulated and Fluorescein Loaded 100nm-A-n-Fl Hybrid NPs

Sample ID	100nm-A-n Hybrid Fl (Combined)
Operator ID	BBGU
Elapsed Time	00:08:00
Mean Diam.	729.7 nm
Rel. Var.	7.813
Skew	3.464

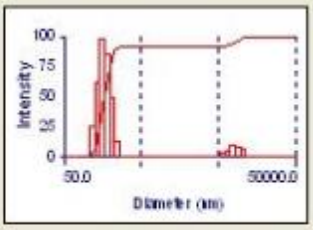

d(nm)	G(d)	C(d)	d(nm)	G(d)	C(d)	d(nm)	G(d)	C(d)
85.7	0	0	440.1	0	93	2259.7	0	93
99.4	0	0	510.6	0	93	2622.1	0	93
115.4	26	7	592.5	0	93	3042.6	0	93
133.9	62	24	687.5	0	93	3530.5	0	93
155.4	100	52	797.8	0	93	4096.7	0	93
180.3	86	76	925.7	0	93	4753.7	0	93
209.2	50	89	1074.2	0	93	5516.0	3	93
242.7	11	93	1246.5	0	93	6400.5	4	95
281.7	0	93	1446.3	0	93	7427.0	8	97
326.8	0	93	1678.3	0	93	8618.0	7	99
379.2	0	93	1947.4	0	93	10000.0	5	100

Figure A.66. Intensity distribution of liposome encapsulated 100nm-A-n-Fl hybrid NPs with fluorescein dye obtained from DLS analysis.

Sample ID	100nm-A-n Hybrid Fl (Combined)
Operator ID	BBGU
Elapsed Time	00:08:00
Mean Diam.	140.6 nm
Rel. Var.	0.034
Skew	32.641

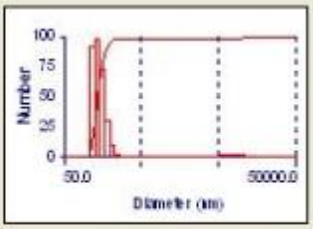

d(nm)	G(d)	C(d)	d(nm)	G(d)	C(d)	d(nm)	G(d)	C(d)
85.7	0	0	440.1	0	100	2259.7	0	100
99.4	0	0	510.6	0	100	2622.1	0	100
115.4	92	30	592.5	0	100	3042.6	0	100
133.9	100	63	687.5	0	100	3530.5	0	100
155.4	73	87	797.8	0	100	4096.7	0	100
180.3	30	97	925.7	0	100	4753.7	0	100
209.2	9	100	1074.2	0	100	5516.0	0	100
242.7	1	100	1246.5	0	100	6400.5	0	100
281.7	0	100	1446.3	0	100	7427.0	0	100
326.8	0	100	1678.3	0	100	8618.0	0	100
379.2	0	100	1947.4	0	100	10000.0	0	100

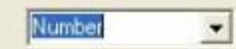

Figure A.67. Number distribution of liposome encapsulated 100nm-A-n-Fl hybrid NPs with fluorescein dye obtained from DLS analysis.

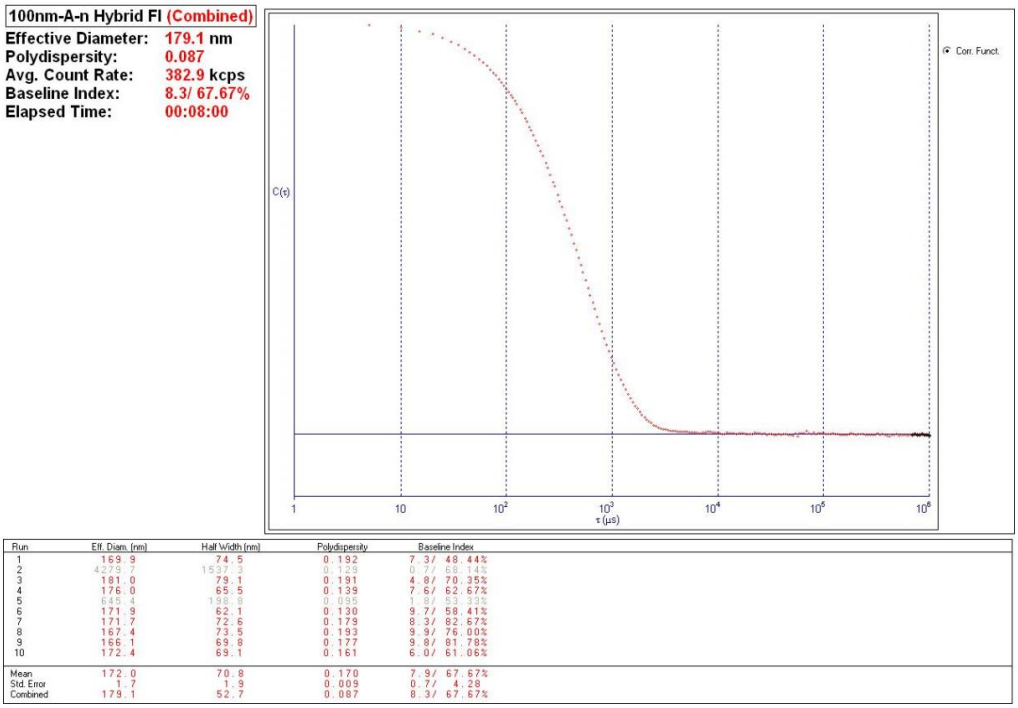

Figure A.68. Effective diameter and polydispersity values of liposome encapsulated 100nm-A-n-Fl hybrid NPs with fluorescein dye obtained from DLS analysis.

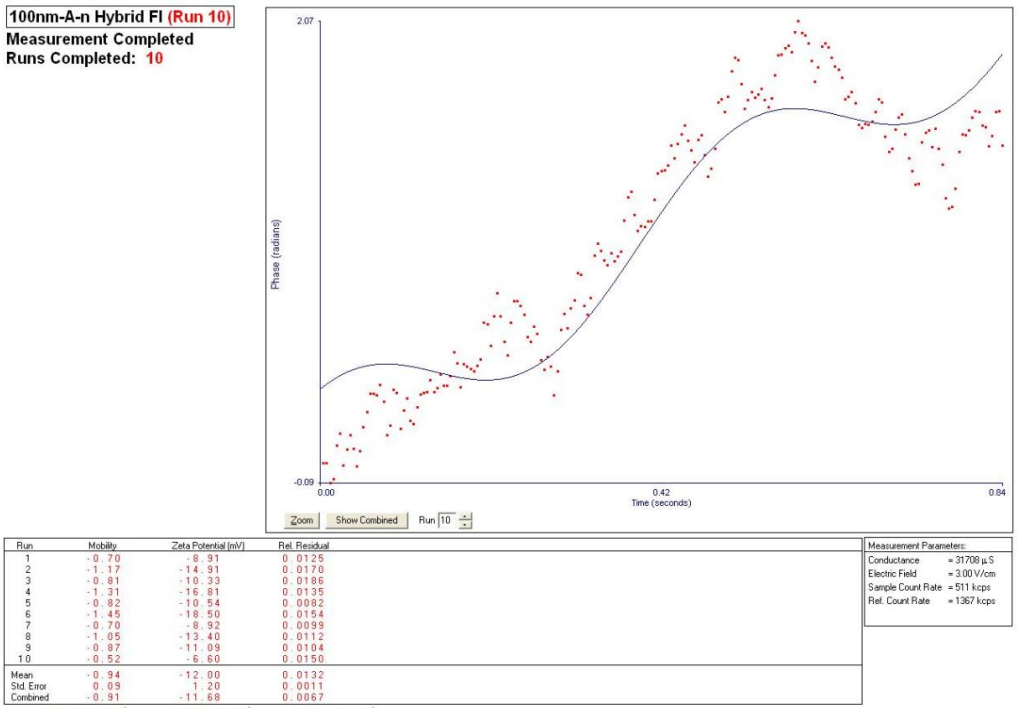

Figure A.69. Zeta potential of liposome encapsulated 100nm-A-n-Fl hybrid NPs with fluorescein dye obtained from ELS analysis.

A.19. Results of DLS and Zeta Potential Analyses for Sac6:RFP tagged *S. cerevisiae* Cells

Sample ID	Sac6 1:1 (Combined)
Operator ID	BBGU
Elapsed Time	00:08:00
Mean Diam.	5826.1 nm
Rel. Var.	0.378
Skew	0.052

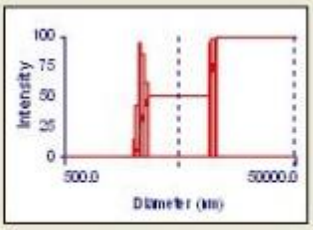

d(nm)	G(d)	C(d)	d(nm)	G(d)	C(d)	d(nm)	G(d)	C(d)
1594.3	0	0	2997.0	0	51	5633.8	0	51
1688.4	0	0	3174.0	0	51	5966.5	0	51
1788.1	0	0	3361.4	0	51	6318.9	0	51
1893.7	0	0	3559.9	0	51	6692.1	0	51
2005.6	14	2	3770.2	0	51	7087.3	0	51
2124.0	43	10	3992.8	0	51	7505.9	0	51
2249.5	96	26	4228.6	0	51	7949.1	0	51
2382.3	87	40	4478.4	0	51	8418.6	0	51
2523.0	63	51	4742.9	0	51	8915.8	97	67
2672.0	0	51	5023.0	0	51	9442.3	100	84
2829.8	0	51	5319.6	0	51	10000.0	97	100

Figure A.70. Intensity distribution of Sac6:RFP tagged *S. cerevisiae* cells obtained from DLS analysis.

Sample ID	Sac6 1:1 (Combined)
Operator ID	BBGU
Elapsed Time	00:08:00
Mean Diam.	2350.6 nm
Rel. Var.	0.176
Skew	6.815

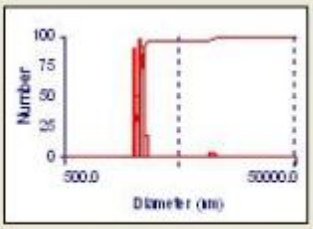

d(nm)	G(d)	C(d)	d(nm)	G(d)	C(d)	d(nm)	G(d)	C(d)
1594.3	0	0	2997.0	0	98	5633.8	0	98
1688.4	0	0	3174.0	0	98	5966.5	0	98
1788.1	0	0	3361.4	0	98	6318.9	0	98
1893.7	0	0	3559.9	0	98	6692.1	0	98
2005.6	92	26	3770.2	0	98	7087.3	0	98
2124.0	51	40	3992.8	0	98	7505.9	0	98
2249.5	100	68	4228.6	0	98	7949.1	0	98
2382.3	92	93	4478.4	0	98	8418.6	0	98
2523.0	17	98	4742.9	0	98	8915.8	3	99
2672.0	0	98	5023.0	0	98	9442.3	2	100
2829.8	0	98	5319.6	0	98	10000.0	2	100

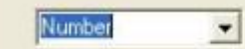

Figure A.71. Number distribution of Sac6:RFP tagged *S. cerevisiae* cells obtained from DLS analysis.

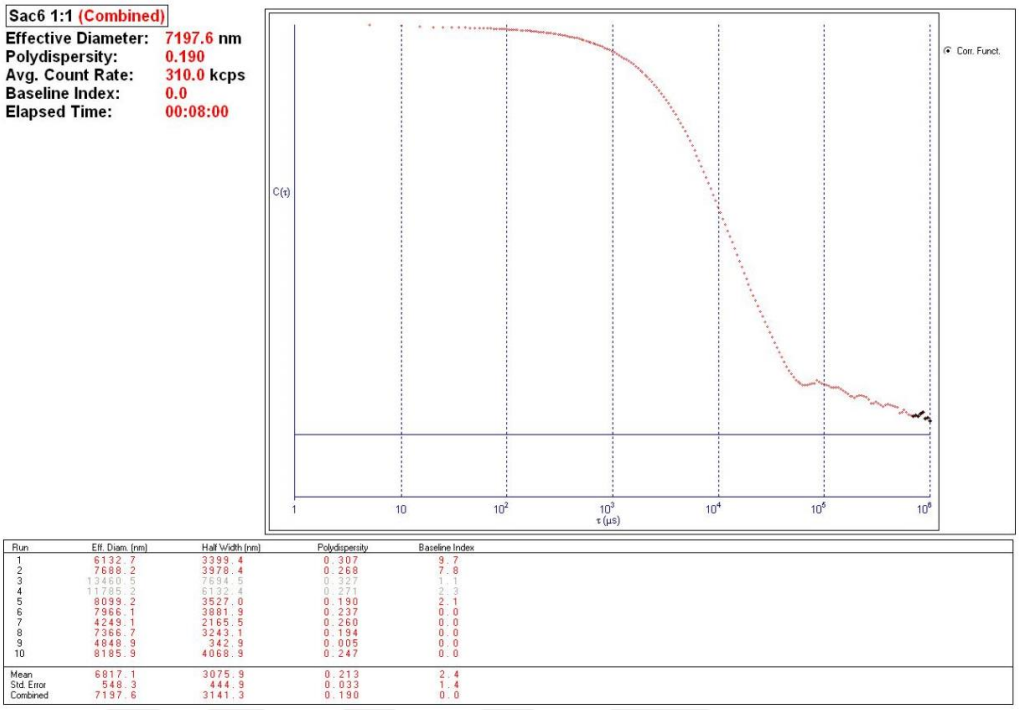

Figure A.72. Effective diameter and polydispersity values of Sac6:RFP tagged *S. cerevisiae* cells obtained from DLS analysis.

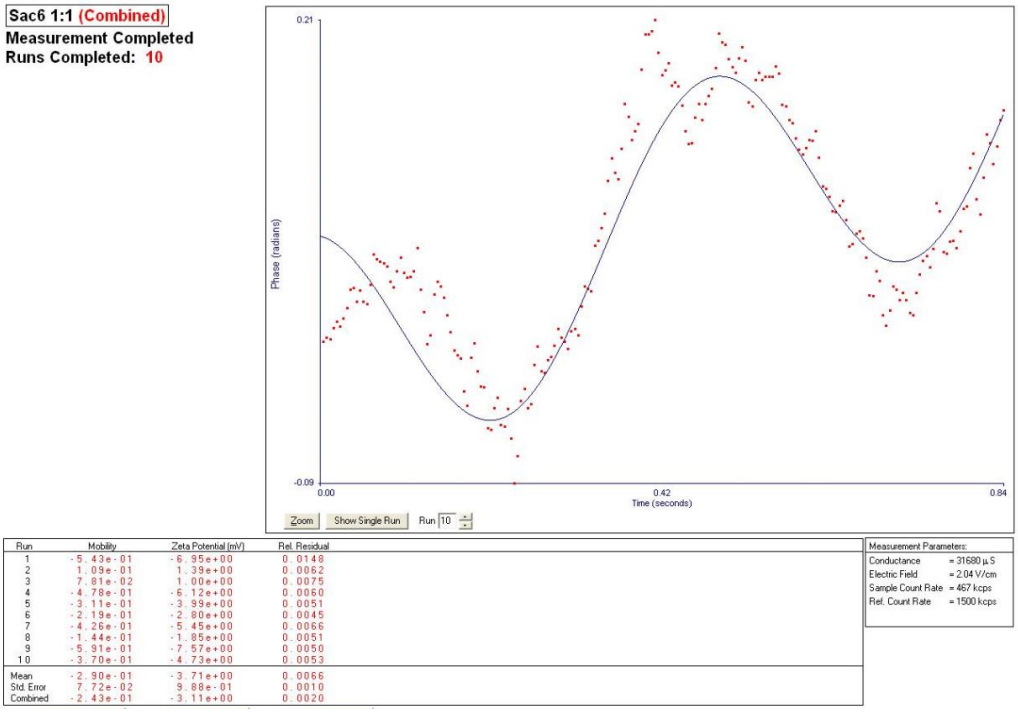

Figure A 73. Zeta potential of Sac6:RFP tagged *S. cerevisiae* cells obtained from ELS analysis.

APPEDIX B: STEM AND TEM ANALYSES OF NANOPARTICLES

B.1. STEM Analysis of DOPC Liposomes

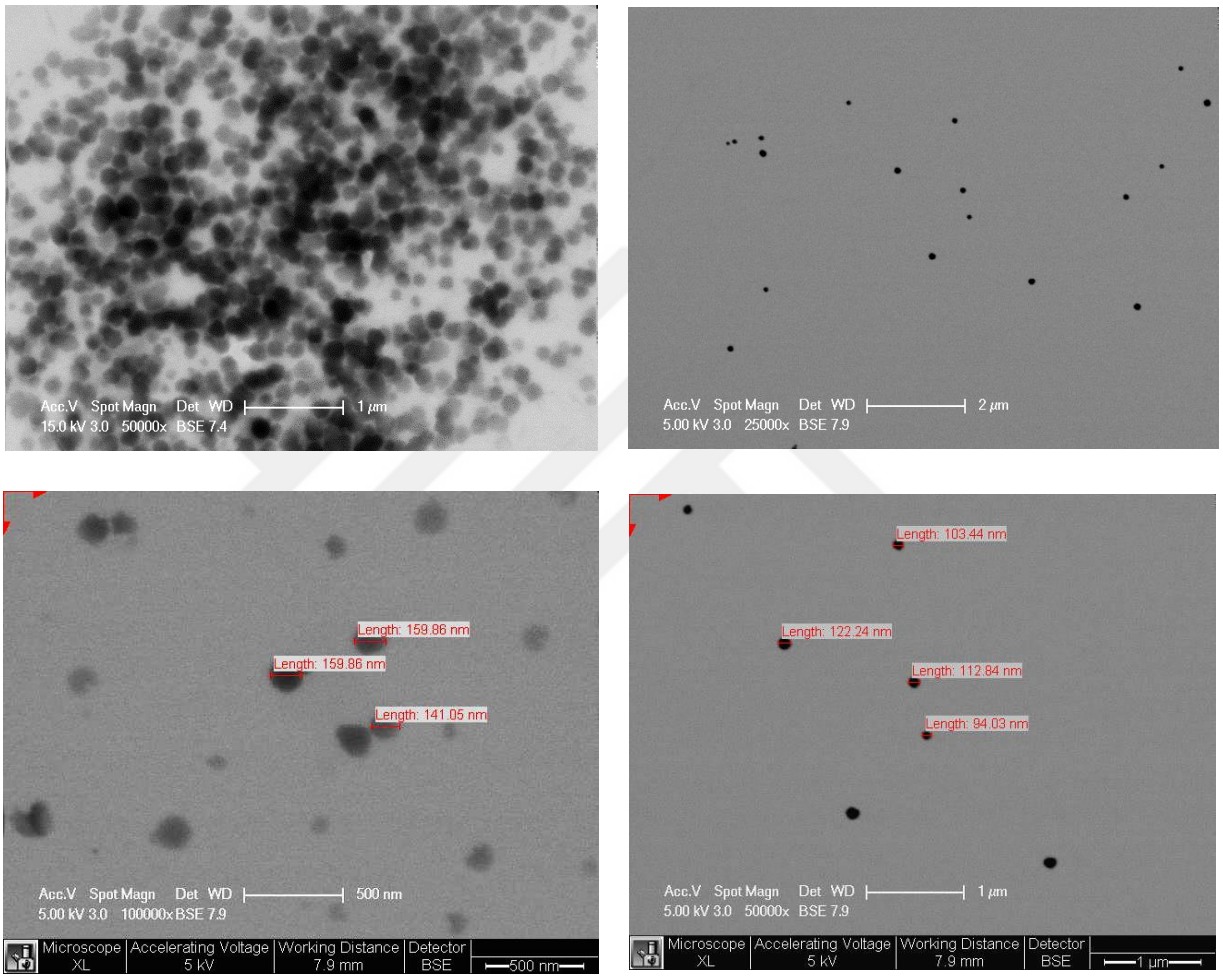

Figure B.1. STEM images of DOPC Liposomes with different magnifications.

B.2. Size Measurement of DOPC Liposomes from STEM Analysis

B.2.1. DOPC Liposome 1

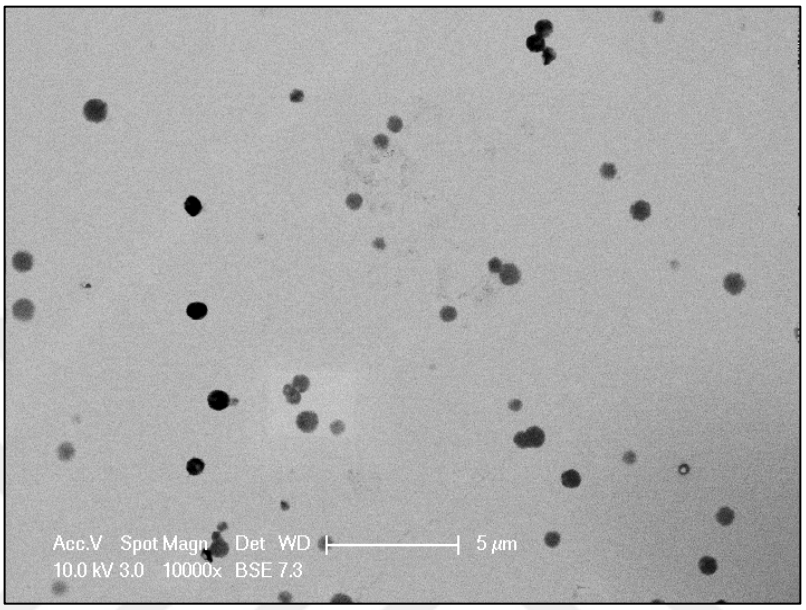

Figure B.2. STEM image of DOPC liposomes.

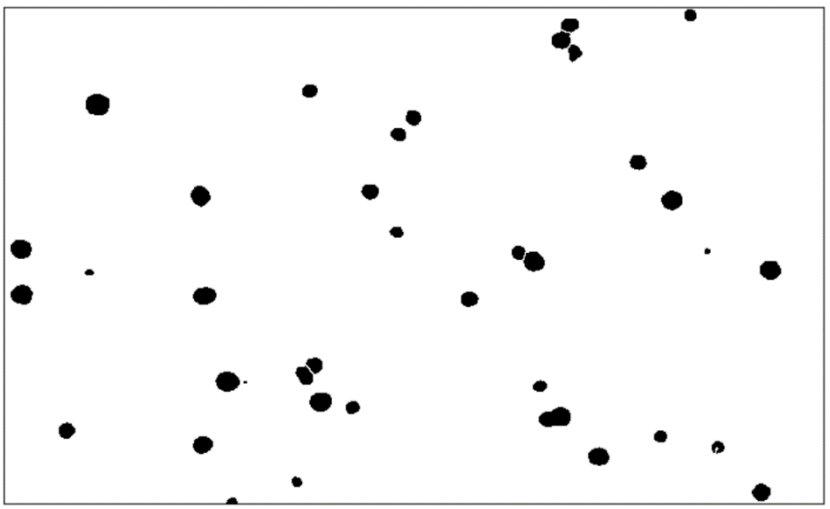

Figure B.3. Thresholded image of DOPC liposomes.

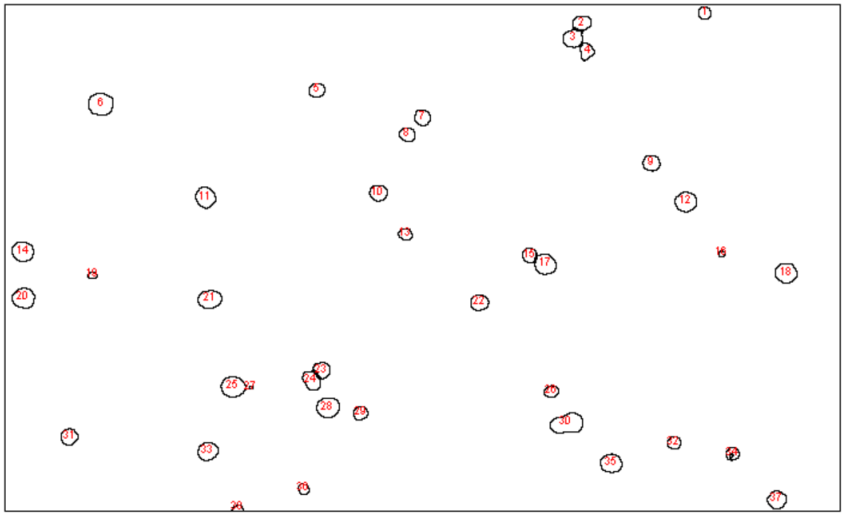

Figure B.4. Circles representing DOPC liposomes of composed in Image-J.

Table B.1. The Diameter of the DOPC Liposomes Present in Figure B.2.

Circle number	Area (nm^2)	Radius (nm)	Diameter (nm)
1	171814.0	233.9	467.8
2	285690.8	301.6	603.3
3	383584.8	349.5	699.0
4	239740.5	276.3	552.6
5	239740.5	276.3	552.6
6	603346.9	438.3	876.7
7	271705.9	294.2	588.3
8	235744.8	274.0	548.0
9	289686.4	303.7	607.5
10	301673.5	310.0	619.9
11	435528.6	372.4	744.9
12	459502.6	382.5	765.1
13	167818.4	231.2	462.4
14	463498.3	384.2	768.4
15	219762.1	264.6	529.1
16	41954.6	115.6	231.2

Table B.1. The Diameter of the DOPC liposomes present in Figure B.2. (cont.)

Circle number	**Area (nm^2)**	**Radius (nm)**	**Diameter (nm)**
17	469491.8	386.7	773.4
18	461500.5	383.4	766.7
19	63930.8	142.7	285.4
20	487472.4	394.0	788.0
21	465496.1	385.0	770.1
22	305669.1	312.0	624.0
23	271705.9	294.2	588.3
24	341630.2	329.8	659.7
25	537418.3	413.7	827.4
26	179805.4	239.3	478.6
27	11987.0	61.8	123.6
28	495463.7	397.2	794.5
29	207775.1	257.2	514.5
30	693249.6	469.9	939.7
31	291684.3	304.8	609.6
32	181803.2	240.6	481.2
33	391576.2	353.1	706.3
34	163822.7	228.4	456.8
35	429535.1	369.9	739.7
36	123865.9	198.6	397.2
37	355615.1	336.5	673.1
38	75917.8	155.5	311.0

B.2.2. DOPC Liposome 2

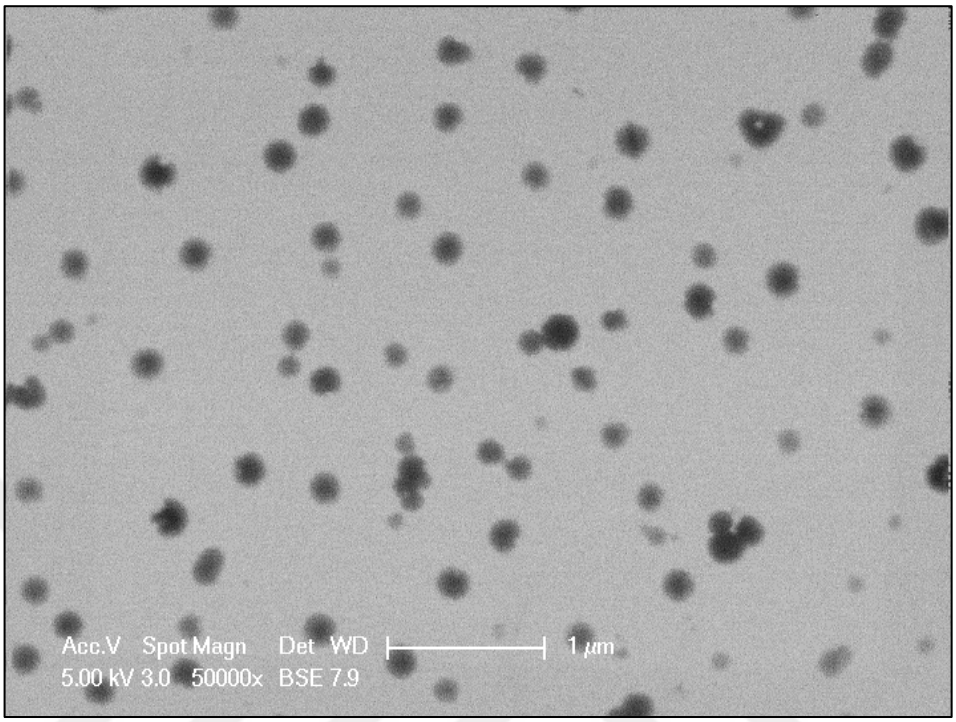

Figure B.5. STEM image of DOPC liposomes.

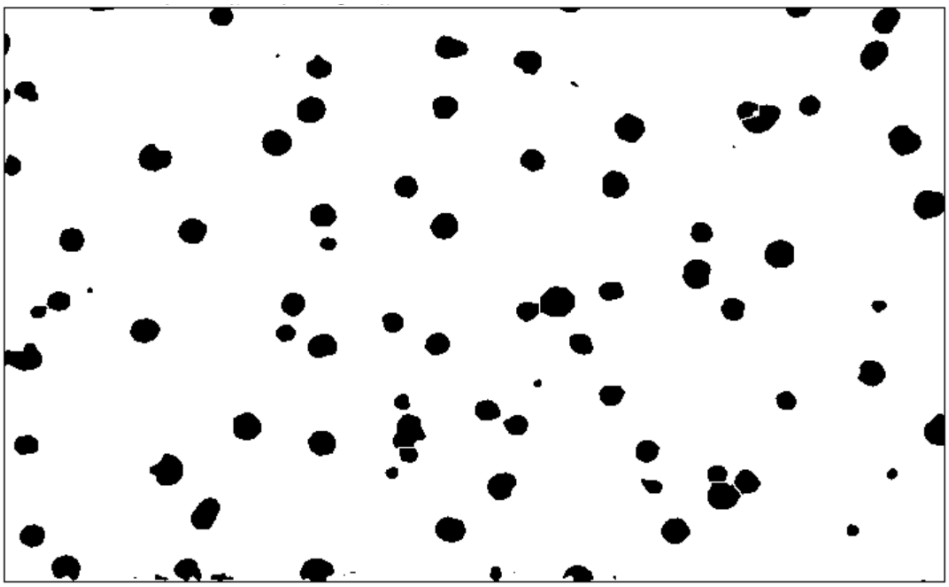

Figure B.6. Thresholded image of DOPC liposomes.

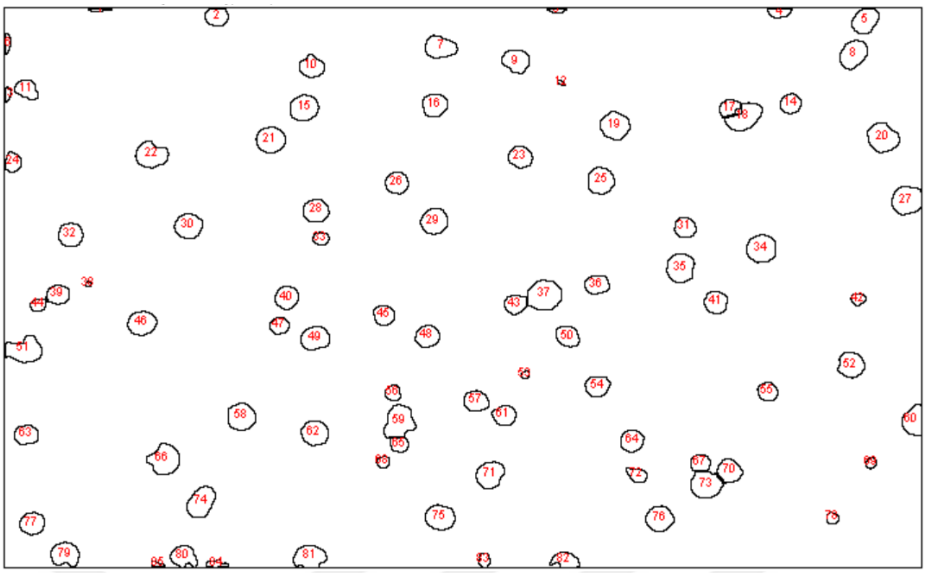

Figure B.7. Circles representing DOPC liposomes of composed in Image-J.

Table B.2. The Diameter of the DOPC liposomes present in Figure B.5.

Circle number	Area (nm^2)	Radius (nm)	Diameter (nm)	Circle number	Area (nm^2)	Radius (nm)	Diameter (nm)
1	2127.3	26	52.1	16	21194.4	82.2	164.3
2	15600.3	70.5	141	17	12133.6	62.2	124.3
3	2678.8	29.2	58.4	18	29782.4	97.4	194.8
4	7957.7	50.3	100.7	19	29152.1	96.4	192.7
5	23873.2	87.2	174.4	20	32382.5	101.6	203.1
6	3939.5	35.4	70.8	21	27655.1	93.8	187.7
7	25212.6	89.6	179.2	22	29230.9	96.5	193
8	27261.1	93.2	186.4	23	18830.7	77.4	154.9
9	22691.4	85	170	24	11660.8	60.9	121.9
10	19067	77.9	155.9	25	26079.3	91.1	182.3
11	15521.5	70.3	140.6	26	18357.9	76.5	152.9
12	1103.1	18.7	37.5	27	32303.7	101.4	202.9
13	2915.2	30.5	60.9	28	21588.3	82.9	165.8
14	15048.8	69.2	138.5	29	25370.2	89.9	179.8
15	27103.6	92.9	185.8	30	25212.6	89.6	179.2

Table B.2. The Diameter of the DOPC liposomes present in Figure B.5. (cont.)

Circle number	Area (nm^2)	Radius (nm)	Diameter (nm)	Circle number	Area (nm^2)	Radius (nm)	Diameter (nm)
31	15994.3	71.4	142.7	59	34746.1	105.2	210.4
32	21430.7	82.6	165.2	60	22139.8	84	167.9
33	7642.6	49.3	98.7	61	17018.5	73.6	147.2
34	30176.3	98	196.1	62	24661.1	88.6	177.2
35	29546	97	194	63	17333.7	74.3	148.6
36	17018.5	73.6	147.2	64	18594.3	77	153.9
37	38212.9	110.3	220.6	65	10321.4	57.3	114.7
38	1103.1	18.7	37.5	66	33091.6	102.7	205.3
39	16230.6	71.9	143.8	67	12369.9	62.8	125.5
40	19618.6	79	158.1	68	5357.7	41.3	82.6
41	19145.8	78.1	156.2	69	4097.1	36.1	72.2
42	6145.6	44.2	88.5	70	20485.3	80.8	161.5
43	15600.3	70.5	141	71	26788.4	92.4	184.7
44	7406.2	48.6	97.1	72	10006.3	56.5	112.9
45	15363.9	69.9	139.9	73	31043	99.4	198.9
46	25212.6	89.6	179.2	74	29546	97	194
47	11818.4	61.4	122.7	75	27182.4	93	186.1
48	19303.4	78.4	156.8	76	25291.4	89.7	179.5
49	24897.5	89	178.1	77	20170.1	80.1	160.3
50	17727.6	75.1	150.3	78	5200.1	40.7	81.4
51	31988.5	100.9	201.9	79	24818.7	88.9	177.8
52	24345.9	88.1	176.1	80	20012.5	79.8	159.7
53	2284.9	27	54	81	26946	92.6	185.3
54	18436.7	76.6	153.3	82	15206.4	69.6	139.2
55	13473	65.5	131	83	6066.8	44	87.9
56	8903.2	53.2	106.5	84	5042.5	40.1	80.1
57	18673.1	77.1	154.2	85	2206.1	26.5	53
58	27891.5	94.2	188.5				

B.2.3. DOPC Liposome 3

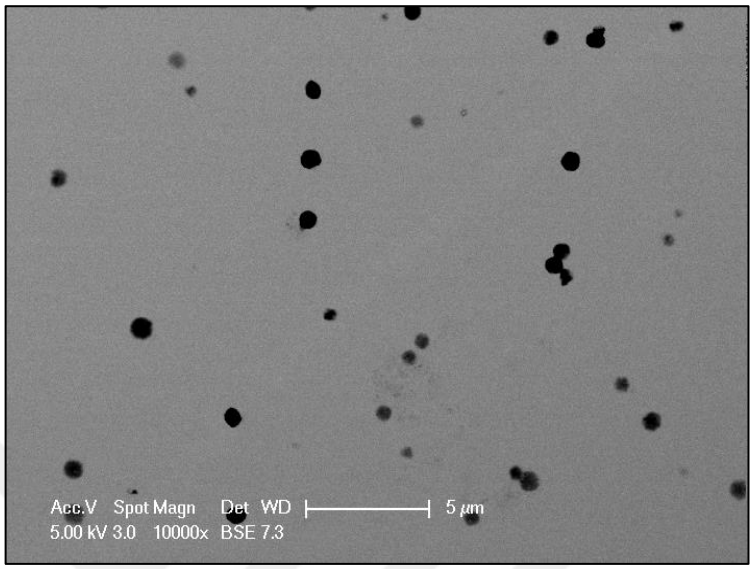

Figure B.8. STEM image of DOPC liposomes.

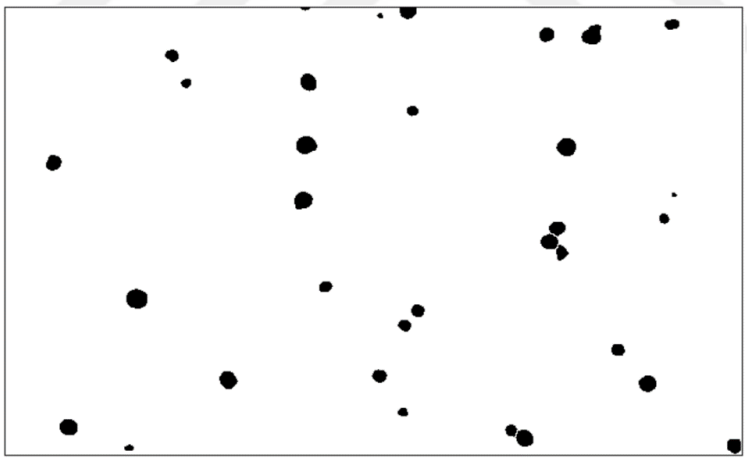

Figure B.9. Thresholded image of DOPC liposomes.

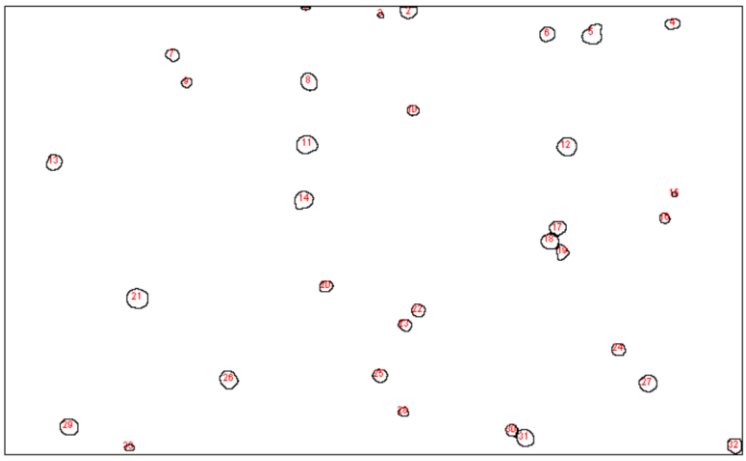

Figure B.10. Circles representing DOPC liposomes of composed in Image-J.

Table B.3. The Diameter of the DOPC liposomes present in Figure B.8.

Circle number	Area (nm^2)	Radius (nm)	Diameter (nm)	Circle number	Area (nm^2)	Radius (nm)	Diameter (nm)
1	33676	103.6	207.1	18	382321.9	348.9	697.9
2	285255.7	301.4	602.8	19	237713.1	275.1	550.3
3	43580.7	117.8	235.6	20	207999	257.4	514.7
4	221865.6	265.8	531.6	21	604187.5	438.7	877.3
5	538816.4	414.2	828.5	22	243655.9	278.6	557.1
6	311008	314.7	629.4	23	211960.9	259.8	519.6
7	225827.5	268.2	536.4	24	239694.1	276.3	552.6
8	396188.5	355.2	710.4	25	267427.3	291.8	583.7
9	134704.1	207.1	414.2	26	435807.4	372.5	745.1
10	166399.2	230.2	460.4	27	414017	363.1	726.2
11	522968.8	408.1	816.2	28	126780.3	200.9	401.9
12	497216.6	397.9	795.9	29	427883.6	369.1	738.3
13	338741.2	328.4	656.9	30	196113.3	249.9	499.8
14	463540.6	384.2	768.4	31	421940.8	366.6	733.1
15	31695.1	100.5	200.9	32	309027	313.7	627.4
16	144608.8	214.6	429.2	33	83199.6	162.8	325.6
17	322893.6	320.7	641.3				

B.3. STEM and TEM Analysis Results of 20nm-C-n PSL and Hybrid NPs

B.3.1. STEM Analysis Results 20nm-C-n Hybrid NPs

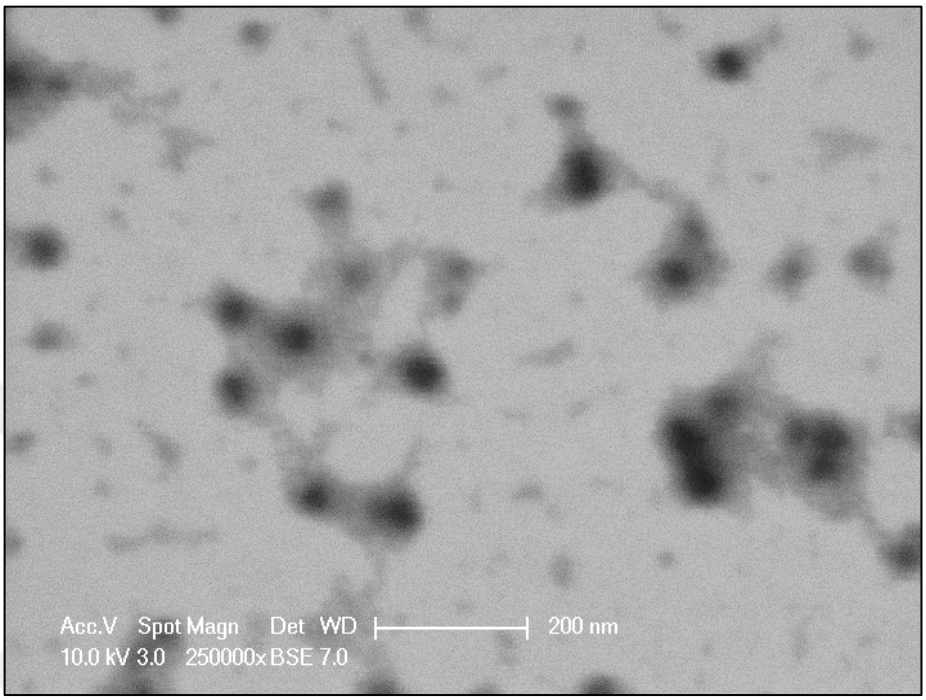

Figure B.11. STEM image of 20nm-C-n hybrid NPs.

B.3.2. TEM Analysis Results of 20nm-C-n PSL and Hybrid NPs

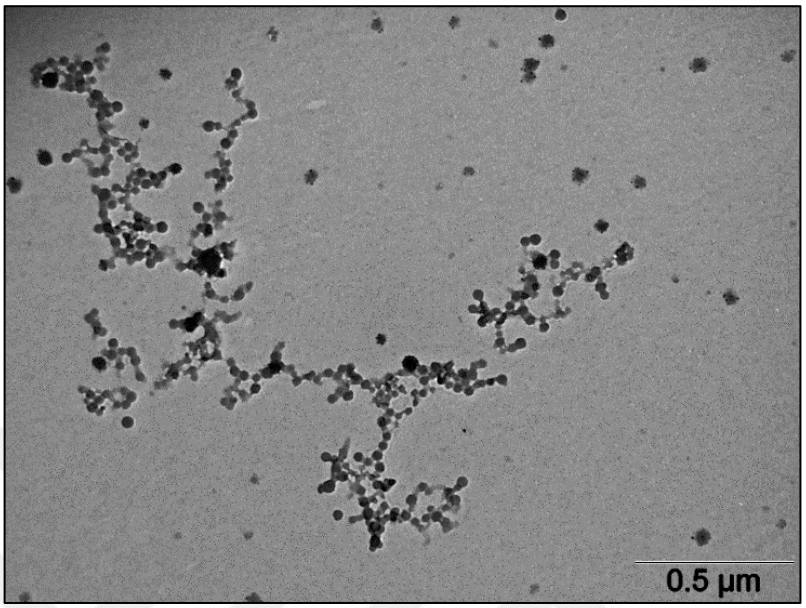

Figure B.12. TEM image of 20nm-C-n PSL NPs.

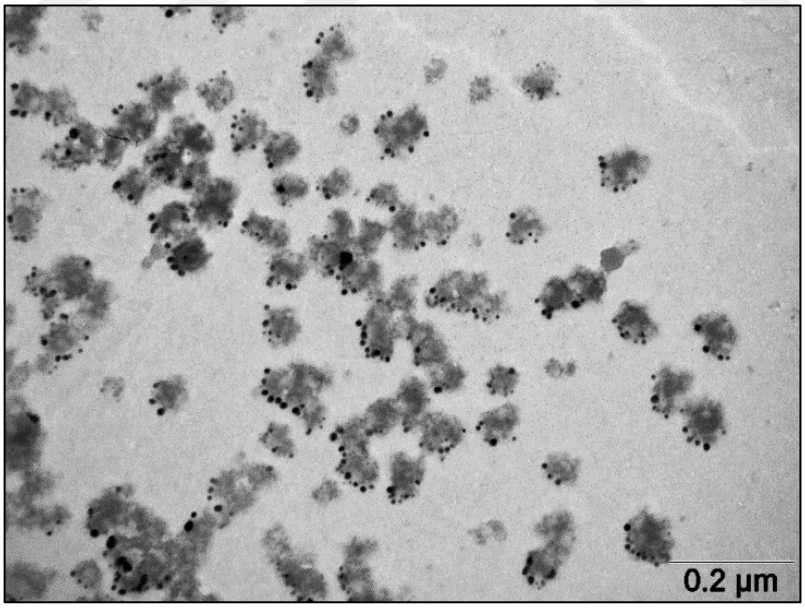

Figure B.13. TEM image of 20nm-C-n hybrid NPs.

APPENDIX C: RESULTS OF FLUORESCEIN DYE LOADING EFFICIENCY INTO DOPC-LIPOSOME

Table C.1. Absorbance value of 15 µg/ml Fluorescein Solution for Different Wavelengths.

Wavelength (nm)	Absorbance
250	0.692
300	0.576
350	0.35
400	0.137
450	0.766
460	1.187
470	1.523
480	2.075
490	2.461
494	2.475
495	2.47
500	2.335
550	0.006
600	0.007

Table C.2. Calibration Curve Data for Fluorescein Dye.

Fluorescein Concentration (µg/ml)	Absorbance Values
0	0
1	0.2450
3	0.7080
6	1.388
9	1.974
12	2.372

APPENDIX D: RESULTS FOR GROWTH CURVE CONSTRUCTION EXPERIMENTS

Table D.1. Optical Density Data for 22 hours of Sac6:RFP Tagged *S. cerevisiae* Cells Growth Curve Measurement.

Time (h)	OD 1	OD 2	Avg. OD	ln (Avg. OD)
1	0.0216	0.0150	0.0183	-4.001
2	0.0172	0.0230	0.0201	-3.907
3	0.0191	0.0270	0.0231	-3.770
4	0.0214	0.0400	0.0307	-3.483
5	0.0287	0.0430	0.0359	-3.328
6	0.0384	0.0580	0.0482	-3.032
7	0.0607	0.0890	0.0749	-2.592
8	0.0999	0.1200	0.1100	-2.208
9	0.1606	0.2100	0.1853	-1.686
10	0.2586	0.2830	0.2708	-1.306
11	0.3868	0.4320	0.4094	-0.893
12	0.5407	0.6350	0.5879	-0.531
13	0.6802	0.7870	0.7336	-0.310
14	0.7691	1.1560	0.9626	-0.038
15	0.8246	1.3580	1.0913	0.087
16	0.9562	1.4240	1.1901	0.174
17	1.0982	1.4940	1.2961	0.259
18	1.2116	1.5820	1.3968	0.334
19	1.2050	1.8640	1.5345	0.428
20	1.2532	1.9680	1.6106	0.477
21	1.2798	1.9800	1.6299	0.489
22	1.2992	1.9840	1.6416	0.496

APPENDIX E: VIABILITY PERCENTAGES OF THE YEAST CELLS UNDER DIFFERENT POLYSTYRENE LATEX NANOPARTICLE (PSL NP) EXPOSURE

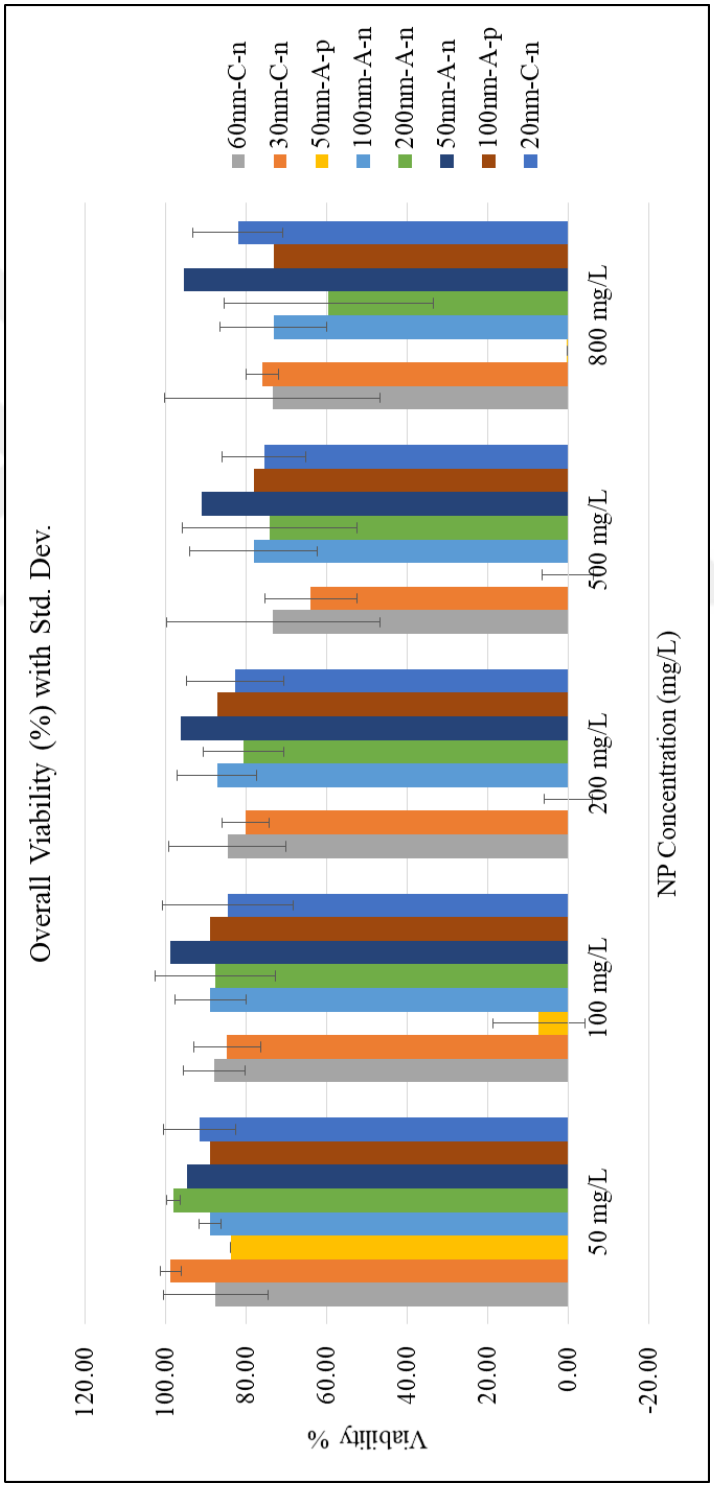

Figure E.1. Overall average viability percentages of different types and concentrations of PSL NP exposed *S. cerevisiae* cells from CFU Analysis.

APPENDIX F: CLSM IMAGES OF THE YEAST CELLS EXPOSED TO NANOPARTICLES WITH OR WITHOUT INHIBITOR TREATMENT

F.1. CLSM Images of the PSL NP Exposed Yeast Cells

F.1.1. CLSM Images 30nm-C-n PSL NP Exposed Yeast Cells

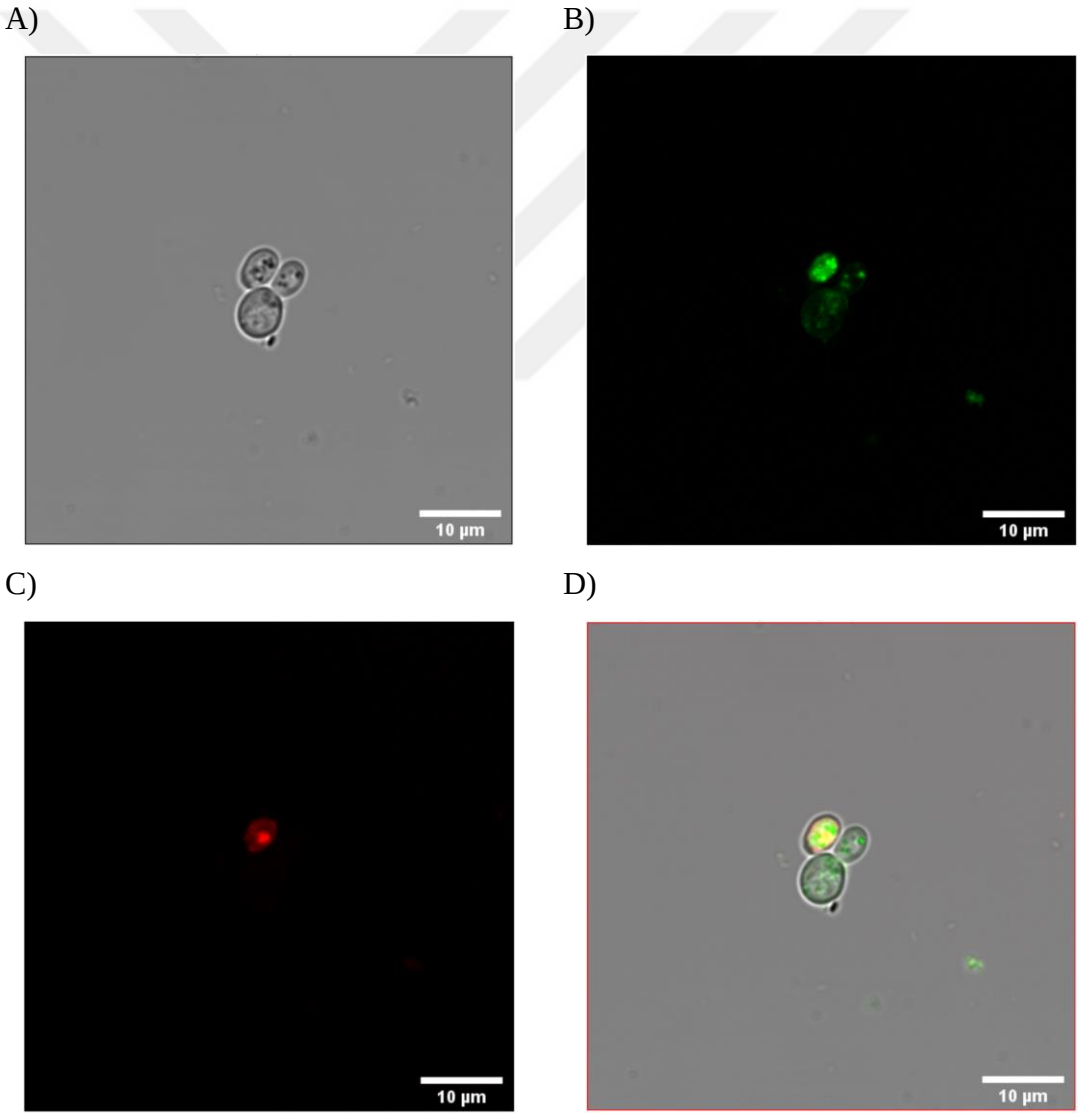

Figure F.1. CLSM images of 100 mg/L 30nm-C-n PSL NP exposed yeast cells A) Bright field B) FITC C) PI D) Merged image.

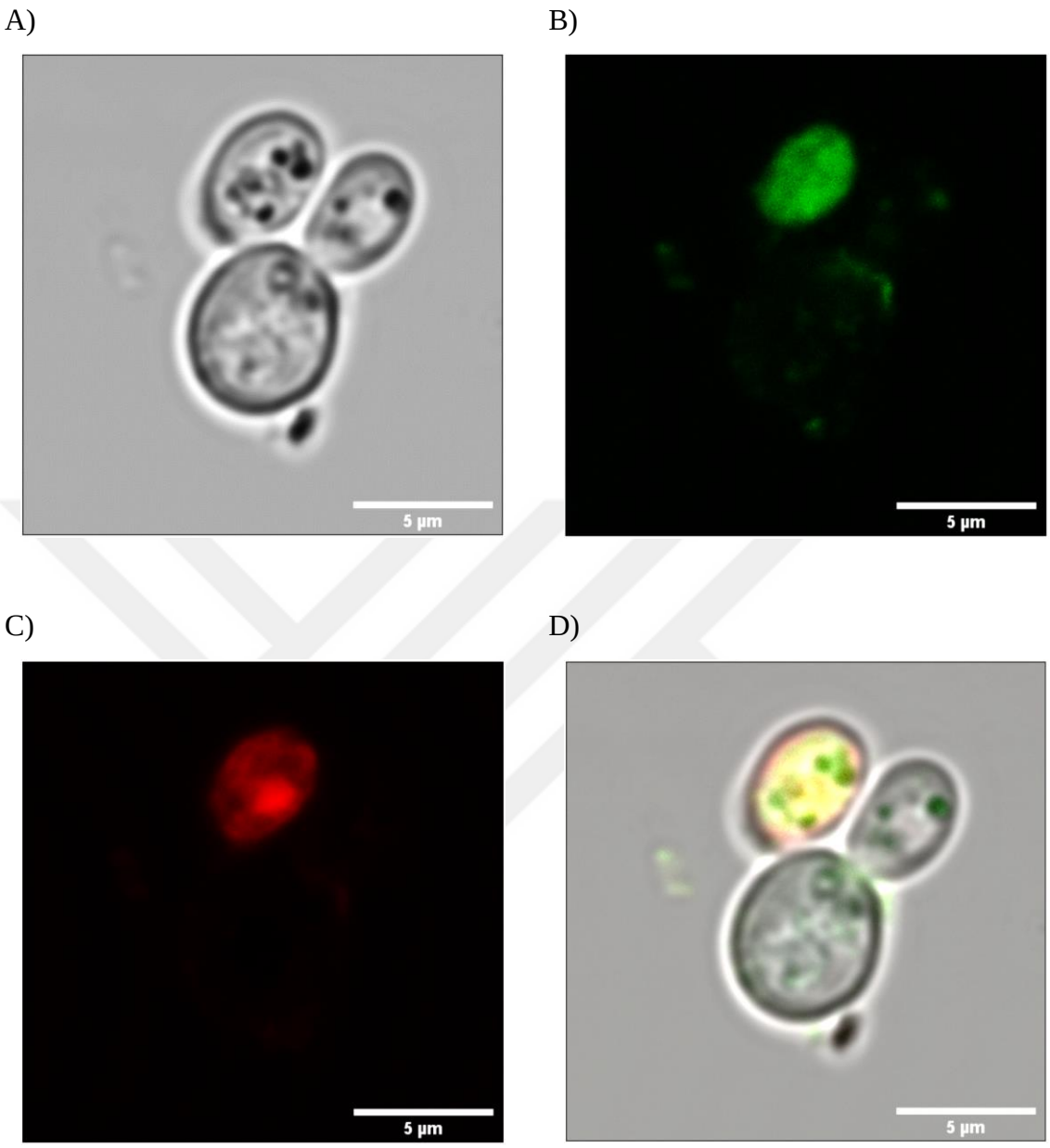

Figure F.2. Zoomed CLSM images of 100 mg/L 30nm-C-n PSL NP exposed yeast cells A) Bright field B) FITC C) PI D) Merged image.

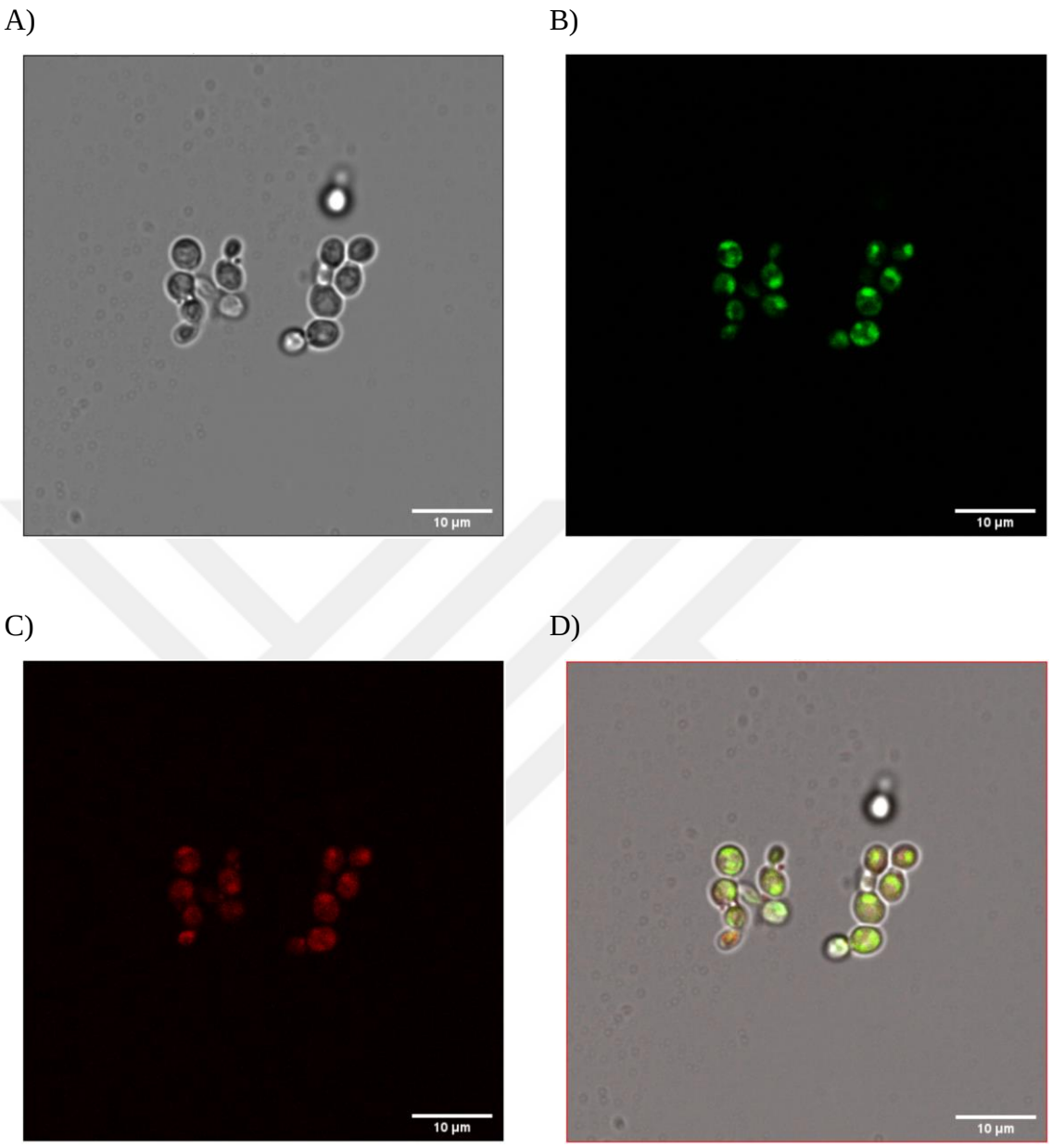

Figure F.3. CLSM images of 100 mg/L 30nm-C-n PSL NP exposed and clustered yeast cells A) Bright field B) FITC C) PI D) Merged image.

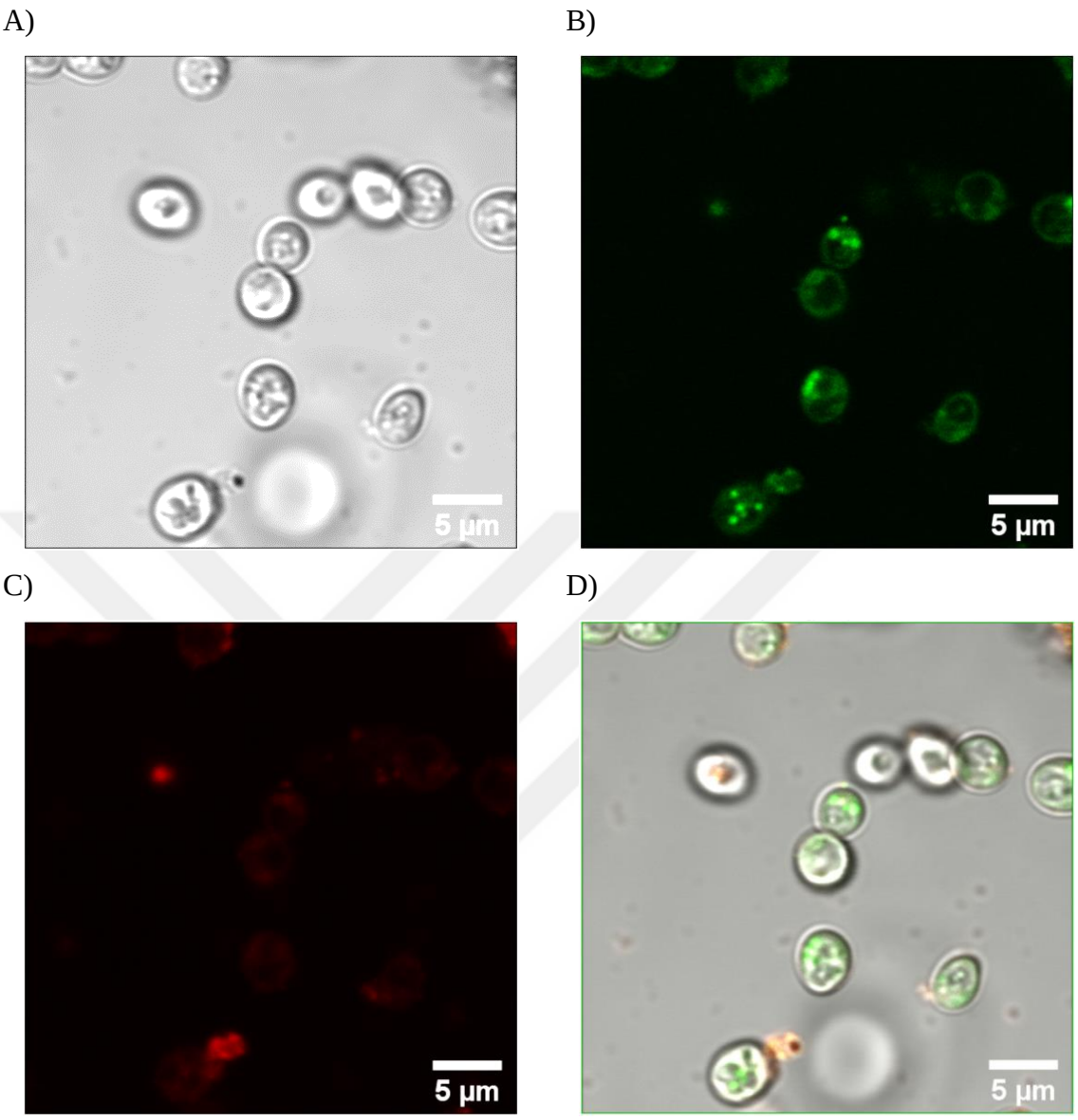

Figure F.4. CLSM images of 100 mg/L 30nm-C-n PSL NP exposed yeast cells showing the agglomeration of NPs as round shapes inside the cells A) Bright field B) FITC C) PI D) Merged image.

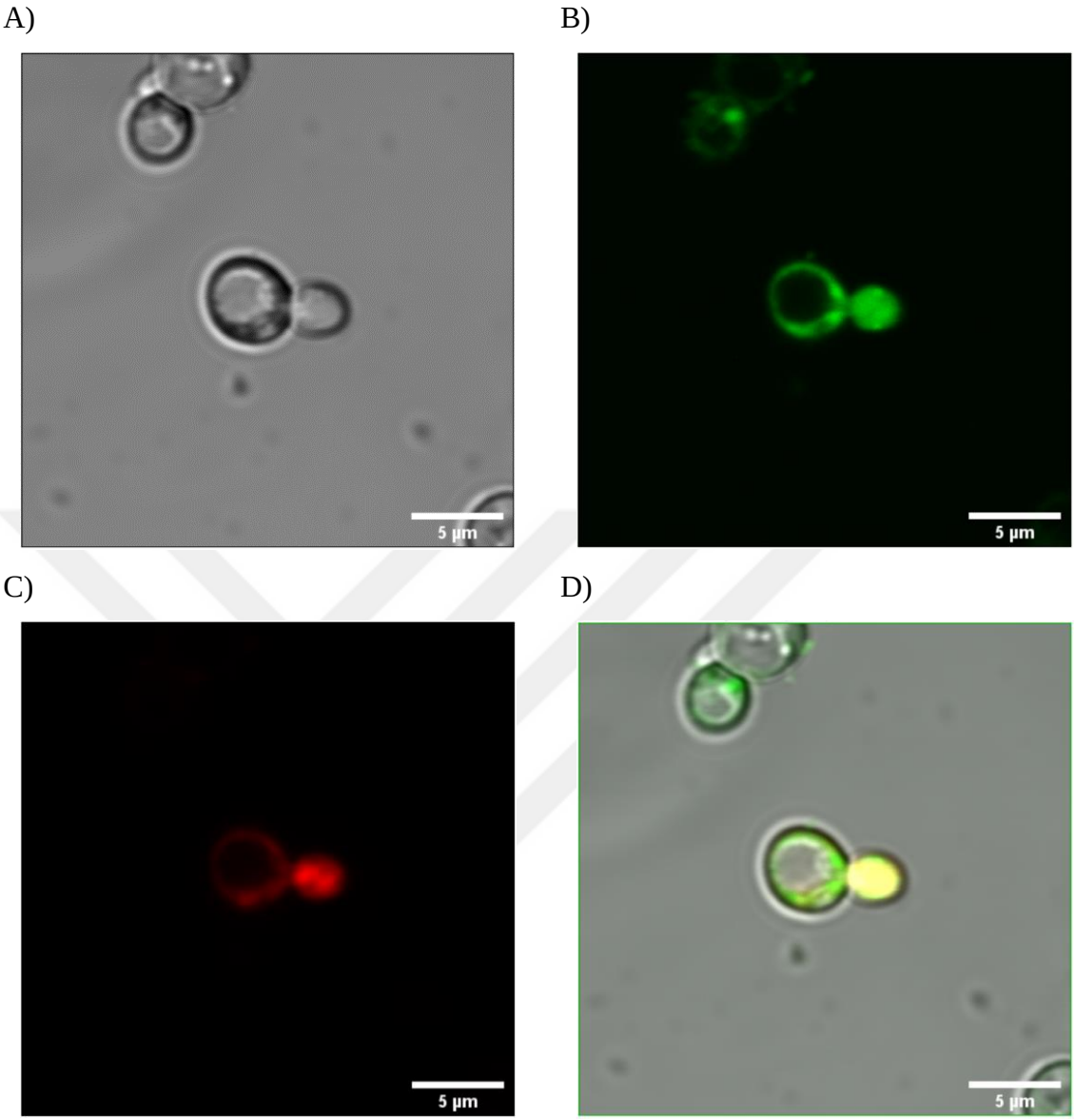

Figure F.5. CLSM images of 100 mg/L 30nm-C-n PSL NP exposed yeast cells showing the accumulation of NPs in cytoplasm and/or nucleus of the cells A) Bright field B) FITC C) PI D) Merged image.

F.1.2. CLSM Images 100nm-A-p PSL NP Exposed Yeast Cells

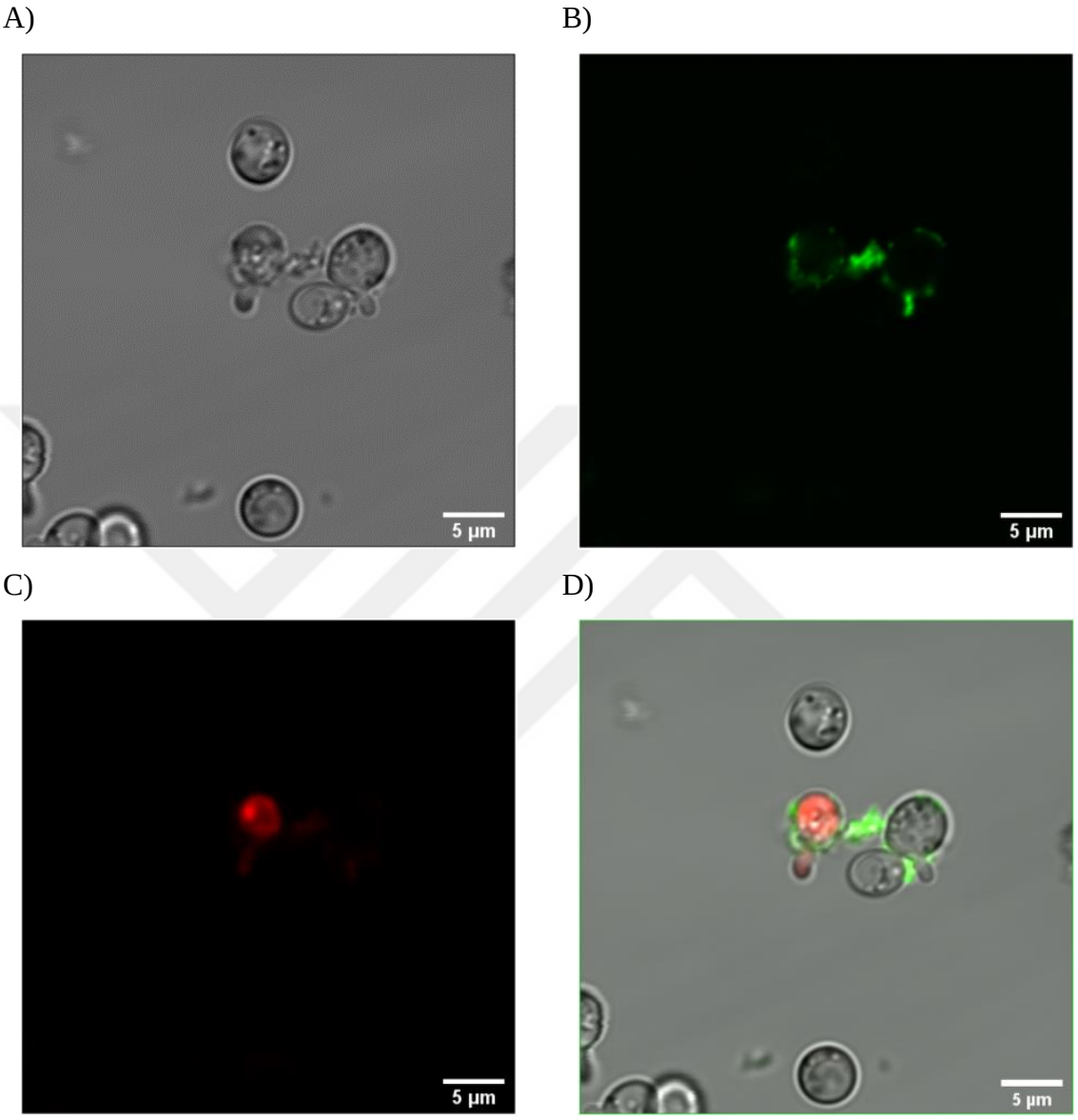

Figure F.6. CLSM images of 50 mg/L 100nm-A-p PSL NP exposed yeast cells A) Bright field B) FITC C) PI D) Merged image.

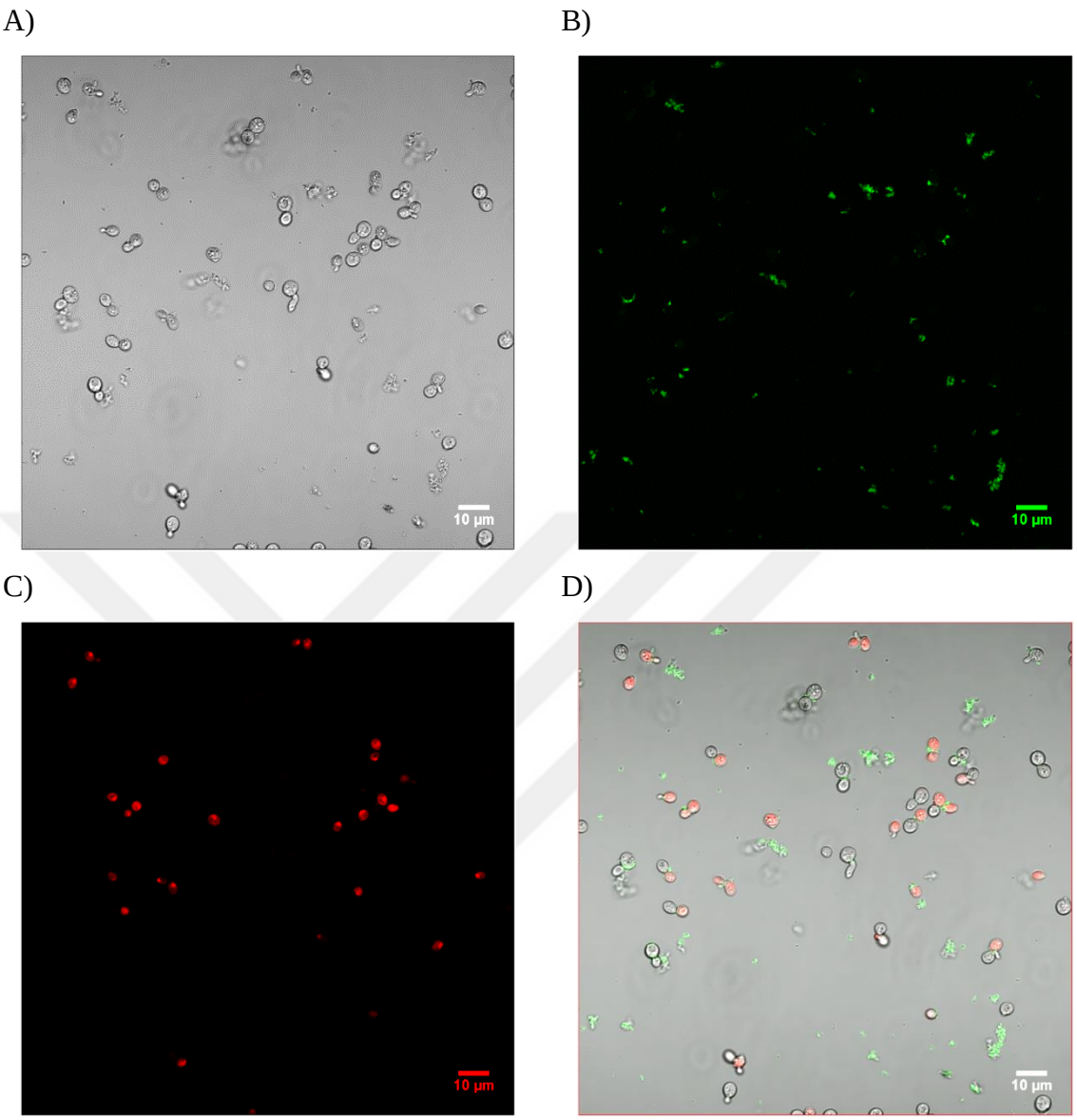

Figure F.7. CLSM images of 100 mg/L 100nm-A-p PSL NP exposed yeast cells as a general appearance A) Bright field B) FITC C) PI D) Merged image.

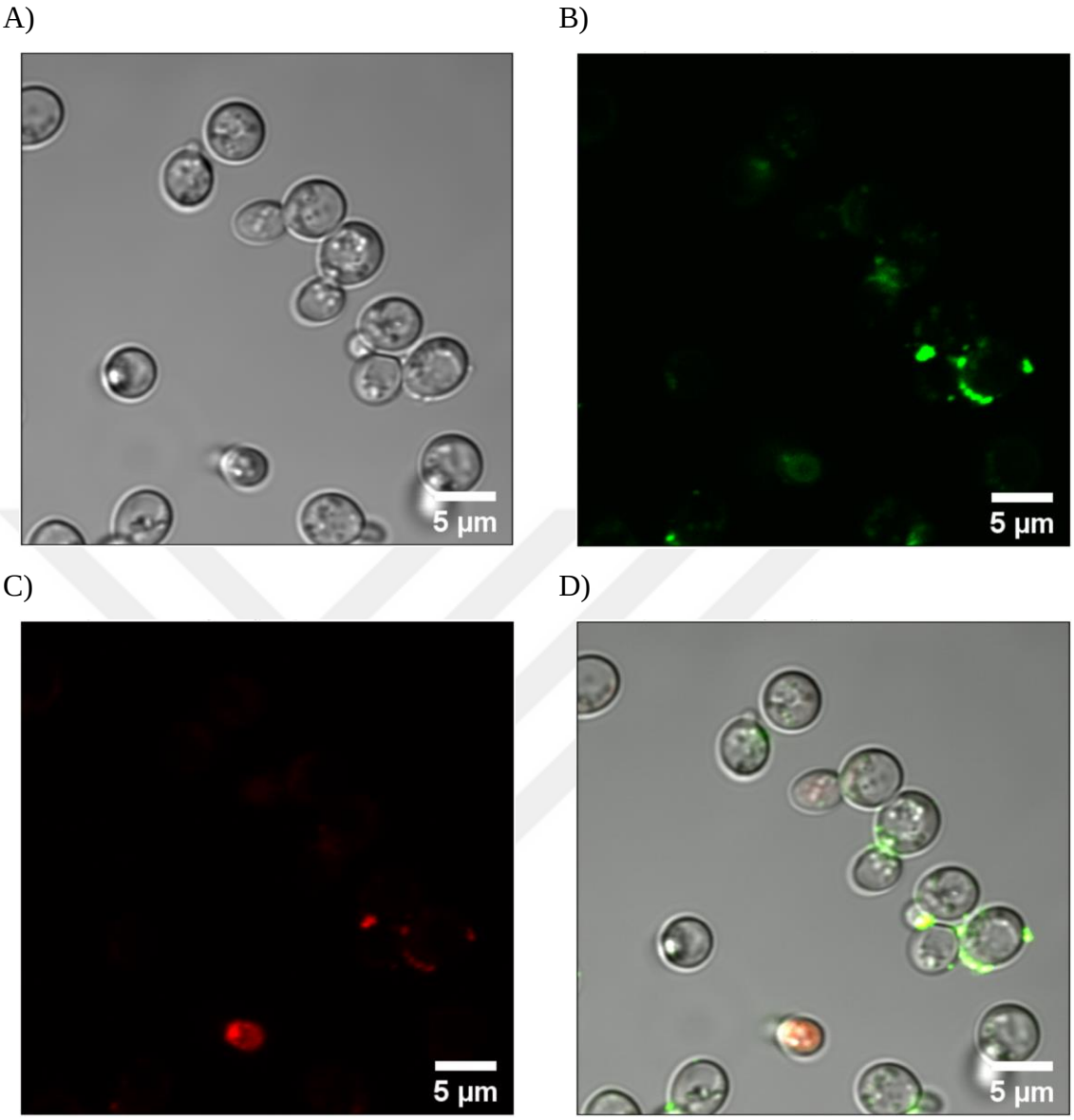

Figure F.8. CLSM images of 100 mg/L 100nm-A-p PSL NP exposed yeast cells A) Bright field B) FITC C) PI D) Merged image.

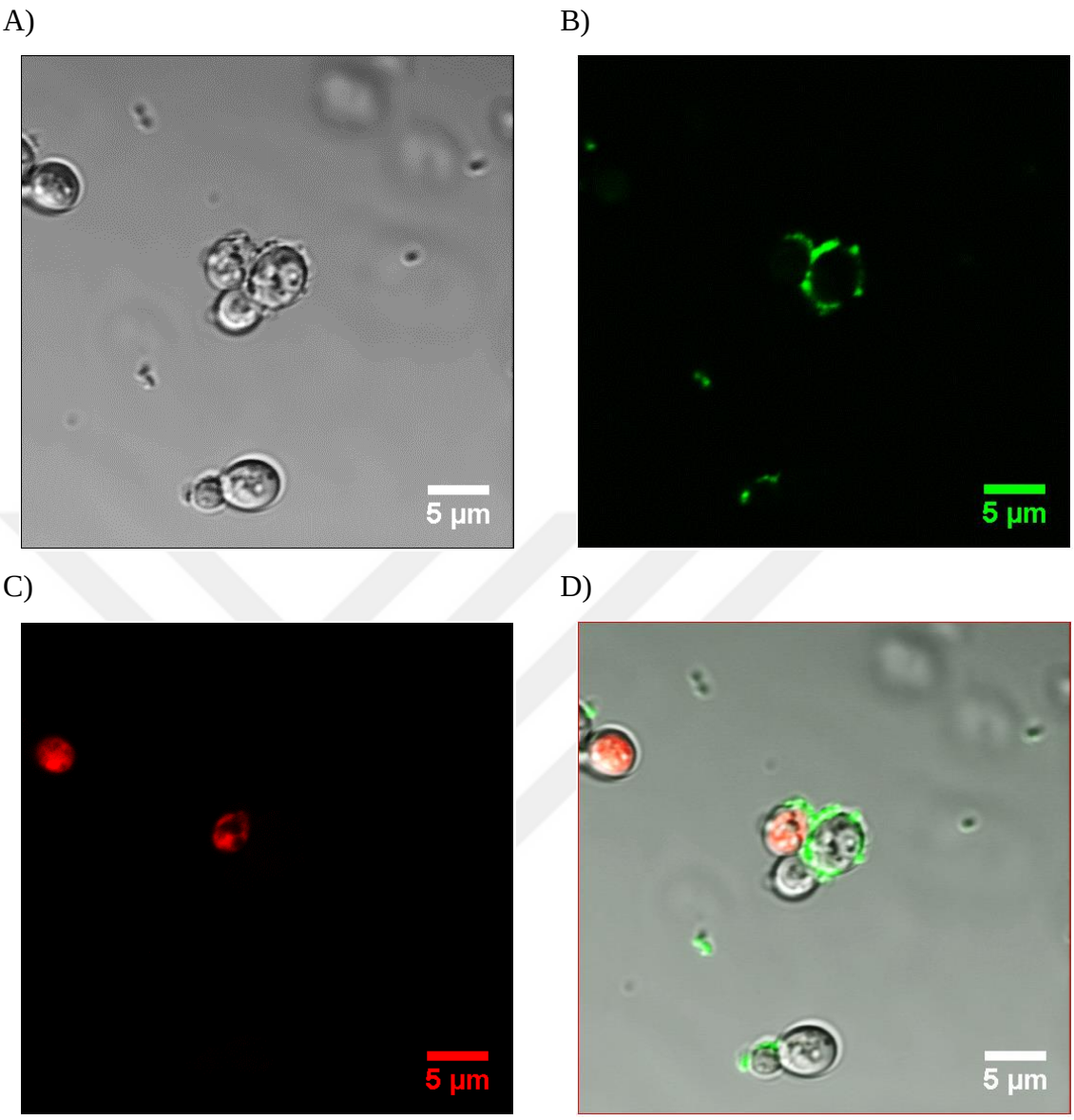

Figure F.9. CLSM images of 100 mg/L 100nm-A-p PSL NP exposed yeast cells emphasizing the surface coverage of NPs A) Bright field B) FITC C) PI D) Merged image.

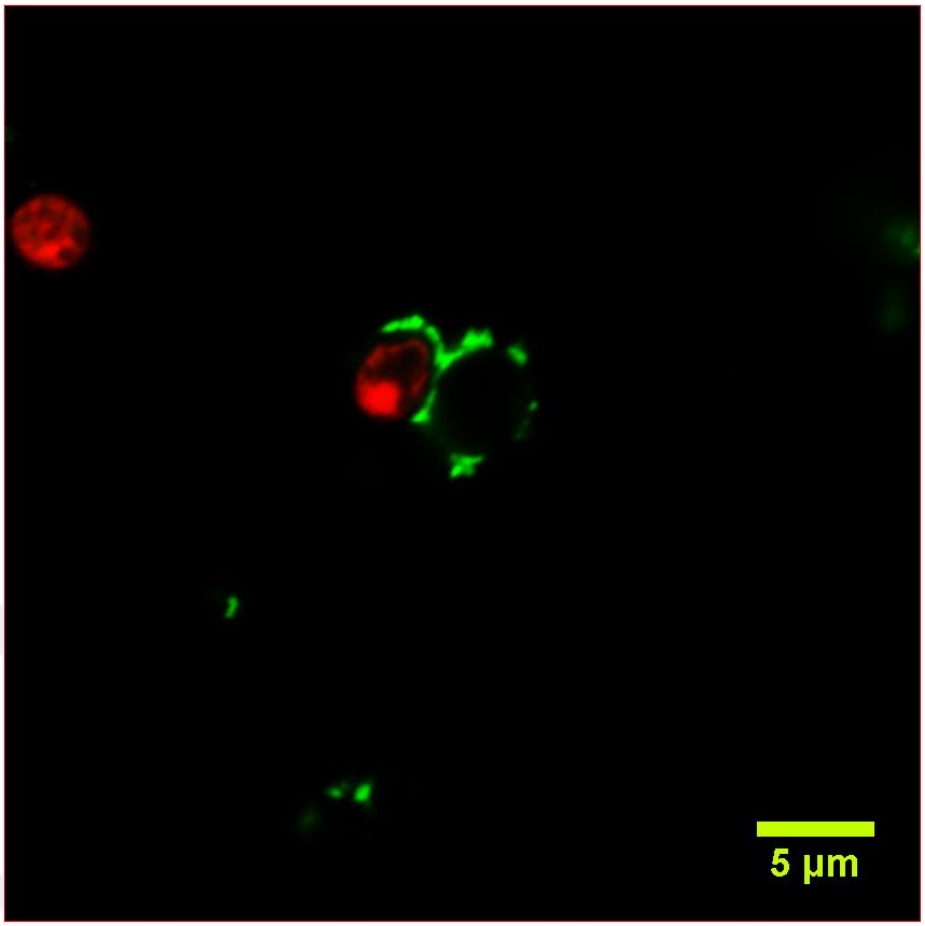

Figure F.10. High resolution and merged CLSM image of 100 mg/L 100nm-A-p PSL NP exposed yeast cells.

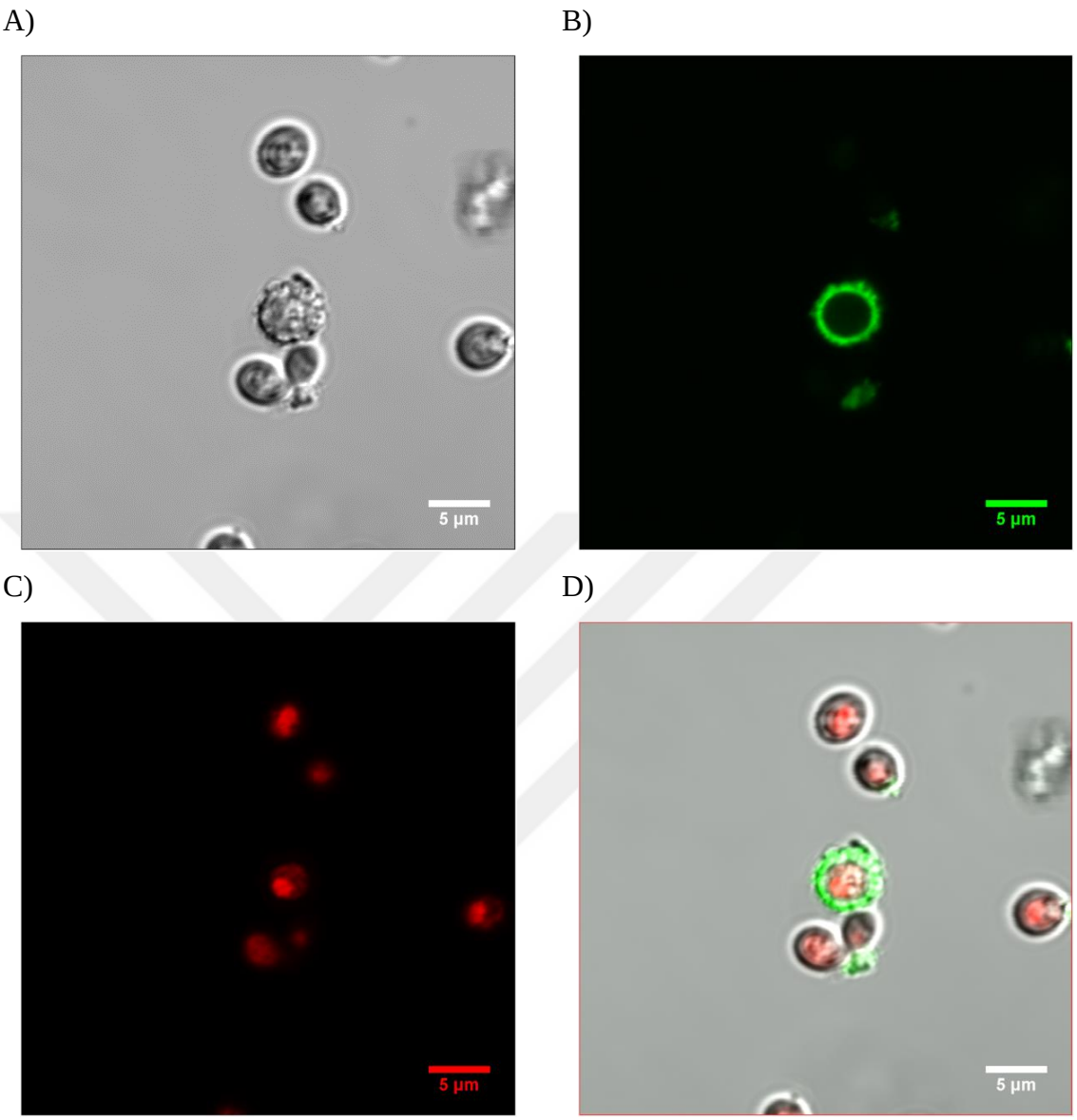

Figure F.11. CLSM images of 500 mg/L 100nm-A-p PSL NP exposed yeast cells emphasizing the surface coverage of NPs A) Bright field B) FITC C) PI D) Merged image.

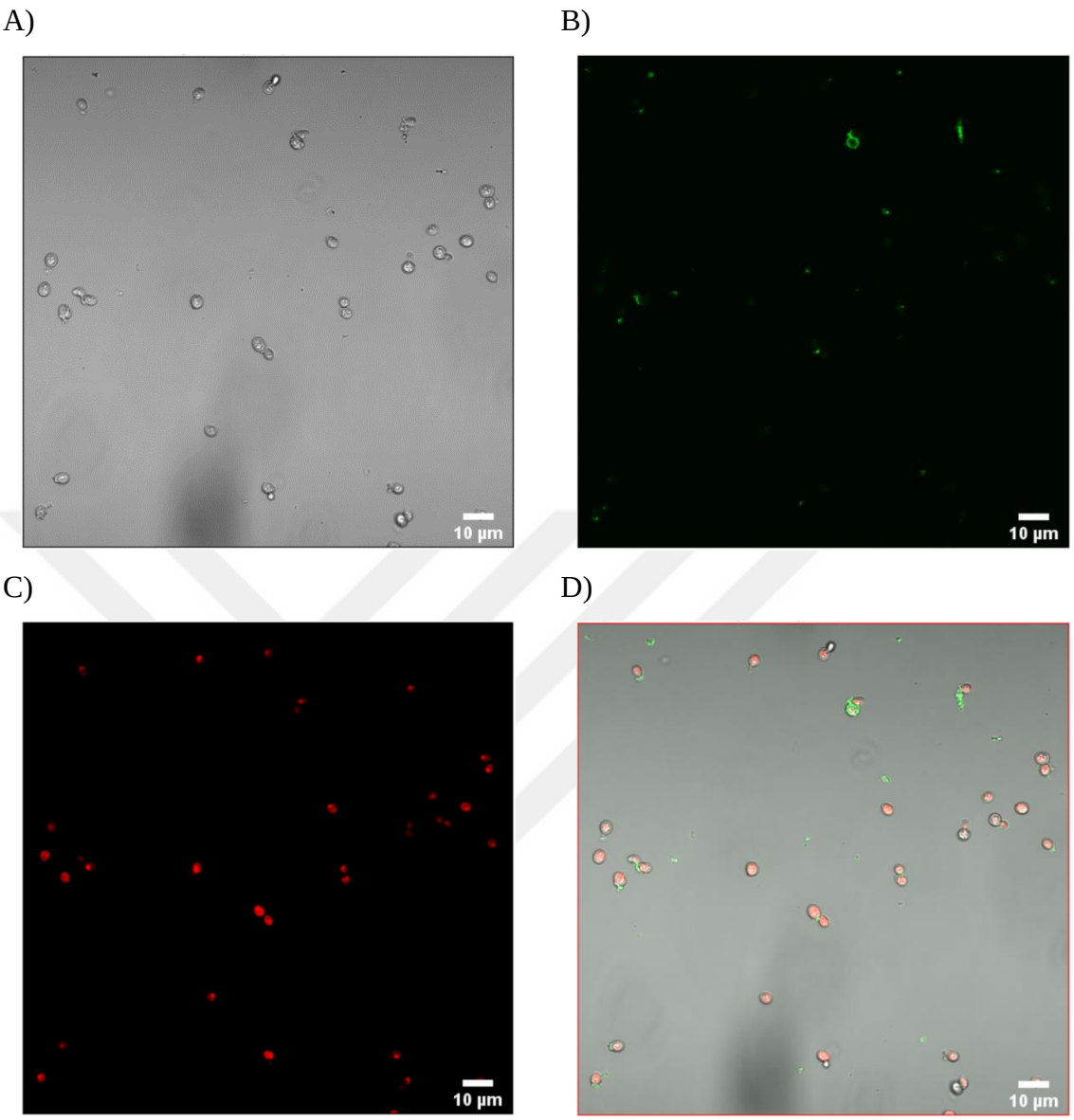

Figure F.12. CLSM images of 800 mg/L 100nm-A-p PSL NP exposed yeast cells A) Bright field B) FITC C) PI D) Merged image.

F.2. CLSM Images Hybrid NP Exposed Yeast Cells

F.2.1. CLSM Images of 100nm-A-n Hybrid NP Exposed Yeast Cells

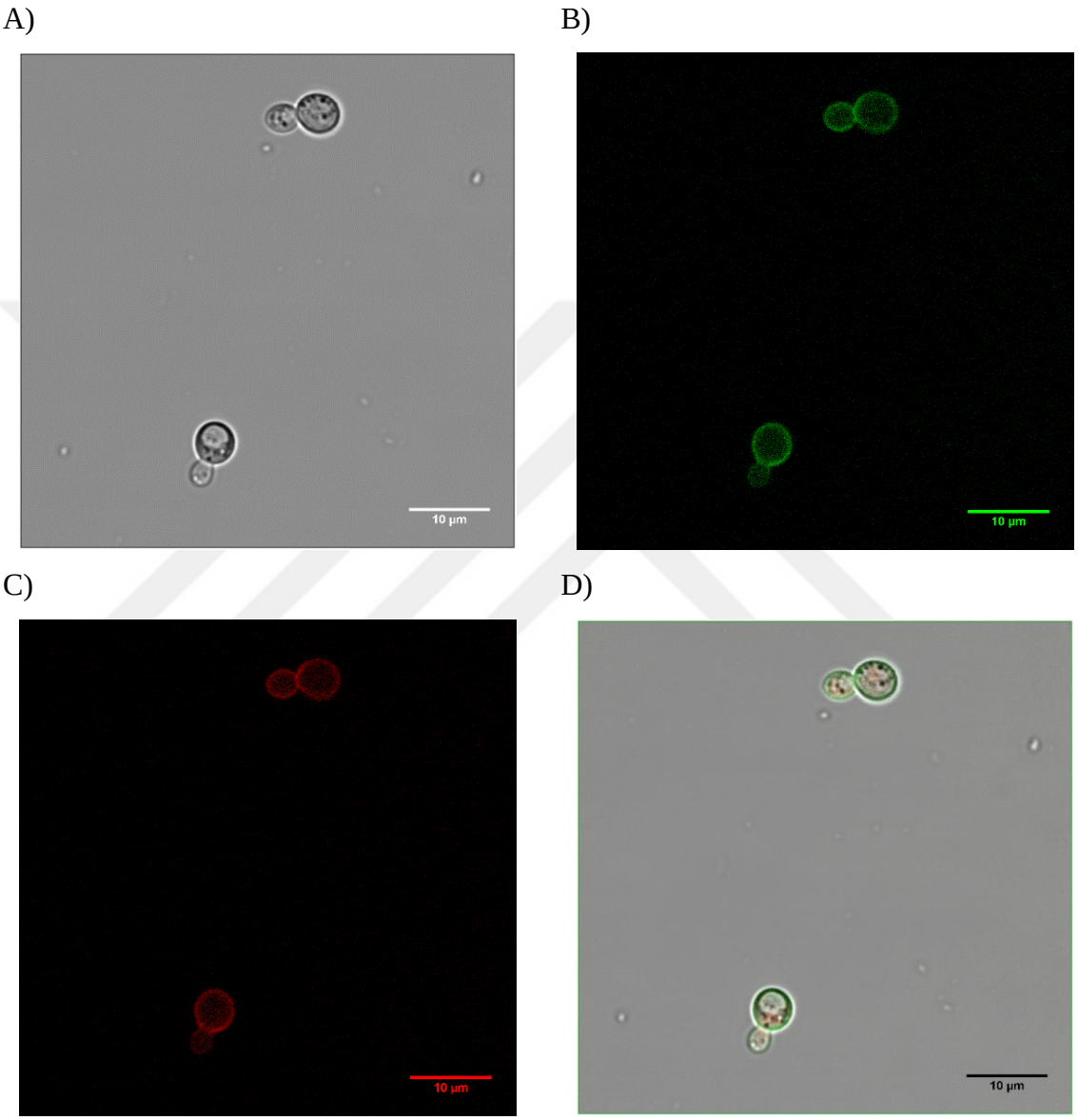

Figure F.13. CLSM images of 100 mg/L 100nm-A-n hybrid NP exposed yeast cells A) Bright field B) FITC C) PI D) Merged image.

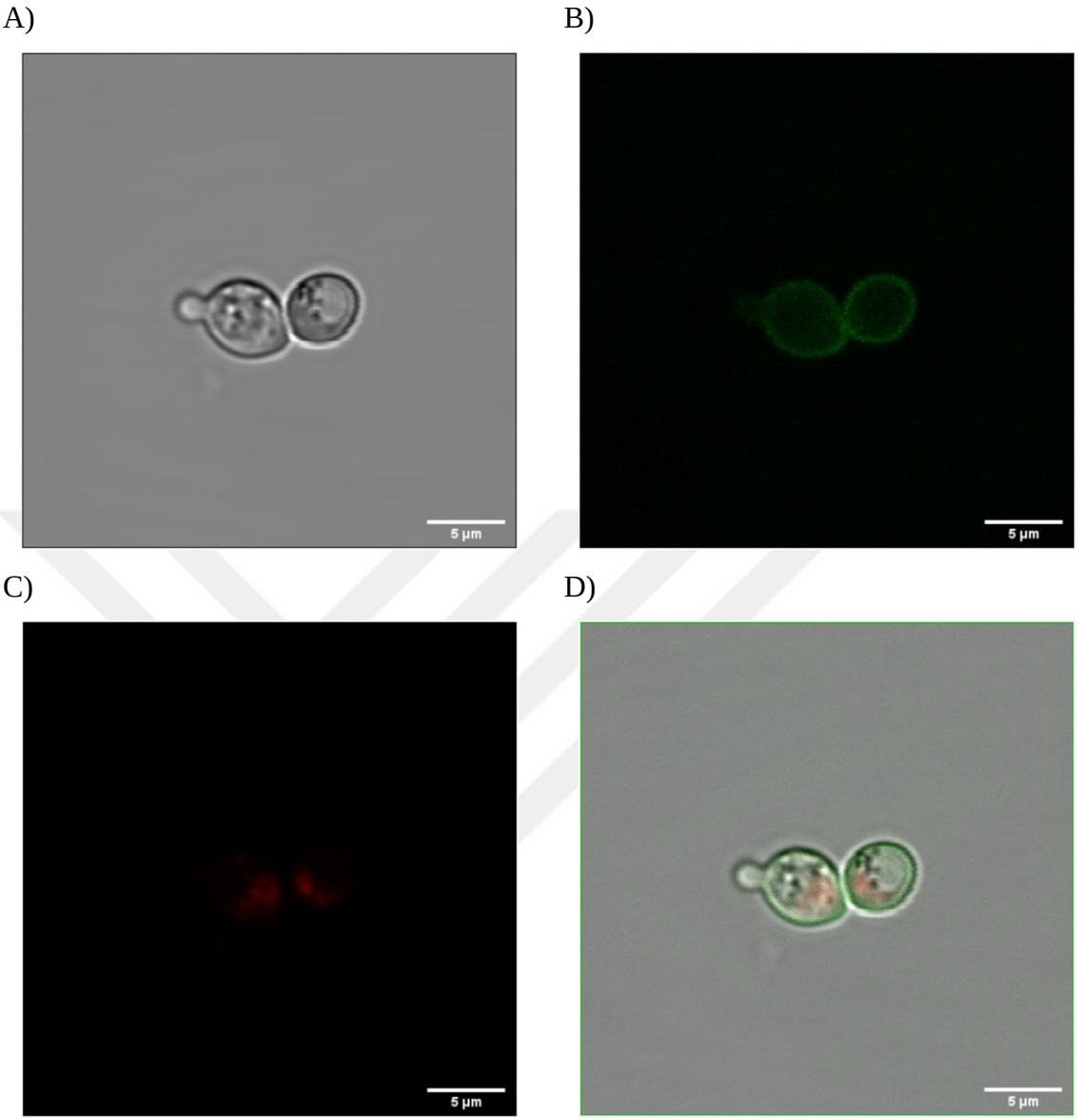

Figure F.14. CLSM images of 100 mg/L 100nm-A-n hybrid NP exposed yeast cells emphasizing the surface coverage of NPs A) Bright field B) FITC C) PI D) Merged image.

F.2. CLSM Images PSL NP Exposed Yeast Cells after Lat-A Treatment

F.2.1. CLSM Images of 30nm-C-n PSL NP Exposed Yeast Cells after Lat-A Treatment

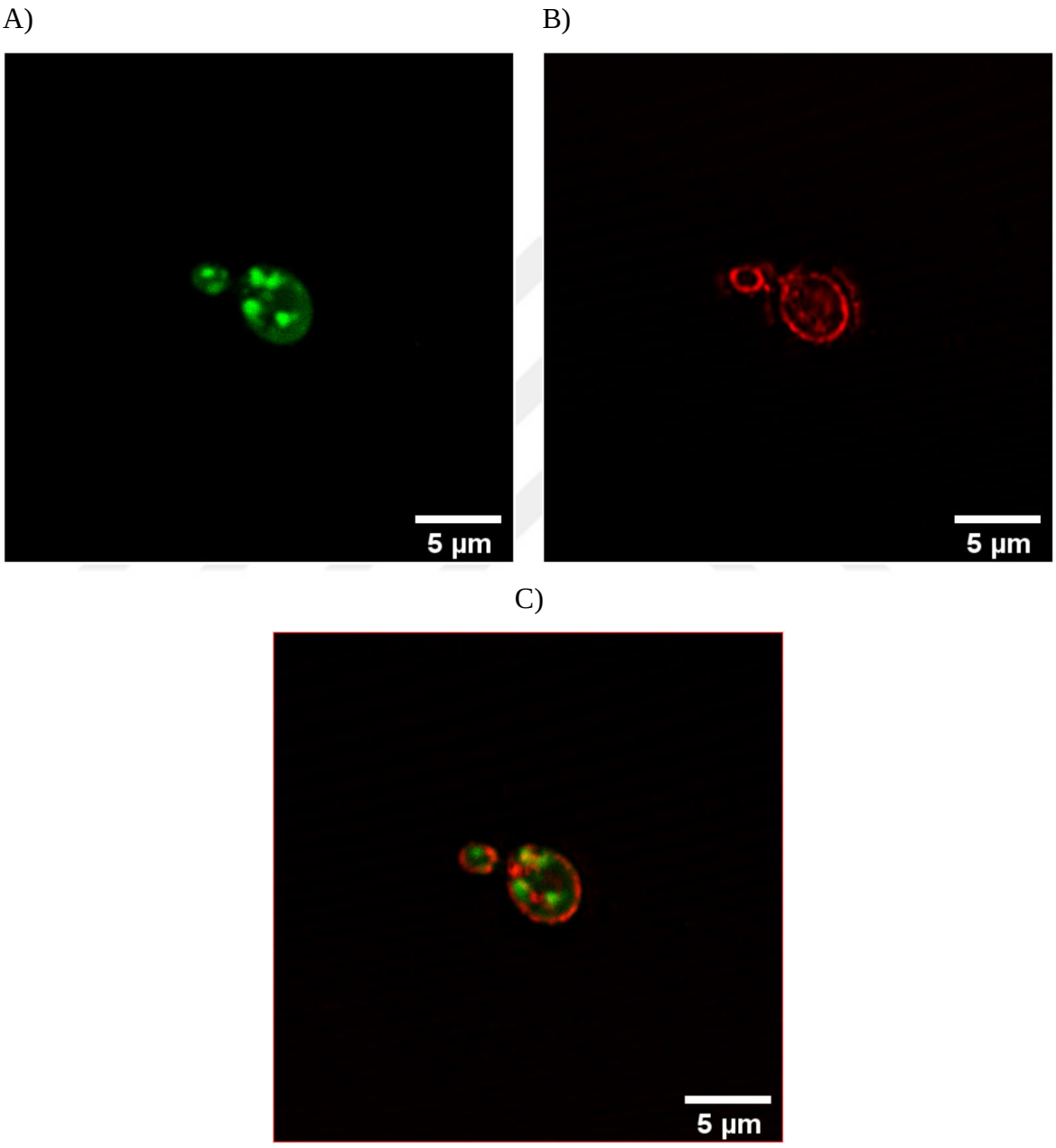

Figure F.15. CLSM images of 100 mg/L 30nm-C-n PSL NP exposed yeast cells after 1 hour of 1 µM Lat-A treatment A) FITC B) PI C) Merged image.

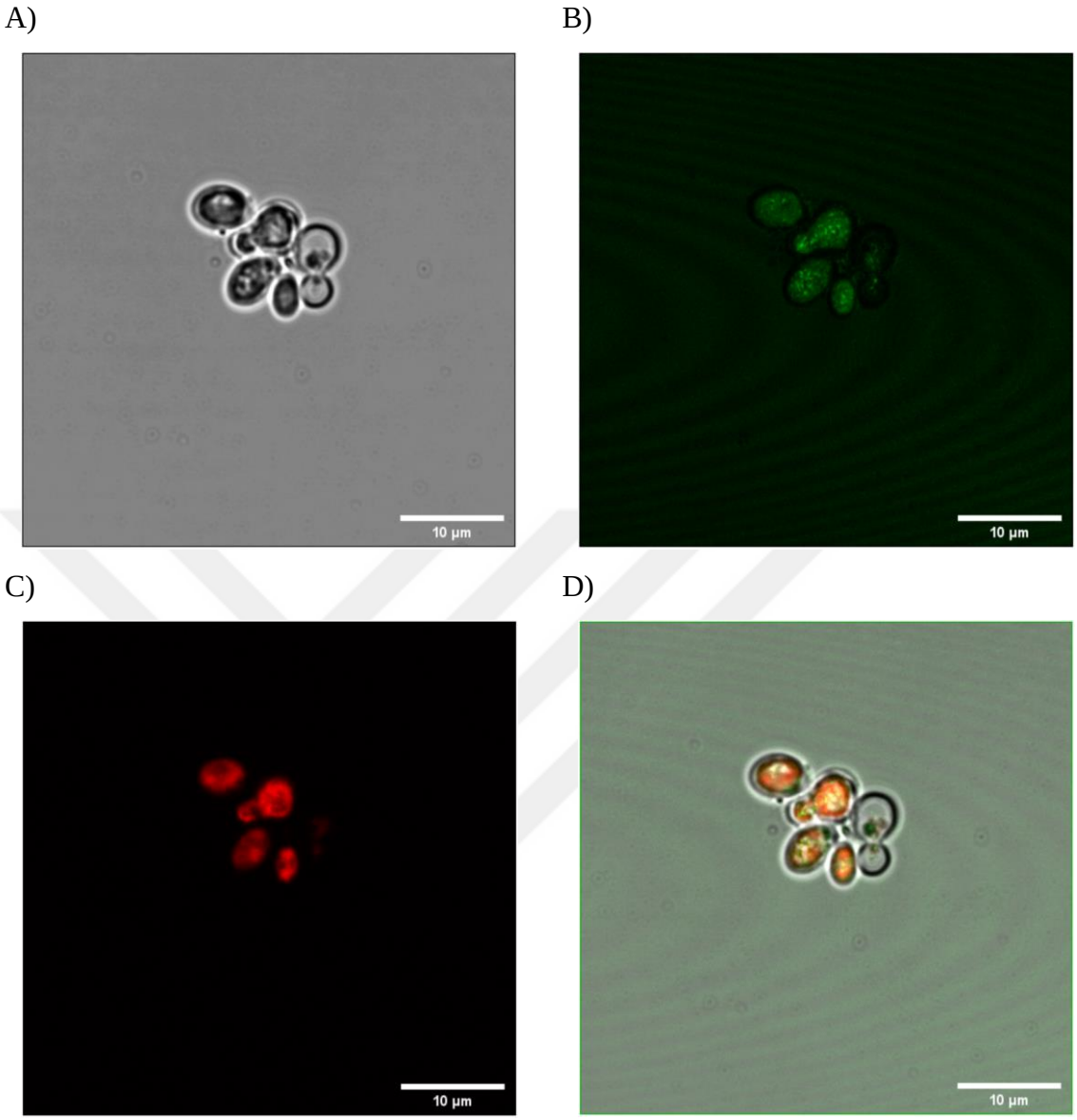

Figure F.16. CLSM images of 100 mg/L 30nm-C-n PSL NP exposed yeast cells after 1 hour of 200 µM Lat-A Treatment A) Bright field B) FITC C) PI D) Merged image.

F.2.2. CLSM Images of 50nm-A-p PSL NP Exposed Yeast Cells after Lat-A Treatment

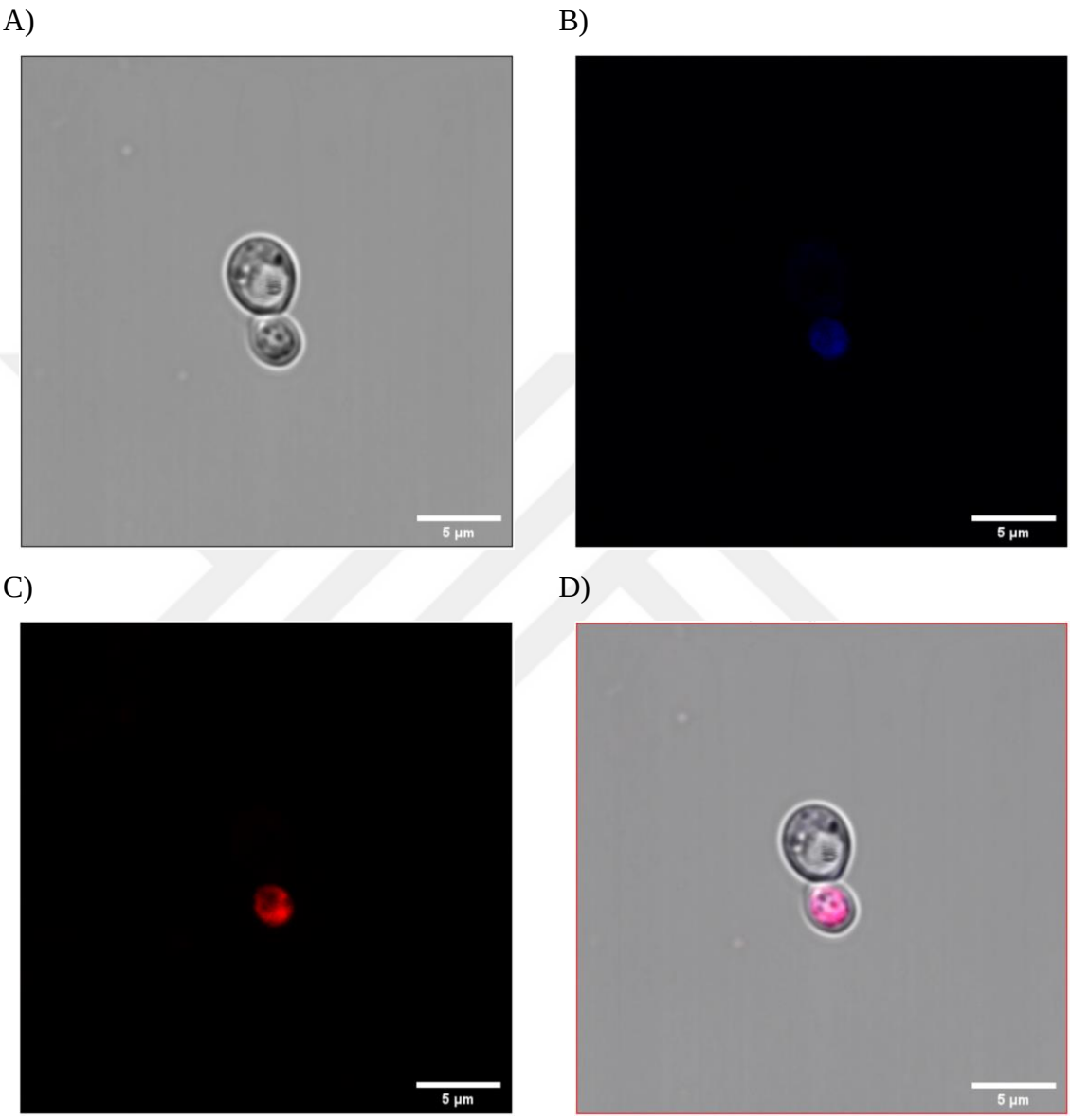

Figure F.17. CLSM images of 100 mg/L 50nm-A-p PSL NP exposed yeast cells after 1 hour of 1 µM Lat-A Treatment A) Bright field B) FITC C) PI D) Merged image.

F.3. CLSM Images PSL NP Exposed Yeast Cells after Nocodazole Treatment

F.3.1. CLSM Images of 30nm-C-n PSL NP Exposed Yeast Cells after 1 hour Nocodazole Treatment

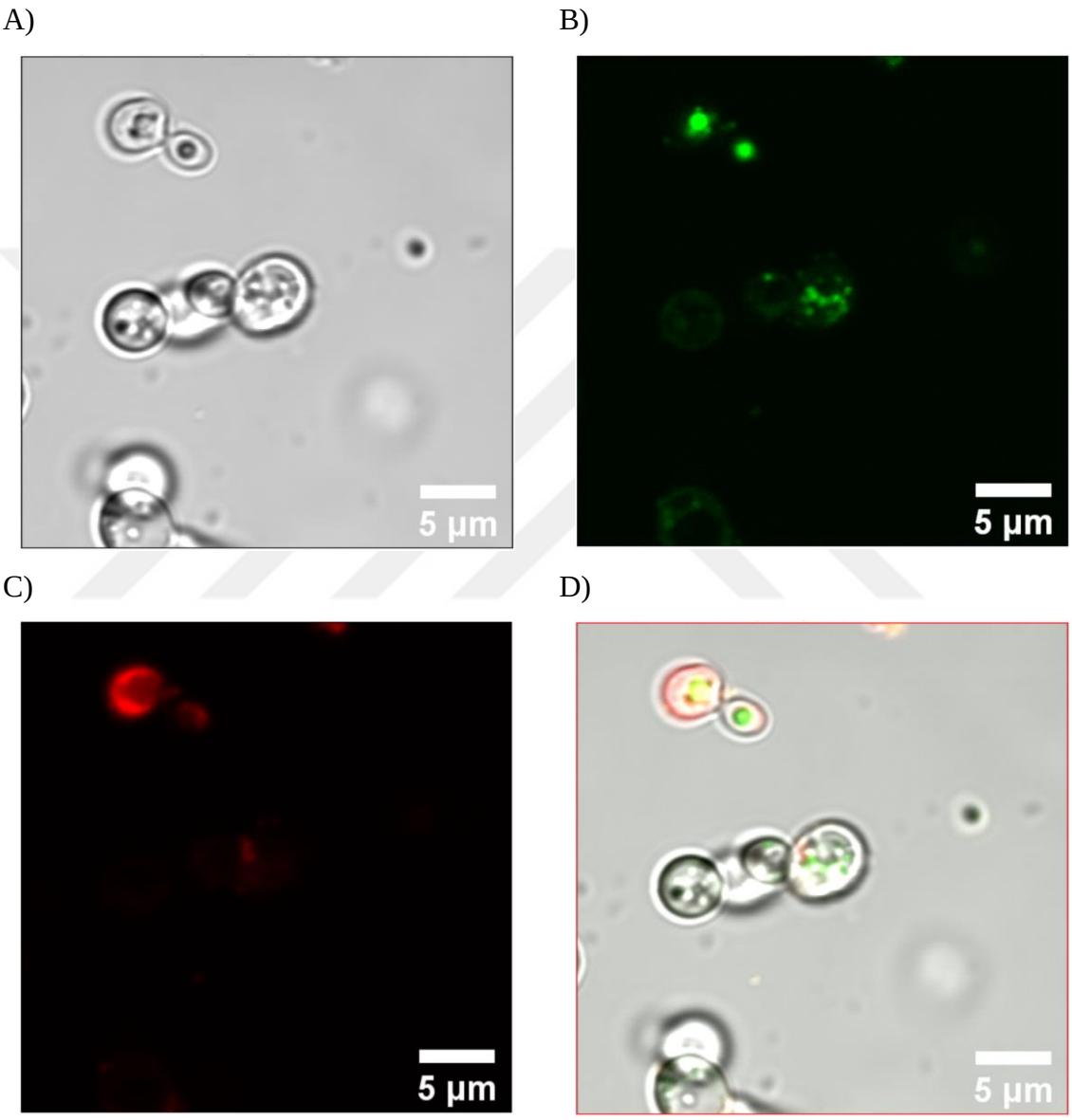

Figure F.18. CLSM images of 100 mg/L 30nm-C-n PSL NP exposed yeast cells after 1 hour of 15 µg/ml Nocodazole Treatment A) Bright field B) FITC C) PI D) Merged image.

F.3.2. CLSM Images of 100nm-A-p NP Exposed Yeast Cells after 1 hour Nocodazole Treatment

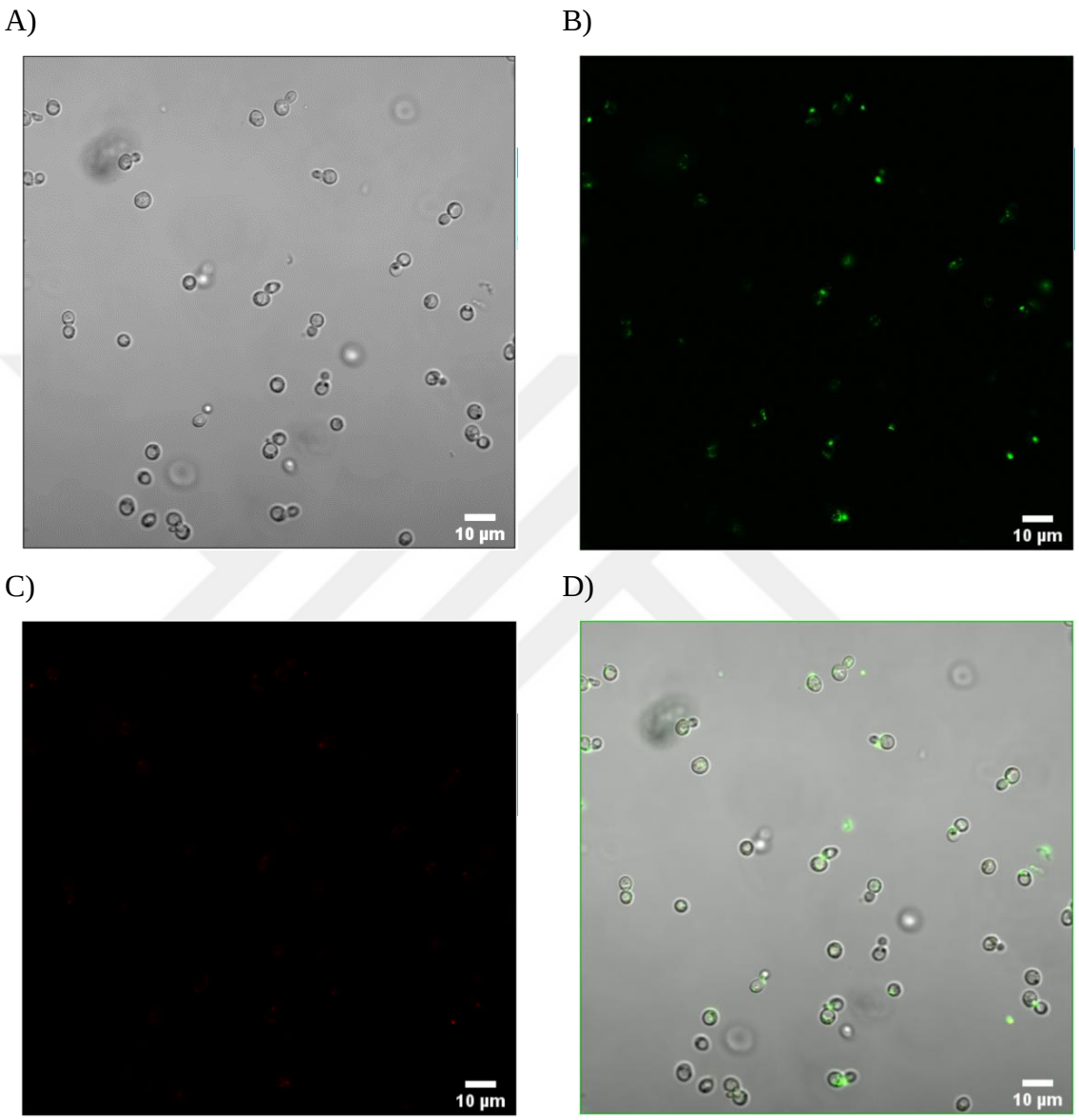

Figure F.19. CLSM images of 100 mg/L 100nm-A-p PSL NP exposed yeast cells after 1 hour of 15 µg/ml Nocodazole Treatment A) Bright field B) FITC C) PI D) Merged image.

F.3.3. CLSM Images of 30nm-C-n PSL NP Exposed Yeast Cells after 2 Hours of Nocodazole Treatment

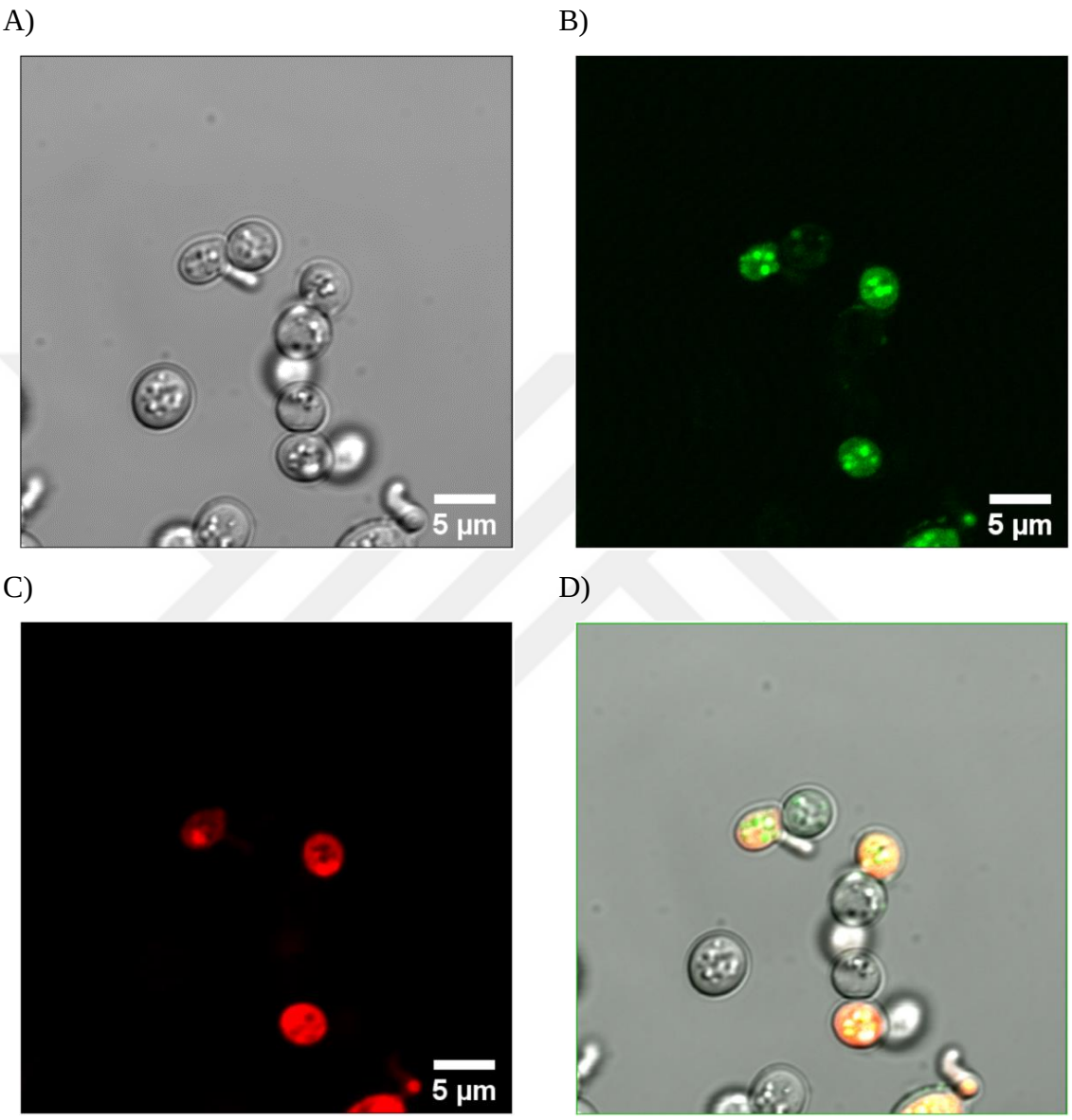

Figure F.20. CLSM images of 100 mg/L 30nm-C-n PSL NP exposed yeast cells after 2 hours of 15 µg/ml Nocodazole Treatment A) Bright field B) FITC C) PI D) Merged image.

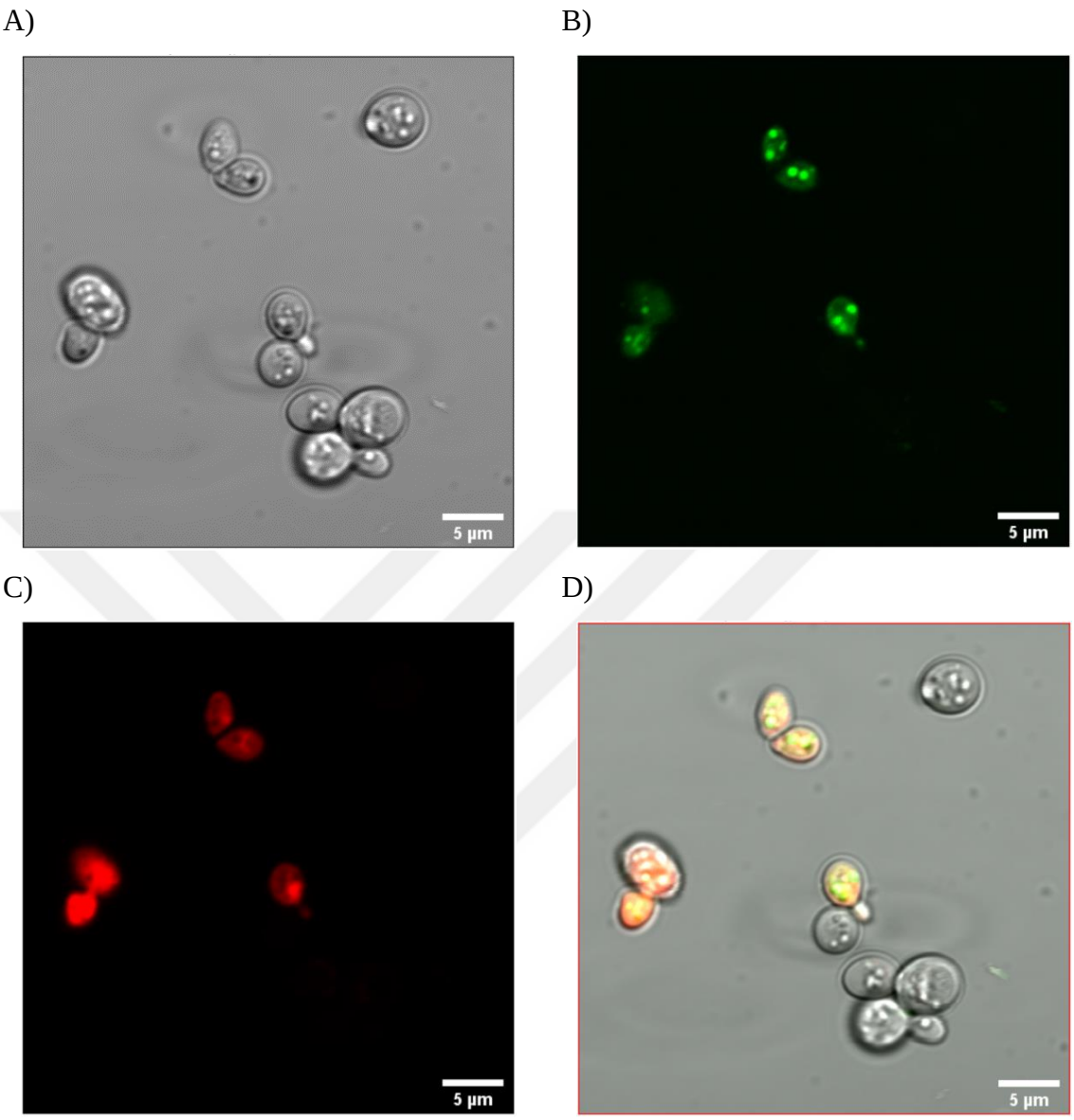

Figure F.21. CLSM images of 100 mg/L 30nm-C-n PSL NP exposed yeast cells after 2 hours of 15 µg/ml nocodazole treatment showing the toxic effect of NPs A) Bright field B) FITC C) PI D) Merged image.

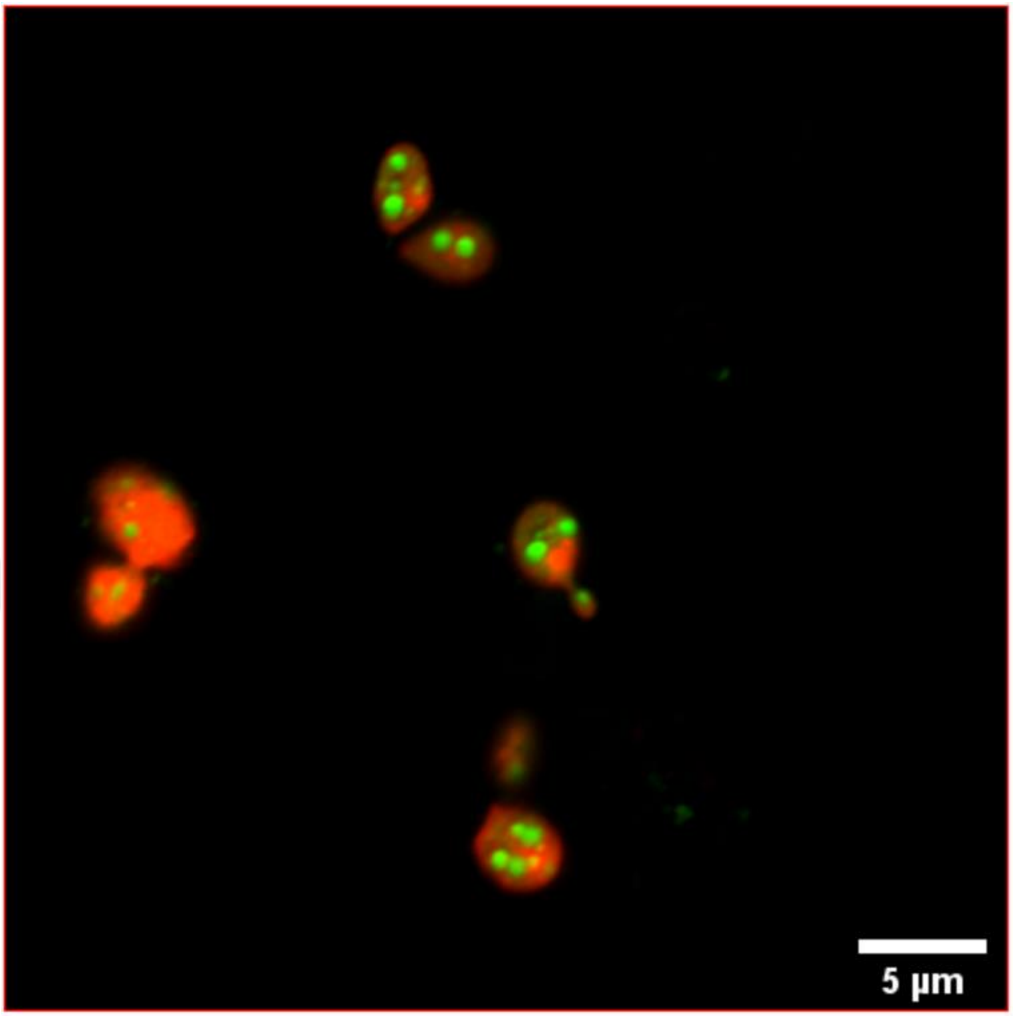

Figure F.22. High resolution merged CLSM image of 100 mg/L 30nm-C-n PSL NP exposed yeast cells after 2 hours of 15 µg/ml nocodazole treatment.

F.3.4. CLSM Images of 100nm-A-p PSL NP Exposed Yeast Cells after 2 Hours Nocodazole Treatment

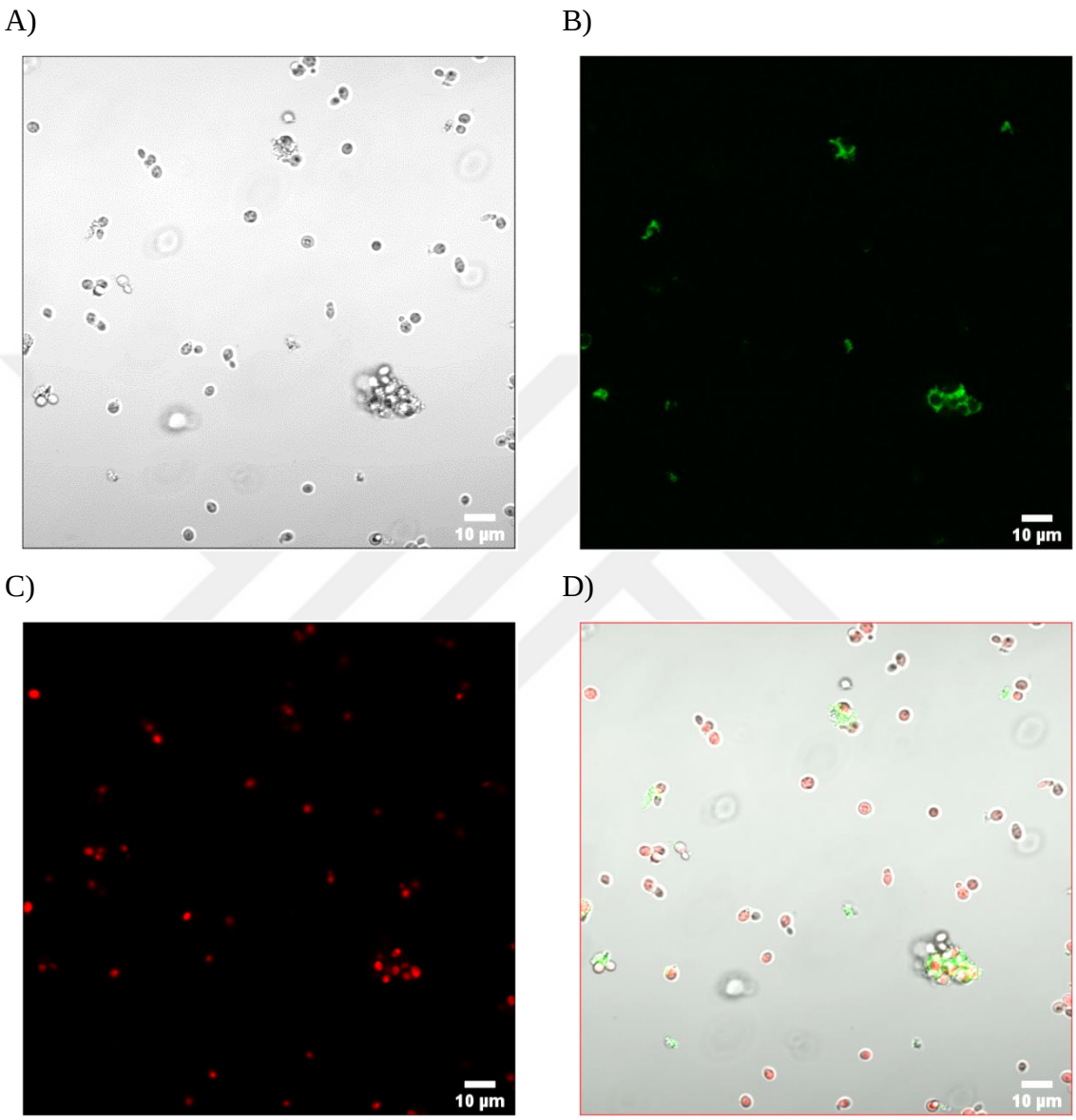

Figure F.23. CLSM images of 500 mg/L 100nm-A-p PSL NP exposed yeast cells after 2 hours of 15 µg/ml nocodazole treatment A) Bright field B) FITC C) PI D) Merged image.

F.4. CLSM Images PSL NP Exposed Yeast Cells after Ethanol Treatment

F.4.1. CLSM Images of 30nm-C-n PSL NP Exposed Yeast Cells after Ethanol Treatment

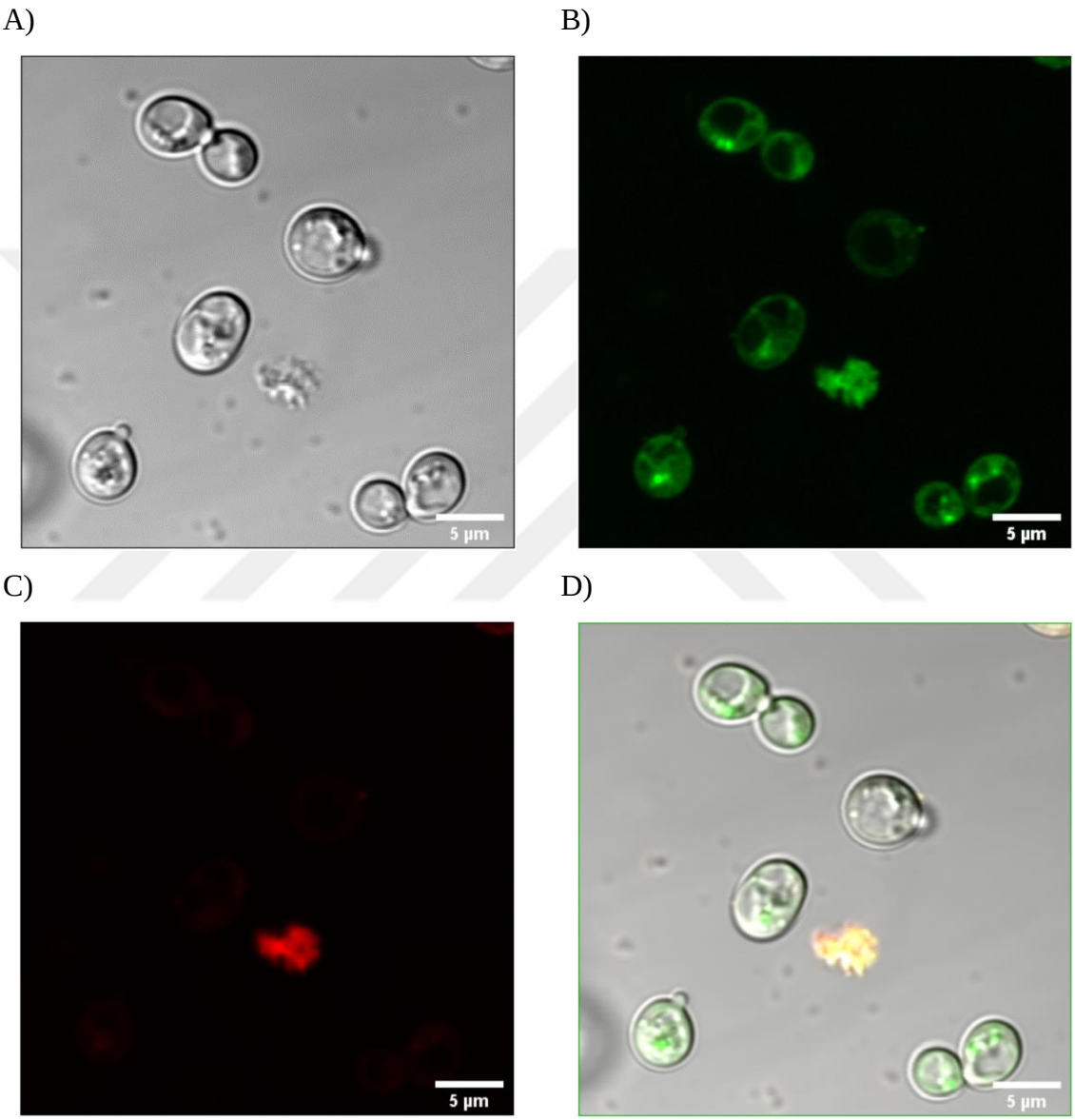

Figure F.24. CLSM images of 100 mg/L 30nm-C-n PSL NP exposed yeast cells after 1 hour of 5% (v/v) ethanol treatment A) Bright field B) FITC C) PI D) Merged image.

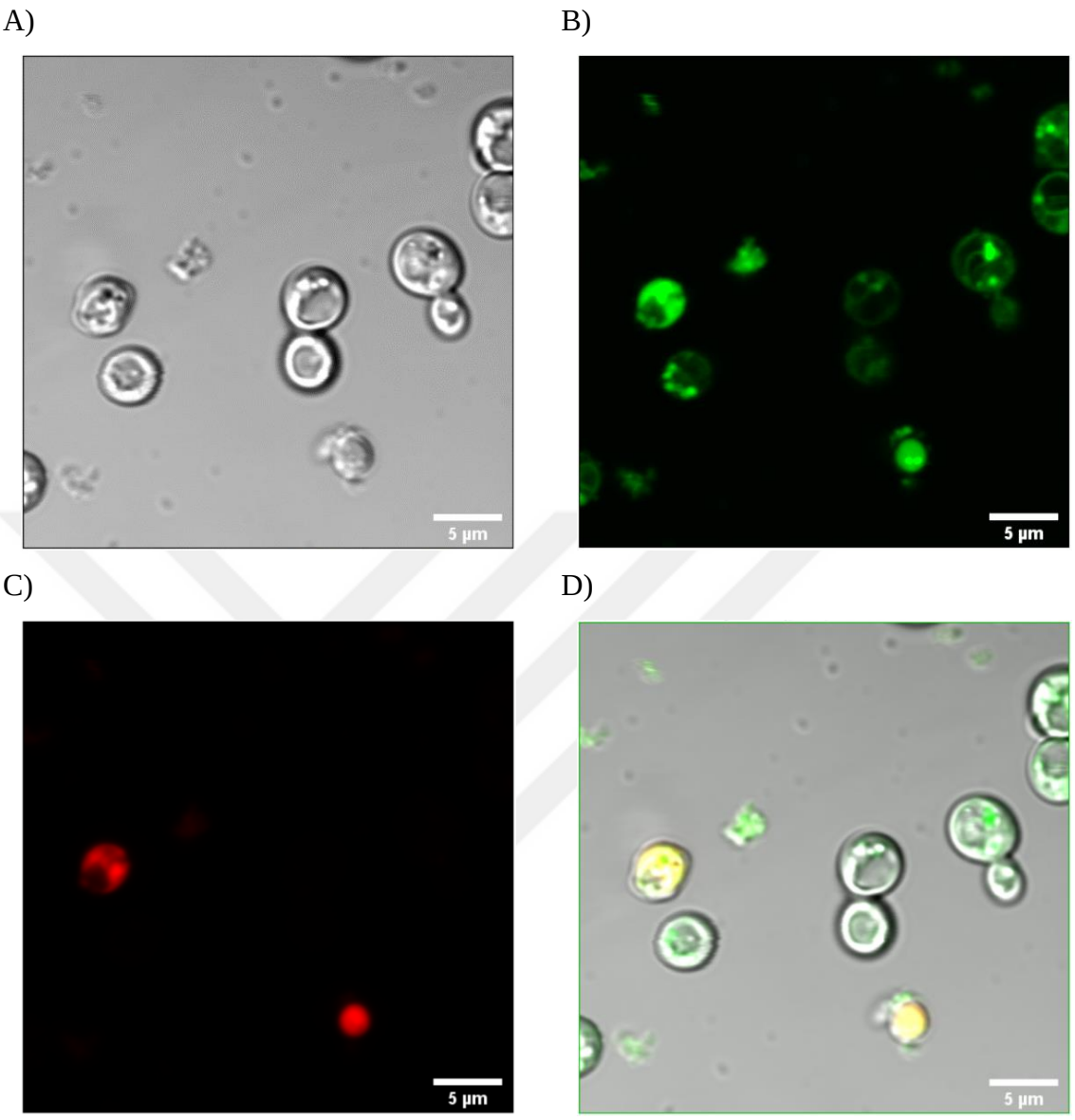

Figure F.25. CLSM images of 100 mg/L 30nm-C-n PSL NP exposed yeast cells after 1 hour of 5% (v/v) ethanol treatment showing the NP internalization in the cytoplasm and/or in the nucleus of the cells A) Bright field B) FITC C) PI D) Merged image.

F.4.2. CLSM Images of 100nm-A-p PSL NP Exposed Yeast Cells after Ethanol Treatment

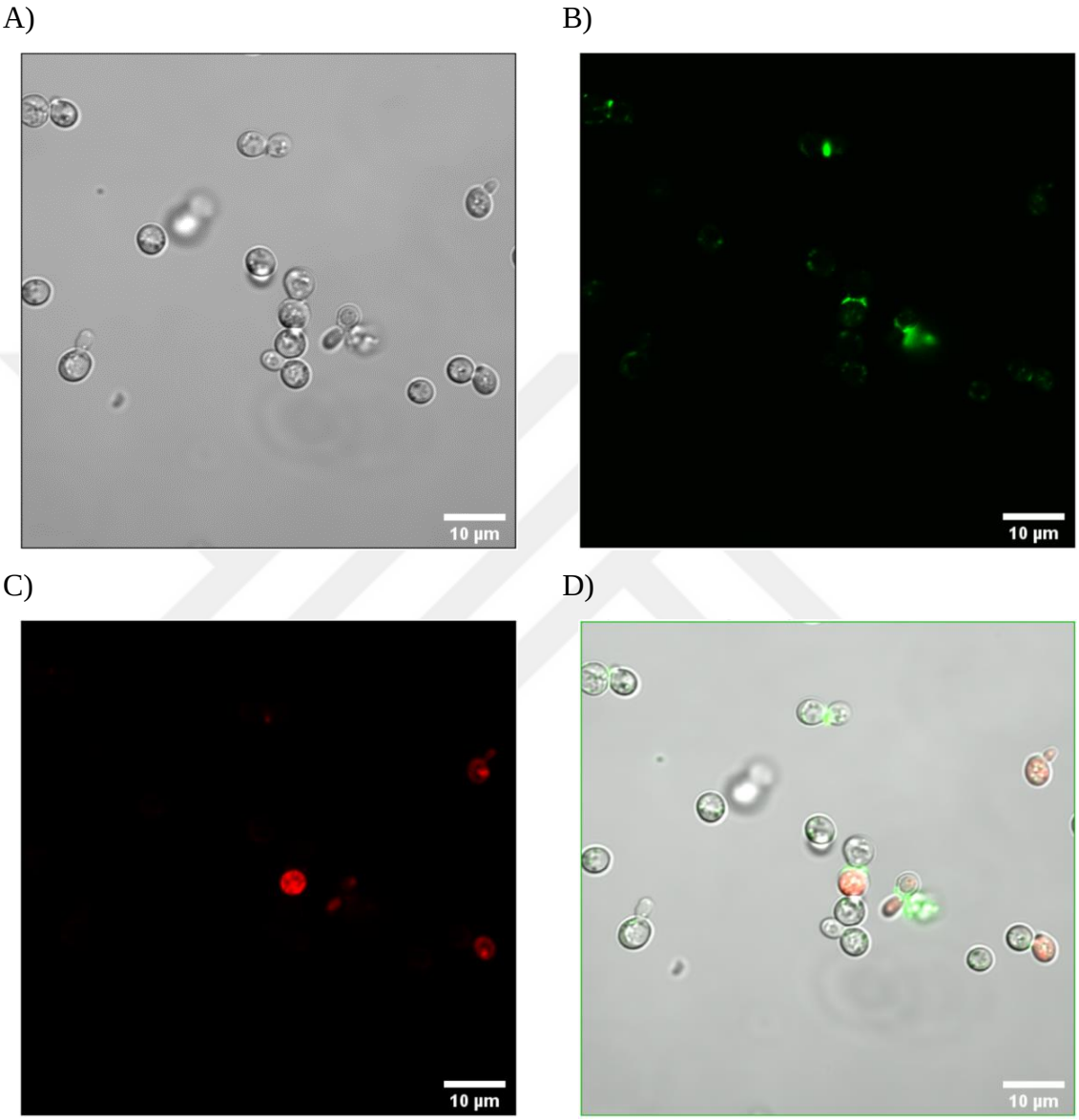

Figure F.26. CLSM images of 100 mg/L 100nm-A-p PSL NP exposed yeast cells after 1 hour of 5% (v/v) ethanol treatment A) Bright field B) FITC C) PI D) Merged image.

APPENDIX G: FLUORESCENCE INTENSITY ANALYSIS OF 30nm-C-n PSL NPs INSIDE THE YEAST CELLS WITH OR WITHOUT INHIBITOR TREATMENT

Table G.1. Fluorescently Labelled Area inside the Yeast Cells Exposed to 30nm-C-n PSL NPs with or without 15µg/ml Nocodazole Treatment.

	Fluorescently Labelled Area in the Cell (μm^2)		
Cell	**No Inhibitor**	**Nocodazole 1 hour**	**Nocodazole 2 hours**
1	12.798	9.440	4.744
2	8.078	8.321	4.915
3	6.618	7.713	5.134
4	5.280	9.172	3.917
5	4.623	11.387	4.550
6	6.156	10.340	10.486
7	7.737	10.413	4.817
8	3.625	4.087	3.674
9	5.182	11.022	2.530
10	12.311	7.640	5.182
11	11.800	4.501	1.873
12	9.489	7.348	3.285
13	13.065	7.007	2.579
14	11.289	3.844	5.280
15	8.005	9.099	4.769
Average	8.404	8.089	4.516

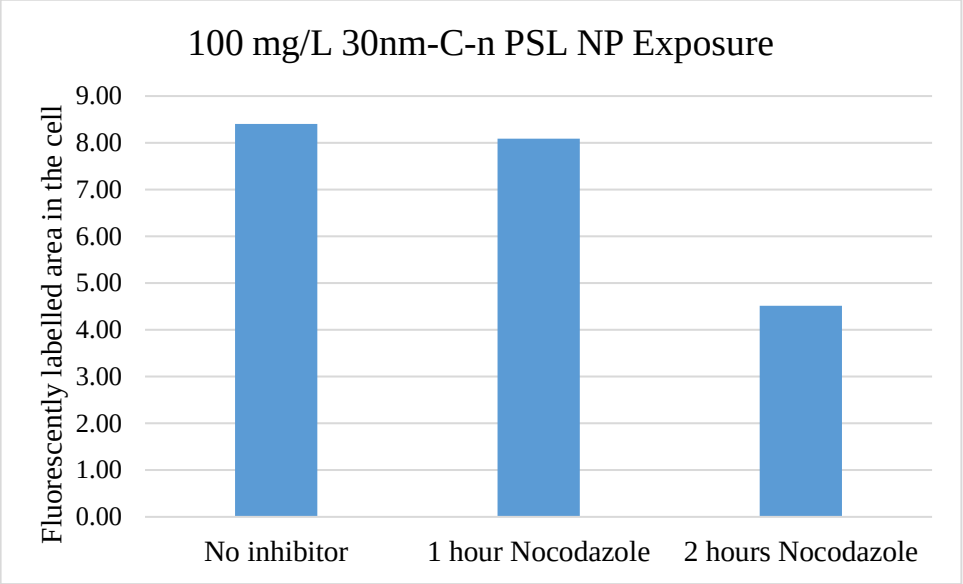

Figure G.1. Fluorescently labelled area in the cell in the absence and the presence of 15µg/ml nocodazole treatment.

Table G.2. Integrated Density of the Fluorescence inside the Yeast Cells Exposed to 30nm-C-n PSL NPs with or without 15µg/ml Nocodazole Treatment.

	Integrated Density (IntDen)		
Cell	**No Inhibitor**	**Nocodazole 1 hour**	**Nocodazole 2 hours**
1	3263.4	2407.2	1209.8
2	2059.8	2121.8	1253.2
3	1687.5	1966.7	1309.1
4	1346.3	2339.0	998.9
5	1178.8	2903.6	1160.2
6	1569.7	2636.8	2674.0
7	1972.9	2655.4	1228.4
8	924.4	1042.3	936.8
9	1321.5	2810.5	645.2
10	3139.3	1948.1	1321.5
11	3009.0	1147.8	477.7
12	2419.6	1873.7	837.6

Table G.2. Integrated Density of the Fluorescence inside the Yeast Cells Exposed to 30nm-C-n PSL NPs with or without 15µg/ml Nocodazole Treatment. (cont.)

	Integrated Density (IntDen)		
Cell	**No Inhibitor**	**Nocodazole 1 hour**	**Nocodazole 2 hours**
13	3331.7	1786.8	657.6
14	2878.8	980.3	1346.3
15	2041.2	2320.4	1216.0
Average	2142.9	2062.7	1151.5

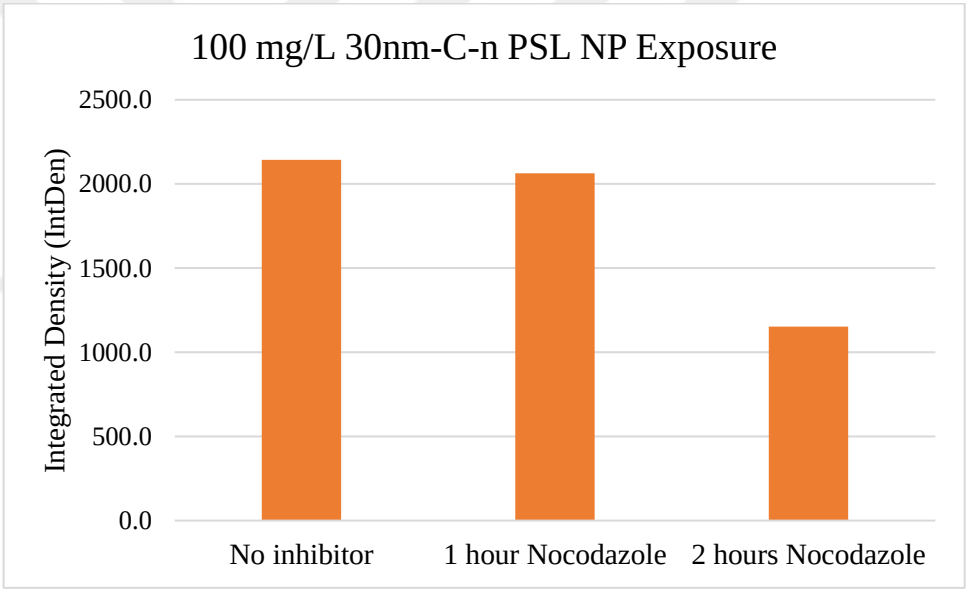

Figure G.2. Integrated fluorescence density in the cell in the absence and the presence of 15µg/ml nocodazole treatment.